Macroscopic forming simulation of unidirectional non-crimp fabrics: Hyperelastic material modeling and 3D-solid-shell approach

Zur Erlangung des akademischen Grades eines

Doktors der Ingenieurwissenschaften (Dr.-Ing.)

von der KIT-Fakultät für Maschinenbau des
Karlsruher Instituts für Technologie (KIT)

angenommene

DISSERTATION

von

M. Sc. Bastian Benjamin Jascha Schäfer
geb. in Köln

Tag der mündlichen Prüfung:	20.03.2024
Hauptreferentin:	Prof. Dr.-Ing. Luise Kärger
Korreferentin 1:	Prof. Emmanuelle Vidal-Sallé
Korreferent 2:	Prof. Dr.-Ing. Frank Henning

Abstract

Forming of an initially flat stack of engineering textiles into a complex three-dimensional shape is the initial step in different liquid composite molding processes to manufacture high-performance components from continuous fiber reinforced plastics (CoFRP). The forming has a decisive influence on subsequent process steps and the structural behavior of the final component. Process design can be supported by suitable simulation methods to ensure defect-free manufacturing and fully realize a material's potential. Thereby, unidirectional non-crimp fabrics (UD-NCF) have the highest lightweight potential due to their straight rovings compared to woven fabrics with undulated fibers. The objective of this work is the experimental analysis of the relevant mechanisms for forming UD-NCF and consequent development of efficient macroscopic modeling approaches.

In the first part of this work (Chapter 4), the inter- and intra-ply deformation mechanisms of UD-NCF are systematically characterized and forming studies of different geometrically challenging shapes quantitatively analyzed. All tests are conducted for a unidirectional and a bidirectional NCF to compare both materials and highlight the specific challenges for UD-NCF. The UD-NCF exhibits a strongly anisotropic and asymmetric behavior, since the transverse behavior is determined by the stitching instead of a second fiber orientation. Thus, a solely shear-focused description of the membrane behavior is insufficient. Different membrane deformation modes with superimposed shear, transverse tensile and perpendicular compressive strains are observed during characterization as well as forming. The transverse bending stiffness is significantly lower than bending in the roving direction, resulting in strong twisting for off-axis loads.

In the second part of this work (Chapter 5), a macroscopic forming model for UD-NCF with 2D-elements based on a hyperelastic membrane and a hypoelastic bending approach is proposed. The different membrane deformation modes are related to suitable invariants. A coupling between the transverse tensile and perpendicular in-plane compressive behavior is introduced to model significant roving slippage. A new generalized approach for the strain energy density and coupling between the deformation modes is proposed that requires significantly less parameters than existing approaches. The objective is to minimize the complexity of the model and thus facilitate its adaptation to other materials. The forces and strains occurring in the characterization tests are well reproduced. In comparison with experimental forming tests for different shapes and layup configurations, a good agreement is observed.

In the third part of this work (Chapter 6), a 3D approach to account for compaction during forming is presented, which enables a prediction of the final thickness and consequently of the fiber volume content. Conventional solid elements are not suitable for forming simulations due to numerical locking phenomena for thin structures under bending. A locking-free 3D solid-shell formulation is extended for highly anisotropic materials and membrane-bending decoupling. It is finally implemented as a user-defined element in ABAQUS/-Explicit. The proposed solid-shell approach accurately models the forming behavior with a single element over the thickness for large element aspect ratios. As a result, the developed 3D solid-shell element is capable of modeling different forming studies as accurately as 2D-element based approaches, but the behavior in thickness direction can be additionally taken into account.

Overall, this work improves the understanding of the relevant mechanisms for forming non-crimp fabrics and their efficient modeling. The developed methods are extensively validated to demonstrate their applicability in various scenarios. The work concludes with recommendations for further method development, e.g. modeling of mesoscopic effects with non-local approaches or application of the solid-shell element to other semi-finished products.

Kurzfassung

Die Umformung zweidimensionaler textiler Halbzeuge in eine komplexe Geometrie ist der erste Schritt verschiedener "Liquid Composite Modling"-Prozesse zur Herstellung von Hochleistungsbauteilen aus endlosfaserverstärkten Kunststoffen. Die Umformung hat signifikanten Einfluss auf die nachfolgenden Prozessschritte und die Eigenschaften des fertigen Bauteils. Die Prozessauslegung kann durch geeignete Simulationsmethoden unterstützt werden, um eine defektfreie Herstellbarkeit zu gewährleisten und das Potenzial des Werkstoffs voll auszuschöpfen. Dabei haben unidirektionale Kohlenstofffasergelege (UD-Gelege) das höchste Leichtbaupotenzial aufgrund ihrer geraden Rovings im Vergleich zu Geweben mit ondulierten Fasern. Ziel dieser Arbeit ist die experimentelle Analyse der relevanten Umformmechanismen von UD-Gelegen und anschließende Entwicklung effizienter makroskopischer Modellierungsansätze.

Im ersten Teil dieser Arbeit (Kapitel 4) werden die inter- und intra-ply Deformationsmechanismen systematisch charakterisiert und das Verhalten in Umformstudien an verschiedenen Geometrien gemessen. Alle Versuche werden für ein unidirektionales und ein bidirektionales Gelege durchgeführt, um beide Materialien zu vergleichen und die besonderen Anforderungen von UD-Gelegen herauszuarbeiten. Das Verhalten von UD-Gelegen ist stark anisotrop und asymmetrisch, da das Verhalten in die Querrichtung nur durch die Vernähung bestimmt wird. Eine isolierte Betrachtung des Schubanteils im Membranverhalten ist daher unzureichend. Sowohl bei der Charakterisierung als auch bei der Umformung treten Deformationsmoden mit überlagerten Schub-, Querzug- und Druckdeformationen auf. Außerdem ist die Biegesteifigkeit in Querrichtung deutlich geringer als in Rovingrichtung, wodurch es zu starken Verdrillungen kommen kann.

Im zweiten Teil dieser Arbeit (Kapitel 5) wird ein makroskopisches Umformsimulationsmodell für UD-Gelege mit 2D-Elementen vorgestellt. Das Membranverhalten wird hyperelastisch und das Biegeverhalten hypoelastisch modelliert. Die Membran-Deformationsmoden werden mit geeigneten Invarianten verknüpft. Starkes Rovingabgleiten wird durch eine Kopplung des Querzug- und Druckverhaltens abgebildet. Ein verallgemeinerter Ansatz wird für die Dehnungsenergiedichte und Kopplung verwendet, welcher weniger Parameter benötigt als existierende Modelle. Ziel ist dabei, die Komplexität des Modells zu minimieren und die Anwendung für andere Materialien zu erleichtern. Die Kräfte und Dehnungen der Charakterisierungsversuche werden gut abgebildet. Im Vergleich mit experimentellen Umformversuchen für verschiedene Geometrien und Lagenaufbauten zeigt sich eine gute Übereinstimmung.

Im dritten Teil dieser Arbeit (Kapitel 6) wird ein 3D-Ansatz zur Berücksichtigung der Kompaktierung während der Umformung vorgestellt. Dadurch kann die Bauteildicke und somit auch der Faservolumengehalt vorhergesagt werden. Konventionelle Volumenelemente sind für Umformsimulationen nicht geeignet, da bei dünnen Strukturen unter Biegung numerische Versteifungseffekte auftreten. Deshalb wird ein sogenanntes Solid-Shell-Element um Modifikationen für stark anisotrope Materialien und eine Membran-Biege-Entkopplung erweitert und als 3D User-Element in ABAQUS/Explicit implementiert. Das Solid-Shell kann das Umformverhalten mit einem einzigen Element über die Dicke für große Aspektverhältnisse immer noch genau abbilden. Dadurch können verschiedene Umformstudien genauso gut modelliert werden wie mit auf 2D-Elementen basierenden Ansätzen, aber das Verhalten in Dickenrichtung kann zusätzlich berücksichtigt werden.

Insgesamt verbessert diese Arbeit das Verständnis der relevanten Mechanismen für die Umformung von Gelegen und deren effiziente Modellierung. Die entwickelten Methoden werden umfangreich validiert und ihre Anwendbarkeit in verschiedenen Szenarien demonstriert. Abschließend werden Möglichkeiten für die weitere Methodenentwicklung motiviert, z.B. die Modellierung mesoskopischer Effekte mit nichtlokalen Ansätzen oder die Anwendung des Solid-Shell-Elements auf andere Halbzeuge.

Contents

Acronyms and symbols

Acronyms

1D, 2D, 3D	One-, two, three-dimensional
ANS	Assumed natural strain method
BC	Boundary condition
BET	Bias-extension test
Biax-NCF	Biaxial non-crimp fabric
C3D8	Fully-integrated 3D element in ABAQUS
C3D8I	Fully-integrated 3D element with incompatible modes in ABAQUS
C3D8R	Reduced-integrated 3D element in ABAQUS
C3D8R-Enh	3D element with enhanced hourglass control in ABAQUS
CAE	Computer-aided engineering
CF	Carbon fiber
CoF	Coefficient of friction
CoFRP	Continuous fiber-reinforced plastics
COS	Coordinate system
DIC	Digital image correlation
DiCoFRP	Discontinuous fiber-reinforced plastics
DOF	Degree of freedom
EAS	Enhanced assumed strain method

FE	Finite element
FRP	Fiber-reinforced plastics
FVC	Fiber volume content
GF	Glass fiber
HP-RTM	High Pressure Resin Transfer Moulding
IP	Integration point
KES-FB2	Kawabata evaluation system for fabric bending
LCM	Liquid composite molding
M3D3	Membrane element in ABAQUS
MDZ	Main deformation zone in off-axis tension tests
NCF	Non-crimp fabric
OAT	Off-axis tension test
PFT	Picture frame test
PP	Ply-ply interface
p-model	Analytical pressure-dependent compaction model
pn-model	Analytical pressure- and layer-dependent compaction model
Q1STs	Solid-shell element formulation by Schwarze and Reese
RTM	Resin Transfer Molding
RUC	Representative unit cell
Sch17	Membrane modeling approach for UD-NCF by Schirmaier et al.
SC8R	Reduced-integrated continuum shell element (SC) in ABAQUS
S3	General-purpose shell element in ABAQUS
SRI	Selective reduced integration scheme
TP	Tool-ply interface
UD-NCF	Unidirectional non-crimp fabric

VUMAT	User-defined material behavior in ABAQUS/Explicit
VUGENS	User-defined shell integration scheme in ABAQUS/Explicit
VUEL	User-defined finite element formulation in ABAQUS/Explicit
WCM	Wet Compression Molding

Scalars

γ	Shear angle
κ	Curvature
$\kappa_{11}^{\max}$	Average maximum roving curvature in off-axis tension tests
μ	Coulomb coefficient of friction
μ_{d}	Dynamic coefficient of friction
μ_{s}	Static coefficient of friction
ν	Poisson ratio
Ω	Spatial domain
Φ	Fiber volume content
ρ	Mass density
ρ_{A}	Areal density
ρ_{CF}	Density of carbon fibers
$\Delta\Theta$	Relative fiber orientation at interfaces
Θ^{P}	Angle of the inclined surface during Peirce cantilever test
Θ_{n}	Roving orientation
ε	Engineering strain
ε_1	Linear strain in fiber direction
ε_2	Linear strain in transverse direction
a	Aspect ratio

A, B, C, D	Parameters of analytical compaction model
$C_i(E_i)$	Non-linear stiffness of the decoupled approach with $i \in [2, \gamma, \perp]$
C_i^{i}	Initial stiffness of the decoupled appraoch
C_i^{m}	Middle stiffness of the decoupled appraoch
C_i^{l}	Locking stiffness of the decoupled appraoch
c_i^{t}	Transition exponent of the generalized strain energy density
C_i^{ini}	Initial modulus of the generalized strain energy density
C_i^{mid}	Middle modulus of the generalized strain energy density
C_i^{lock}	Locking modulus of the generalized strain energy density
e_{11}	Exponent controling onset of coupling function
E	Young's modulus
$E_\perp, \varepsilon_\perp$	Perpendicular strain
E_i^{i}	Final strain of initial part of the decoupled approach
E_i^{m}	Initial strain of middle of the decoupled approach
E_i^{l}	Initial strain of locking part of the decoupled approach
f	Point force
f_{n}	Pulling force normalized by initial width
f_{s}	Sled pulling force
F_{l}	Length-related gravity force during cantilever tests
F_{f}	Tangential friction force
g	Gravitational constant
δg_{HW}	Hu-Washizu two-field variational principle
δg^{ext}	Virtual work of external loads
$G_{\mathrm{w}}^{\mathrm{P}}$	Width-related bending stiffness according to Peirce
I_1, I_2, I_3	Isotropic invariants of the right Cauchy-Green deformation tensor

I_4	Pseudo-invariant corresponding to quadratic stretch along $\boldsymbol{a}_0$
I_6	Pseudo-invariant corresponding to shear
I_8	Pseudo-invariant corresponding to quadratic stretch along $\boldsymbol{b}_0$
I_{10}	Pseudo-invariant corresponding to shear angle
I_{11}	Pseudo-invariant corresponding to stretch along $\boldsymbol{b}^{\perp}$
I_i^{a}	Absolute invariant
I_i^{lock}	Locking invariant of the generalized strain energy density
I_i^{t}	Transition invariant of the generalized strain energy density
J	Jacobian determinate
$k_{11}(I_{11})$	Perpendicular compression coupling function
$k_{11}^{\min}$	Slippage-compression parameter of coupling function
l_{bend}	Overhang length in a Peirce cantilever test
l_{e}	Lagest in-plane edge length of an element
l_0	Initial length
M	Bending moment
N	Normal load
n_{IP}	Number of integration points
n_{L}	Number of layers
p_{comp}	Compaction pressure
p_{n}	Compaction pressure normalized by $1\,\mathrm{MPa}$
q	weight per unit length
R^2	Coefficient of determination
$R_{12,\Gamma}$	Shear yield curve coupling γ_{12} and $\varepsilon_{\perp}$ (Schirmaier et al.)
$R_{2,\Gamma}$	Tensile yield surface coupling γ_{12} and $\varepsilon_{\perp}$ (Schirmaier et al.)
s	Curvlinear coordinate

s_{11}	Intensity coefficient of coupling function
S_i^{ini}	Initial stress limit of the generalized strain energy density
$\Delta S_i^{\mathrm{mid}}$	Middle stress range of the generalized strain energy density
t_{rem}	Remaining stack thickness
t_0	Initial thickness
Δt	Thickness correction due to machine compliance
u	Displacement
Δu	Relative tool stroke
V_0	Initial volume
W_{tot}	Total strain energy density
$W_i^{\mathrm{G}}(I_i)$	Generalized strain energy density function with $i \in [4, 6, 8, 11]$
Δw_{n}	Relative necking
w_0, w_1	Initial and current width

Vectors

$\boldsymbol{\alpha}$	Enhanced degrees of freedom
$\boldsymbol{a}, \boldsymbol{b}, \boldsymbol{b}^{\perp}$	Principle material directions of UD-NCF
$\boldsymbol{A}_i$	Principle material orientations
$\boldsymbol{N}(\boldsymbol{\xi})$	Vector form of linear isoparametric shape functions
$\boldsymbol{t}_1^*, \boldsymbol{t}_2^*, \boldsymbol{t}_{\perp}^*$	Material directions in the alternative configuration
$\boldsymbol{R}_{\mathrm{u}}$	Internal nodal forces
$\boldsymbol{u}$	Displacement vector
$\boldsymbol{v}$	Velocity vector
$\boldsymbol{X}$	Initial material coordinates
$\boldsymbol{x}$	Current material coordinates

$\boldsymbol{\xi} = [\xi, \eta, \zeta]^{\mathsf{T}}$	Isoparametric coordinates

Matrices

$\boldsymbol{B}$	B-matrix relating strains to virtual displacements
$\boldsymbol{H}$	Inverse Jacobian matrix in the initial configuration
$\check{\boldsymbol{H}}$	Inverse Jacobian matrix in the current configuration
$\boldsymbol{J}$	Jacobian matrix in the initial configuration
$\check{\boldsymbol{J}}$	Jacobian matrix in the current configuration
$\boldsymbol{M}$	Element mass matrix
$\boldsymbol{T}$	Transformation matrix between contravariant and cartesian components
$\boldsymbol{u}^{\mathrm{node}}$	Matrix of nodal displacements
$\boldsymbol{X}^{\mathrm{node}}$	Matrix of nodal coordinates

Tensors (second-order and fourth-order)

$\Delta\boldsymbol{\kappa}$	Incremental curvature
$\Delta\boldsymbol{\varepsilon}^{0}$	Incremental logarithmic membrane strain
$\boldsymbol{A}, \boldsymbol{B}$	Alternative stretch and idividual rotaton tensor
$\boldsymbol{C}$	Right Cauchy-Green deformation tensor
$\boldsymbol{D}$	Strain rate tensor
$\boldsymbol{E}$	Green-Lagrange strain tensor
$\boldsymbol{\varepsilon}$	Logarithmic strain tensor
$\boldsymbol{F}$	Deformation gradient
$\boldsymbol{G}$	Metric coefficients
$\boldsymbol{I}$	Second-order identity tensor

$\boldsymbol{M}$	Section moments
$\boldsymbol{R}$	Orthogonal rotation tensor
$\boldsymbol{S}$	Second Piola-Kirchhoff stress tensor
$\boldsymbol{\sigma}$	Cauchy stress tensor
$\boldsymbol{\sigma}_{\mathrm{pm}}$	Stress in the principal material directions
$\boldsymbol{\sigma}_{\perp}$	Stress perpendicular to the fiber direction
$\boldsymbol{\sigma}^{\triangledown}$	Cauchy stress rate
$\boldsymbol{\tau}$	Kirchhoff stress tensor
$\boldsymbol{U}$	Right stretch tensor
$\mathbb{C}$	Stiffness tensor
$\mathbb{I}$	Fourth-order identity tensor

Coordinate frames and configurations

Note. For the 2D case applies $i, j = [1, 2]$ and for the 3D case $i, j = [1, 3]$.

$\mathscr{B}_0$	Initial (reference) configuration
$\mathscr{B}_1$	Current configuration
$\{\boldsymbol{e}_i\}$	Orthogonal Green-Naghdi's frame
$\{\boldsymbol{a}_i\}$	Non-orthogonal principal material frame
$\{\boldsymbol{g}^i\}$	Covariant non-orthogonal frame
$\{\boldsymbol{g}_i\}$	Contravariant non-orthogonal frame

Operators, math symbols and additional notations

$\det(\bullet)$	Determinant
$\mathrm{tr}(\bullet)$	Trace
$\nabla(\bullet)$	Spatial gradient
$(\bullet)^\top$	Transpose of a matrix, e.g. $A_{ij}^\top = A_{ji}$
$(\bullet)^{-1}$	Inverse of a matrix
$\cdot$	Single contraction, e.g $\boldsymbol{A} \cdot \boldsymbol{B} = A_{ij} B_{jk}$
$:$	Double contraction, e.g. $\boldsymbol{A} : \boldsymbol{B} = A_{ij} B_{ij}$
$\otimes$	Dyadic product, e.g. $\boldsymbol{A} \otimes \boldsymbol{B} = A_{ij} B_{kl}$
$\dot{(\bullet)}$	Material time derivative
$\lvert\bullet\rvert$	Absolute value
$\triangle(\bullet)$	Incremental value during explicit time integration
$\hat{(\bullet)}$	Voigt notation
$\bar{(\bullet)}$	Covariant components
$(\bullet)^{\xi_i}$, $(\bullet)^{\xi_i \xi_i}$	Derivative with respect to ξ_i or $\xi_i \xi_i$ evaluated at an element's center
$(\bullet)^0$	Evaluated at an element's center
$(\bullet)^\star$	Evaluated at integration points along an element's normal
$(\bullet)_\mathrm{c}$	Compatible part
$(\bullet)_\mathrm{e}$	Enhanced part
$(\bullet)^\mathrm{hg}$	Hourglass part
$(\bullet)^\mathrm{mem}$	Membrane part
$(\bullet)^\mathrm{bend}$	Bending part
$(\bullet)^{,\mathrm{s}}$, $(\bullet)^{,\mathrm{a}}$	Material parameters for low shear angles (Schirmaier et al.)
$(\bullet)^{,\mathrm{e}}$, $(\bullet)^{,\mathrm{b}}$	Material parameters for high shear angles (Schirmaier et al.)

Remark on attributions. Excerpts of this work have been previously published as manuscripts with my significant personal contribution as lead author. This is indicated by footnotes with attributions to the original publication and further details in the beginning of applicable sections of this work. Unless otherwise stated, the sections are based on the results of the original publication, which have been revised and adapted. Reproduced paragraphs or sections are explicitly noted and have been modified only marginally due to the notation and structure of this work. The footnotes to the corresponding publications are numbered in the order in which they appear to provide a consistent reference.

1 Introduction

Lightweight engineering is a holistic development strategy to design a system to accomplish its functions as efficient as possible, rather than just reducing its mass. It is an interdisciplinary challenge that requires a profound understanding of available materials, methods and production technologies. One option is the application of composite materials, as the material itself can be tailored to a specific application by selecting suitable constituents and processing technologies. Composites provide a particularly high lightweight potential due to their excellent weight-specific properties. However, the strong link between the manufacturing process and the resulting properties leads to high technical and economic requirements in the design phase. [1, 2]

Fiber-reinforced plastics (FRP) are an important group of composite materials comprising load-bearing fibers (commonly made from glass or carbon) embedded in a polymer matrix (thermoplastic or thermoset), which binds the fibers together, transfers loads and protects fibers from abrasion and the environment. FRP can be broadly categorized into continuous FRP (CoFRP) with aligned fibers of similar length to the component and discontinuous FRP (DiCoFRP) with shorter chopped fibers. DiCoFRP provide increased design freedom due to better formability and are cost efficient [3, pp. 2-3]. They are mainly applied with a focus on function integration and more complex shapes that take advantage of geometric stiffening effects. However, DiCoFRP are mainly applied in semi-structural applications due to their lower mechanical properties, such as strength and stiffness [2]. CoFRP provide the highest lightweight potential among composites due to large fiber volume contents and high alignment of fibers. They are popular for high-performance applications in the aerospace industry [4], performance cars [5] and wind energy sector [6]. The initially higher

material price and cycle time of CoFRP are tolerated in these industries due to their stringent technical requirements with forecasts for further growth [6, 7].

A more widespread application of CoFRP in the otherwise unit-cost oriented automotive industry is being hampered by the increasing ecological requirements and the lack of more economical recycling options [8, 9]. However, the increasing demand for a reduction in CO_2 emissions in the transport sector and the higher weight of batteries in electric cars also offer opportunities for new applications within the automotive industry [6, 7]. Critical success factors are short cycle times, structural reliability, and specific numerical methods for FRP-compatible designs of components, as well as corresponding robust process technologies [10].

CoFRP design and manufacturing involve different challenges to fully exploit the lightweight potential. The forming of an initially flat stack of engineering textiles into a complex three-dimensional shape is the initial manufacturing step in different liquid composite molding processes. Forming influences the fiber structure as well as orientation, and manufacturing defects such as wrinkling, gapping or fiber undulations must be avoided. The forming process therefore has a decisive influence on infiltration, curing and structural behavior of the final component.

These complex interdependencies require a detailed understanding of the physical mechanisms involved and their consideration along the entire manufacturing chain in order to enable efficient process and system design. A comprehensive engineering approach to this challenge is the reliable and accurate virtual prediction of the individual process steps and their integration into a continuous CAE chain, as described by Kärger et al. [11], cf. Figure 1.1. Suitable simulation approaches can predict relevant information, convey it along the CAE chain and the impact on subsequent steps can be considered, resulting in potential for optimization and increased prediction accuracy of the whole process.

The forming simulation is a central element for the CAE chain of CoFRP due to its significant influence on the subsequent process steps. A profound experimental understanding of the involved deformation mechanisms of the

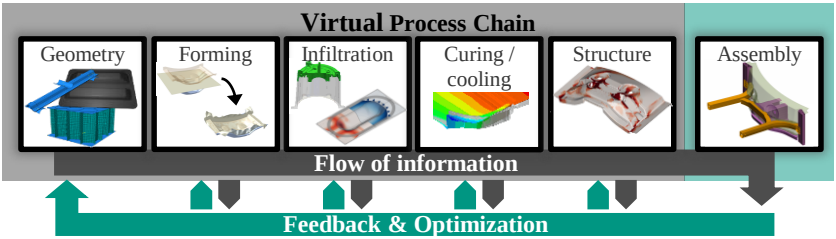

Figure 1.1: Schematic illustration of a continuous CAE chain for the virtual analysis of manufacturing and structural behavior of continuous fiber-reinforced plastics (adapted from [11])

utilized material is essential for the development of suitable simulation methods. At the same time, a sensible level of complexity for the approaches must be selected so that relevant effects are predicted with sufficient accuracy, but unnecessary parameters are avoided. This facilitates the transferability to other materials and ensures a sustainable development of the methods, as well as the modularity and efficiency of a CAE chain.

This work addresses the experimental analysis and consequent development of a macroscopic modeling approach for the forming behavior of a uni- and a bidirectional non-crimp fabric (UD- and Biax-NCF). A special emphasis is laid on UD-NCF as it has the highest lightweight potential among engineering textiles but is prone to wrinkling and gapping during forming of complex geometries. The objective is to develop a generalized approach that predicts the deformation behavior accurately despite a limited complexity. Additionally, the consideration of the transverse compaction behavior during forming simulations is addressed to incorporate its decisive influence on the fiber volume content along the CAE chain.

In the following Chapter 2, relevant literature in the context of the forming processes of CoFRP is summarized, from which research gaps are identified. These are utilized to specify the main objectives of this work and outline the further structure in Chapter 3.

2 Fundamentals and state of research

Forming processes of continuous fiber-reinforced plastics (CoFRP) can be broadly categorized based on the formed material system, which can be dry engineering textiles or preimpregnated textiles (prepregs). Both material systems are formed in very different processes with specific requirements for their characterization. Nevertheless, many similarities and synergies in regard to their modeling approaches exist, due to the high stiffness in fiber direction and comparably compliant behavior for all other deformation modes which govern the forming behavior. For these reasons, first, the material systems and their respective manufacturing processes are outlined in Section 2.1. Second, characterization methods for the individual deformation modes and the overall forming behavior are presented in Section 2.2. Based on this, relevant finite element simulation methods are introduced in Section 2.3. Finally, three-dimensional approaches that enable the consideration of the compaction behavior in forming simulations with large deformations are presented in Section 2.4. According to the scope of this work, an emphasis is put on the relevant state of research for dry engineering textiles.

2.1 Continuous fiber-reinforced materials and processing

CoFRP are made from two constituents – fiber and matrix – that differ in their mechanical properties and assume different functions in the composite.

Fibers The fibers take advantage of a 'size effect' maximizing their mechanical performance by limiting the possibility of defects due to their small cross section. This effect is further enhanced by the strong orientation of the internal microscopic structure in longitudinal direction due to the manufacturing process [12, pp. 22-24]. Fibers carry the load transferred from the matrix and primarily provide the macroscopic stiffness and strength of the composite [3, pp. 2-3]. Depending on the application different materials are used as reinforcement, such as natural fibers (e. g. flax, sisal, hemp), anorganic fibers (e. g. glass) or organic fibers (e. g. aramid, polyamide, carbon). This work focuses on carbon fibers (CF) as the most common type in high-performance applications [6].

Matrix The polymer matrix binds the fibers together in the final shape, transfers loads and protects fibers from abrasion and the environment [3, pp. 2-3]. The matrix is usually either a thermoset or thermoplastic. It decisively determines the mechanical properties in the non-fiber-dominant directions as well as the thermal and chemical properties of the final composite [12, pp. 83-86]. Thermoset polymers (e.g. epoxy, polyurethane or vinyl resins) often provide better mechanical properties and higher temperature resistance due to the closed and spatial cross-linking of the polymer chains during curing. Their major drawback is the irreversible curing process which needs to be carefully controlled during processing [13, 14] and limits recyclability [9, 15]. Thermoplastic polymers (e.g. poly-propylen or polyamid) are not spatially cross-linked and can be amorphous or more common for composites semi-crystalline. Their solidification process is reversible, enabling a re-shaping and better recyclability. However, the mechanical properties are highly dependent on temperature and the corresponding degree of crystallization, which must be monitored and adjusted both during processing and in use [16, 17].

Manufacturing processes for the large-scale production of CoFRP often require short cycle times to be economically viable, especially in the automotive industry [2,5,6]. The most relevant processes can be divided into two groups, depending on the moment when fibers are infiltrated with the matrix. Pre-infiltrated semi-finished products are often referred to as prepregs and are formed into their final shape at elevated temperatures. Thermoplastic prepregs are increasingly

important due to their material efficiency, fast processing and recyclability. In liquid composite molding processes, dry engineering textiles are formed to the final shape and infiltrated with a low-viscosity, fast-curing matrix during or after mold closure. Both groups and their manufacturing processes are presented in the following sections.

2.1.1 Thermoplastic prepreg forming

Thermoplastic prepregs Continuous fiber-reinforced thermoplastic prepregs are available as organosheets or unidirectional (UD) tapes. Organosheets are impregnated, rectangular sheets with an embedded NCF or woven fiber architecture. In comparison, UD tapes are usually supplied on rolls as impregnated stripes with a unidirectional fiber-reinforcement direction. UD tapes can be cut to size and placed in various orientations and positions to optimize material effort and reduce waste. Near-net shaped tailored laminates are manufactured as pre-product by stacking several stripes of UD tapes, fixating them locally and applying a pre-consolidation [12, 18].

Thermoforming Organosheets or tailored laminates are shaped into the final part in a multi-stage thermoforming process as shown in Figure 2.1.

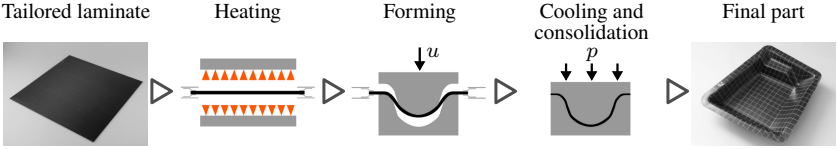

Figure 2.1: Illustration of the different staged in the thermoforming process of a tailored laminate from UD tapes (based on [18]).

The pre-consolidated laminates are heated well above the melting temperature of the thermoplastic with an infrared heater or convection oven. Subsequently, the heated laminate is transferred and positioned in the mold and thermoformed into its final shape. Finally, the part is cooled under additional transverse pressure

to ensure good surface quality and low porosity. A tool temperature lower than the laminate induces rapid cooling and enables low cycle times [17, 18].

Forming defects Forming defects such as wrinkling, gapping, matrix cracking or fiber undulations are observed during thermoforming. The number, magnitude and location of defects strongly depend on the material system, layup sequence and process parameters, as extensively studied in literature [17,19–26]. The molten polymer matrix induces friction and tacking between the individual layers and leads to large tangential and normal stresses, resulting in a strong influence of the relative layer orientation. The likelihood of wrinkling increases for organosheets and UD tapes as the relative orientation increases [17, 19, 24]. Sachs et al. [22] also observed increased wrinkling in critical areas for UD tapes compared to organosheets with the same layup. The highly temperature- and rate-dependent behavior reported for all forming mechanisms results in a strong influence of the initial tool and laminate temperature and forming velocity [25, 26]. A general recommendation for the process parameters is difficult due to the numerous interactions, but a tendency for improved formability was observed for configurations with higher laminate temperatures [17, 18, 20, 24]. An experimental analysis of the influence of process parameters is very time- and cost-consuming, but can be supplemented by suitable simulation models to improve the development process and prevent defects [21, 27–29]. The prediction of the transversal behavior is particularly interesting for the evaluation of the consolidation behavior [30–32].

2.1.2 Liquid composite molding

CoFRP from liquid composite molding (LCM) processes are manufactured from dry engineering textiles which are infiltrated with a liquid matrix material during or after forming. The most suitable processes for automated large-scale production are resin transfer molding (RTM) and wet compression molding (WCM). Other liquid composite molding processes, such as vacuum-assisted resin injection [1, 33] or double diaphragm [34–36] require manual process steps and longer cycle times.

Engineetring textiles Most high-performance applications include a woven fabric or different types of non-crimp fabrics (NCF), cf. Figure 2.2.

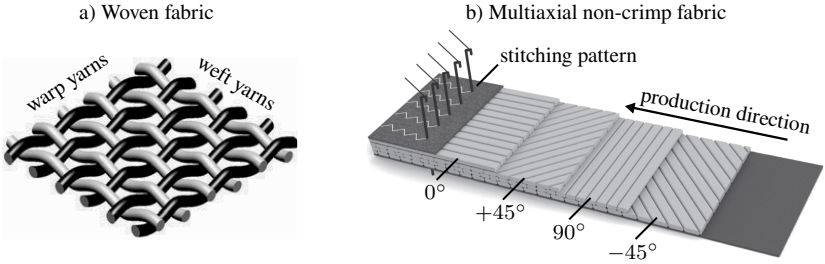

Figure 2.2: Schematic illustrations of a a) woven fabric [33, p. 175] and b) multiaxial non-crimp fabric [37].

Woven fabrics consist of usually orthogonal interlaced yarns in warp (production) and weft direction. Their handleability, formability and mechanical properties depend on the number of crosspoints as well as the number of fibers in each yarn [12, pp. 60-62]. The resulting yarn undulations reduce the stiffness especially under compressive load [1, p. 355].

NCFs consist of one (UD-NCF), two (Biax-NCF) or more directions of fibers linked together with a polymer stitching. The most common stitch types are pillar, tricot and chain, cf. Figure 2.3.

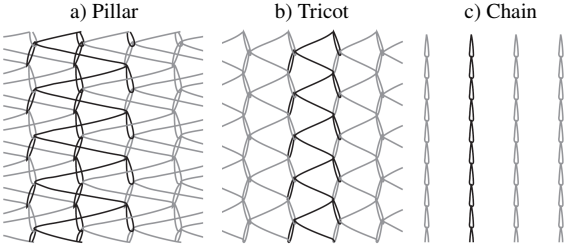

Figure 2.3: Stitiching types - a) pillar, b) tricot and c) chain [38].

The resulting fiber bundles are straight without undulations and often referred to as rovings. This makes it possible to achieve a higher stiffness and strength than woven fabrics, but handling is more difficult [1, p.356]. The mechanical properties of dry NCF are determined by the number, areal weight and orientation of layers, as well as during forming by the applied stitching pattern [39].

Resin Transfer Molding The RTM process chain is a two-step process that consists of the preforming of an initially flat stack of textiles into a 3D shape and the subsequent injection as well as curing of a resin, cf. Figure 2.4. The initial process has been further developed to handle highly reactive resins to reduce the cycle-times by modifications to the injection strategy [40, 41] and injection pressure (HP-RTM) [42, 43] or sequential pressure-controlled mold closure [2, 44–46].

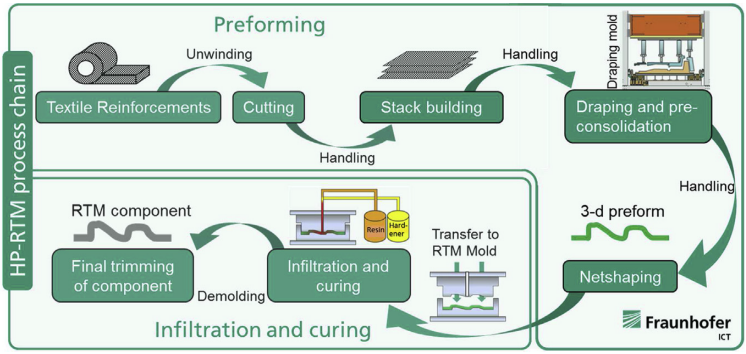

Figure 2.4: Schematic illustration of the preforming as well as infiltration and curing during the RTM process chain [2].

The preforming step, cf. Figure 2.4 top, includes the cutting and stacking of the desired layup sequence with subsequent near-net shaped forming. A binder is often applied during this step to ensure dimensional stability during handling [46]. The initially flat stack is transferred to the mold and formed into a complex 3D preform. Inevitable forming effects include the reorientation of fibers, relative slippage between layers and changes in the fiber volume content (FVC). These must be predicted and considered for a successful process

design due to the influence on subsequent infiltration, curing and final part performance [2, 11]. However, forming defects such as wrinkling, gapping, fiber misalignment or fiber waviness can also occur [47, 48]. These must be avoided as much as possible with appropriate strategies [49,50], otherwise local weaknesses will be introduced into the final part [51, 52].

The infiltration and curing step, cf. Figure 2.4 bottom, comprises the injection of a resin and hardener combination as well as simultaneous and subsequent complete curing. Fast injection is required to prevent premature hardening of the highly reactive resin system before the cavity is filled and induces high fluid pressure particularly in Injection-RTM. This can induce notable flow-induced fiber displacements [53–55]. The infiltration is affected by permeability variation due to local changes in the FVC and fiber orientation resulting from the preforming step [56]. Resin-rich areas can form in edges, corners or areas with gapping and reduce the mechanical properties of the final part [57].

Wet Compression Molding WCM is a closed-mold process implemented by the automotive industry in the last decade as an alternative to RTM [2, 56, 58–61]. Two process variants can be distinguished, as illustrated in Figure 2.5.

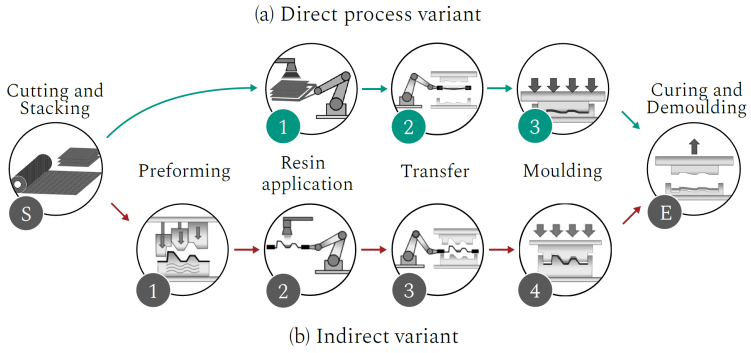

Figure 2.5: Schematic illustration of the a) direct and b) indirect variant of the WCM process [56].

The first step in both variants is the preparation of the desired layup by cutting and stacking dry engineering textiles. In the direct process variant, cf. Figure 2.5 a, resin is applied in a designated area on the surface of the stack, which is then transferred to the mold. The liquid resin seeps into the fabric through the thickness-direction during transfer and pre-infiltrates large sections. The forming and infiltration of the remaining fabric occur simultaneously due to the pressure during molding. Finally, the part is cured in the heated tools and subsequently demolded. This variant enables short cycle time due to relatively short infiltration distances and requires lower cavity pressures compared to RTM [2, 56].

The indirect process variant, cf. Figure 2.5 b, includes an additional preforming step. The resin is applied to the surface of the preformed stack, which is transferred to the mold and infiltrated in a compression step. Forming and infiltration are decoupled in this process variant similar to RTM, but it also requires lower cavity pressures like the direct variant.

Similar forming and infiltration defects as outlined above for RTM can occur in both variants [2, 56, 58, 60–62]. The simultaneous infiltration with a low viscosity resin in the direct variant can have a positive influence on the forming behavior and reduce defects [62]. In addition, the reduced number of process steps makes the direct variant even more economically attractive. The strong interaction between resin infiltration and textile deformation makes experimental [59–63] and numerical investigations [56, 58, 61, 64–66] very challenging and subject of ongoing research.

Manipulation of textile forming behavior The forming behavior of engineering textiles is often systematically manipulated to achieve a desired fiber orientation and prevent defects. The different forming defects of engineering textiles can be categorized into in-plane and out-of-plane defects, as demonstrated in a comprehensive review by Azzouz et al. [47]. In-plane defects are often observed locally in the form of fiber waviness, fiber ruptures, gapping, and buckling. Different types of wrinkles or even folds are the most common and severe out-of plane forming defects. The mechanisms for wrinkling are

well understood, as shown in a review by Boisse et al. [67]. In a study of over 10 different woven fabrics and NCF, Bai et al. [68] demonstrated that one of the key factors is the ratio of shear to bending stiffness, called the drapability ratio. Wrinkling-free forming is favored by low shear stiffness and high bending stiffness. The drapability ratio is strongly influenced by the weaving pattern or stitching type [68–72]. Thus, one fundamental option to avoid in- and out-of-plane defects is the selection of a suitable fabric.

Active manipulation of the forming behavior is achieved by inducing additional tensile forces with local grippers or blankholders [49, 50, 73–76]. These concepts can successfully reduce the occurrence of forming defects, often with a focus on avoiding wrinkles. At the same time, it is imperative not to introduce other undesirable forming defects by their application [50, 77, 78]. Thus, the positioning and pressure of blankholders [79, 80] and grippers [81–83] require experience and iterative optimization. An alternative in preforming is the segmentation of the forming tool into several tools. This emulates the manual smooth-out of wrinkles of hand-layup processes in a fully automatized process [84–86].

2.2 Characterization of forming behavior

The forming of an initially flat layup into a complex 3D shape is an essential step during manufacturing of CoFRP. Thus, a comprehensive characterization and understanding of the forming behavior is essential. Engineering textiles are multi-scale materials and their deformation can be categorized into separate mechanisms at the micro-, meso- and macro-scale [87–91]. Investigations on the microscale focus on individual fibers inside of rovings [92, 93]. Mesoscopic investigations analyze the deformation of entire rovings and the stitching pattern as well as their mutual interactions [94–96]. This work focuses on the macroscopic perspective, which considers the plies as a homogenized, anisotropic continuum. However, an understanding of the mesoscopic structure of the textile is still required to explain macroscopically measured effects.

The macroscopic deformation behavior is further categorized into intra-ply and inter-ply mechanisms [17, 21, 56]. The most relevant mechanisms are summarized in Figure 2.6.

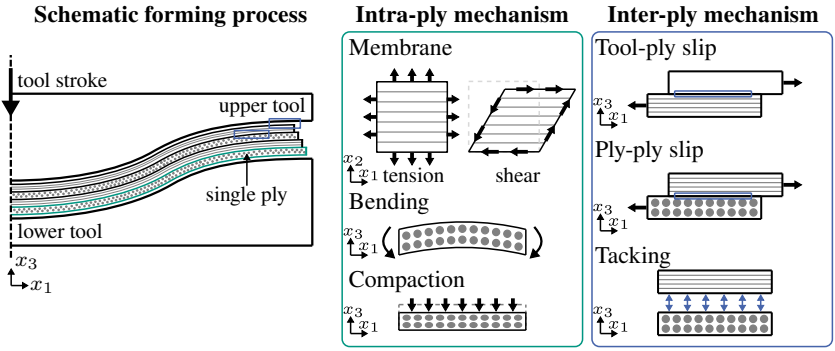

Figure 2.6: Schematic illustration of the forming process and associated deformation mechanisms, divided into intra-ply and inter-ply mechanisms.

Intra-ply mechanisms comprise the membrane, bending and compaction behavior of individual plies in a laminate stack. Most engineering textiles have a high membrane stiffness in their respective fiber directions and lower stiffness under shear, or transverse tension for unidirectional reinforcements. The bending stiffness is also comparatively low due to intra-roving slip between fibers [97]. The compaction behavior determines the final thickness and FVC of the textile.

Inter-ply mechanisms represent the deformation mechanisms between individual plies (ply-ply) in the laminate stack as well as between the tool and laminate (tool-ply). Additionally, tacking at the interfaces due to applied binder or infiltration can occur.

Different experimental setups are proposed in literature to characterize the introduced macroscopic deformation mechanism, cf. Figure 2.6. Specialized setups are necessary for the investigation of infiltrated textiles [56, 64, 65, 98–101] or prepreg [17, 18, 21, 25, 26]. The most relevant characterization setups for dry engineering textiles are outlined in the following, with a focus on the special requirements for NCF.

2.2.1 Membrane behavior[1]

Membrane behavior characterization usually focuses on tension in different directions and in-plane shear, cf. Figure 2.6. For woven fabrics a non-linear tensile behavior is observed in both fiber directions. Initial undulations are stretched out under tensile load, resulting in an increasing stiffness until the yarns are fully straightened [64, 103, 104]. This also results in a tension-tension coupling under biaxial loads [105, 106]. Only minimal non-linear behavior is observed for NCF in fiber direction due to the nearly straight rovings [107–109]. On the contrary, a non-linear behavior and strong influence of the clamping conditions in the transverse direction is observed for UD-NCF due to small amounts of glass fibers (GF) usually necessary for handleability [109, 110]. Schirmaier et al. [110] demonstrated this in transverse tensile tests with different clamping conditions to transfer the load either through the stitching and only friction with the GF or additionally through fully clamped GF.

The shear behavior of fabrics has mainly been characterized with the picture frame test (PFT) or bias extension test (BET) [110–117]. Both tests are shown in Figure 2.7 a and b.

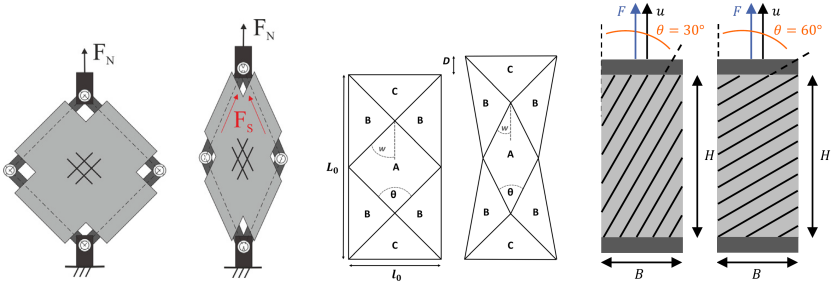

a) Picture frame [118] b) Bias extension [119] c) Off-axis-tension [86]

Figure 2.7: Membrane characterization setups for engineering textiles.

[1] Extracts from Section 2.2.1 have been previously published in [102], i.e. B. Schäfer, R. Zheng, N. Naouar, L. Kärger. Membrane behavior of uni- and bidirectional non-crimp fabrics in off-axis-tension tests. *International Journal of Material Forming*, 16(6):68, 2023 - Reproduced paragraphs are marked with [1].

The PFT induces a pure shear by deforming the fabric in a square-hinged frame to a rhombus. For woven fabrics in PFT a tension-shear coupling is observed with additional yarn tension [118, 120] and a compression-shear coupling with additional transverse pressure [121]. The BET is a tensile test on a rectangular specimen with the fibers oriented at an offset angle of $45°$. This results in three distinct deformation zones with a shear-dominated main deformation zone (A) in the specimen's center.[1]

For woven fabrics, the PFT and BET were extensively studied and theoretical descriptions of their shear deformation were developed together with normalization methods to compare them under the assumptions of inextensible fibers, no slippage and pure shear [111, 115, 122–126]. Under proper initial placements of the specimens and prevention of fiber tension during the PFT, comparable results for both tests were achieved even for different specimen sizes [111].[1]

However, NCFs do not intrinsically deform under pure shear, which leads to significant differences in the results of BET and PFT in the case of Biax-NCF [94, 114, 127] as well as UD-NCF [110, 128, 129]. This is most notable in a comparison of the theoretical and measured shear angle [94, 95]. NCFs deform under a combination of relative fiber rotation (pure shear) and slippage between fiber rovings (simple shear) as well as the different fiber layers [130–132]. This specific deformation behavior together with an easier setup made the BET more commonly used for Biax- [94, 95, 119, 127, 133–136] and UD-NCF [95, 109, 110, 128, 137–140] compared to the PFT [76, 94, 107, 127, 141].[1]

Pourtier et al. [119, 142] proposed an alternative method to investigate the deformation of NCFs in the BET under the assumption of simple shear, which is a macroscopic description of slippage for UD materials. For the investigated Biax-NCF the main deformation mode was slippage (simple shear) during the test's beginning and changed to rotation of the fibers (pure shear). Krogh et al. [143] combined the pure and simple shear theories with the observations of Harrison et al. [124] that the relative slip can be estimated by the specimen

[1] Reproduced paragraph from [102], cf. footnote p. 15 for details.

width at half height. For the investigated quasi-UD-NCF, a transition from pure to simple shear was observed and the shear angle could be predicted based on the width. The deformation behavior of NCF strongly depends on the material architecture, fiber and stitching type [71, 144]. Therefore, there is currently no universal method for the characterization of the membrane behavior of NCFs available.[1]

In addition, existing theoretical investigations concerning the deformation during BETs neglect mesoscopic effects like in-plane fiber bending. These manifest in the form of transition zones between different shear zones (cf. Figure 2.8) instead of sharp changes assumed in kinematic models or theories based on classical continuum theories [89, 134, 145]. However, no method for the experimental measurement of in-plane bending is reported in the literature.[1]

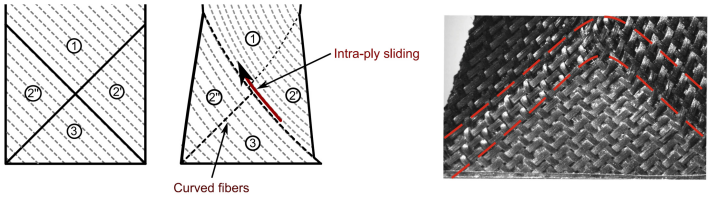

a) Curved fibers and sliding in BET [131] b) Transition zone [145]

Figure 2.8: Observed areas with curved fibers and slippage for a Biax-NCF [131] and b) transition zone due to in-plane bending in a woven fabric [145].

Since NCFs do not adhere to theoretical kinematic models, Boisse et al. [114] recommended in their review paper to measure the deformation independent of the machine displacement. Commonly the shear strain has been measured during the BET via digital image correlation (DIC) [116, 134, 138, 143] or other discrete methods based on individual measurement points [146] or lines [115, 119, 123, 126]. Thereby, the influence of the measuring system is often neglected in literature but can have a significant influence on the deformation as demonstrated by Trejo et al. for UD-NCF [138].[1]

[1] Reproduced paragraph from [102], cf. footnote p. 15 for details.

Schirmaier et al. [137] and later Ghazimoradi et al. [109] conducted so-called off-axis-tension tests (OAT) with fiber angles of 30° and 60° in addition to BETs for UD-NCF, cf. Figure 2.7 c. OATs impose different ratios of superimposed transverse tensile and shear deformation with a relatively simple setup without requiring a multiaxial tensile machine [147]. They reveal a complex deformation behavior under different multiaxial strain conditions, which is not sufficiently characterized in tests exclusively considering shear [109, 128, 140].[1]

2.2.2 Bending behavior

In bending characterization, a specimen is systematically deflected usually due to its own weight under gravity or by external devices. Comprehensive reviews on textile bending have been presented by Boisse et al. [67, 91]. Popular setups with different mechanisms are shown in Figure 2.9.

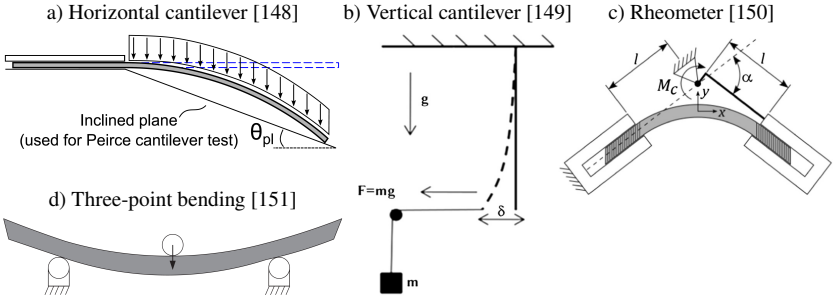

Figure 2.9: Bending characterization setups for engineering textiles

The horizontal cantilever test is commonly applied for dry engineering textiles, cf. Figure 2.9 a. The specimen under gravity is pushed over an edge and the overhang length successively increases until it makes contact with an inclined surface. For an incline angle of $\Theta = 41.5°$, the setup is referred to

[1] Reproduced paragraph from [102], cf. footnote p. 15 for details.

as Peirce test and the bending stiffness is analytically approximated assuming a linear relationship between curvature and moment [152]. Other authors have also applied additional optical measurement systems to determine the exact deflection curve of the specimen [65, 148, 153–156]. Their work revealed a non-linear moment-curvature relationship with a maximum at the clamped end. The optical evaluation enables the investigation of variable overhang lengths to determine the bending behavior for a variety of curvatures. Moreover, dissipative effects can be determined, as shown by Bilbao et al [153]. Poppe et al. [65] demonstrated an estimation of the rate-dependent behavior in cantilever tests, by evaluating different overhang lengths of the specimen with a constant feed rate. Beyond that, vertical arrangements of the cantilever, cf. Figure 2.9 b, have been proposed to better control the magnitude and rate of the applied load [149, 157].

The Kawabata evaluation system for fabric bending (KES-FB2) [153, 158, 159] and the later adaptation of its concept for the rheometer bending test [22, 28, 65, 148, 150] impose a constant curvature to the specimen, cf. Figure 2.9 c. They directly measure the moment-curvature-relation without additional optical measurement systems. Non-linear, rate-dependent and hysteretic material behavior can be studied with both setups [65, 148, 153, 159]. The modifications in the rheometer test and addition of a thermal chamber enable the investigation of temperature-dependent behavior [22, 28, 150]. Poppe et al. [64] studied the rate- and viscosity-dependent bending response of a dry as well as low viscous infiltrated woven fabric in the rheometer test and compared the results to infiltrated cantilever tests. Despite some systematical differences in the results, they concluded a fast assessment of the elastic bending properties is acceptable with the cantilever test. In contrast, the rheometer test was recommended for a more accurate determination of rate-dependent, plastic and hysteretic bending behavior.

The three-point bending test, cf. Figure 2.9 d, is used in literature to study the unique bending response of thick interlock woven fabrics [151, 160–162]. The setup requires a sufficiently high bending stiffness of the material and is therefore only suitable for thick textiles or short specimens [67].

In an early study, Lomov et al. [70] compared different Biax-NCF in the KES-FB2 and reported a non-linear bending behavior with decreasing stiffness for increasing curvature. In general, higher stiffness was measured in the direction of tighter stitched rovings, as this prevents in-plane slippage, and for rovings with higher linear density. In addition to this study, the bending behavior of UD- [109, 110, 156, 163] and Biax-NCF [133, 164–166] has been investigated primarily in horizontal cantilever tests. The bending response strongly depends on the loading direction of the stitching pattern, with a higher stiffness for the stitching under tension [109, 110, 163, 164].

2.2.3 Compaction behavior[2]

The compaction behavior determines the resulting FVC and consequently influences the permeability, necessary press forces as well as resulting mechanical properties of components produced from LCM [66]. For dry engineering textiles, the compaction behavior is commonly investigated in plate-to-plate or punch-to-plate setups mounted to a tensile testing machine, cf. Figure 2.10 a.

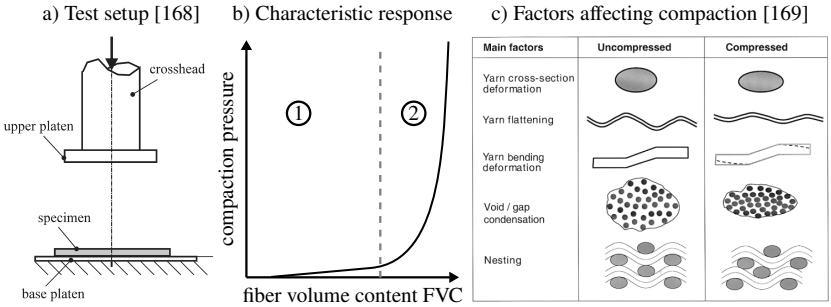

Figure 2.10: a) Common compaction test setup; b) Characteristic exponential response; c) Factors affecting the compaction response of dry engineering textiles.

[2] Extracts from Section 2.2.3 have been previously published in [167], i.e. B. Schäfer, R. Zheng, P. Boisse, L. Kärger. Investigation of the compaction behavior of uni- and bidirectional non-crimp fabrics. *Materials Research Proceedings*, 28:331–338, 2023 | Reproduced paragraphs are marked with [2].

The typically measured pressure vs thickness or FVC behavior has an exponential characteristic with two distinct phases, cf. Figure 2.10 b. A classification of the main factors contributing to the observed response was presented by Chen et al. [169] and is shown in Figure 2.10 c. The first phase is dominated by a low compression resistance due to the low bending stiffness of crimped yarns, yarn flattening and condensation of initial voids between the fibers. The second phase progresses as all gaps are condensed and fibers come into contact with each other. During this phase the compression resistance is more dominated by an increasing number of high Hertzian contact forces [91].

Woven fabrics as well as Biax-NCF have been investigated more extensively [107, 168–175], compared to UD-NCF [168, 176–178]. The compaction behavior is largely determined by the architecture of the textile, the type of fiber and the areal density [107, 171, 177]. Textiles with a higher areal density tend to have a smaller resistance to compaction because they have more yarns in a roving and usually a more rounded shape of fiber bundles [107, 171, 173]. Additional factors influencing the compaction of multi-ply stacks are the number of layers and layup sequence [173, 175]. Increasing the number of plies in a layup reduces the resistance to compaction, due to rovings of different layers sliding into gaps at the inhomogeneous interfaces. This effect is called nesting, cf. Figure 2.10 c, and usually more pronounced for woven fabrics compared to NCFs [179]. For NCFs the compaction behavior is also influenced by the superposition of the stitching patterns and tension in the stitching during production [173, 175, 177, 179].[2]

In a recent benchmark by Yong et al. [174] two glass-fiber fabrics (woven and Biax-NCF) were investigated at over 20 institutes in dry and wet conditions in order to investigate the conformity of compaction test results. Thereby, no distinct influence could be attributed to the size of the specimen, shape of the testing device or weight determination method. However, three main sources for

[2] Reproduced paragraph from [167], cf. footnote p. 20 for details.

variability were identified: thickness measurement method, machine compliance and specimen saturation in wet compression tests. However, a correction of the machine compliance as described by Sousa et al. [181] led to a good agreement between different institutions for different thickness measurement methods.[2]

2.2.4 Inter-ply behavior[3]

Inter-ply behavior encompasses tangential friction as well as adhesion or tacking in the normal direction. Both mechanisms are observed superposed for bindered [183–185] or infiltrated [56, 101, 185–187] textiles, prepregs [188–194] and thermoplastic tapes [17, 195–198]. Thereby, adhesion in normal direction is less commonly studied because it is difficult to isolate the mechanism and requires more complex test setups [17, 56, 189, 197, 199]. Tangential friction is the dominant mechanism for dry textiles and therefore the focus of this section.

The characterization of friction is commonly conducted via relative motion between a fabric ply and either another fabric ply (ply-ply) or a tool (tool-ply) under controlled transverse pressure. Usually Coulomb's friction is assumed for the analysis of dry textiles

$$F_\mathrm{f} = \mu N, \tag{2.1}$$

where, F_f is the tangential friction force, N the applied normal load, μ the Coulomb coefficient of friction (CoF).[3]

[2] Reproduced paragraph from [167], cf. footnote p. 20 for details.

[3] Extracts from Section 2.2.4 have been previously published in [182], i.e. B. Schäfer, N. Naouar, and L. Kärger. Investigation of the friction behavior of uni- and bidirectional non-crimp fabrics. *Materials Research Proceedings*, 41:540–548, 2024 | Reproduced paragraphs are marked with [3].

In a benchmark study, Sachs et al. [185] compared different experimental setups from three design categories (cf. Figure 2.11) for the same material, i.e. pull-out-tests, pull-through-tests and sled pull-over-tests. Comparable results were achieved for all setups, but systematic errors were observed and attributed to edge effects and uneven pressure distributions. Thus, sled pull-over- or pull-through-tests with a sufficiently large contact area and chamfered edges were recommended. However, the sled-test was originally developed for thin plastic film materials (ASTM standard D1894-14 [200]) and therefore mainly suitable for lower transverse pressure to prevent balancing problems and stick-slip effects [175, 201].[3]

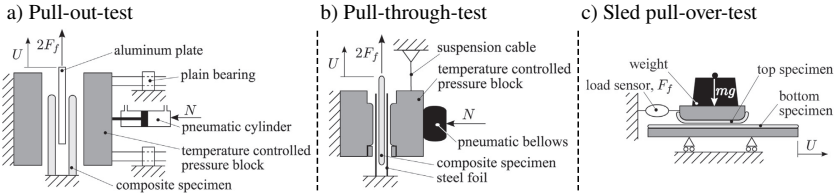

Figure 2.11: Common characterization setups for tangential friction (extracted from [185]).

The friction behavior of a textile reinforcement depends on the mesoscopic structure of its unit cell and the materials of its constituents. Protruding high points of the material are especially notable during ply-ply contact due to stick-slip or shock effects. These result from undulations in woven fabrics [73,96,202] or the stitching in non-crimp fabrics [108,175]. Additionally, pressure- and rate-dependency as well as an impact of a layer's relative orientation and deformation state (shear) is reported for dry textiles.[3]

Tool-ply friction is usually found to be independent of the relative velocity [56,185], the ply's relative orientation [36,108,187] and shear deformation [77]. An increasing normal pressure reduces the CoF [56,191,203,204], because of its effect on the surface roughness and true contact area between fibrous material as demonstrated by Avgoulas et al. [204] based on Hertzian theory. However, this

[3] Reproduced paragraph from [182], cf. footnote p. 22 for details.

correlation applies mainly for high pressures (>10 kPa), while for low pressures often no or even a slightly positive influence is measured [185, 204, 205].[3]

Ply-ply friction is also reported as nearly rate-independent [56,206], but increasing under shear deformation [77]. The effective CoF between plies decreases for high transverse pressure [56, 191, 206], due to the lateral spreading of the fabric under compaction that results in smaller undulations and thus less shock effects [206]. The reported influence of the relative orientation is most heavily dependent on the specific material being tested. The most common observation for woven fabrics is a lower CoF for relative orientations unequal to 0° or 90° [186, 207], with the lowest value often, but not always measured for 45° [77, 96]. In contrast, the behavior of NCFs does not follow a distinct trend and depends on the specific architecture [36, 108, 175]. However, Quenzel et al. [108] recently measured an increasing CoF by decreasing the stitching length of Biax-NCFs manufactured from the same materials as it increases the number of stitch yarn loops.[3]

2.2.5 Forming behavior[4]

The characterization of the overall forming behavior of engineering textiles is often performed on simplified geometries to facilitate more controlled investigations [90, 91, 209, 210]. The selected shapes typically represent challenging features, like double-curved surfaces or various radii of edges and corners. The results can be used for a detailed validation of simulation models, which enable a more efficient process and part design for complex components. Different shapes frequently used in literature are shown in Figure 2.12.

[3] Reproduced paragraph from [182], cf. footnote p. 22 for details.

[4] Extracts from Section 2.2.5 have been previously published in [208], i.e. B. Schäfer, R. Zheng, J. Colmars, A. Platzer, N. Naouar, P. Boisse, L. Kärger. Experimental analysis of the forming behavior of uni- and bidirectional non-crimp fabrics for different geometries. *[submitted for review]* | Reproduced paragraphs are marked with [4].

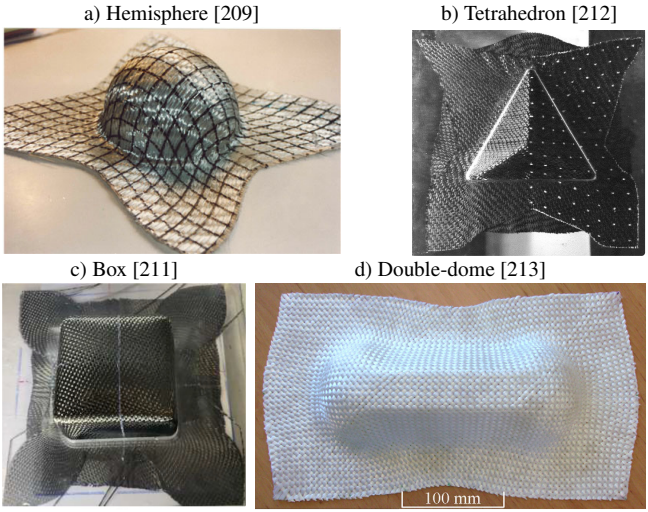

Figure 2.12: Common shapes for characterization of the forming behavior.

The *hemispherical* punch, cf. Figure 2.12 a, is the most common shape and is often used for studying the formability of woven fabrics [214–217], as well as NCFs [110, 128, 218]. It is a rather simple double-curved geometry that still imposes significant in-plane shear deformation. Bel et al. [131] analyzed and measured sliding between fiber plies in a Biax-NCF for this shape. Schirmaier et al. [110] and Ghazimoradi et al. [128] observed notable gapping due to the low stiffness of the stitching and wrinkling parallel to the fiber yarns for a UD-NCF in hemisphere tests.[4]

The *tetrahedral* punch, cf. Figure 2.12 b, was developed to represent a slanted corner of more complex components and provoke higher shear angles as well as the formation of out-of-plane defects [35,79,212,219,220]. Viisainen et al. [79] compared the hemisphere and tetrahedron for a $\pm 45°$-Biax-NCF and found similar types of wrinkles as well as deformation modes for both shapes, but significantly higher shear angles and severity of the wrinkles for the tetrahedron.[4]

[4] Reproduced paragraph from [208], cf. footnote p. 24 for details.

The *square box* punch, cf. Figure 2.12 c, is commonly used for metal forming analysis [221, 222], but few researchers have shown its capability to induce very high shear angles for textile reinforcements [211, 215, 217, 223]. Bai et al. [68] compared a large variety of woven fabric architectures as well as some NCFs in box tests and identified a strong correlation between a fabric's membrane-to-bending stiffness ratio and the formation of wrinkles.[4]

The largest popular shape is the *double-dome*, cf. Figure 2.12 d, which represents a transition between concave and convex double-curved surfaces and was used in benchmarks for woven fabrics [64, 213, 224, 225].[4]

Forming metrics The deformation behavior and the formation of defects in forming tests can be analyzed through various metrics. The required punch force can be used for comparison between different materials to evaluate their drapability and indicate changes in the deformation behavior [72, 226–228]. The outer contour of the blank after forming gauges the material draw-in and is frequently used for the validation of forming simulations [35, 213, 215, 216, 229]. The measurement of global and local strains is accomplished by a variety of different methods. Many researchers utilize point-wise measurements to determine shear angles, as in-plane shear is a primary deformation mode of most balanced fabrics [216, 217, 219, 228, 229]. In these approaches, grids are reconstructed from local markers on the fabric or images are analyzed to locally measure the angle between visible fiber directions. Alternatively, different DIC methods are utilized to measure the 3D geometry and full strain field of the deformed fabric. However, those methods require either the possibility to remove the fabric from the mold without further deformation [116, 213, 230–232], or specialized stereo camera systems in combination with an open die [79, 128, 225].[4]

[4] Reproduced paragraph from [208], cf. footnote p. 24 for details.

2.3 Finite element forming simulation

The simulation approaches for forming processes of CoFRP can be categorized as kinematic or mechanics-based approaches [112,233]. Kinematic approaches are exclusively based on geometric mapping algorithms, with the general assumption of incompressible and inextensible fibers [233]. In addition, pure shear deformation is assumed for bidirectional reinforcements [234–236] or simple shear for unidirectional reinforcements [237]. The main advantage of kinematic approaches is the comparably low computational effort. However, they neglect more complex in-plane deformation modes, the bending behavior and its related forming effects, interaction between plies in a stack as well as process conditions in general. Due to the outlined severe limitations, kinematic approaches are not further considered in this work.

Finite Element Analysis (FEA) is commonly applied for mechanics-based forming simulations as evident from comprehensive reviews [67, 88–91, 209, 210]. The material behavior and process conditions are considered by constitutive modeling of the deformation mechanisms (cf. Section 2.2) and appropriate boundary conditions, respectively. This enables the investigation of complex interactions during the process, such as contact in multi-layer stacks, blankholders, grippers, temperature or the infiltration state. FE approaches have to account for the internal architecture of the composite reinforcement. Engineering textiles consist of thousands of fibers that allow for relative motion, which are bundled together by the weaving pattern or stitching. Thus, reinforcements are multi-scale materials that require specific modeling approaches depending on the analyzed micro-, meso- or macro-scale, cf. Figure 2.13. Approaches on the micro-scale focus on the interaction between individual fibers for detailed investigations and virtual characterization, but they are rarely used for forming simulations due to their numerical effort [88, 89, 238].

In the following, Section 2.3.1 introduces common constitutive approaches for textile forming, Section 2.3.2 gives a brief overview of mesoscopic approaches, and Section 2.3.3 presents a more detailed overview of relevant macroscopic approaches.

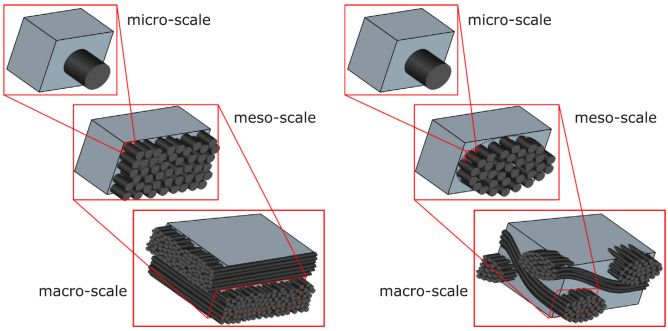

Figure 2.13: Schematic illustration of the micro-, meso- and macro-scales of a) unidirectional and b) woven reinforcements [89].

2.3.1 Constitutive approaches

Simulation approaches for composite forming are commonly based on hypoelastic or hyperelastic constitutive models [88–91, 209]. Recently, some researchers proposed to apply generalized continua approaches to incorporate the mesoscopic heterogeneity of fabrics during material modeling based on higher strain gradients [67, 89, 239]. The fundamentals of the different constitutive approaches are outlined in the following.

Hypoelastic approaches Hypoelastic approaches are called rate constitutive laws. They relate the rate-of-deformation tensor $\boldsymbol{D}$ to an objective Cauchy stress rate $\boldsymbol{\sigma}^{\nabla}$ in the linear case by a fourth-order tangent stiffness tensor $\mathbb{C}$ according to [240, p. 243]

$$\boldsymbol{\sigma}^{\nabla} = \mathbb{C} : \boldsymbol{D}. \tag{2.2}$$

The stiffness $\mathbb{C}$ may depend on the stress, in which case it must be an objective function of the stress state. The most common objective stress rates are those of Green-Naghdi and Jaumann, both imply an orthogonal material-fixed frame $\{\boldsymbol{e}_1, \boldsymbol{e}_2\}$ under rigid body rotation in the current configuration $\mathscr{B}_1$ [241]. This

enables an incremental integration w.r.t. time as presented by Hughes and Winget [242]

$$\boldsymbol{\sigma}^{n+1} = \boldsymbol{\sigma}^{n} + \Delta\boldsymbol{\sigma}^{n+1} \quad \text{with} \quad \Delta\boldsymbol{\sigma}^{n+1} = \mathbb{C} : \Delta\boldsymbol{\varepsilon}^{n+1}, \tag{2.3}$$

where $\Delta\boldsymbol{\varepsilon}^{n+1}$ is the logarithmic strain increment within the temporal integration step n.

For forming simulations, it can be advantageous to describe the constitutive equations in a non-orthogonal frame [90, 209, 241]. As demonstrated by Willems [243] and Dörr [17] for the Green-Naghdi rate, this can be achieved by introducing an additional covariant fiber-parallel frame $\{\boldsymbol{g}_1, \boldsymbol{g}_2\}$, cf. Figure 2.14. This frame remains aligned with the principle material orientations

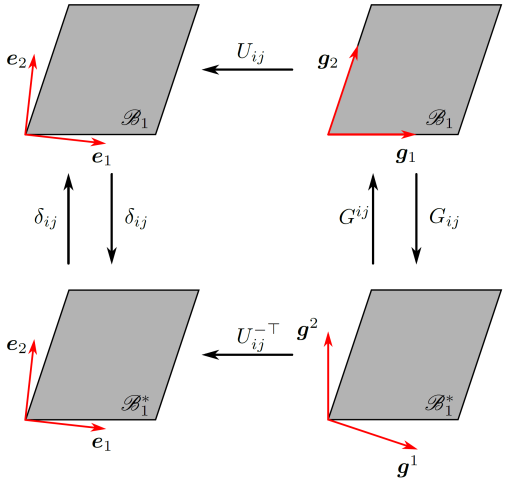

Figure 2.14: Schematic illustration of the transformations in the current configuration $\mathscr{B}_1$ between Green-Naghdi's frame $\{\boldsymbol{e}_i\}$ and the covariant $\{\boldsymbol{g}_i\}$ and contravariant $\{\boldsymbol{g}^i\}$ fiber parallel frame [17].

even for arbitrary deformations, such as large shear during forming. The according covariant $\{\boldsymbol{g}_i\}$ and contravariant $\{\boldsymbol{g}^i\}$ base are determined by the right

stretch tensor $\boldsymbol{U}$ and Green-Naghdi's frame $\{\boldsymbol{e}_i\}$. The right stretch tensor is normalized by the resulting metric coefficients G_{ij}, according to [17, 28]

$$U^*_{ij} = \frac{1}{\sqrt{G_{\underline{jj}}}} U_{ij} \quad \text{with} \quad G_{ij} = U^{\mathsf{T}}_{ik} U_{kj} \quad \text{and} \quad \sqrt{G_{\underline{ii}}} = \|\boldsymbol{g}_i\|. \tag{2.4}$$

Here, the underlined indices indicate that the summation convention does not apply. The base transformation between the normalized covariant $\{\boldsymbol{g}^*_i\}$ and contravariant $\{\boldsymbol{g}^{*i}\}$ non-orthogonal frame and Green-Naghdi's orthogonal frame $\{\boldsymbol{e}_i\}$ are achieved according to

$$\boldsymbol{g}^*_i = U^*_{ij} \boldsymbol{e}_j \quad \text{and} \quad \boldsymbol{g}^*_i \cdot \boldsymbol{g}^{*j} = \delta^j_i. \tag{2.5}$$

This enables the transformation of Equation 2.3 for an evaluation in the fiber-parallel frame of the current configuration $\mathscr{B}_1$

$$[\Delta\boldsymbol{\sigma}^{n+1}]_{\{\boldsymbol{g}^*_i \otimes \boldsymbol{g}^*_j\}} = [\mathbb{C}]_{\{\boldsymbol{g}^*_i \otimes \boldsymbol{g}^*_j \otimes \boldsymbol{g}^*_k \otimes \boldsymbol{g}^*_l\}} : [\Delta\boldsymbol{\varepsilon}^{n+1}]_{\{\boldsymbol{g}^{*k} \otimes \boldsymbol{g}^{*l}\}}. \tag{2.6}$$

It has to be noted that incremental hypoelastic material formulations are path-dependent and time step dependent for multiaxial deformations [240, p. 237], which can be problematic for non-constant tangent stiffness tensor $\mathbb{C}$ or non-monotonous deformations.

Hyperelastic approaches Hyperelastic approaches are defined by a strain energy density function W as a potential for the resulting stress [244]

$$\boldsymbol{S} = 2\frac{\partial W(\boldsymbol{C})}{\partial \boldsymbol{C}}, \tag{2.7}$$

where $\boldsymbol{S}$ is the second Piola-Kirchhoff stress tensor and $\boldsymbol{C}$ is the right Cauchy-Green deformation tensor. In case of a Saint Venant-Kirchhoff approach, a linear relation between the Green-Lagrange strain $\boldsymbol{E}$ and second Piola-Kirchhoff stress is assumed [240, p. 237]

$$\boldsymbol{S} = \mathbb{C} : \boldsymbol{E} \quad \text{with} \quad \boldsymbol{E} = \frac{1}{2}\left(\boldsymbol{C} - \boldsymbol{I}\right), \tag{2.8}$$

where $\boldsymbol{I}$ is the second-order identity tensor. The strain energy density can alternatively be expressed by a set of independent invariants I_i of the strain by

$$\boldsymbol{S} = 2\sum_{i}^{N} \frac{\partial W}{\partial I_i}\frac{\partial I_i}{\partial \boldsymbol{C}}. \tag{2.9}$$

The principal isotropic invariants of the right Cauchy-Green deformation tensor are defined as [245, p. 201]

$$I_1 = \mathrm{tr}(\boldsymbol{C}) \quad , \quad I_2 = \frac{1}{2}\left(\mathrm{tr}(\boldsymbol{C})^2 - \mathrm{tr}(\boldsymbol{C}^2)\right) \quad \text{and} \quad I_3 = \det(\boldsymbol{C}) \tag{2.10}$$

For anisotropic materials it can be advantageous to instead use a set of directional pseudo-invariants that depend on chosen principal material orientations $\boldsymbol{A}_1$ and $\boldsymbol{A}_2$, cf. Figure 2.15.

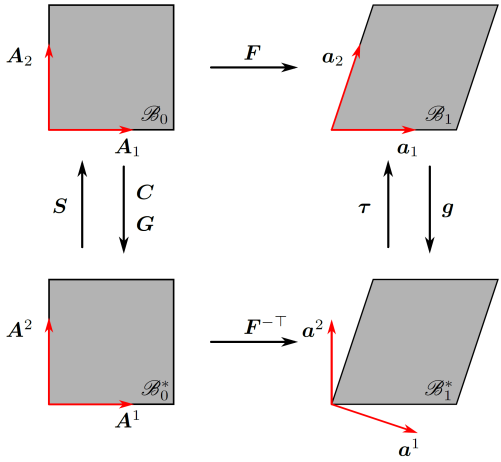

Figure 2.15: Schematic illustration of the definition of the metric and stress tensors as mapping between the covariant initial $\mathscr{B}_0$ and covariant current $\mathscr{B}_1$ and the according contravariant configurations $\mathscr{B}_0^*$ and $\mathscr{B}_1^*$ [17].

The most utilized pseudo-invariants in the context of engineering textiles are [245, p. 274]:

$$I_4 = \boldsymbol{A}_1 \cdot \boldsymbol{C} \cdot \boldsymbol{A}_1 = \lambda_{A_1}^2, \tag{2.11}$$

$$I_6 = \boldsymbol{A}_1 \cdot \boldsymbol{C} \cdot \boldsymbol{A}_2, \tag{2.12}$$

$$I_8 = \boldsymbol{A}_2 \cdot \boldsymbol{C} \cdot \boldsymbol{A}_2 = \lambda_{A_2}^2, \tag{2.13}$$

$$I_{10} = \arccos\left(\boldsymbol{A}_1 \cdot \boldsymbol{A}_2\right) - \arccos\left(\frac{I_6}{\sqrt{I_4 I_8}}\right) = \gamma_{12}, \tag{2.14}$$

where I_4 and I_8 are the quadratic stretches along $\boldsymbol{A}_1$ and $\boldsymbol{A}_2$ respectively, I_6 is the shear strain, I_{10} is the shear angle γ_{12}. It is commonly assumed that the contributions to the strain energy density due to these deformation modes are independent [67, 90]. Alternatively, couplings between the different modes can be introduced to describe effects like the tension-tension coupling observed for woven fabrics [106, 246, 247].

Hyperelastic approaches have two fundamental advantages. First, the strain energy density only depends on the final deformation state and therefore results in a path-independent behavior. Second, the Green-Lagrange strain and second Piola-Kirchhoff stress are work-conjugated Lagrangian measures and defined in the initial contravariant $\mathscr{B}_0^*$ and covariant $\mathscr{B}_0$ configuration, respectively [17]. Thus, the principle material orientations can be aligned with the Cartesian base vectors, leading to an intrinsic consideration of a fiber-parallel frame, cf. Figure 2.15. Additionally, $\boldsymbol{S}$ can be directly mapped to the current configuration $\mathscr{B}_1$ by a so-called "push-forward" operation by [240, p. 315]

$$\boldsymbol{\tau} = \boldsymbol{F} \cdot \boldsymbol{S} \cdot \boldsymbol{F}^{\mathsf{T}} \quad \text{and} \quad \boldsymbol{\sigma} = \frac{1}{J}\boldsymbol{\tau} \quad \text{with} \quad J = \det(\boldsymbol{F}), \tag{2.15}$$

where $\boldsymbol{\tau}$ and $\boldsymbol{\sigma}$ are the Kirchhoff and Cauchy stress, respectively.

Generalized continua approaches Models based on the classical Cauchy continuum theory describe homogeneous deformation based on the first gradient of the displacement field, the deformation gradient $\boldsymbol{F}$. In contrast, generalized continua approaches introduce additional terms to the balance equations to

incorporate information about an embedded micro- or mesoscopic structure of a heterogeneous material into a macroscopic model [240, 248]. This can be accomplished with higher-grade or higher-order continuum theories [240, pp. 686-691]. Higher-order approaches take into account higher gradients of the displacement field derived from the degrees of freedom (DOF) at a material point. Examples are second-gradient approaches, which introduce the second gradient of the displacement field $\nabla \boldsymbol{F}$ to describe the curvature. Higher-grade approaches introduce additional DOF to each material point to extend the kinematics. Examples are micromorphic models, which introduce a second-order tensor field $\boldsymbol{\psi}(\boldsymbol{X})$ that accounts for deformations associated with the microstructure, e.g. its rotation. If some constraints are introduced on the tensor $\boldsymbol{\psi}$, a second-gradient theory is obtained as the limit case of a micromorphic theory [145, 161].

In forming simulations of engineering textiles generalized continua approaches based on the second-gradient of the displacement field are the most common [67, 89, 90, 239]. They introduce an additional contribution to the strain energy density

$$W\left(\boldsymbol{F}, \nabla \boldsymbol{F}\right) = W_{\mathrm{I}}(\boldsymbol{F}) + W_{\mathrm{II}}(\nabla \boldsymbol{F}), \tag{2.16}$$

where W_{I} and W_{II} are the first- and second-gradient energies, respectively. In particular, the bending stiffness of rovings has been successfully modeled with this approach [145, 161, 239].

2.3.2 Mesoscopic approaches

Meso-scale approaches model all constituents of engineering textiles individually [89, 210]. The main advantage is that the heterogeneity of the material is discretely considered. However, the number of DOF is very high, which makes these approaches computationally expensive. Depending on the representation of the constituents, mesoscopic approaches can be divided into two groups. First, discrete approaches model each constituent in an abstract manner with 1D or 2D elements. Second, geometrical approaches represent the individual

constituents in their geometric dimensions with 2D or 3D elements in different levels of detail, depending on the application to virtual material characterization or forming simulations. The differences between these modeling approaches are outlined in the following.

Discrete approaches Discrete approaches model representative unit cells of a fabric as a network of 1D truss, beam, bar and spring elements or a combination of 1D elements with 2D membrane or shell elements, cf. Figure 2.16.

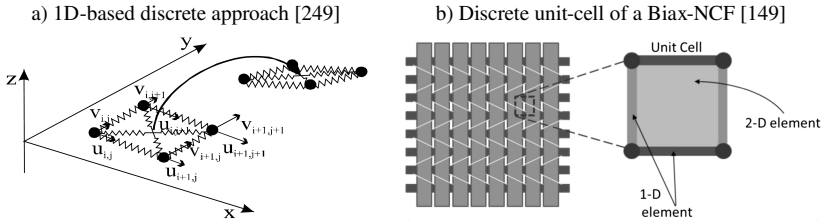

Figure 2.16: Illustration of discrete approaches based on a) only 1D-elements or b) combination of 1D- and 2D-elements

In 1D-element based approaches trusses and beams usually represent fibers or yarns under tension [250–252]. Additional truss or rotational springs are introduced to account for shear [250, 253] and bending [249, 254, 255]. Thus, these models directly account for mesoscopic effects via conventional elements [17]. However, they are missing surface elements for a proper contact formulation, limiting their application to single layers.

The unit cell of a fabric can alternatively be described by membrane elements superimposed with mutual constrained truss elements [20, 235, 256]. These approaches neglected out-of-plane bending behavior, which was subsequently introduced by utilizing truss and shell elements [257] or later bar and shell elements [149]. Some semi-discrete approaches have been developed to predict inter-ply slippage between two fiber layers of Biax-NCF, by describing the roving layers in a continuous manner and the stitching between fiber layers and plies with bar elements [132, 258].

Recently, discrete approaches based on beam elements [259, 260] or beam elements superimposed with membrane elements [134, 261] introduced an in-plane bending stiffness of rovings to successfully model shear transition zones observed during BET of woven fabrics, cf. Figure 2.8 b. A more detailed overview of the individual discrete approaches and their differences is discussed in comprehensive reviews in literature [89, 90, 209, 210].

Geometrical approaches The constituents are represented in their actual geometric dimensions and their behavior is modeled with suitable constitutive approaches. Different levels of detail are utilized depending on the intended application for characterization or forming simulations.

In *detailed* approaches, yarns or rovings are discretized with volume elements and the corresponding weaving or stitching pattern are accurately represented, cf. Figure 2.17 a. They are applied for virtual material characterization [88, 238, 262] to predict in-plane tensile and shear behavior as well as the coupled tension-shear-behavior for woven fabrics [263–266], the impact of the stitching pattern in NCFs [267, 268] or the compaction behavior of different textiles [262, 265, 269, 270]. Detailed approaches are too computationally expensive to be used on a large scale, but occasionally applied for forming simulations of single layers to investigate local effects [229, 271, 272]. An alternative for larger components are so-called meso-macro approaches, which first conduct a macroscopic analysis to obtain boundary conditions for a critical area that are applied to solve a detailed mesoscopic analysis [273–275].

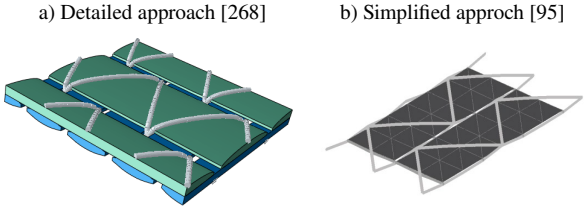

Figure 2.17: Illustration of the different levels of detail in geometrical mesoscopic approaches for a) a Biax-NCF and b) a UD-NCF.

In *simplified* approaches, fewer details are modeled to reduce the total number of DOF in the model, cf. Figure 2.17 b. They are rarely used for woven fabrics [276], but more commonly used for NCF by representing the rovings using only a few solid [94, 227] or shell [11, 95, 277–279] elements and the stitching using suitable 1D-elements. These approaches are used to predict local forming effects like in-plane roving slippage and gapping.

2.3.3 Macroscopic approaches

Macroscopic approaches consider the material as a homogenized, anisotropic continuum and model the observed deformation mechanisms (cf. Figure 2.6) by suitable constitutive equations (cf. Section 2.3.1). The key advantage of macroscopic approaches is their comparably low computational effort and the possibility to account for process-related boundary conditions in multi-layer stacks. However, modeling of forming processes for CoFRP has some specific requirements due to the multi-scale nature of fibrous reinforcements. Those requirements will be outlined in the following. Subsequently, an overview of relevant models based on stress-resultant, continuous and generalized continua approaches is presented.

Requirements for CoFRP forming First, a *decoupling of the membrane and bending behavior* is necessary in macroscopic forming simulations of CoFRP. This originates from the very low friction between fibers, which allows relative movement under bending deformation. In contrast, the fibers have a very high stiffness and are quasi-inextensible. This behavior cannot be modeled with conventional thickness-based plate or shell theories. Membrane and bending behavior is therefore usually considered in a decoupled fashion [67, 280]. This can be accomplished intrinsically within a single element by specific shell approaches [219,281] or in three-dimensional elements by generalized continua approaches [239,282]. Alternatively, an asymmetric axial modulus with significantly reduced compressive stiffness [149,283,284] or a variable stiffness over the thickness within a virtual layup for each layer [165,285] can be introduced.

An extrinsic decoupling can be accomplished by superimposing membrane and shell elements [28, 65, 198].

Second, predicting *changes of the fiber orientation* during forming is a main objective of macroscopic process simulations. Therefore, rigid body rotations due to large deformations in general as well as fiber-reorientation due to shear deformation need to be considered, cf. Figure 2.18. Rigid body rotations $\boldsymbol{R}$ are usually taken into account by rotation of an orthogonal coordinate system such as the Green-Naghdi frame $\{\boldsymbol{e}_1, \boldsymbol{e}_2\}$. The principal material orientations in the fiber directions $\{\boldsymbol{a}_1, \boldsymbol{a}_2\}$ become non-orthogonal during forming due to shear $\boldsymbol{F}_{\mathrm{ps}}$. The requirements to account for changes of the fiber orientation apply to all macroscopic constitutive approaches. Suitable methods for hypo- as well as hyperelastic approaches were already outlined in Section 2.3.1.

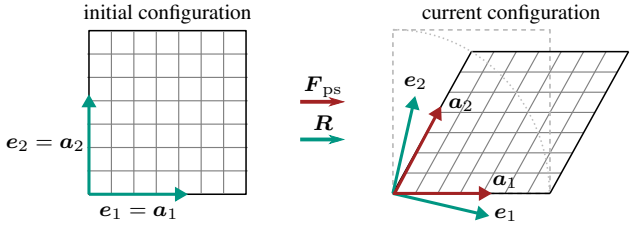

Figure 2.18: Schematic illustration of the rigid body rotation $\boldsymbol{R}$ of the orthogonal Green-Naghdi frame $\{\boldsymbol{e}_1, \boldsymbol{e}_2\}$ and non-orthogonal fiber-parallel frame $\{\boldsymbol{a}_1, \boldsymbol{a}_2\}$ under pure shear deformation $\boldsymbol{F}_{\mathrm{ps}}$.

Third, *numerical locking* phenomena can occur in the form of artificial stiffening effects in some cases, if the FE approximations made by the discretization are not compatible with a specific deformation mode [240, pp. 584-589]. Several geometric locking phenomena are well understood and intrinsically prevented in most commercial shell elements or can be alleviated with suitable methods for three-dimensional elements (will be further discussed in Section 2.4.2). However, a specific material locking phenomenon is observed during CoFRP forming, which is called tension locking and induces too stiff shear behavior. This effect was first observed by Yu et al. [286] and later thoroughly investigated

by Hamila et al. [287] in virtual BET. Tension locking originates in fully-integrated quadrilateral elements from artificial fiber strains in combination with an inextensibility constraint in fiber direction. Different methods are proposed to alleviate this locking phenomenon. A selective reduced integration scheme with under-integration of the inextensibility constraint and a specific hourglass control achieves good results for non-aligned meshes [287,288]. Thije et al. [288] proposed different multi-field elements with additional strain DOF to successfully prevent tension locking, but at the same time requiring a higher computational effort. A pragmatic approach to avoid this phenomenon is to initially align the element edges with the fiber directions [286–288].

Stress-resultant approaches Stress-resultant shell approaches were first proposed for woven fabrics by Boisse et al. [289]. They decompose the element into representative unit cells (RUC) of the material and combine the individual stress resultant forces and moments due to tension, shear and bending into the internal virtual work [90]

$$\delta W_{\mathrm{int}}^{\mathrm{RUC}} = \delta W_{\mathrm{int}}^{\mathrm{tension}} + \delta W_{\mathrm{int}}^{\mathrm{shear}} + \delta W_{\mathrm{int}}^{\mathrm{bending}}. \tag{2.17}$$

The approach was initially developed for woven fabrics [216,219,223,289–292] and later adapted for thick interlock woven fabrics [217, 293], thermoplastic prepregs [154, 294] and Biax-NCF [136].

Ghafour et al. [292] utilized a stress-resultant approach for a woven fabric to investigate the importance of accounting for irreversibilities in the material behavior. An inelastic model with significant dissipative effects in the membrane as well as bending behavior was directly compared to an elastic model of the same material. The predicted outer contours and wrinkling behavior were nearly identical for monotonous displacements of the punch during hemisphere, tetrahedron and box forming tests. Differences were mainly observed for the predicted residual stresses or when considering the removal of the punch.

Continuous approaches[5] Woven fabrics have often been the focus of research on macroscopic forming simulations due to their better formability, cf. Figure 2.19 a, as evident from comprehensive reviews in literature [67, 88–91, 238]. Thereby, hypoelastic [212, 213, 215] or hyperelastic [64, 160, 244, 295] approaches are most commonly used to model their behavior. Additionally, biaxial tension as well as tension-shear interactions were investigated for woven fabrics by introducing suitable couplings between the deformation modes [106, 246, 247, 296].[5]

a) Woven fabric [212] b) UD-NCF [86]

Figure 2.19: Examples for a continuous approach for a) a woven fabric and b) a UD-NCF.

In contrast, Biax-NCF [133, 165, 166, 232] or UD-NCF [137, 139, 297] have been investigated much less. Membrane approaches for NCFs need to consider not only shear, which is the main deformation mode for woven fabrics during forming [89], but also stitching deformation and roving slippage.[5]

Yu et al. [141] developed a non-orthogonal hypoelastic model for Biax-NCF considering an asymmetrical shear behavior due to the tricot stitching oriented at $45°$ relative to the fibers. They highlight the influences of friction between the blanks and tools, blankholder forces and blank shape in numerical forming studies on a hemispherical shape. A similar approach was later developed by Chen et al. [113]. Khiêm et al. [133] proposed a hyperelastic model as a

[5] Extracts from this Section have been previously published in [180], i.e. B. Schäfer, D. Dörr, R. Zheng, N. Naouar, L. Kärger. A hyperelastic approach for modeling the membrane behavior in finite element forming simulation of unidirectional non-crimp fabrics (UD-NCF). *[submitted for review]* | Reproduced paragraphs are marked with [5].

user-defined material in ABAQUS for a Biax-NCF with a chain stitch oriented at $45°$. The model considers stitching and fiber tension as well as in-plane shear. Fiber slippage was neglected in the approach, but despite the simplicity of the approach good agreement with experimental forming tests on a double dome geometry was achieved. Mallach et al. [232] modeled the behavior of a Biax-NCF primarily based on a nonlinear shear stress-strain curve in PAM-FORM. Acceptable results were obtained for the global forming behavior of a complex geometry for different blankholder configurations, but neglecting roving slippage resulted in noticeable deviations in the fiber orientation in areas of large shear deformation. Yu et al. [165, 166] investigated the impact of the non-linear bending behavior observed for Biax-NCF on wrinkling during hemisphere forming tests.[5]

All approaches for Biax-NCFs neglect intra-ply slippage between rovings and large tensile strains of the stitching, which are highly relevant mechanisms for UD-NCF during forming due to the lack of a second fiber direction [109, 110]. Therefore, the exclusive focus on the shear behavior during characterization and modeling is not sufficient. This is also evident in the study of Krogh et al. [139], in which the ABAQUS built-in FABRIC material model is utilized to describe the shear behavior of a quasi-UD glass-fiber NCF. The model predicts the early force-displacement-relation in a BET well. However, the model overestimates the shear response for larger deformations as UD-NCF deforms more under simple shear instead of pure shear.[5]

A very comprehensive macroscopic approach was proposed by Schirmaier et al. [137], cf. Figure 2.19 b. It consists of an elastic-plastic transverse tensile behavior coupled to the elastic-plastic shear behavior via a 2D-yield surface and is superimposed with a 2D-elastic compressive stiffness perpendicular to the fiber rovings which is also coupled to the shear angle. The model is inversely parameterized using $30°$-, $45°$-, and $60°$-OATs, approximating the applied forces well but underestimating the local strains in the main deformation zones of the

[5] Reproduced paragraph from [180], cf. footnote p. 39 for details.

specimen centers. Nevertheless, it achieves good results in qualitative [137] and quantitative [297] comparisons to component forming results. However, the complex model requires a high number of material parameters to describe the membrane behavior, resulting in a difficult and time-consuming parameterization process and limited applicability to other materials.[5]

Ghazimoradi and Montesano [298] recently parameterized *MAT_249 of LS-DYNA for a binder-stabilized UD-NCF by introducing three independent fiber families for the carbon rovings, glass fibers and stitching. They calibrated the model with tensile tests in the longitudinal and transverse direction as well as $45°$-OATs. $30°$- and $60°$-OATs were used for the validation and a good agreement of the resulting forces and shear angles was achieved, but notable out-of-plane wrinkling was predicted which was not observed during the experiments. During application to hemispherical forming tests, the location and orientation of wrinkling were qualitatively predicted but the resulting shear angles were overestimated and other strains were not further investigated in their study.[5]

Generalized continua approaches For textile forming, most approaches based on generalized continuum mechanics are based on the second-gradient to account for the in-plane and out-of-plane effects of mesoscopic roving bending stiffness in macroscopic models [48, 67, 89, 90, 97, 239]. The main challenge is to calculate the gradient representing the roving curvature, as this is not directly available for linear elements often used for efficient forming approaches. Ferretti et al. [145] proposed to calculate the curvature in three-dimensional elements as limit case of a micromorphic theory in the multi-physics solver COMSOL. This requires the introduction of a second-order tensor field $\boldsymbol{\psi}(\boldsymbol{X})$ describing microscopic deformations and additional constraints based on a penalty energy contribution with Lagrange multipliers to ensure continuity of the utilized gradients. This approach has been applied by multiple researchers to introduce an in-plane roving bending stiffness and model in BETs the transition zones of woven fabrics (cf. Figure 2.20 a) [48, 145, 259, 299] or the deformation

[5] Reproduced paragraph from [180], cf. footnote p. 39 for details.

behavior of strongly unbalanced woven fabrics [260, 299]. Additionally, it was utilized to show the influence on the out-of-plane bending stiffness of a thick interlock woven fabric in three-point bending tests [161] as well as the wrinkling behavior during deep drawing of a hemisphere (cf. Figure 2.20 b) [282] and other lightweight components [300]. However, this implementation strategy is limited to specific solvers, because the introduction of micromorphic theories is not possible in many commercial solvers.

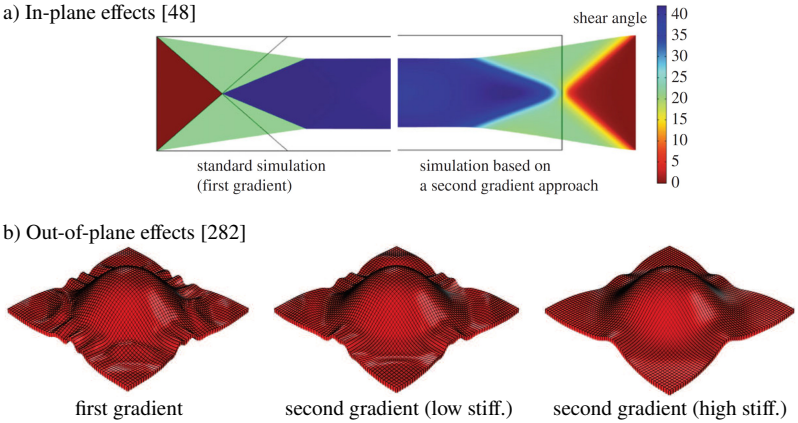

Figure 2.20: Examples for the effect of generalized continua approaches on the a) in-plane behavior of a woven fabric in BET and b) out-of-plane behavior of a thick interlock woven fabric in a hemisphere test.

The curvatures can also be approximated based on the displacement degrees of freedom of neighboring elements to show the above described effects on the in-plane [301] and out-of-plane [162, 302] behavior. An intrinsic calculation of especially the in-plane curvature requires higher-order shape functions, as demonstrated by Duong et al. [303] for an isogeometric shell element. For thin reinforcements, the approaches to account for a decoupling of the membrane and bending behavior resemble the introduction of a second-order energy strain density for out-of-plane bending as it is independently calculated based on curvature. Approaches based on generalized continua are a promising strategy to incorporate mesoscopic effects in macroscopic approaches and to fulfill the

requirements for CoFRP forming in three-dimensional elements. However, the efficient calculation of higher strain gradients in commercial solvers and the experimental validation based on quantitative measurements of the observed effects demands further research.

2.4 Three-dimensional approaches for forming with large deformations

The compaction behavior of an engineering textile is an important intra-ply deformation mechanism, cf. Figure 2.6. It determines the resulting thickness as well as FVC and consequently influences the permeability, necessary press forces as well as resulting mechanical properties of components produced from LCM [66]. Compaction of CoFRP is often investigated based on mesoscopic approaches [179, 270, 304] or by isolated macroscopic simulations of critical corners [305, 306]. Modeling compaction during forming requires a three-dimensional material behavior in an appropriate element formulation. However, it is neglected in most macroscopic simulation approaches as they are based on 2D shell and membrane elements, cf. Section 2.3.3. Three-dimensional solid elements are prone to numerical stiffening effects during bending deformation of thin structures, which prohibits their direct application in forming simulations. Those effects are also called numerical locking phenomena and their elimination requires specific methods, which will be discussed in the following Section 2.4.1. Section 2.4.2 introduces the class of solid-shell elements, which are 3D locking-free elements designed for bending deformation of thin structures. Subsequently, an overview of existing approaches for the consideration of compaction during CoFRP forming is presented in Section 2.4.3.

2.4.1 Numerical locking

The advantages of linear elements based on $\mathcal{C}^0$-smooth shape functions are their efficiency due to the low polynomial degree as well as their convergence behavior. A disadvantage of these elements is the occurrence of numerical locking phenomena, which cause a too high stiffness for different deformation modes. The term locking describes the occurrence of purely numerically caused parasitic stresses if the approximations made by the FE discretization are not compatible with a specific deformation mode and the predicted behavior is too stiff [240, pp. 584-589]. Characteristics of locking phenomena are their sensitivity to a critical parameter that depends on either the element's geometry or the material and their slower convergence when increasing the number of DOF compared to a locking-free element [307]. Locking has been and is still an active field of research for the development of new element formulations, as a result of which many different terminologies and classifications exist [240, 307–309]. In the following, the most relevant geometrical and material locking phenomena in the context of forming are shortly introduced, whereby this work is based on the classifications by Bischoff [308] and Koschnick [307]. Subsequently, methods to prevent locking phenomena are introduced.

Geometrical locking The most relevant geometrical locking phenomenon is *shear locking* for bending deformation modes of elements with linear shape functions. This effect is schematically illustrated for a quadrilateral element in Figure 2.21. The expected quadratic displacements u_y in y-direction and bilinear displacements u_x in x-direction analytically result in a linear normal stress σ_x without shear stresses τ_{xy}. The same displacements applied to the nodes of a quadrilateral element result in non-zero, parasitic shear stresses as the shape functions cannot represent the curved edge deformation. The energy contribution of the parasitic shear stresses is proportional to the element's in-plane aspect ratio $a^{\text{in-plane}} = \frac{l_x}{l_y}$, which is the critical parameter for this locking problem. Shear locking can occur for in-plane deformations as well as out-of-plane deformations, where it is referred to as transverse shear locking.

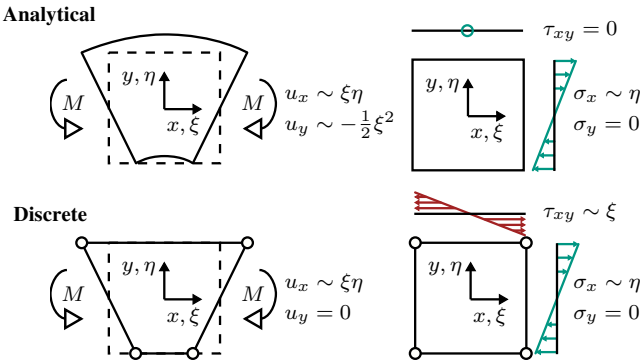

Figure 2.21: Schematic illustration of shear locking for pure bending of a linear quadrilateral elements (based on [307]).

Curvature-thickness or *trapezoidal locking* occurs during bending of elements with a trapezoidal shape, when the element edges are not perpendicular to the element mid-plane. This locking phenomenon results in parasitic normal stresses and is mainly observed for initially curved structures, as the natural undeformed meshes have a trapezoidal shape in thickness direction. The critical parameter is the out-of-plane aspect ratio $a^{\text{thick}} = \frac{l_e}{t}$, based on the element's thickness t and its characteristic length defined by the highest edge length l_e. This type of locking does not occur for the usually flat initial discretization with regular elements utilized in forming simulations.

Material locking *Volumetric* or *Poisson thickness locking* is observed for deformation modes that induce lateral contraction. The origin of volumetric locking is schematically illustrated in Figure 2.22. As a result of lateral contrac-

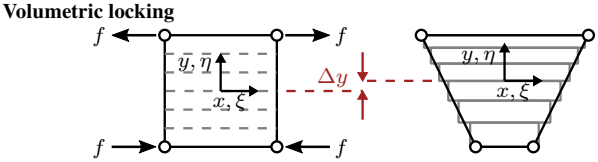

Figure 2.22: Schematic illustration of the origin for volumetric locking (based on [307]).

tion, the compressive regions expand while the tensile regions contract, so the

centerline should shift. However, this cannot be represented by linear elements as the nodes do not move in y-direction. Therefore, the material centerline remains in its original position at the geometric center. The resulting parasitic tensile stresses increase with the Possion ratio ν of the material, which is the critical parameter of this locking type.

Tension locking is a material locking phenomenon specific to CoFRP. Its origin and methods for its prevention are already outlined in Section 2.3.3.

Methods to prevent locking Different methods to completely prevent or at least alleviate locking are described in literature and the fundamental principles are outlined in the following. A detailed mathematical description is omitted due to its complexity, and the interested reader is referred to the comprehensive explanations available in literature [240, 307, 308, 310].

First, *increasing the polynomial order of the shape functions* alleviates many locking phenomena by increasing the capabilities of the element to comply with deformation modes. However, this approach significantly increases the numerical effort and is often not recommended for explicit integration schemes commonly utilized for forming simulations [309, p. 258].

Second, *selected reduced integration schemes (SRI)* can be used. The integration points of components with parasitic stresses are strategically positioned to only include the locking-free constant part of these stresses in the strain energy. An example location in the case of shear locking is the element's center, cf. Figure 2.21. SRI is computationally very efficient due to the reduced number of integration points. However, it results in a singular, rank-deficient stiffness matrix and requires specific stabilization procedures to prevent energy-free deformation modes, called hourglassing.

Third, *modifications to the interpolation of strains* can be applied. Locking is usually limited to specific parts of the stress tensor resulting from parasitic strains and stresses. Thus, the strain tensor $\boldsymbol{E}$ can be separated into a part responsible for locking $\boldsymbol{E}^{\mathrm{lock}}$ and a locking-free part $\boldsymbol{E}^{\mathrm{free}}$. Then, collocation

points are selected within the elements at known zero points of the specific parasitic stresses and thus at locations of correct strains. Examples of collocation points in the case of shear locking are the centers of the upper and lower element edges, cf. Figure 2.21. Subsequently, the strain components are re-interpolated over the element with new shape functions based on the collocation points. This approach was initially proposed by Bathe and Dvorkin [311] and is referred to *assumed natural strain method (ANS)*.

Fourth, *mixed variational energy functionals* can be applied during the formulation of the virtual work. The Hu-Washizu variational principle is the most common for the development of locking-free element formulations. It is a more general form of the balance equations where, in addition to displacements, also stresses and strains need to be satisfied only in the integral mean. This enables the introduction of additional internal strain DOFs within the elements to comply with more deformation modes. The method is referred to as *enhanced assumed strain method (EAS)* or alternatively as incompatible mode elements, because the internal DOFs do not have to be continuous and therefore compatible across element boundaries. Thus, the total strain tensor $\boldsymbol{E}$ is additively split into a compatible part $\boldsymbol{E}_{\mathrm{c}}(\boldsymbol{u})$ depending on the displacements $\boldsymbol{u}$ and an enhanced part $\boldsymbol{E}_{\mathrm{e}}(\boldsymbol{\alpha})$ depending on the enhanced DOFs $\boldsymbol{\alpha}$. This approach was initially proposed by Simo and Rifai [312] and results in the commonly implemented two-field variational functional

$$\delta g_{\mathrm{HW}}(\boldsymbol{u},\boldsymbol{\alpha}) = \int_{\Omega} \boldsymbol{S}^{\boldsymbol{E}} \colon \delta(\boldsymbol{E}_{\mathrm{c}} + \boldsymbol{E}_{\mathrm{e}})\mathrm{d}\Omega + \int_{\Omega} \rho\ddot{\boldsymbol{u}} \cdot \delta\boldsymbol{u}\mathrm{d}\Omega - \delta g^{\mathrm{ext}} = 0, \quad (2.18)$$

in combination with the orthogonality condition

$$\int_{\Omega} \boldsymbol{S}^{\boldsymbol{E}} \colon \delta\boldsymbol{E}_{\mathrm{e}}\mathrm{d}\Omega = 0, \quad (2.19)$$

where ρ is the density, δg^{ext} denotes the virtual work of external loads and $\boldsymbol{S}^{\boldsymbol{E}}$ is the stress depending on the total strain. The orthogonality condition is utilized

for static condensation of the enhanced DOF $\boldsymbol{\alpha}$ within the element, eliminating the requirement of an additional global DOF and enabling an efficient implementation in many solvers.

2.4.2 Solid-shell elements

Solid-shell elements are a group of three-dimensional elements with a predefined thickness direction, which combine different methods to achieve a locking-free behavior, especially during bending of thin structures. In contrast to classical or degenerated shell elements, these elements allow the use of general three-dimensional material models and have only translational DOFs. In addition, the modeling of contact boundary conditions does not require additional kinematic assumptions. Table 2.1 summarizes the locking phenomena outlined in Section 2.4.1 and the methods how they are commonly prevented in solid-shell elements. Various formulations of solid-shell elements have been proposed in literature, which are compared to each other in different studies [313–315]. The main distinguishing features are the integration scheme, the number of collocation points for the ANS and the number of enhanced DOF for the EAS (EAS-DOF). The locking-free behavior is validated with several well-known benchmarks for geometrically linear and non-linear deformation modes. A detailed overview of common benchmarks is for example presented by Mostafa [316].

Table 2.1: Overview of locking phenomena and methods for their prevention.

Locking phenomenon		**Crit. parameter**	**Prevention**
geometrical	in-plane shear	aspect ratio $a^{\text{in-plane}}$	SRI, ANS
	transverse shear	aspect ratio a^{thick}	SRI, ANS, EAS
	curvature-thickness	aspect ratio a^{thick}	ANS, EAS
material	volumetric	Poisson ratio	EAS
	tension	inexentibility	alignment, SRI

Hauptmann and co-authors [317, 318] presented some of the first studies on fully integrated solid-shell formulations, comparing different combinations of 2-point ANS and four EAS-DOF for the in-plane and thickness approximation. A geometrical locking-free behavior was observed for most combinations and the formulation was enhanced to account for material locking by reduced integration of the volumetric strain parts [319, 320]. The solid-shell elements were later extended for explicit time integration schemes [321, 322]. The implementation of a variable number of EAS-DOF and incompatible modes to tailor the approach for specific application was presented by symbolic programming within the software AceGEN for runtime optimization [323]. Similar fully integrated solid-shell elements were developed by Vu-Quoc and Tan for structural simulations of multilayered composites [324–326].

Reduced-integration schemes are inherently less prone to locking due to the location of integration points, but require suitable hourglass stabilization. A solid-shell element based on reduced integration was initially proposed by Reese et al. [327] with a single integration point and three EAS-DOF. However, the incremental calculation of stabilization factors was computationally expensive and slight locking remained for large deformations. Sousa et al. [328, 329] proposed an alternative solid-shell element with SRI. It utilized one in-plane integration point in the center, variable integration points in thickness direction and only a single EAS-DOF. The stabilization components for the membrane part required a stabilization parameter similar to [327], but the transverse parts were analytically calculated based on the material stiffness. The solid-shell element showed promising results for linear [328] and non-linear [329] benchmarks as well as sheet metal forming simulations [330]. The performance and stability was further improved by introducing ANS for the transverse shear modes based on four collocation points instead of two, which is required for reduced integrated elements to ensure full rank of the stiffness matrix [331].

Schwarze and Reese [314,332] proposed a solid-shell element denoted as Q1STs with SRI, four-point ANS and a single EAS-DOF. They additionally introduced a Taylor expansion of the strains and stresses to enable a fully stiffness-based

analytical hourglass stabilization. They directly compared their element's performance to previous approaches [324, 328, 331] and found an increased performance in particular for very high out-of-plane aspect ratios. Pagani et al. [333] later extended the Q1STs element to an explicit formulation, which enabled improvements of the computational efficiency by reducing necessary iterations on the element level due to the small time steps. The Q1STs element showed promising results for structural simulations of fiber-reinforced composites [334, 335], deep drawing of sheet metals [333, 336] as well as packaging simulation of cardboard [337].

2.4.3 Approaches for CoFRP forming

Solid-shell elements show promising results for sheet metal forming [331, 333, 336, 338–340], but specific requirements (cf. Section 2.3.3) have to be considered for CoFRP forming. Chen et al [341] outlined an early solid-shell concept for a thermoplastic woven composite. The internal energy is decomposed into tension, shear, bending and compression. However, no details on the implementation or methods to prevent locking are described. Plausible results are obtained for the final state with closed tools without any wrinkling during numerical hemisphere and box forming tests, but not compared to experimental results. The relative inter-ply slippage during thermoforming was investigated in a second study with the same element formulation [342], but bending was ignored and compaction was not further discussed.

A 6-node prismatic element for composite forming was proposed by Xiong et. al. [30, 31] for thermoplastic prepregs to investigate consolidation. The membrane part is based on a constant strain triangle formulation. The bending part is based on a discrete Kirchhoff plate theory formulation for zero transverse shear strains and hourglass stabilization. However, it requires an additional global degree of freedom in the element center to avoid Poisson locking and to improve the prediction of pinching stresses, in contrast to an internal degree of freedom based on EAS.

Generalized continua approaches for the investigation of the out-of plane roving stiffness are based on special 3D element formulation and also include the compaction behavior in their material model, cf. Section 2.3.3. However, they have been exclusively applied for thick interlock woven composites. This eliminates the need for elements with high out-of-plane aspect ratios, and the textiles have significant transverse shear stiffness, eliminating the need for complete decoupling of membrane and bending behavior.

A unique approach has been proposed by Poppe et al. [66, 343] to model the simultaneous infiltration during forming in WCM. The compaction behavior is modeled by a user-defined element superimposed with a built-in prismatic continuum shell (SC6R) in ABAQUS/Explicit to circumvent the limitation of a constant compressive stiffness in the SC6R-element. This approach models the low bending stiffness of the fabric with a significantly reduced transverse shear stiffness rather than decoupling. This limits the approach to an isotropic bending behavior and prevents the implementation of a more complex bending model originally proposed for this process [65].

2.5 Literature summary and research gap

Summary The forming of an initially flat stack of engineering textiles into a complex 3D shape is the initial step in different LCM processes for high-performance CoFRP components. Non-crimp fabrics have a higher lightweight potential as base material due to their straight rovings compared to woven fabrics with undulations. The objective of a successful process design is to minimize waste and avoid defects through suitable manipulation methods and clever material selection. This requires a comprehensive understanding of the deformation behavior of the material as well as the related process conditions and can be supported by suitable simulation methods.

Characterization methods for dry engineering textiles have been the focus of many studies and a variety of experimental setups are available for the different inter-ply and intra-ply mechanisms. Woven fabrics in particular have been extensively investigated and many setups have initially been developed for their specific requirements. They have been utilized in several benchmark studies, comparing the measured behavior in fundamentally different setups for the same mechanism or similar setups at different institutions. As a result, their deformation behavior is well understood and many general trends for different weaving types have been identified. Most characterization setups are directly transferable to NCF and can be used without significant modifications for the bending, compaction and inter-ply behavior. During membrane characterization, it is essential to consider that pure shear is not an intrinsic deformation mode of NCFs. They deform under a combination of stitching strains, relative fiber rotation and slippage between fiber rovings or different fiber layers. This requires additional or modified setups for membrane characterization and the strains should be measured optically as conventional theories are not valid. Additionally, NCFs are available in a wide variety of architectures and the different stitching patterns in particular have a notable influence on their behavior. This often makes direct comparisons between architectures complicated and general trends more difficult to identify.

Simulation approaches for engineering textiles have to account for their multi-scale nature by suitable modeling strategies and constitutive approaches. Mesoscopic approaches directly account for the architecture of the constituents and are well suited for detailed investigations. However, they are computationally expensive and rarely applied for forming simulations of large components.

Macroscopic approaches are more efficient and mainly used for component forming simulations under consideration of process conditions. They have to fulfill specific numerical requirements to still account for the inherent multi-scale nature of the textile. The main deformation modes of woven fabrics during forming are commonly described by a low bending stiffness, high fiber stiffness and non-linear pure shear, despite slight tensile-tensile and tensile-shear couplings due to the undulations. Similar approaches were also applied for

Biax-NCF, with the main modifications consisting of introducing the stitching as an additional stiffness and resulting in asymmetric shear behavior depending on its orientation. Macroscopic models for UD-NCF need to account for notable intra-ply slippage between rovings and superimposed large tensile or compressive strains due to the lack of a second fiber direction. Simplified approaches that focus mainly on the shear behavior therefore achieve insufficient results. Even highly complex approaches with multiple couplings cannot perfectly describe this behavior under all conditions.

A better consideration of mesoscopic effects based on generalized continuum mechanics in macroscopic approaches has been successfully demonstrated for woven fabrics. However, they were not yet applied for other engineering textiles and their application in commercial solvers requires further research.

The consideration of compaction during forming of thin structures is very rare despite its known influence on the FVC and the consequent effects. It requires a 3D element formulation and material model. However, the majority of conventional solid elements are not suitable due to numerical locking phenomena, whose elimination requires specific techniques. The class of solid-shell elements combines these techniques to prevent locking for bending of thin structures. Locking-free solid-shell based approaches have been successfully applied to metal forming, but not yet for dry engineering textiles. Alternative 3D approaches have been proposed in the context of thermoforming or WCM. However, they require additional assumptions with respect to their transverse shear behavior, thus limiting the applicable constitutive models for their bending behavior.

Research gap Several studies focus on the characterization of individual deformation mechanisms of NCF, but the highly individual nature of the specific architectures limits the comparability and generalizability of results. Few comprehensive characterizations of all mechanisms are available, making it difficult to identify the relevant mechanisms of each deformation mode for forming. Especially, quantitative studies and strain measurements of component forming

tests are very sparse for NCF and existing studies often only focus on the measured shear angle. The limited database of studies for UD-NCF in particular makes the comparison of new materials and development of suitable modeling approaches challenging.

The most advanced macroscopic model for UD-NCF requires a large number of material and coupling parameters that are difficult to determine, which severely limits the direct transferability to new materials with different architectures. At the same time, oversimplified approaches lead to an inadequate representation of the complex behavior. An intermediate solution that can describe all essential deformation modes and still has a sensible level of complexity to simplify the parameterization process is therefore missing.

Solid-shell elements have demonstrated the advantages of a locking-free bending behavior in the context of metal forming. However, they must be further modified to account for the specific requirements of CoFRP forming. The impact of a locking-free bending behavior in combination with a necessary membrane-bending decoupling on the forming behavior was never demonstrated or discussed.

3 Objectives and outline

3.1 Objectives

The evaluation of the state of the art for dry engineering textiles reveals an emphasis on woven fabrics, both in the availability of experimental studies as well as suitable simulation methods. Non-crimp fabrics, and unidirectional NCF (UD-NCF) in particular, have been the subject of much less studies and there are still gaps in their research. This work therefore focuses on establishing an advanced understanding of the forming behavior of non-crimp fabrics and developing suitable macroscopic simulation methods for the efficient application to virtual process design. In order to fully exploit the potential of unidirectional NCFs in particular, new approaches are needed that are capable of describing the complex behavior and yet can be efficiently transferred to new materials. In addition, a three-dimensional approach is desirable to account for compaction during forming and to better study the resulting effects.

Given these challenges, the following three main objectives of this thesis are derived:

Objective O-1. Systematic characterization of the inter- and intra-ply deformation mechanisms and quantitative analysis of the forming behavior of non-crimp fabrics with an emphasis on the specific challenges of unidirectional non-crimp fabrics (UD-NCF) to enable process modeling and its validation.

Objective O-2. Development of a 2D macroscopic forming model for UD-NCF based on a hyperelastic approach with a sufficient complexity to accurately describe the relevant deformation modes, but still facilitate a simplified parameterization process and the transferability to other materials.

Objective O-3. Development of a 3D solid-shell element to account for compaction during the forming of engineering textiles, which exhibits locking-free behavior for slender structures and takes into account the specific requirements of continuous fiber-reinforced plastics (CoFRP).

Delimitation This work investigates dry non-crimp fabrics to specifically identify the truly fundamental mechanisms of the material and translate them into a modeling approach. Although important, activated binders or superimposed infiltration are neglected in the experiments and modeling in this work. Proper consideration of these superimposed effects requires a comprehensive understanding and a suitable modeling approach of the underlying fibrous material which is developed in this thesis.

3.2 Outline

This thesis is divided based on the objectives into three main Chapters 4-6 that are illustrated in Figure 3.1, followed by a conclusion in Chapter 7.

Chapter 4 presents the experimental results of this work and focuses on objective O-1. First, the different intra- and inter-ply deformation mechanisms are individually characterized in Section 4.1-4.5. Subsequently, the overall forming behavior is investigated and quantitatively measured in forming tests for different layup configurations and common punch shapes, cf. Section 4.6. All tests are conducted for a unidirectional and a bidirectional NCF to compare both materials and highlight the specific challenges for UD-NCF.

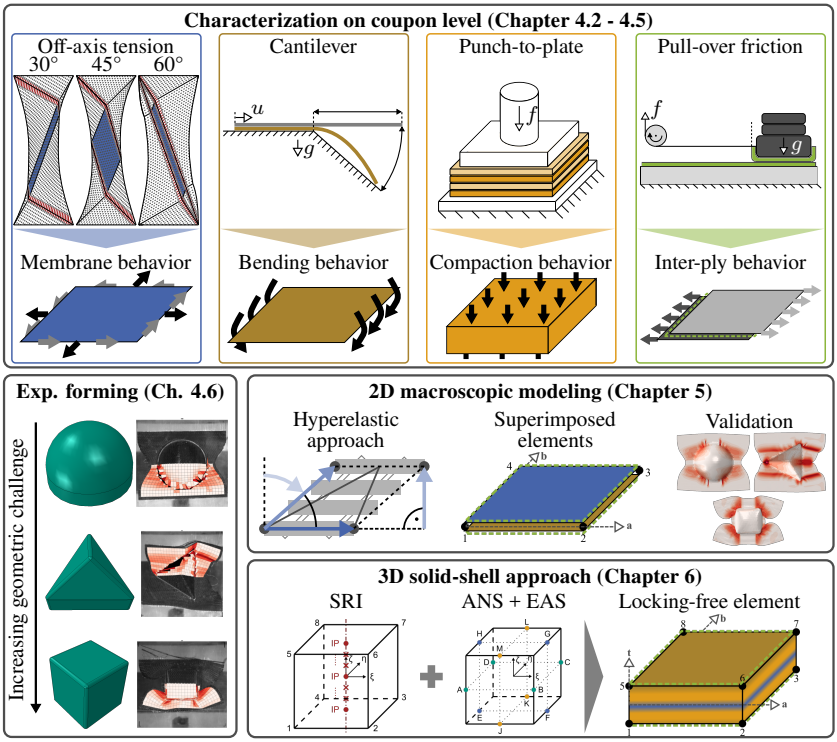

Figure 3.1: Overview of the main contents of the thesis.

Chapter 5 presents a 2D macroscopic forming model for UD-NCF and focuses on objective O-2. The necessary complexity to describe the membrane behavior is evaluated in a preliminary study and a new hyperelastic modeling approach is presented. Subsequently, the transferability of the approach is demonstrated by an application to Biax-NCF.

Chapter 6 presents a 3D solid-shell element for forming simulation of engineering textiles and focuses on objective O-3. First, the fundamentals of the element formulation for a locking-free behavior and modifications to account for the specific requirements of CoFRP are outlined. Second, the locking-free behavior in general is demonstrated and validated by forming simulations of

isotropic as well as anisotropic materials. Third, the solid-shell element is applied to forming of engineering textiles.

Finally, the main conclusions in relation to the three objectives are presented in **Chapter 7**, followed by recommendations for further research.

4 Experimental analysis of the textile forming of NCFs

Outline

The following chapter presents a comprehensive analysis of the macroscopic deformation mechanisms for the utilized materials in this work. First, the investigated unidirectional and bidirectional non-crimp fabrics are introduced in Section 4.1. Second, the different intra- and inter-ply deformation mechanisms (i. e. membrane, bending, compaction and inter-ply behavior) are individually characterized in Section 4.1-4.5. All experiments are conducted for both materials to identify similarities and differences between the nearly balanced Biax-NCF and highly unbalanced UD-NCF. In particular, the influence of the stitching results in many differences compared to the well-understood behavior of woven fabrics, for which most characterization methods were originally developed. Third, the overall forming behavior is investigated and quantitatively measured in forming tests for different layup configurations and common punch shapes in Section 4.6. The main objective of the forming tests is to identify the most relevant deformation mechanisms and to create a detailed database for later validation of the simulation models. Subsequently, the findings are summarized and resulting requirements for the development of a suitable forming model are discussed in Section 4.7.

4.1 Investigated materials

In this work, a unidirectional (UD300) and a bidirectional (MD600) non-crimp fabric both without binder are investigated, cf. Table 4.1. The fabrics are manufactured by Zoltek™ from their PX35-50K continuous carbon (CF) fiber heavy tows and stitched together in a tricot pattern. The UD300 consists of a single layer of aligned CF rovings with thin glass fibers (GF) on the back for improved handleability. The MD600 consists of two layers in a 0°/90° orientation. Both fabrics have a similar number of CFs in each layer with about $300\,\mathrm{g\,m^{-2}}$ in their respective main reinforcing directions. All specimens investigated in this work were prepared from the same roll of UD- and Biax-material on an automated cutting table by Zünd Systemtechnik AG, Switzerland.

Table 4.1: Characteristics of the investigated NCFs by Zoltek™

		UD-NCF (UD300)	Biax-NCF (MD600)
Stitching pitch	[mm]	7.2	5.2
Initial thickness	[mm]	0.4959	1.004
Areal density ρ_A			
Total	$[g/m^2]$	328.86	602.24
0°	$[g/m^2]$	309.86	301.53
90°	$[g/m^2]$	9.7 (GF)	292.52
PES stitching	$[g/m^2]$	9.3	8.19
front - f		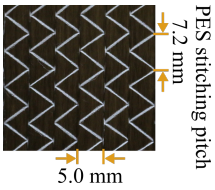	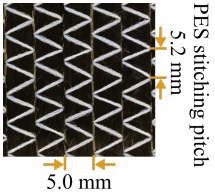
back - b		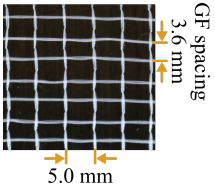	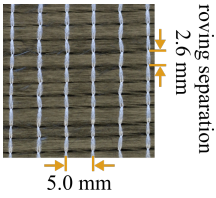

4.2 Membrane behavior[1]

The membrane behavior is a particularly important deformation mechanism for engineering textiles, cf. Section 2.2.1. It enables the transformation from an initially flat 2D stack into a 3D component via fiber reorientation due to shear and superimposed strains. In this work, the membrane behavior of a UD- and Biax-NCF is investigated in off-axis tension tests (OATs) of three different bias angles (i.e. $30°$, $45°$ and $60°$). A dot pattern aligned with the rovings is applied to the specimens, enabling a macroscopic strain measurement using DIC. Furthermore, a method is presented to measure in-plane roving bending based on the curvature in fiber direction. The influence of the measuring method is evaluated based on its impact on the resulting forces as well as discrete measurements of the fiber orientation and deformed sample width. Finally, implications regarding the relevance of the individual experiments for a comprehensive characterization of the membrane behavior for forming simulations are discussed.

4.2.1 Experimental test setup and procedure[1]

Experimental setup A Zwick-Roell Z2.5 universal testing machine with a $500\,\mathrm{N}$ load cell is used to conduct all tests at room temperature. The OATs were performed on the UD-NCF for three different bias angles (i.e. $30°$, $45°$ and $60°$) and on the Biax-NCF for $30°$ as well as $45°$. These bias angles were selected to impose different ratios of in-plane shear and tensile strains based on the results of the study by Schirmaier et al. [137]. An aspect ratio $a = {}^{l_0}/_{w_0} = 2$ with an initial specimen length l_0 of $320\,\mathrm{mm}$ and width w_0 of $160\,\mathrm{mm}$ was used with a

[1] Extracts from Section 4.2 have been previously published in [102], i. e. B. Schäfer, R. Zheng, N. Naouar, L. Kärger. Membrane behavior of uni- and bidirectional non-crimp fabrics in off-axis-tension tests. *International Journal of Material Forming*, 16(6):68, 2023 | Section 4.2.1 reproduces Section 3 of [102]; Sections 4.2.2-4.2.3 reproduce Section 4 of [102].

velocity of $v = 60\,\mathrm{mm/min}$, cf. Figure 4.1 a. Each test was repeated five times for each configuration with and without a dot pattern.

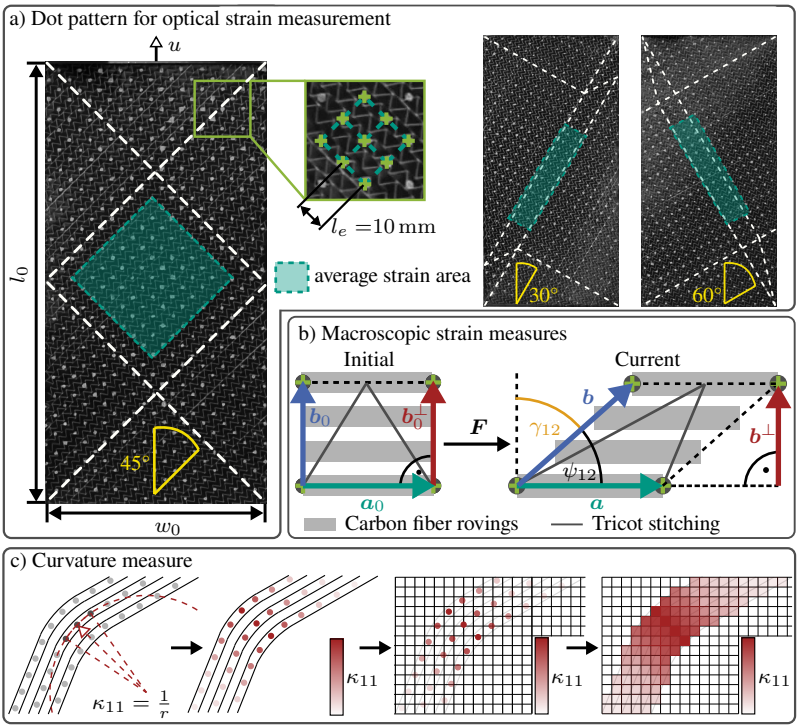

Figure 4.1: (a) Dot pattern utilized during 2D-DIC to measure (b) macroscopic strains as well as (c) resulting curvature in fiber direction (adapted from [102]).

Strain and curvature measurement method The macroscopic deformation is measured via Digital Image Correlation (DIC). A regular grid of white dots of acrylic paint with an approximate diameter of 2 mm is applied to the specimens using a stencil with a distance of $l_\mathrm{e} = 10\,\mathrm{mm}$, c.f. Figure 4.1 a. Acrylic paint was used because other white markers, paint colors, or spray paints either soaked strongly into the fabric or had too little contrast on the rovings compared to the seams. The grid is aligned with the principal fiber direction

during the test and each dot is manually positioned as centered as possible on the rovings. The deformation is recorded with a Canon EOS 70 D DSLR camera at 30 frames per second. The displacement of each dot was tracked with an open-source MathWorks Matlab DIC tool [344], which was enhanced to account for the regular grid [110,137]. Subsequently, four dots are combined into a 2D quadrilateral element and the deformation gradient $\boldsymbol{F}$ rotated in the initial fiber direction is calculated based on linear shape functions [240].

During the tests, especially for UD-NCF, large shear strains superimposed with transverse tensile deformation in the stitching direction and compression perpendicular to the carbon fiber rovings are expected on a macroscopic level [137]. Therefore, in addition to the components of the Green-Lagrange strains E_{11} and E_{22} representing the quadratic stretches along the directions $\boldsymbol{a}$ and $\boldsymbol{b}$ respectively, two other strain measures are tracked. First, the shear angle γ_{12} is calculated according to

$$\gamma_{12} = \frac{\pi}{2} - \psi_{12} = \frac{\pi}{2} - \arccos\left(\frac{C_{12}}{\sqrt{C_{11}}\sqrt{C_{22}}}\right) \tag{4.1}$$

where $\boldsymbol{C}$ is the right Cauchy-Green tensor. Second, the perpendicular stretch $E_{\perp}$ in the derived direction $\boldsymbol{b}^{\perp}$, which is the component of $\boldsymbol{b}$ that remains perpendicular to the carbon fiber direction $\boldsymbol{a}$, is calculated according to

$$E_{\perp} = \sqrt{2\,E_{22} + 1}\sin(\psi_{12}) - 1. \tag{4.2}$$

Directions $\boldsymbol{a}$, $\boldsymbol{b}$ and $\boldsymbol{b}^{\perp}$ are defined based on the principal material directions $\boldsymbol{a}_0$, $\boldsymbol{b}_0$ and $\boldsymbol{b}_0^{\perp}$ as shown in in Figure 4.1 b. The non-orthogonal orientation of the principal directions under large deformations (material frame) is intrinsically considered by the Green-Lagrange strains, since the coordinate system is initially aligned with the fiber direction. For a quantitative evaluation of the strain development during the tests, the strains are averaged over three local zones for each shape, cf. Figure 4.1 c.

To investigate fiber bending, a method to measure the curvature κ_{11} in roving direction on a macroscopic scale is proposed, cf. Figure 4.1 c. All dots along

an individual fiber roving are interpolated as a smoothed spline using Matlab's "Curve Fitting Toolbox ™ ". For each roving 100 uniformly distributed points are derived to increase the resolution and compensate for placement inaccuracies of dots deviating from the roving's center. The curvature at each point is calculated based on the inverse radius of a circle placed through the point and both neighbors. Finally, the curvatures are linearly interpolated onto an evenly distributed 100x100 grid.

Membrane deformation modes of NCFs The outlined strain measurements, combined with the regular grid pattern of dots aligned with the rovings, allow distinction between different deformation modes, cf. Figure 4.2.

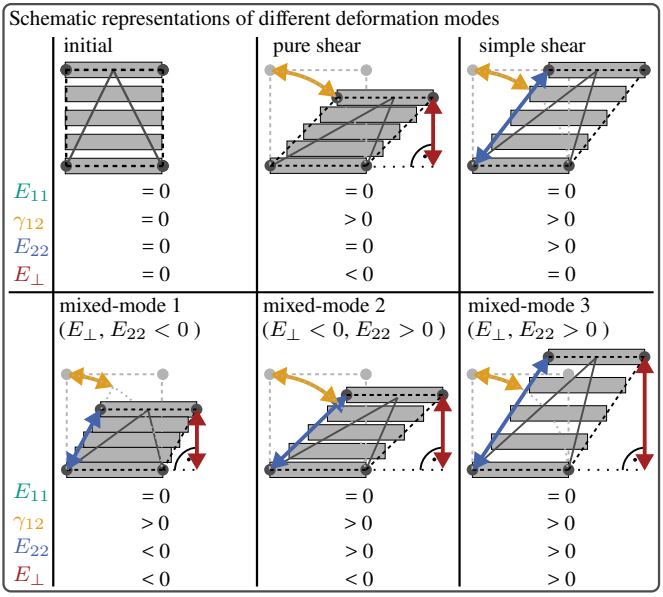

Figure 4.2: Schematic representation of different deformation modes and the corresponding resulting strains (adapted from [102]).

In the case of pure shear, E_{22} is zero and thus $E_\perp$ is directly coupled to γ_{12}, cf. Equation 4.2, while both strains are independent of each other for mixed

deformation modes. The perpendicular strain quantifies the distance between rovings and thus allows identifying gapping ($E_\perp > 0$) as well as transverse compression of rovings ($E_\perp < 0$). Thus, it is strongly correlated to the local fiber volume content of the fabric [345]. Positive transverse tensile strains $E_{22} > 0$ indicate large slippage between rovings parallel to each other as well as tension in the stitching direction assuming limited slippage between the stitching and rovings. However, E_{22} does not necessarily indicate gapping, as is evident for example for simple shear or mixed-mode 2 in Figure 4.2.

4.2.2 Results [1]

4.2.2.1 Kinematic analysis of OATs

Figure 4.3 presents schematic illustrations of undeformed and deformed specimens of unbalanced fabrics during OATs. Three distinct types of zones are identifiable independent of the bias angle. In zone "C" the fibers are clamped along one edge and barely deform during the test. Zone "A" does not share a boundary with "C" and fibers passing through it are free on both edges. Therefore, the largest deformations in the form of fiber slippage (simple shear) and rotation (pure shear) occur in this main deformation zone (MDZ). Depending on the initial orientation, fibers in zones "B" pass through either "A" or "C", thus these areas must be distinguished more precisely [119]. The fibers in zones "B2" are subjected to a force perpendicular to their orientation due to the deformation in "A". This causes them to rotate and remain relatively parallel to the fibers in "A". The fibers in zone "B1" are strained along their orientation which causes them to slide relative to each other and remain similarly oriented to the fibers in zone C. The fibers in zone "B3" during the $60°$-OAT behave similarly to those in "B1". Zones "B1" and "B2" are more distinct from each other for highly unbalanced textiles such as UD-NCF than for Biax-NCF.

[1] Reproduced section from [102], cf. footnote p. 61 for details.

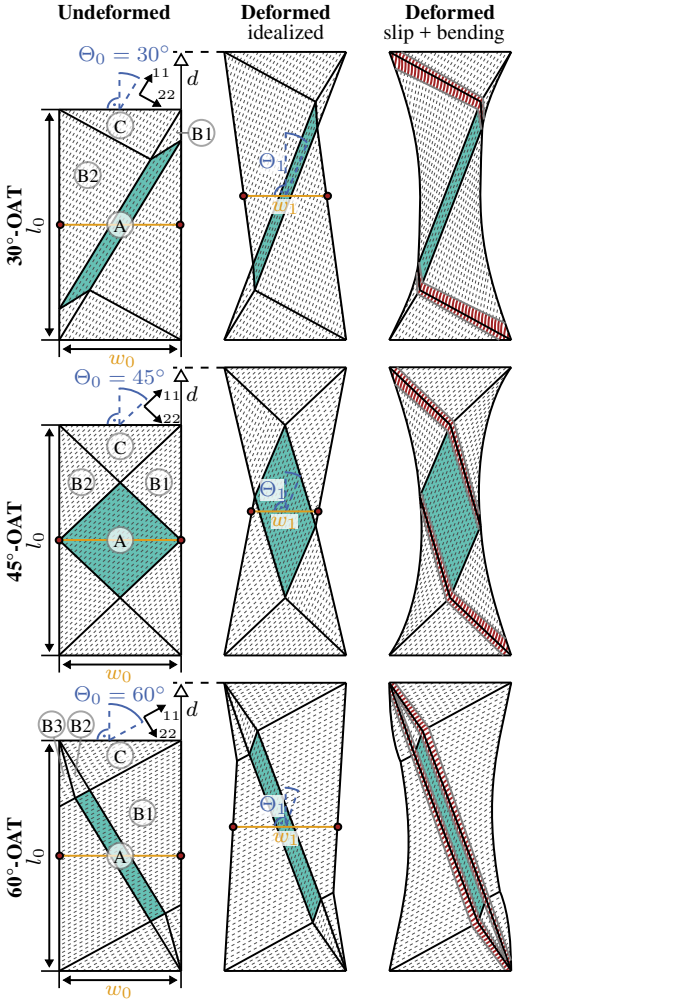

Figure 4.3: 30°-, 45°- and 60°-off-axis-tensions tests (OATs) - Undeformed geometries, idealized deformed specimens and deformed specimens taking into account fiber slip and bending deformation in the transition zones [102].

In idealized models based on classical continuum mechanics, all zones are sharply defined without transition zones and the relative fiber slip is limited resulting in straight outer contours, cf. Figure 4.3 [115, 346]. However, general slippage between the fibers and stitching as well as highly localized slippage at the boundaries from zones "A" to "B", results in a curved outer contour. Additionally, transition zones with high in-plane fiber curvatures form between the zones "C" to "B2" as well as "B1" to "A". The size of the transition zones depends on the in-plane bending stiffness of the fibers [145].

4.2.2.2 Machine forces

To investigate the influence of the dot pattern on the deformation behavior, the tests were performed both with and without dots on the front (f) side of all specimens. Additionally, the tests were performed with dot patterns on the back (b) side for the Biax-NCF and the $45°$-OAT for the UD-NCF.

The resulting machine forces for the Biax-NCF are shown in Figure 4.4 and for the UD-NCF in Figure 4.5. Normalization of the results was deliberately omitted in this section since the common assumption of a symmetrical deformation in the $45°$-OAT is not fulfilled for unbalanced fabrics and the methods are not directly transferable for the $30°$- and $60°$-OAT [346].

Biax-NCF The Biax-NCF curves can be divided into two sections, a relatively linear increase at the beginning and a stronger force increase (locking) for larger strains, cf. Figure 4.4. The onset of locking is significantly earlier at $\varepsilon \approx 0.1$ for the $30°$-OAT compared to $\varepsilon \approx 0.16$ for the $45°$-OAT. This results from a higher localization of strain in a smaller MDZ and, together with the stronger orientation in load direction, leads to significantly higher forces in the $30°$-OAT.

The application of a dot pattern on the front or back of the specimen increases the measured forces for the Biax-NCF, cf. Figure 4.4. The acrylic paint mechanically reinforces the fabric and introduces additional adhesion between the fibers and stitching. This effect is more pronounced with a higher variation for a pattern on the front of the fabric in the $30°$-OAT, since the zigzag pattern

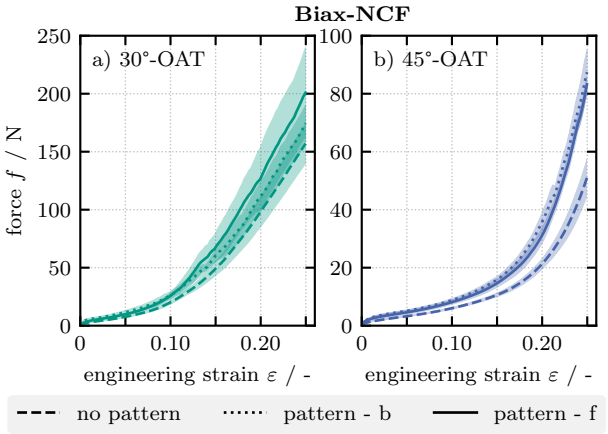

Figure 4.4: Forces in the a) 30°- and b) 45°-OATs for medium-sized specimens (320 x 160 mm) of the Biax-NCF (MD600) with and without a dot pattern on the front (f) or the back (b) [102].

of the tricot stitch is covered more often by the dots compared to the straight stitch constellation on the backside. Besides the increased forces, the general progressions of the curves with and without patterns are similar to each other with similar transition points between the different curve regions.

UD-NCF In the 45°-OAT for the UD-NCF, the dot pattern was applied either on the front or back. However, this caused the glass fibers and rovings to stick together at the dots on the back, resulting in significantly higher forces, cf. Figure 4.5 b. Furthermore, the distinction between the white dots and glass fibers was problematic for the DIC algorithm resulting in a worse correlation for high deformations. Therefore, the dot patterns were only applied on the front side of the UD-NCF for the other bias angles.

The UD-NCF curves can be divided into three sections, a relatively linear increase at the beginning, followed by a region with a decreased slope and locking for larger strains, cf. Figure 4.5. Similar to the Biax-NCF, these sections are small in the 30°-OAT due to the localized deformation in a small MDZ. However, the dot pattern results in an earlier onset of locking and a slight

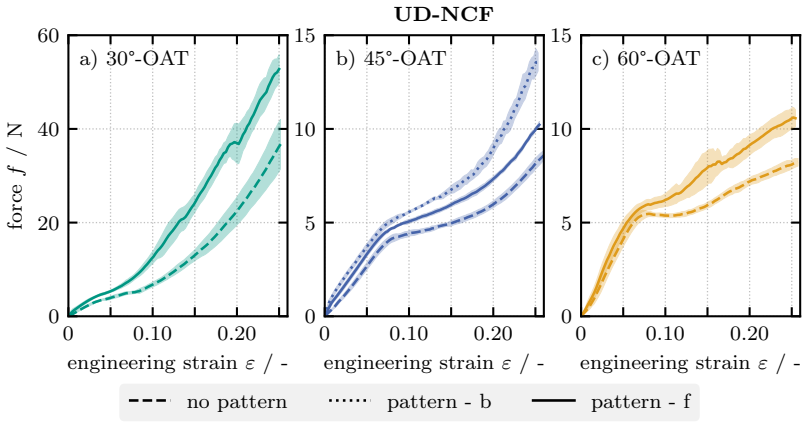

Figure 4.5: Forces in the a) 30°-, b) 45°- and c) 60°-OATs for medium-sized specimens (320 x 160 mm) of the UD-NCF (UD300) with and without a dot pattern on the front (f) or the back (b) [102].

drop in the forces with high variation for $\varepsilon \approx 0.2$ as the bond between the paint, stitching, and rovings tears loose. The forces during the $45°$- and $60°$-OAT are in the same order of magnitude despite the different bias angles. However, the stitching in the early phase of the $60°$-OAT is under higher tension compared to more roving rotation and sliding in the $45°$-OAT, resulting in a higher initial linear slope. The transition to the second, shear-dominated, phase with a distinctively shaped MDZ occurs at a similar engineering strain of $\varepsilon \approx 0.075$ for both tests. The secondary slope in the $60°$-OAT without a dot pattern is slightly negative before an early onset of locking after $\varepsilon \approx 0.12$. This transition is barely noticeable for the dot pattern applied on the front. The acrylic paint leads to a stronger adhesion between the rovings and stitching, making it more resistant to mutual slippage. This also results in a higher variation, as the stitching tears loose for higher forces.

4.2.2.3 Observed deformation and impact of the DIC

Due to the observed increase in the measured machine force, cf. Section 4.2.2.2, the influence of the dot pattern on the deformation behavior must be estimated. A qualitative comparison of the video recordings of tests with and without the dot pattern did not show any noticeable differences and a similar deformation was observed, as exemplarily shown by the images at a displacement of $80\,\mathrm{mm}$ in Figure 4.7. To quantitatively confirm this observation, for three tests of each configuration with and without a dot pattern, image analysis was used at a displacement of 20, 40, 60 and $80\,\mathrm{mm}$ to measure the relative necking Δw_n and the roving orientation Θ_n relative to the vertical axis at three positions in the MDZ, cf. Figure 4.6.

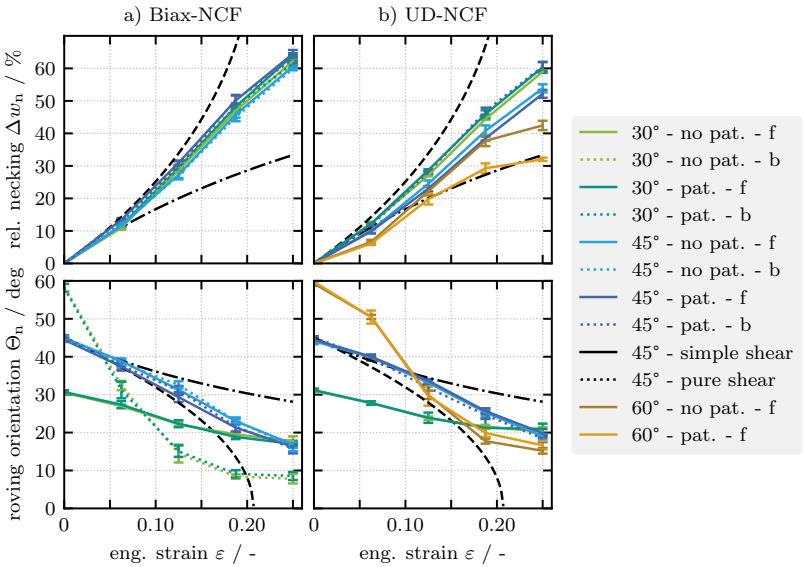

Figure 4.6: Relative necking Δw_n and roving orientation Θ_n in the MDZ of the OATs for the (a) Biax-NCF and (b) UD-NCF for all tests with and without a dot pattern (pat.) on the front (f) or back (b) of the medium-sized specimens (320 x 160 mm) [102].

The fiber orientation was chosen because only one layer of rovings is visible on each side and significant slippage between the rovings and stitching is observed, making a direct estimation of the shear angle or other strains impossible from individual images. The relative necking is calculated from the initial w_0 and current w_1 width at half specimen height (cf. Figure 4.3) according to

$$\Delta w_\mathrm{n} = \frac{w_0 - w_1}{w_0}. \tag{4.3}$$

Krogh et al. [139] have shown for a quasi UD-NCF that the necking in the $45°$-OAT directly correlates with the shear strain development and can even be used for its analytical estimation based on a scaled combination of pure and simple shear theory. The results for the Biax-NCF and UD-NCF are shown in Figure 4.6, together with the theoretical values according to pure shear and simple shear theory as derived by Krogh et al. [139] for the $45°$-OAT .

Biax-NCF The relative necking Δw_n of the Biax-NCF is similar in the $30°$- and $45°$-OATs, cf. Figure 4.6 a. In the $30°$-OAT the application of the dot pattern on the front or back of the fabric has no significant influence on Δw_n. In the $45°$-OAT about $\sim 4\,\%$ more necking is measured with a dot pattern on either side. These observations are also reflected in the roving orientation. Similar to Korgh et al. [139], the development of the relative necking in the $45°$-OAT strongly correlates with the resulting roving orientation and remains between the theoretical results for pure and simple shear. Overall, the application of the dot pattern has very little effect on the deformation behavior of the Biax-NCF and only slightly increases shear due to fiber rotation in the $45°$-OAT.

UD-NCF In the case of the UD-NCF, the relative necking and roving orientation are only minimally affected by applying the dot pattern on the front during the $30°$- and $45°$-OATs, cf. Figure 4.6 b. Applying the dot pattern on the back increases the relative necking noticeably, similar to the impact on the required machine force, cf. Section 4.2.2.2. However, the roving orientation in the MDZ decreases only slightly, indicating that the deformation in this area remains similar. Taking a closer look at the images of the specimens in Figure 4.7, gaps between the rovings in the edge areas of zones "B1" and "B2"

can be identified in tests without a dot pattern or with a pattern on the front. At the dots on the back, the glass fibers and the rovings stick together, which prevents the glass fibers from slipping and inhibits the formation of gaps in the edge areas. In the $60°$-OAT, the application of the pattern on the front significantly reduces Δw_{n}, compared to only slightly higher Θ_{n} in the MDZ for larger engineering strains. Analyzing the images of the $60°$-OAT, the rovings in the zone "B1" of tests without a dot pattern, especially around half height of the specimen, are less rotated towards the load direction (larger Θ_{n}), indicating less shear deformation in these areas. This shear deformation is increased in tests with a dot pattern, since the additional adhesion between the rovings and stitching probably prevents relative slippage between them, resulting in more fiber rotation (pure shear).

Conclusion In conclusion, the dot pattern required for DIC has little influence on the deformation of the Biax-NCF in general and should be applied to the front of the UD-NCF to reduce its impact. However, the effect on the deformation in the MDZ appears to be minimal for all tests, as indicated by the similar roving orientations with often overlapping scatter. Comparing the utilized point-based method, with the methods based on random speckle patterns investigated by Trejo et al. [138], it is evident how small the influence is due to the minimal surface area of the fabric that is covered by paint. Trejo et al. compared three traditional areal speckle patterns from different paint types for DIC on a very similar UD-NCF in the $45°$-OAT. Although their method achieved a higher resolution, the measured force already increased by $\sim 50\,\%$ and the estimated shear strain in the MDZ decreased by $\sim 25\,\%$ even for the best of the investigated speckle patterns at $\varepsilon \approx 0.14$.

4.2.2.4 Macroscopic strains measured with DIC

The resulting strains and roving curvature measured by DIC as described in Section 4.2.1 are shown in Figure 4.7. The measured strains in the visible fiber direction E_{11} were negligible due to the high fiber stiffness and therefore not discussed in the following. For all tests, the different zones shown in Figure 4.3

and described in Section 4.2.2.1 are distinguishable. The highest shear angles γ_{12} occur in the MDZ for all bias angles together with significant perpendicular compressive strains $E_{\perp}$.

Contour plots The Biax-NCF has a relatively symmetric shear behavior in the $45°$-OAT, compared to the UD-NCF with a smaller shear angle in zone "B2" than "B1". In the $30°$-OAT, large transverse tensile strains E_{22} occur in the MDZ on the front for both materials. In conjunction with large positive γ_{12} & $E_{\perp}$, and negative E_{22} strains in the adjacent zones "B2", these indicate significant relative roving slippage. Similar, but less pronounced, behavior is observable in the transition zones between "A" and "B2" of the $45°$-OATs. In contrast, large transverse tensile strains E_{22} along with positive perpendicular strains $E_{\perp}$ occur in the edge regions of zones "B2" in the $45°$-OAT and "B1" as well as "B2" in the $60°$-OAT of the UD-NCF. In these areas, significant gaps develop between the rovings due to large stitching strains.

Strains in the main deformation zone (MDZ) The strains in the MDZ of each test averaged over the areas highlighted in Figure 4.1 a are shown for the Biax-NCF and UD-NCF in Figure 4.8.

The behavior of the Biax-NCF is mainly shear-dominated (γ_{12}) in the MDZ, which also induces perpendicular compaction $E_{\perp}$, cf. Equation 4.2. Both increase relatively linear until the textile for large $E_{\perp} < -0.4$ starts to exhibit the typical locking behavior, evident from the degressive curve of both strains. Due to the stitching, the rovings on the front and back side of the fabric are coupled resulting in similar $E_{\perp}$- as well as γ_{12}-strains in the $45°$-OAT. On the front of the $30°$-OAT positive transverse tensile deformation E_{22} occurs after the onset of locking, which indicates relative slipping of the rovings. Since the shear angle is only measured on the visible side of the NCF as a deformation of the dot pattern, this results in a slightly higher γ_{12}, cf. Equation 4.1.

For the UD-NCF, different deformation states occur in the MDZ depending on the bias angle due to the different loading directions relative to the fiber orientation, cf. Figure 4.8 b. At the beginning of the $30°$-OAT the rovings rotate

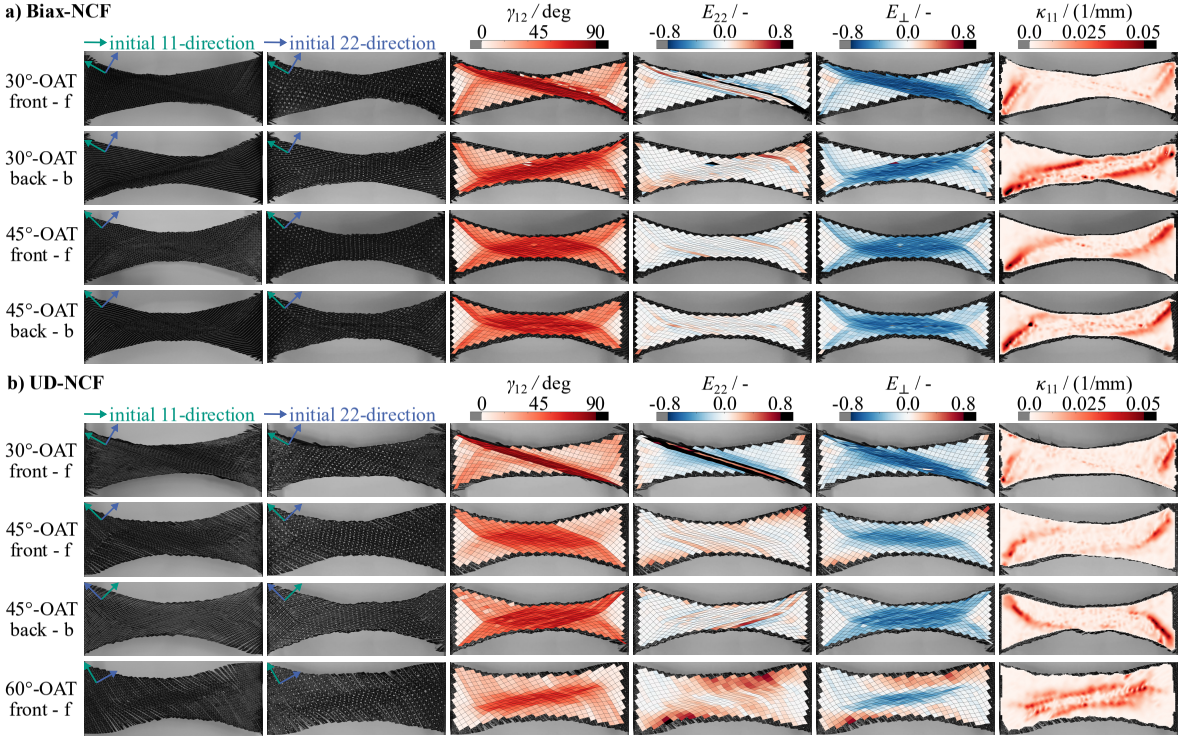

Figure 4.7: Deformed specimens without (left) and without (second-left) dots as well as resulting strain distributions at an engineering strain of $\varepsilon = 0.25$ during off-axis-tension tests (OATs) for medium-sized specimens (320 x 160 mm) of (a) Biax-NCF and (b) UD-NCF [102].

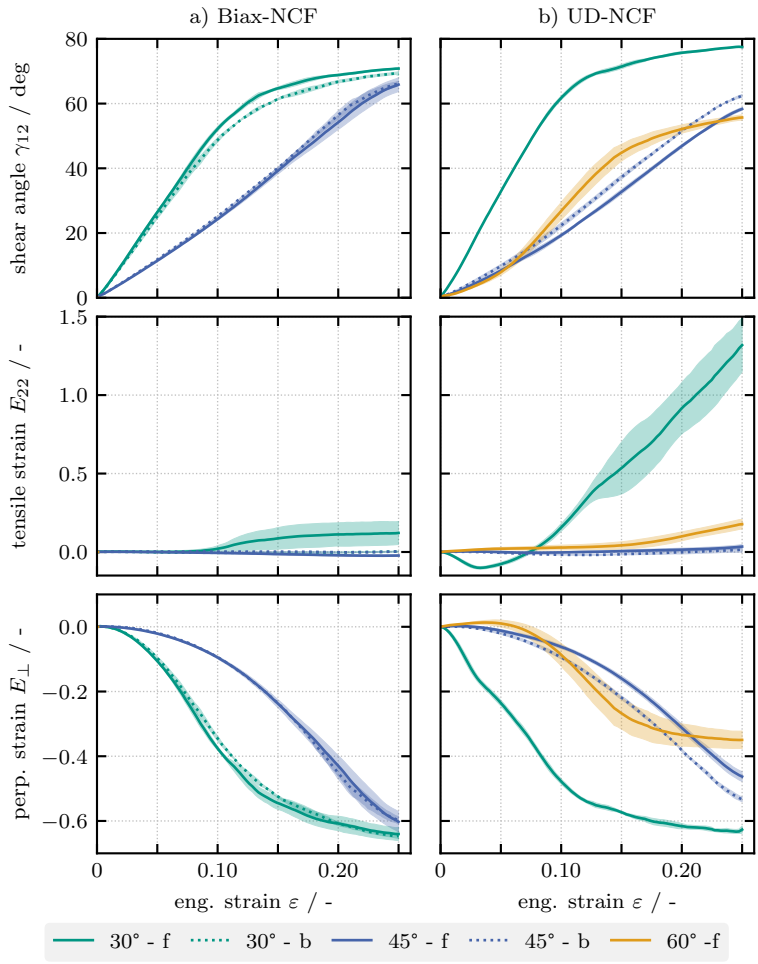

Figure 4.8: Averaged strains in the MDZ of the OATs for medium specimens (320 x 160 mm) of the (a) Biax-NCF (MD600) and (b) UD-NCF (UD300) [102].

towards the load direction, resulting in additional perpendicular compression which is not caused by shear as can be seen from the negative transverse tensile strains. Subsequently, large fiber slippage can be observed, causing large

transverse tensile strains E_{22} superimposed with high shear strains γ_{12} and perpendicular compression $E_{\perp}$. As a result, the measured shear angle is significantly larger compared to the Biax-NCF while the maximum perpendicular compression is similar. In the $45°$-OAT mainly shear deformation occurs in the MDZ, which is larger for the tests with the dot pattern on the back. This observation fits the greater influence of the dots when applying to the glass fiber side, which also resulted in less slippage, larger forces and larger necking, cf. Sections 4.2.2.2 and 4.2.2.3. In the early phase of the $60°$-OAT the stitching is under high tension with simultaneously positive E_{22}- and $E_{\perp}$-strains. After $\varepsilon \approx 0.075$, the MDZ starts to form in the center resulting in a strong increase in the shear angle and perpendicular compression. These flatten again for larger engineering strains since roving slippage starts as indicated by the increasing E_{22}-strain.

Roving curvature Based on the method described in Section 4.2.1, the roving curvature κ_{11} in the specimen can be measured, cf. right column in Figure 4.7. In the $30°$-OAT the highest curvature occurs in the transition zones from "C" to "B2", but not necessarily between zones "B1" and "A" due to roving slippage. In the $60°$-OAT for UD-NCF, cf. Figure 4.7 b, the gapping in zone "B2" prevents the formation of transition zones between "B3 and "C". This transition zone is observable for the $60°$-oriented fibers on the back of the $30°$-OAT for Biax-NCF. In general, the resulting curvatures are higher for Biax-NCF than for UD-NCF and the transition zones are larger. The second high-stiffness fiber direction prevents slippage and gapping along the edges. This improves the load transition resulting in higher in-plane moments and thus higher in-plane bending in the transition zones.

To evaluate the development of the roving curvature during the OATs the average of the maximum curvature $\bar{\kappa}_{11}^{\max}$ of all measurement points n in each roving N^{rov} is calculated according to

$$\bar{\kappa}_{11}^{\max} = \frac{1}{N^{\mathrm{rov}}} \sum_{i=1}^{N^{\mathrm{rov}}} \max_{n \epsilon \{\mathrm{roving}\}_i} \kappa_{11}(n). \tag{4.4}$$

The maximum curvature of each roving was chosen as a reference because it occurs in the transition zones, although these vary in size and location depending on the bias angle, cf. Figure 4.7. The results are shown in Figure 4.9. The average curvature shows slightly progressive trends for the $45°$-OAT and the rovings on the front of the $30°$-OAT. Again the greater influence of the dots when applying to the back side in the $45°$-OAT of UD-NCF is reflected in higher curvatures. The curvature of the rovings with an initial orientation of $\Theta = 60°$ in the $60°$-OAT and on the back of the $30°$-OAT of the Biax-NCF develops strongly degressive. In general, both materials show similar characteristic trends during the different OATs as already observed from the deformation images, although the average curvature for the Biax-NCF is higher in magnitude and increases earlier.

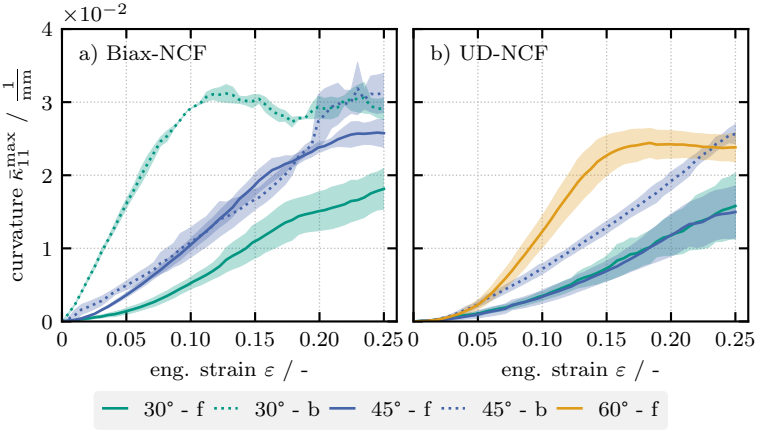

Figure 4.9: Averaged curvature of the OATs for medium specimens (320 x 160 mm) of the (a) Biax-NCF (MD600) and (b) UD-NCF (UD300) [102].

4.2.2.5 Comparison of 30°-, 45°- and 60°-OATs

In order to better compare the different OATs with each other, the machine force normalized by the initial width, $f_\mathrm{n} = f/w_0$, is shown as a function of the measured shear angle γ_{12} in Figure 4.10. A calculation of the normalized shear force was deliberately omitted to allow comparison between the bias angles. Additionally, the classical assumption of a symmetrical shear behavior does not necessarily apply for NCF ($\gamma_{12}(\text{"A"})/2 \neq \gamma_{12}(\text{"B1"}) \neq \gamma_{12}(\text{"B2"})$) and the most common theories do not consider large slippage or transverse tensile strains [346]. However, the application of, for example, the three theories compared by Härtel et al [346] for the 45°-OAT would not change the relative position of the curves to each other and thus allow the same conclusions to be drawn.

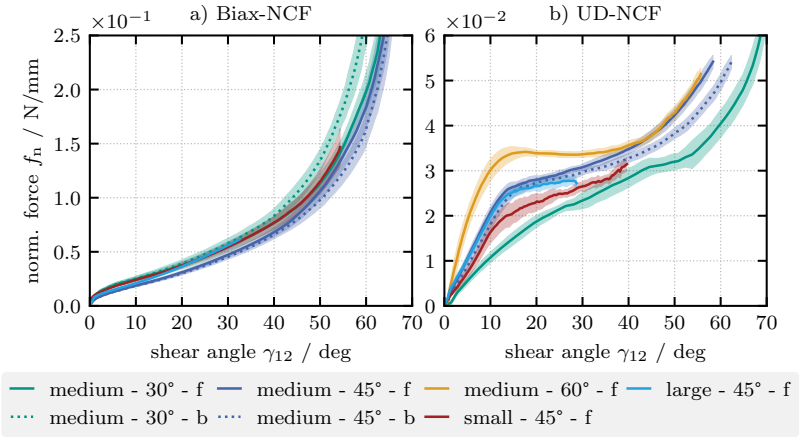

Figure 4.10: Shear angle vs. force normalized by initial width for (a) Biax-NCF (MD600) and (b) UD-NCF (UD300) [102].

Furthermore, 45°-OAT were performed on smaller specimens with $a_2^{\mathrm{small}} = {}^{160\,\mathrm{mm}}/_{80\,\mathrm{mm}}$ and on larger specimens for $a_3^{\mathrm{large}} = {}^{480\,\mathrm{mm}}/_{160\,\mathrm{mm}}$ to estimate an influence of the specimen size. Pourtier et al. [119] have shown that for

Biax-NCF a sufficiently large sample is required to obtain converged results, while this has not yet been investigated for UD-NCF. Details of the experiments and the deformations that occurred are given in Appendix A.1.1.

Biax-NCF The behavior of the Biax-NCF is mainly shear-dominated independent of bias angle or the specimen size, cf. Section 4.2.2.4 and Appendix A.1.1. This results in a reasonable agreement of all $30°$- and $45°$-OAT within the range of experimental scatter for smaller γ_{12} and similar trends for larger γ_{12}, cf. Figure 4.10 a. Only the results for the $30°$-OAT with the strains measured on the back are notably higher, especially for higher shear angles. The results for the dot pattern on the front of the $30°$-OAT would presumably also be higher without the observed roving slippage on the front, which increased the average shear angle, cf. Figure 4.8 a.

UD-NCF The behavior of UD-NCF strongly depends on the stitching deformation, which results in a greater influence of the specimen size in the $45°$-OAT, cf. Figure 4.10 b. The results for medium and large specimens agree well within the tested range. However, the results for small specimens are noticeably lower, which can be attributed to observed slippage, gapping, and lack of roving bending, cf. Appendix A.1.1. This indicates a likely convergence of the measured behavior only for a sufficiently large specimen size, as also observed by Pourtier et al. [119] for Biax-NCF. The γ_{12}-related consideration also illustrates the influence of the bias-angle in the different OATs. In the early phase of the $60°$-OAT the stitching is strongly tensioned and the slower increasing shear angle, cf. Figure 4.8 b, leads to a higher initial slope. In contrast, the MDZ in the early phase of the $30°$-OAT deforms under perpendicular compression, cf. Section 4.2.2.4. Thus, the stitching is not under tension and shear deformation is facilitated, resulting in a smaller initial slope.

4.2.3 Summary and discussion[1]

The membrane behavior of fabrics under different ratios of superimposed shear, transverse tension and in-plane roving compaction is investigated by different bias angles in OATs. Since NCFs do not adhere to either pure or simple shear theories, cf. Section 4.2.2.3, and only one fiber direction is visible from each side, a DIC measurement of the strains is essential for an accurate analysis. The DIC method used in this work introduces additional adhesion between the roving and the stitching through a dot pattern. This results in higher forces, cf. Section 4.2.2.2, but has only limited influence on the deformation behavior of the whole specimen and especially in the MDZ, cf. Section 4.2.2.3. However, the influence is relatively small compared to other methods [138]. By aligning the points along the rovings, the shear γ_{12}, transverse E_{22} and perpendicular $E_{\perp}$ strains can be used to identify different deformation modes and to distinguish stitching deformation, roving slippage and gapping, cf. Figure 4.2. In addition, a newly proposed method allows the measurement of fiber curvatures κ_{11}, which is neglected in most idealized theories, cf. Figure 4.3.

The behavior of Biax-NCF is mainly shear-dominated with a minor asymmetry and only for large deformations limited roving slippage can be observed. The shear angle γ_{12} in the $30°$- and $45°$-OAT increases nearly linearly in the beginning until the onset of locking for $E_{\perp} < -0.4$, cf. Figures 4.8 and A.1, which is also reflected in the resulting forces, cf. Figures 4.4 and 4.10 a. Thus, the characterization of the shear properties is relatively independent of the specimen size and bias angle, cf. Figure 4.10. The $30°$-OAT mainly provides additional characterization opportunities regarding roving slippage and a different configuration of transition zones with higher fiber curvatures.

The behavior of UD-NCF strongly depends on the stitching deformation, resulting in a behavior characterized by superimposed shear, transverse tensile strains and perpendicular compression. In the $45°$-OAT, the MDZ is mainly

[1] Reproduced section from [102], cf. footnote p. 61 for details.

shear-dominated similar to the Biax-NCF, cf. Figure 4.7. However, the behavior over the whole sample is strongly asymmetric and larger roving slippage is observable in combination with gapping in the edge regions of the secondary deformation zone. In addition, the results are distinctly dependent on the specimen size and a sufficiently large specimen is required to characterize a converged shear behavior, cf. Figure 4.10 b. In the $30°$- and $60°$-OAT, positive transverse tensile strains are superimposed with shear deformation in the MDZ, indicating roving slippage that is not primarily limited to transition zones. This effect is much more pronounced in the $30°$-OAT due to initial compression of the stitching and rovings, compared to the $60°$-OAT where tensioning of the stitching limits the shear deformation, cf. Figure 4.8. In summary, it can be concluded that the $45°$-OAT is presumably sufficient for a characterization of the shear behavior of UD-NCF. However, a complete characterization of the membrane behavior additionally requires the characterization of the transverse tensile and perpendicular compressive behavior as well as their interaction, which can be better understood by using different bias angles such as $30°$ and $60°$. Furthermore, if the fiber bending stiffness of the rovings is to be taken into account, the different OATs also provide differently shaped transition zones and curvature amplitudes, cf. Figure 4.7 and 4.9.

4.3 Bending behavior

Bending behavior is another important deformation mechanism that must be investigated separately, as it is decoupled from the membrane behavior for most engineering textiles, cf. Section 2.2.2. The ratio of bending stiffness to membrane stiffness is critical to the formation of wrinkles and other out-of-plane defects [67, 68]. In this work, the bending behavior of a UD- and Biax-NCF is investigated in cantilever tests in different configurations. Compared to woven fabrics, it is important to consider not only the fiber orientation but also the stitch orientation and its position due to the different behavior under tension or compression. The results are analyzed based on the Peirce method [152] to analytically estimate the bending stiffness. Additionally, an optical evaluation method is applied to obtain more detailed information about the non-linear behavior.

4.3.1 Experimental test setup and procedure

Peirce method A cantilever test as described in test standard DIN53362 [347] is used in this study and the setup is schematically shown in Figure 4.11 a.

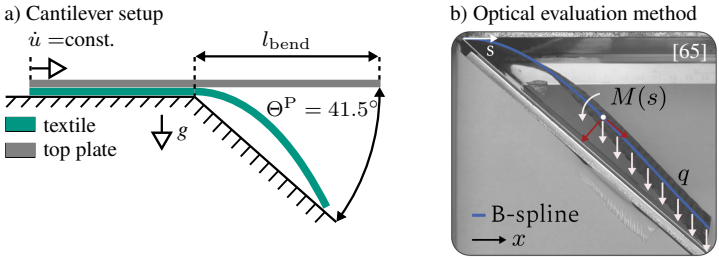

Figure 4.11: Schematic illustration of the (a) cantilever test setup and (b) optical evaluation method proposed by Poppe et al [65] to determine the bending moment $M(s)$ along the curvilinear coordinate s of a fitted B-spline based on the areal weight.

The specimen with a width of $w_0 = 100\,\mathrm{mm}$ is clamped between two plates and due to movement of the top plate pushed over an edge with an angle of $\Theta^{\mathrm{P}} = 41.5\,^\circ$ at a constant velocity of $\dot{u} = 6.5\,\mathrm{mm\,s^{-1}}$. The specimen bends under its own weight due to gravity and the overhang length l_{bend} of its first contact with the inclined surface is measured. The width-related bending stiffness is calculated according to Peirce [152] by

$$G_{\mathrm{w}}^{\mathrm{P}} = \frac{F_{\mathrm{l}}}{w_0} \frac{l_{\mathrm{bend}}^3}{8} \frac{\cos(\Theta^{\mathrm{P}}/2)}{\tan(\Theta^{\mathrm{P}})} \quad \text{with} \quad F_{\mathrm{l}} = g \rho_{\mathrm{A}} w_0, \tag{4.5}$$

where g denotes gravity, ρ_{A} is the total areal weight of the fabric (cf. Table 4.1) and F_{l} is the length-related gravity force of the specimen. A correction factor of $\cos(\Theta^{\mathrm{P}}/2)$ was introduced by Peirce to account for large deformations. The Peirce method results in an approximation of a linear moment-curvature relation based on a constant bending stiffness.

Optical evaluation The measurement of a non-linear bending behavior in cantilever tests requires the optical measurement of the specimen's curvature and subsequent calculation of the bending moment. In this work, the optical evaluation method proposed by Poppe et al. [65] based on the approaches by Bilbao et al. [153] and Liang et al. [155] is utilized. An edge detection algorithm is combined with a B-spline fit and implemented in MATLAB to approximate the specimen's shape profile. The curvature κ and bending moment $M(s_p)$ are calculated at every point p along the curvilinear coordinate s (cf. Figure 4.11 b) by

$$M(s_p) = \int_{s_p}^{l_{\mathrm{bend}}} q(s - s_p) \cos\left(\theta(u)\right) \,\mathrm{d}s \;\text{ and }\; \kappa(s_p) = \frac{s''}{(1 + s'^2)^{2/3}}, \tag{4.6}$$

where q is the weight per unit length and s_p the curvilinear coordinate of each point. The curvature is calculated based on the first s' and second s'' derivative of the B-spline fitted to the detected edge of the deflected profile. The solution is based on Kirchhoff's theory and assumes straight cross-sections perpendicular to the mid-surface and neglects transverse shear stresses.

Configurations The bending behavior is investigated for different fiber and stitching orientations. The tests are conducted with fiber orientations of $0°$ and $90°$ to determine the bending stiffness in both principal directions and additionally for a $45°$ orientation to investigate the behavior under off-axis loading. The tests of each fiber orientation are carried out with the front and back sides facing upwards, respectively. The CF orientation of the front side of each fabric was defined as the global $0°$ direction for a consistent naming convention, cf. Figure 4.12. Each test was repeated six times for each configuration.

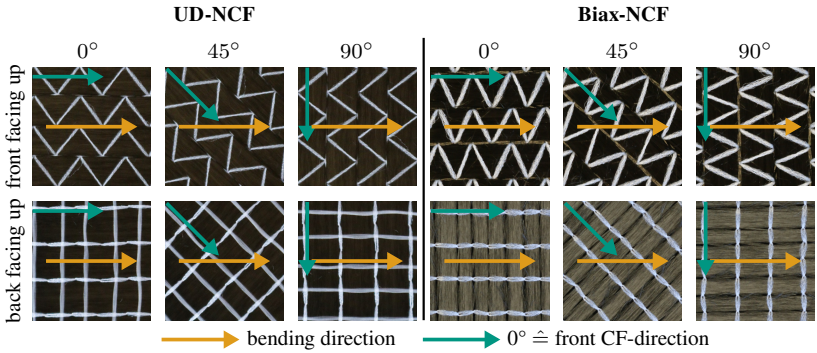

Figure 4.12: Naming convention for the cantilever bending tests.

4.3.2 Results

Overhang Length The measured overhang lengths of all tests are shown in Figure 4.13 and the resulting bending stiffnesses based on Equation 4.5 are summarized in Table A.1.

For **UD-NCF**, the bending behavior is strongly anisotropic. In the $0°$-tests the bending direction coincides with the CF rovings, resulting in a significantly higher overhang length compared to the other orientations. In the $90°$-tests the load is mainly transmitted via the few GF on the back, the stitching and relative friction between the constituents. The anisotropic behavior also results in a

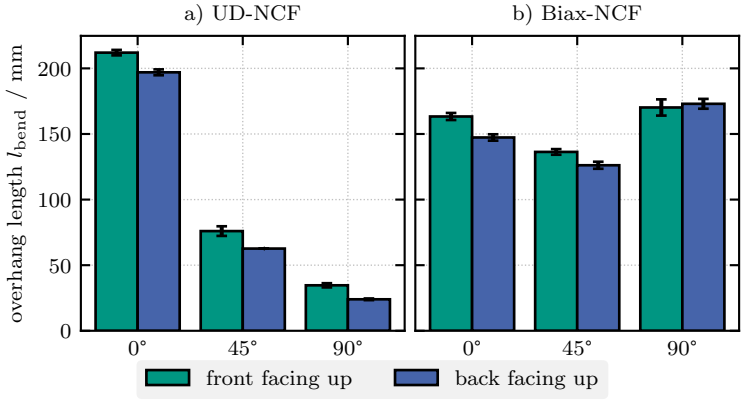

Figure 4.13: Resulting overhang length l_{bend} from the cantilever tests for (a) UD-NCF and (b) Biax-NCF.

significant twist of the specimen for tests with a $45°$ orientation as shown in Figure 4.14 a. This accidentally invalidated all $45°$-tests with the back facing upwards except for one, because the twisted specimen touched the back wall of the setup, that was attached to add contrast for the optical evaluation. The overhang length is consistently higher when the front is facing upwards. The zigzag pattern of the stitching is under tension in these configurations and actively contributes to bending stiffness, compared to the negligible stiffness of the stitching under compression.

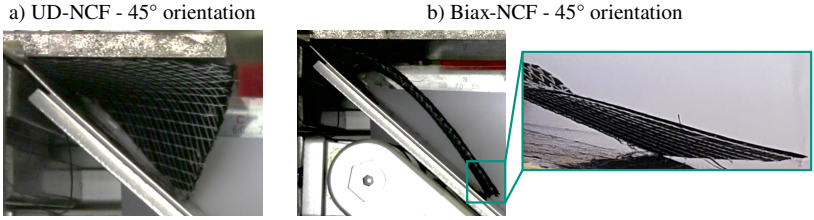

Figure 4.14: Cantilever tests with 45° orientation of (a) UD-NCF and (b) Biax-NCF.

For **Biax-NCF**, the bending behavior is only slightly anisotropic. The overhang length of tests with a $90°$ orientation was the highest, cf. Figure 4.13 b. The

Biax-NCF has a similar areal weight for both fiber layers (cf. Table 4.1), but the rovings in $90°$-direction are less wide. The smaller diameter of the rovings and the different stitch pattern probably impedes slippage between the individual fibers of the rovings, resulting in a higher bending stiffness for the $90°$-tests. This observation agrees with the study of Lomov et al. [70], where a higher bending stiffness was measured for Biax-NCF with tighter stitched rovings. The overhang length for the back side of the fabric facing up in the $90°$-orientation is highest, because the rovings are aligned with the bending direction and under tension in this configuration (cf. Figure 4.12). In the $0°$-tests l_{bend} is higher for the front side facing up, because the bending direction aligns with the CF rovings and zigzag pattern to induce tension. In the $45°$-tests, a slight sagging of the specimen in the center is observed as shown in Figure 4.14 b. This sag is stronger if the back side is facing up and touches the inclined surface earlier, resulting in a lower overhang length.

Moment-curvature The constant Peirce bending stiffness is compared to the optical evaluations for both materials in Figure 4.15. Due to the observed twist for UD-NCF and sag for Biax-NCF only the tests with a $0°$ and $90°$ orientation are compared. The optical moment-curvature curves can be divided into two sections, a relatively linear increase at the beginning and degressive behavior for higher curvatures. This indicates an initially elastic bending behavior for small curvatures and a non-elastic behavior for larger curvatures [153]. In the first section, the results of the optical evaluation are close to the Peirce approximation and fall below it in the second section for higher curvatures. The transition point is within a curvature range of $0.007 < \kappa < 0.009$ for the $0°$-test for UD-NCF as well as both orientations of Biax-NCF. In the $90°$-test for UD-NCF a similar qualitative behavior is observed but on a different magnitude due to the significantly lower bending stiffness.

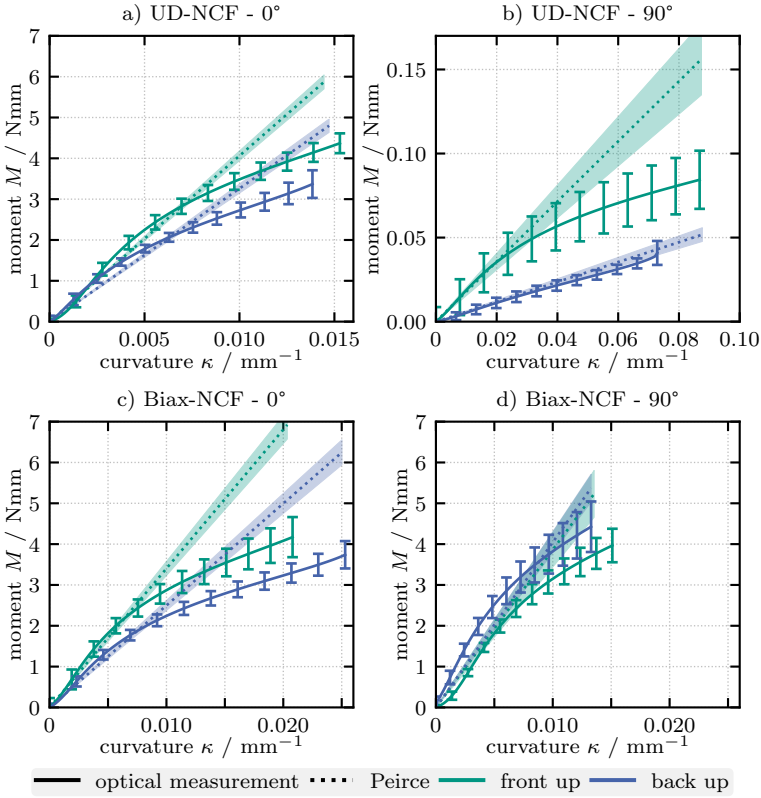

Figure 4.15: Results of the cantilever tests | Comparison between the moment-curvature-curves based on Pierce (dotted lines) and optical measurement (continuous lines) for different orientations for UD- and Biax-NCF.

4.3.3 Summary and discussion

The bending behavior of a UD- and a Biax-NCF is investigated for different configurations in cantilever tests. A comprehensive analysis is conducted based on the overhang length, analytically calculated Peirce bending stiffness as well as optical evaluation of the membrane-curvature relation.

The bending behavior of NCFs depends on the fiber as well as stitching orientation. A strongly anisotropic behavior is observed for UD-NCF with a higher bending stiffness in the CF roving direction and configurations with the stitching under tension. The bending behavior of Biax-NCF is slightly anisotropic due to the different roving sizes in both directions despite a similar areal weight of CF. Additionally, a higher stiffness results from configurations with the rovings aligned in bending direction facing upwards and under tension. The optical evaluation of the tests reveals a typically non-linear curvature-moment relation [153]. The Peirce bending stiffness is for both fabrics an acceptable approximation of the initial linear bending behavior for small curvatures. A non-linear behavior with a degressive behavior for larger curvatures is observed for both materials, which is very similar to observations in literature for other UD-NCF [148,156] and Biax-NCF [165,166]. In summary, it can be concluded that a Peirce cantilever test is presumably sufficient for a characterization with small observed curvatures, while the optical evaluation method can provide more detailed results for the investigation of higher curvatures.

4.4 Compaction behavior[2]

The through-thickness compaction behavior of engineering textiles significantly influences the resulting component properties. It determines the final fiber volume content, the necessary press force, the permeability as well as the final mechanical properties. The compaction behavior of textiles is strongly dependent on the individual architecture of the fabric and care must be taken when conducting the experiments to obtain reliable results, cf. Section 2.2.3. In this work, the compaction behavior of a UD- and a Biax-NCF with the same fiber type and areal density of fibers in the respective main reinforcement directions are tested. The setup is based on the principles of the measuring method outlined in a recent benchmark on compaction [174]. The influence of the relative fiber orientation at the interfaces of a layup as well as the number of plies is investigated. Subsequently, analytical approaches are applied to approximate the compaction behavior.

4.4.1 Experimental test setup and procedure

Punch-to-plate compaction test[2] The compaction behavior is investigated with a punch-to-plate setup mounted on a universal testing machine with a $50\,\mathrm{kN}$ load cell, cf. Figure 4.16 a. Undeformed stacks of n_L-plies with a size of $200\mathrm{x}200\,\mathrm{mm}^2$ are compacted with a $150\mathrm{x}160\,\mathrm{mm}^2$ punch at a constant speed of $1\,\mathrm{mm\,min}^{-1}$. The area of the punch is used to approximate the exerted pressure p_comp. Each measurement is repeated four times with a new stack of material for each test. Additionally, three different layups for each material are investigated with relative orientations of $\Delta\Theta = 0\,^\circ,\ 45\,^\circ$ or $90\,^\circ$ between the CFs at the interfaces of each ply in a stack, cf. Figure 4.16 b. In the UD-NCF

[2] Extracts from Section 4.4 have been previously published in [167], i.e. B. Schäfer, R. Zheng, P. Boisse, L. Kärger. Investigation of the compaction behavior of uni- and bidirectional non-crimp fabrics. *Materials Research Proceedings*, 28:331–338, 2023 | Reproduced paragraphs and subsections are marked with [2].

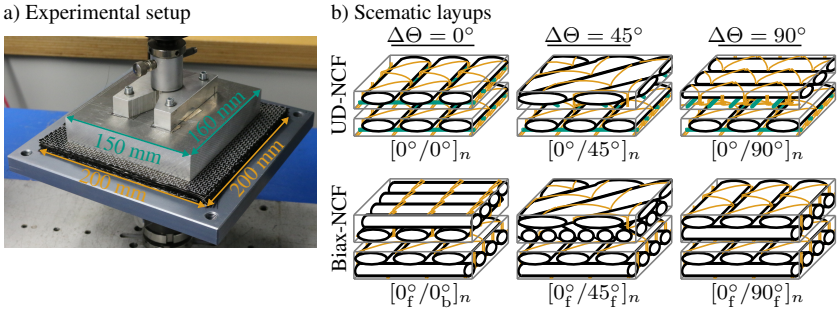

Figure 4.16: (a) Experimental punch-to-plate compaction test setup; (b) Schematic lay-ups of the investigated combinations for different relative fiber orientations at the interfaces with the PES stitching of the NCFs in orange and the GF in green [167].

layups, the front side (f) of the fabric with a zigzag pattern is facing up for each ply. This is the same for the Biax-NCF in layups with a relative interface orientation of $\Delta\Theta = 45\,°$ or $90\,°$, while every second ply is flipped over with its back side (b) facing up for $\Delta\Theta = 0\,°$. The fabrics were stacked randomly without intentional alignment of superposed rovings to represent the typical case of an automated stacking process.

The theoretical FVC Φ is calculated based on the remaining thickness t_{rem} according to

$$\Phi = \frac{\rho_{\mathrm{A}}^{\mathrm{CF}} \cdot n_{\mathrm{L}}}{\rho^{\mathrm{CF}} \cdot t_{\mathrm{rem}}} = \frac{(\rho_{\mathrm{A}}^{\mathrm{total}} - \rho_{\mathrm{A}}^{\mathrm{stitching}} - \rho_{\mathrm{A}}^{\mathrm{GF}}) \cdot n_{\mathrm{L}}}{\rho^{\mathrm{CF}} \cdot t_{\mathrm{rem}}}, \tag{4.7}$$

where $\rho^{\mathrm{CF}} = 0.00181\,\mathrm{g\,mm^{-3}}$ is the density of the utilized CFs and $\rho_{\mathrm{A}}^{\mathrm{CF}}$ is the areal density of CFs in the stack, which is approximated by subtracting the areal density of the stitching $\rho_{\mathrm{A}}^{\mathrm{stitching}}$ and GFs $\rho_{\mathrm{A}}^{\mathrm{GF}}$ from the total measured areal density $\rho_{\mathrm{A}}^{\mathrm{total}}$. The theoretical FVC for a single layer of UD-NCF and Biax-NCF is shown in Figure 4.17 a.

The initial set of tests was designed to investigate the influence of the relative interface orientations $\Delta\Theta$ and the number of layers n_{L} in different configurations of two, four, six or eight plies. The undeformed stacks were compacted to a remaining theoretical fiber volume content of $\Phi^{\mathrm{target}} = 65\,\%$, cf. Figure 4.17

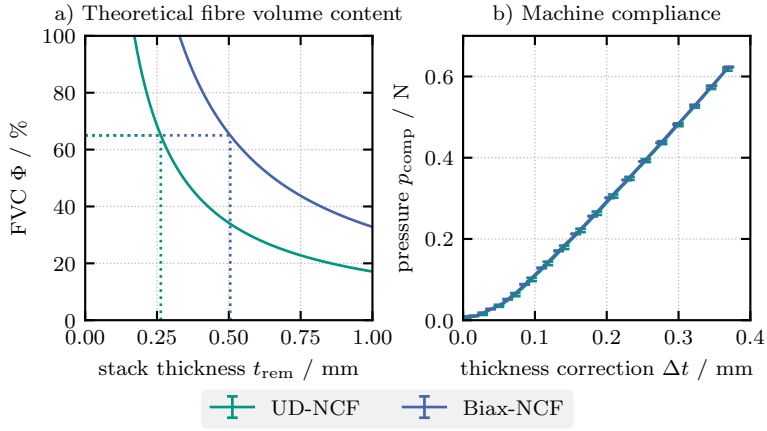

Figure 4.17: (a) Theoretical fiber volume content Φ for a single layer ($n_L = 1$) according to Equation 4.7 with dashed lines indicating the remaining thickness t_{rem} for $\Phi = 65\,\%$; (b) Machine compliance curve during the loading stage (adapted from [167]).

a. The initial neglect of machine compliance led to results that contradicted the observations in literature, which will be discussed in the next Section. A second set of tests was conducted to determine thresholds of the expected nesting behavior (cf. Section 2.2.3), so additional tests were performed with $n_L \in [1, 5, 10, 15]$ and the front of each layer facing upwards.

Machine compliance adjustment[2] Based on the results of the recent benchmark conducted by Yong et al. [174], machine compliance has a significant influence on the measured thickness due to the high forces during compaction tests and must be accounted for to achieve accurate results. The machine compliance was measured based on the method outlined by Sousa et al. [181]. Without a fabric, the top and bottom plates are brought into contact with each other ($\Delta t = 0$) and further pressed together with a prescribed speed of $1\,\mathrm{mm\,min^{-1}}$. The machine force is measured as a function of the cross-head

[2] Reproduced subsection from [167], cf. footnote p. 89 for details.

displacement, cf. Figure 4.17 b. The results were used to correct the true remaining stack thickness t_{rem} of each trial according to

$$t_{\mathrm{rem}} = t_{\mathrm{meas}} - \Delta t(p_{\mathrm{comp}}), \tag{4.8}$$

where t_{meas} is the measured thickness according to the cross-head displacement reading and $\Delta t(p_{\mathrm{comp}})$ is the thickness correction depending on the compaction pressure. The slight non-linearity of the curves indicates a small instability in the testing setup caused by non-controlled elements in the testing fixtures used (e.g. un-parallelism of the plates, internal friction, different materials). However, a good agreement is found between the compliance curve measured prior to testing of the UD- and Biax-NCF.

Analytical model The compaction behavior of engineering textiles can be analytically described with a two-parameter power model for a pressure-dependent fiber volume content Φ^{p}, referred to as p-model in the following, as initially proposed by Robitaille and Gauvin [170]:

$$\Phi^{\mathrm{p}}(p) = A \cdot p_{\mathrm{n}}^{B} \quad \text{with} \quad p_{\mathrm{n}} = \frac{p_{\mathrm{comp}}}{1\,\mathrm{MPa}}, \tag{4.9}$$

where A and B can be referred to as the initial fiber volume content at the unit compaction pressure and the growth parameter respectively. A higher value for B indicates less resistance to compaction. The analytical model can be used to extrapolate experimental results and quickly determine the required pressure for a desired FVC. However, the model must be individually fitted to each test since the influence of the number of layers or relative interface orientation is not considered. To account for the impact of the number of layers n_{L}, an extension of the analytical approach to a four-parameter power model (additional parameters C and D) for a pressure- and n_{L}-dependent model Φ^{pn}, referred to as pn-model in the following, is proposed:

$$\Phi^{\mathrm{pn}}(p, n_{\mathrm{L}}) = A \cdot p_{\mathrm{n}}^{B\left(1-\frac{C}{n_{\mathrm{L}}^{D}}\right)} \quad \text{with} \quad p_{\mathrm{n}} = \frac{p_{\mathrm{comp}}}{1\,\mathrm{MPa}}. \tag{4.10}$$

4.4.2 Results

Influence of machine compliance[2] In order to highlight the importance of adjusting the results for machine compliance, especially for varying number of layers n_L, Figure 4.18 shows the results of UD-NCF for $[0°/0°]_{n_\mathrm{L}}$-layups with ($[0°/0°]_{n_\mathrm{L}}$) and without ($[0°/0°]^{\mathrm{raw}}_{n_\mathrm{L}}$) machine compliance adjustment.

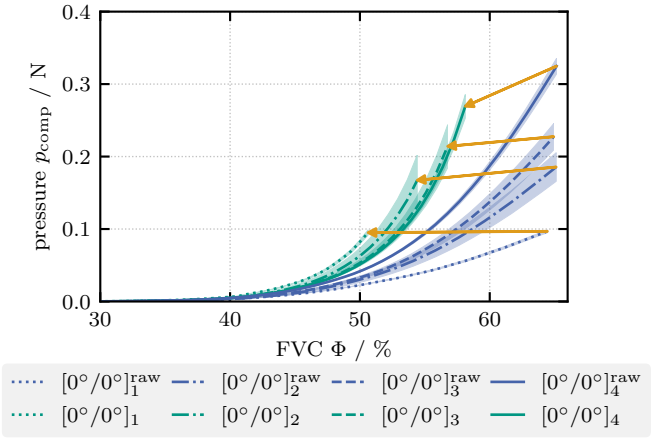

Figure 4.18: Influence of the machine compliance adjustment on the results for UD-NCF with a $[0°/0°]_{n_\mathrm{L}}$-layup. $(\bullet)^{\mathrm{raw}}$ indicates the raw measured machine force before the compliance adjustment (adapted from [167]).

The theoretical FVC Φ is linear in n_L but very sensitive to small changes in the individual ply thickness, cf. Equation 4.7. Since the required compaction pressure for all configurations is of the same order of magnitude, the thickness correction Δt results in larger deviations for the final FVC for fewer layers. This results in a deviation of $\Delta\Phi = 8 - 15\,\%$ from the targeted final FVC of $\Phi^{\mathrm{target}} = 65\,\%$. The maximum pressure reduces due to the averaging over the smallest common resulting stack thickness t_{rem} among all trials after adjustment according to Equation 4.8. Most importantly, however, the position

[2] Reproduced subsection from [167], cf. footnote p. 89 for details.

of the curves relative to each other changes. While an increase in the resistance to compaction is observed for the raw data, a decrease is observed after taking the machine compliance into account.

Influence of the number of layers[2] The resulting forces over fiber volume content for different relative interface orientations $\Delta\Theta$ are shown in Figure 4.19.

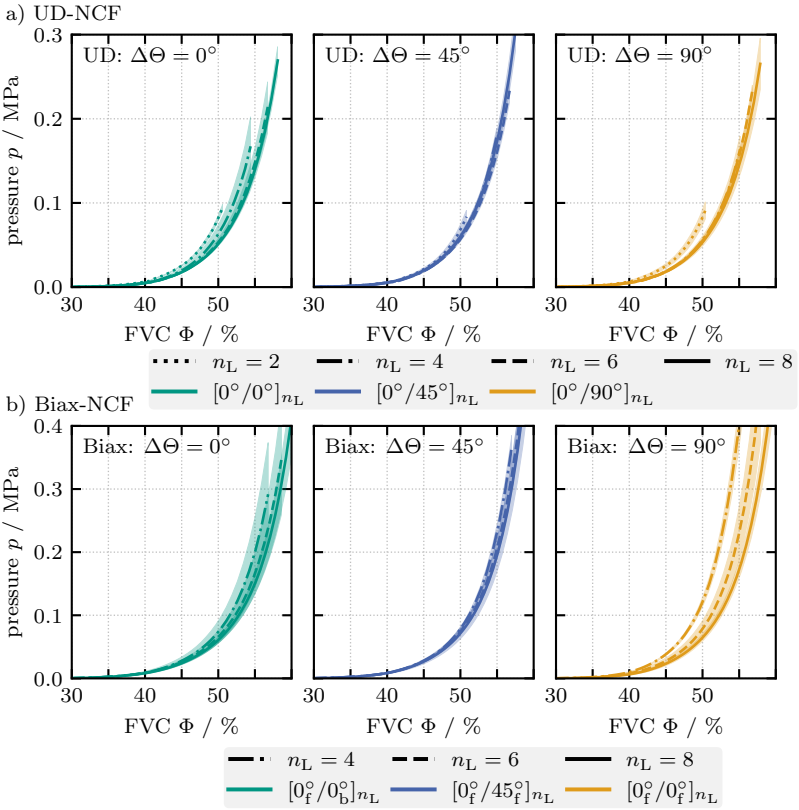

Figure 4.19: Compaction test results for different relative interface orientations $\Delta\Theta$ | (a) UD-NCF; (b) Biax-NCF (adapted from [167]).

[2] Adapted and revised from [167] with additional results, cf. footnote p. 89 for details.

All compaction curves show the well-known non-linear shape with progressively increasing forces, cf. Section 2.2.3.

For UD-NCF the resistance to compaction decreases most notably for an increase of n_L from two to four, cf. Figure 4.19 a. This observation is more pronounced in test with $\Delta\Theta = 0°$ or $90°$. A further increase of the number of layers only slightly affects the compaction response with strongly overlapping experimental scatter. The influence of n_L is usually induced by different nesting effects, when two layers of fabric come into contact and constituents slide into gaps of the adjacent layer, cf. Section 2.2.3. For NCF, nesting of rovings as well as stitching is reported [173, 175, 178, 348] and schematically illustrated in Figure 4.20. However, it is also possible for stitching patterns to

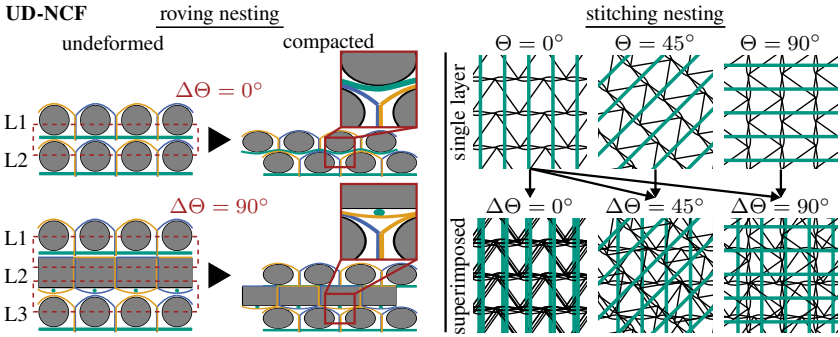

Figure 4.20: Schematic illustration of roving and stitching nesting opportunities for UD-NCF with a tricot stitching pattern by superposition of multiple cross-sections and stitching patterns.

coincide between the layers resulting in high-points in the stack, which causes an increased resistance to compaction for some of the trials as shown by Korkiakoski et al. [177]. For $\Delta\Theta = 0°$, superimposed rovings as well as stitching patterns present many opportunities for nesting, which explains the observed influence on the pressure. However, a pronounced rovings nesting is presumably limited by the GF on the back. The superimposed stitching in $\Delta\Theta = 45°$- and $\Delta\Theta = 90°$-configurations is spread evenly over the area, resulting in smaller stitching nesting and less scatter. In the $\Delta\Theta = 90°$-configuration the GF on

the back can nest into adjacent layers, while roving nesting is constrained. The threshold for the influence of n_L for the UD-NCF seems to be nearly reached for eight layers for all relative interface orientations.

Similar trends are observed for Biax-NCF and the resistance to compaction decreases for increasing n_L independent of the layup sequence, cf. Figure Figure 4.19 b. This observation is again more pronounced for a $\Delta\Theta$ of $0°$ or $90°$. For Biax-NCF, $\Delta\Theta = 0°$ and $90°$ have similarly oriented stitching since it requires flipping a layer upside down instead of rotation. Therefore, the potential for stitching nesting is increased in these configurations, cf. Figure 4.21. Additionally, roving nesting is possible for $\Delta\Theta = 0°$, while it is strongly limited for the other relative interface orientations. The limited influence of n_L and reduced scatter for $\Delta\Theta = 45°$ is comparable to the observations of UD-NCF. The decrease in resistance to compaction seems to diminish as the number of layers increases, indicating a threshold for higher n_L.

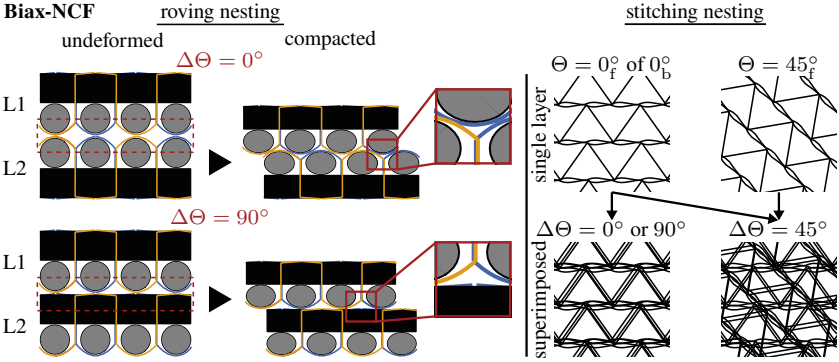

Figure 4.21: Schematic illustration of roving and stitching nesting opportunities for Biax-NCF with a tricot stitching pattern by superposition of multiple cross-sections and stitching patterns.

Additional tests with $n_\mathrm{L} \in [1, 5, 10, 15]$ were conducted for both materials to investigate a potential threshold for the observed nesting effects, cf. Figure 4.22. The threshold for UD-NCF as well as Biax-NCF seems to be reached around ten layers. This is similar to the reported thresholds between 10-15 layers for other

textiles in literature [169, 170, 172, 178]. The overall compaction behavior of Biax-NCF is stronger influenced by the number of layers compared to UD-NCF. This observation agrees with existing literature [107, 171, 173], where textiles with a higher areal density tend to have a smaller resistance to compaction because they have more yarns in a roving and usually a more rounded shape of fiber bundles.

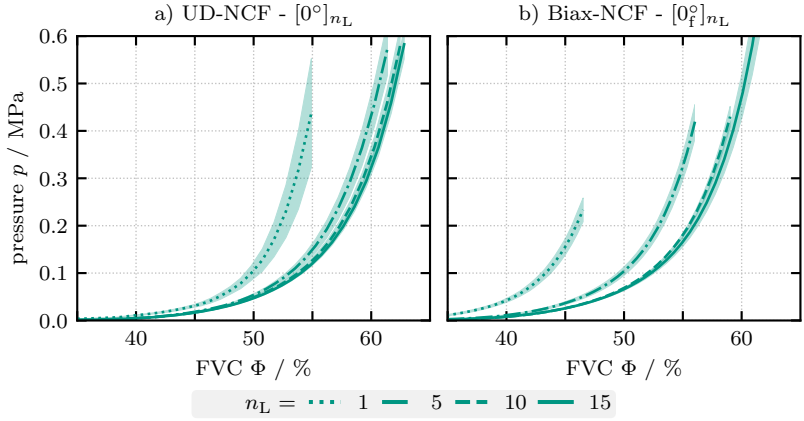

Figure 4.22: Compaction test results to investigate the threshold for nesting effects of (a) UD-NCF and (b) Biax-NCF.

Influence of relative interface orientation[2] To make it easier to assess the influence of the relative interface orientations, the results are shown again in Figure 4.23 depending on n_L. The compaction behavior of UD-NCF is barely influenced by the relative layer orientation and very similar for the respective number of layers. For Biax-NCF the $[(0°_f)/(0°_b)]_{n_L}$-layup requires the smallest compaction force to achieve a targeted FVC independent of n_L. This reinforces the assumption that the influence of the number of layers is caused by a combination of roving nesting as well as the influence of superimposed stitching

[2] Reproduced subsection from [167], cf. footnote p. 89 for details.

patterns. For the $[(0^\circ_\mathrm{f})/(0^\circ_\mathrm{f})]_{n_\mathrm{L}}$-layups, mainly superposition of stitching causes a decreasing resistance to compaction for larger stacks.

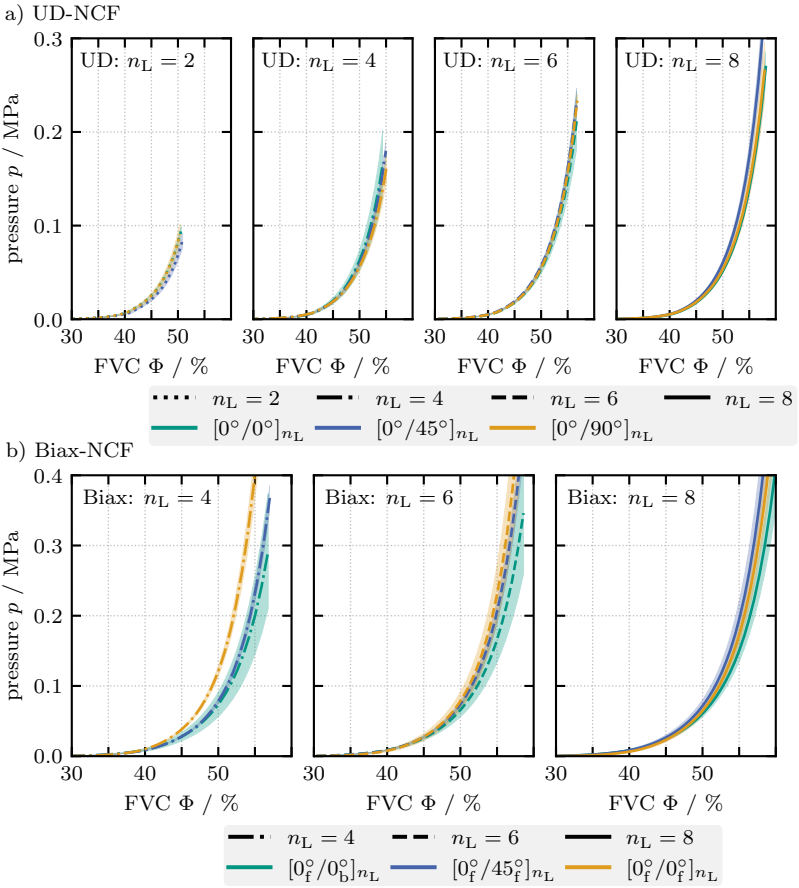

Figure 4.23: Compaction test results for different number of layers n_L | (a) UD-NCF; (b) Biax-NCF (adapted from [167]).

Analytical model The experimental compaction results were fitted to the p-model $\Phi^{\mathrm{p}}(p)$ (cf. Equation 4.9) as well as the proposed pn-model $\Phi^{\mathrm{pn}}(p, n_{\mathrm{L}})$ (cf. Equation 4.10). The resulting parameters are listed in Table A.2 and Table A.3, respectively. A good agreement was achieved with the p-model as well as pn-model for all tests with $R^2 > 0.99$, except for Biax-NCF with $\Delta\Theta = 90°$ ($R^2 \approx 0.964$). This shows the general validity of both approaches. The parameter A and resulting exponent B for the configurations of both materials with the most tests are shown in Figure 4.24 and further discussed in the following. Similar observations and conclusions can also be made for the other configurations, cf. Section A.1.3.

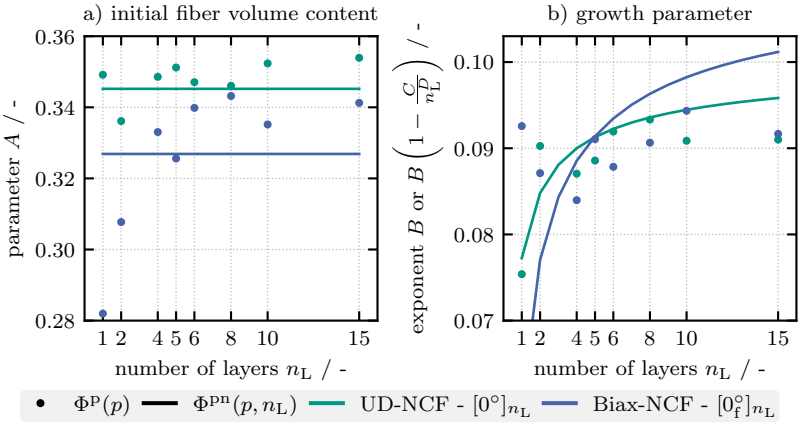

Figure 4.24: Overview of the parameters for the analytical p-model $\Phi^{\mathrm{p}}(p)$ and pn-model $\Phi^{\mathrm{pn}}(p, n_{\mathrm{L}})$.

The parameter A of both models can be interpreted as the initial fiber volume content and it is thus inversely related to the initial thickness of each ply, cf. Equation 4.7. For both materials, A tends to increase for more layers in the stack in the p-model. This observation can be attributed to nesting during the initial stacking of layers. This effect has been deliberately omitted when adapting to the pressure- and n_{L}-dependent pn-model, because in conventional

simulation approaches the parameterization and subsequent modeling are based on a constant initial virtual thickness for each layer. The parameter A in the pn-model thus corresponds to a kind of averaged initial thickness over all conducted tests.

The growth parameter B in the p-model and the equivalent total exponent in the pn-model indicate the compliance to compaction. A slight tendency for increasing B with higher n_{L} with individual outliers for both materials is observed for the p-model. This indicates a decrease in the resistance to compaction due to nesting. This effect was the main assumption for the extension of the exponent in the pn-model and is well represented.

The analytical investigation of the compaction behavior allows conclusions regarding the origin of the observed impact of the number of layers in the layup. For UD-NCF, nesting during compaction is particularly relevant. In comparison, the influence for Biax-NCF results from a combination of the nesting during the initial stacking and the nesting during compaction. This results in a better approximation of the pn-model for UD-NCF ($R^2 \approx 0.994$) compared to Biax-NCF ($R^2 \approx 0.964$) due to the assumption of a constant initial FVC. This is also evident from the relative position of the p-model and pn-model parameters in Figure 4.24.

The results of the threshold tests are used to demonstrate the estimation of the analytical model in Figure 4.25. For UD-NCF, the experimental results and both analytical approaches are close to each other and the behavior for large as well as small n_{L} is well represented. For Biax-NCF, the p-model describes the experimental results well, while the pn-model underestimates or overestimates the results for very small or large n_{L}, respectively. However, for both materials, the pn-model can be used to approximate the compaction behavior for an untested configuration with a different number of layers without additional experiments.

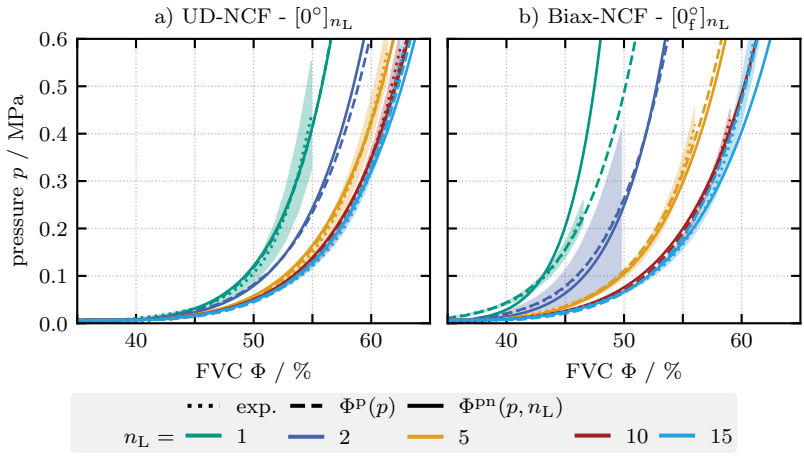

Figure 4.25: Comparison of p-model and pn-model to approximate compaction results | (a) UD-NCF; (b) Biax-NCF.

4.4.3 Summary and discussion

The compaction behavior of a UD- and a Biax-NCF is investigated for different configurations in a punch-to-plate setup. A comprehensive analysis is conducted based on the experimental results as well as analytical approaches.

The compaction behavior of UD- and Biax-NCF depends on the relative fiber orientation at the interfaces between layers as well as the overall number of layers. In general, the consideration of machine compliance is important to study the behavior for different numbers of layers and in particular for a lower number of layers. Comparing UD- and Biax-NCF with each other, some similarities can be observed. With an increasing number of layers, the resistance to compaction for both materials decreases independent of relative interface orientation, due to stitching as well as roving nesting. The stiffness decrease is smaller for the UD-NCF, which is presumably due to the glass fibers preventing more pronounced nesting. For both fabrics, the influence of n_L is diminishing and a threshold is

observed for these effects. An influence of the relative interface orientation is more distinctly observed for Biax-NCF.

Analytical models are applied to inter- and extrapolate the experimental data. Typical compaction results can be accurately described by the p-model $\Phi^{\mathrm{p}}(p)$ and subsequent parameter analysis provides insight into the origin of the influence of n_{L}. The behavior of UD-NCF is dominated by nesting during compaction, while for Biax-NCF additional influence on the initial FVC due to nesting during stacking is observed. An extension to an analytical pn-model $\Phi^{\mathrm{pn}}(p, n_{\mathrm{L}})$ is proposed to describe the influence of n_{L} based on the assumption of a constant initial FVC for each layer. This assumption results in good agreement for UD-NCF, while the behavior of Biax-NCF for very few and high number of layers is underestimated or overestimated, respectively. Additionally, the model neglects the influence of the relative layer orientation, which further limits the application for Biax-NCF. For UD-NCF, the pn-model is suitable to describe the compaction behavior over a large range of n_{L} with few parameters, instead of individual parameterizations for each configuration.

4.5 Inter-ply behavior[3]

Inter-ply behavior at interfaces between a fabric ply and a tool or another ply is an important forming mechanism during forming. In forming tests of dry engineering textiles large relative slip between plies and the tools is observed [65,216,349]. This induces membrane forces due to tangential friction that influence the material draw-in [141] and can result in defects [175]. The inter-ply behavior depends on the mesoscopic structure of the material and the architecture of its constituents as well as process conditions, cf. Section 2.2.4. In this work, the tangential friction behavior at interfaces between ply and tooling (TP) and between plies (PP) of a UD- and a Biax-NCF is investigated in sled pull-over-tests. The behavior is analyzed with respect to the applied normal forces, the relative velocity and the relative fiber orientation.

4.5.1 Experimental test setup and procedure[3]

The inter-ply behavior is investigated with a sled-pull-over setup based on ASTM standard D1894-14 [200] mounted to a universal testing machine, cf. Figure 4.26.

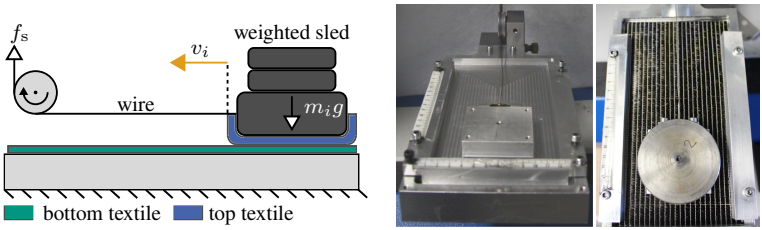

Figure 4.26: Schematic illustration of the experimental friction setup and test bench on tensile machine.

[3] Extracts from Section 4.5 have been previously published in [182], i.e. B. Schäfer, N. Naouar, and L. Kärger. Investigation of the friction behavior of uni- and bidirectional non-crimp fabrics. *Materials Research Proceedings*, 41:540–548, 2024 | Sections 4.5.1-4.5.3 reproduce Section 2, 3 and 4 of [182]

A dry specimen is clamped to the bottom surface of the setup and a sled with a surface area of $65\text{x}65\,\mathrm{mm}^2$ is pulled over a distance of $100\,\mathrm{mm}$ at a constant velocity v_i over the fabric to investigate tool-ply friction (TP). The influence of the applied normal force is investigated with three different sled weights of $m_i \in [218\,\mathrm{g}, 720\,\mathrm{g}, 1222\,\mathrm{g}]$. Two different velocities are applied during the tests with $v_1 = 50\,\mathrm{mm\,min^{-1}}$ and $v_2 = 150\,\mathrm{mm\,min^{-1}}$. An additional specimen is wrapped around the sled to investigate ply-ply friction (PP). The front and back of both fabrics are investigated separately due to the different visible stitching patterns. Each test was repeated at least three times for each configuration with new specimens. The fiber orientation of the visible side of each fabric is used for a consistent naming convention to investigate different fabric orientations, cf. Figure 4.27.

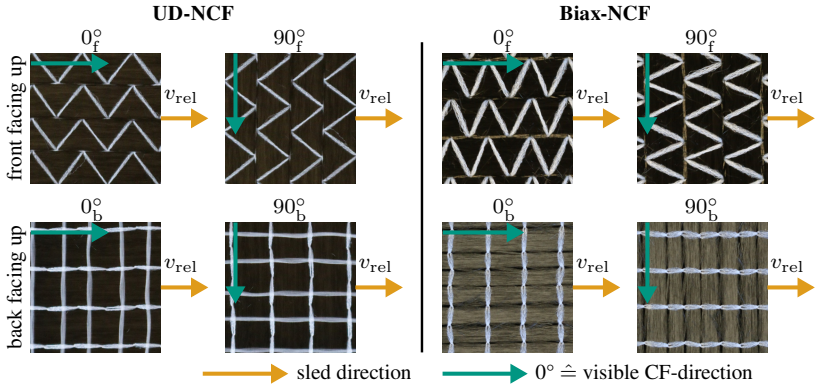

Figure 4.27: Naming convention for the inter-ply characterization tests.

The measured pulling force of the sled f_s is used to calculate the resulting coefficient of friction (CoF)

$$\mu = \frac{f_\mathrm{s}}{g m_i}. \tag{4.11}$$

The static CoF μ_s is obtained as the maximum within the first $10\,\mathrm{mm}$ of sled-displacement. The dynamic CoF μ_d is calculated as the average between a displacement of $40\,\mathrm{mm}$ and $90\,\mathrm{mm}$, where a steady state behavior was observed

for all tests. The calculation of both CoF is demonstrated in Figure 4.28. The wavelength of the oscillations in the PP-tests agrees closely with the stitching pitch (7.2 mm) of UD-NCF, cf. Table 4.1. This behavior is similar to stick-slip and shock effects observed for other NCFs [108, 175] as well as the effect of undulations in woven fabrics [73, 96, 202]. The static and dynamic CoF show very similar tendencies in comparisons for different configurations. The results are therefore discussed below on the basis of the dynamic CoF. Complementary overviews of μ_s are shown in Section A.1.4.

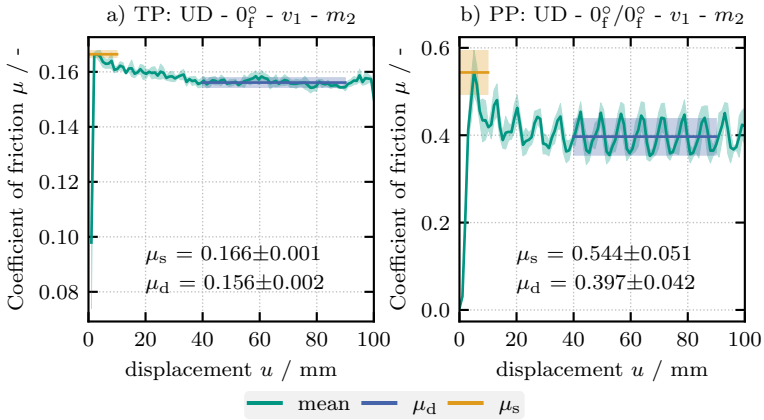

Figure 4.28: Schematic illustration of the calculation of the static μ_s and dynamic μ_d coefficient of friction.

4.5.2 Results[3]

Tool-ply The influence of the sled weight and velocity on the tool-ply behavior are investigated for the 0°_f-configuration of both materials, cf. Figure 4.29. The dynamic CoF is independent of the sled velocity for both materials (same colored bars). A higher sled weight results in a slight increase of the measured

[3] Reproduced section from [182], cf. footnote p. 103 for details.

μ_d (each column) for both materials and reduces the standard deviation for UD-NCF. This behavior is similar to observations for other engineering textiles at low pressure [185, 204, 205].

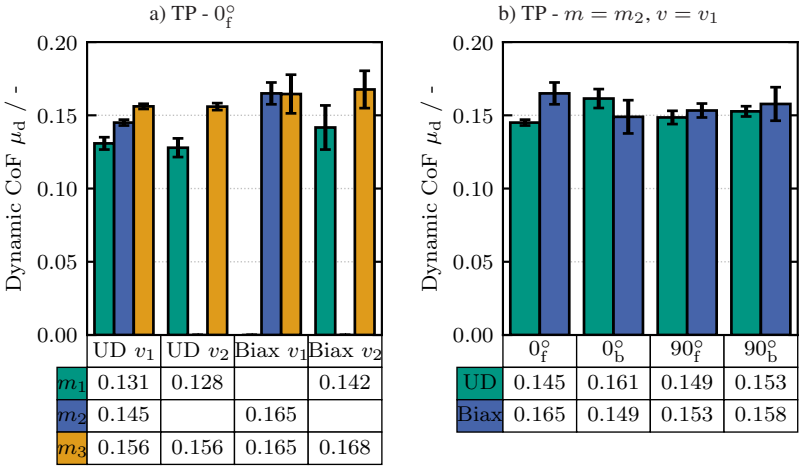

	UD v_1	UD v_2	Biax v_1	Biax v_2
m_1	0.131	0.128		0.142
m_2	0.145		0.165	
m_3	0.156	0.156	0.165	0.168

	0°_f	0°_b	90°_f	90°_b
UD	0.145	0.161	0.149	0.153
Biax	0.165	0.149	0.153	0.158

Figure 4.29: Experimental results of the tool-ply (TP) dynamic CoF | (a) Influence of the applied mass m and velocity v in a 0°_f-configuration for both materials; (b) Influence of the relative interface orientations with an applied mass of $m = m_2$ and velocity $v = v_1$.

The influence of the fiber orientation and fabric side on the TP behavior of both materials is investigated at a constant sled weight m_2 and velocity v_1, cf. Figure 4.29 b. The dynamic CoF is slightly higher for the back side of UD-NCF, but no clear influence of the fiber orientation is observed. For Biax-NCF, no clear trend is observed for the ply's side or orientation.

Overall, Biax-NCF has a slightly higher CoF in the TP-tests despite the similar surface architecture of both fabrics. The measured dynamic CoF for both materials remains relatively small for all tests $\mu_\mathrm{d} < 0.17$, which agrees with measurements of other dry textiles [77, 108, 185, 187].

Ply-ply The influence of the sled weight and velocity on the ply-ply behavior are investigated for the $0^\circ_f/0^\circ_f$-configuration of UD-NCF, cf. Figure 4.30, under the assumption of a similar behavior for the $0^\circ_f/0^\circ_f$-configuration of Biax-NCF. The dynamic CoF is independent of the sled velocity but decreases for an increasing normal pressure. The higher sled weight flattens the roving and stitching, reducing shock effects, which is reflected in the lower amplitude of the observed oscillations [108, 175].

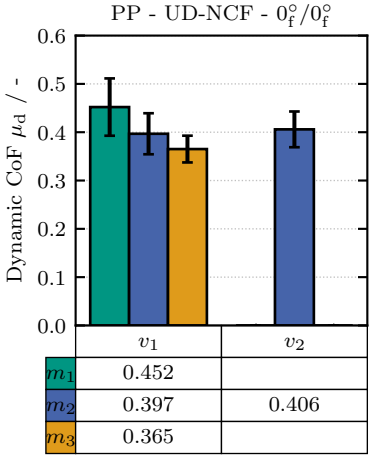

Figure 4.30: Influence of the applied mass m and velocity v on the dynamic CoF for the ply-ply behavior of UD-NCF in a $0^\circ_f/0^\circ_f$-configuration.

The influence of the fabric side and relative fiber orientation at the interface on the PP behavior of both materials is investigated at a constant sled weight m_2 and velocity v_1, cf. Figure 4.31. First, configurations with different sides of the fabrics and same fiber orientations at the interface are compared, i. e. $0^\circ_{\square}/0^\circ_{\square}$, $0^\circ_{\square}/90^\circ_{\square}$ and $90^\circ_{\square}/90^\circ_{\square}$, cf. Figure 4.31. The dynamic CoF decreases for configurations with the back side of one or two plies at the interface for both fabrics (e. g. $0^\circ_f/0^\circ_f > 0^\circ_f/0^\circ_b > 0^\circ_b/0^\circ_b$). This effect is observed independent of the relative fiber orientation at the interface and indicates a higher μ_d for the front side of the fabric with the tricot pattern. A particularly high amplitude of

the oscillations is measured for the $0^\circ_b/0^\circ_b$-configuration of Biax-NCF, which is presumably caused by significant shock effects due to the linear stitching pattern on the back side. This assumption is supported by a significantly higher static CoF in this configuration, cf. Figure A.6. This behavior is not observed for UD-NCF because the linear stitch pattern is recessed between the rovings instead of crossing rovings on the back as for Biax-NCF, cf Figure 4.27.

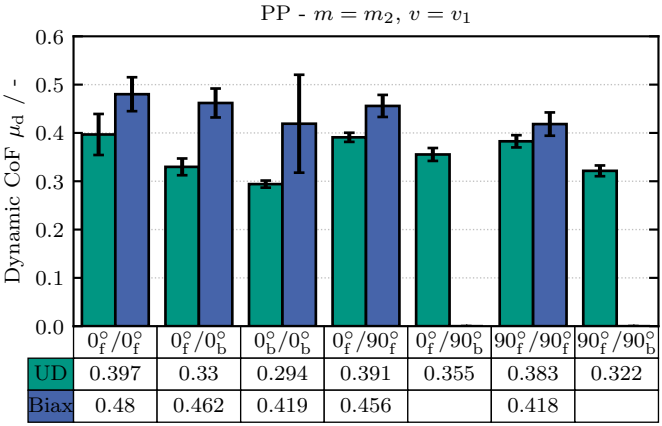

	$0^\circ_f/0^\circ_f$	$0^\circ_f/0^\circ_b$	$0^\circ_b/0^\circ_b$	$0^\circ_f/90^\circ_f$	$0^\circ_f/90^\circ_b$	$90^\circ_f/90^\circ_f$	$90^\circ_f/90^\circ_b$
UD	0.397	0.33	0.294	0.391	0.355	0.383	0.322
Biax	0.48	0.462	0.419	0.456		0.418	

Figure 4.31: Influence of the relative interface orientations on the dynamic CoF for the ply-ply behavior with an applied mass of $m = m_2$ and velocity $v = v_1$.

Second, configurations with similar sides of the fabric and different fiber orientations are compared, i. e. $\square^\circ_f/\square^\circ_f$ for both materials and additional $\square^\circ_f/\square^\circ_b$ for UD-NCF. A decrease of μ_d is measured for more 90° plies when both tricot stitch patterns on the front are in contact ($0^\circ_f/0^\circ_f > 0^\circ_f/90^\circ_f > 90^\circ_f/90^\circ_f$). This effect is notably stronger for Biax-NCF and only very small for UD-NCF. It is not observed in the $\square^\circ_f/\square^\circ_b$-configurations of UD-NCF.

Overall, the CoF for PP-contact is significantly higher compared to the TP-contact and strongly influenced by the specific configuration of the stitching at the interface.

4.5.3 Summary and discussion[3]

The inter-ply behavior of a UD- and a Biax-NCF is investigated for different configurations at the tool-ply as well as ply-ply interfaces. A comprehensive analysis is conducted based on the dynamic CoF, but similar behavior is observed for the static CoF.

The inter-ply behavior of UD- and Biax-NCFs is significantly different for ply-ply (PP) compared to tool-ply (TP) contact. The tangential friction is rate-independent for both cases and significantly higher during PP-contact compared to TP-contact. For an increased sled weight, the CoF increases slightly for TP-contact and notably decreases for PP-contact. This effect can be explained for PP-contact due to flattening of the rovings and stitching for increased normal pressure. The positive pressure-dependency during TP-contact is also observed for other engineering textiles at low pressure [185, 204, 205], but no conclusive reason is known.

The relative fiber orientation between two plies has no clear influence, except for a slight reduction of μ_d for Biax-NCF, in contrast to the behavior of woven fabrics [77, 96, 186, 207]. Instead, the most relevant factor for the PP-behavior of both materials is the architecture of the contacting side of the fabric. Configurations with plies in contact with the zigzag pattern of the tricot stitching on the front have a notably higher CoF. Additionally, the stitching pattern results in strong oscillations in the measured behavior due to stick-slip and shock effects, similar to the observations for undulations in woven fabrics. The measured μ_d is in all tests higher for Biax-NCF than UD-NCF despite similar materials and areal weight of the constituents in the respective directions (cf. Table 4.1). This potentially results from the smaller stitching pitch of Biax-NCF, but would require further investigations for a conclusive claim.

[3] Reproduced section from [182], cf. footnote p. 103 for details.

4.6 Forming behavior [4]

The forming behavior results from the superposition of all individual deformation mechanisms and their interaction with each other. Woven fabrics have often been the focus of forming tests due to their easier formability, while non-crimp fabrics have been investigated much less, resulting in a limited availability of experimental studies as basis for a comprehensive understanding, cf. Section 2.2.5. In particular, to identify the most relevant mechanisms, the forming behavior must be tested for different scenarios and boundary conditions. In addition, a quantitative analysis of the results is important for a detailed validation of new simulation approaches. Therefore, forming experiments of the UD- and Biax-NCF are conducted in cooperation with the LaMCoS laboratory at INSA Lyon (Villeurbanne, France) for different layup configurations and punch shapes, including hemisphere, tetrahedron, and box. The macroscopic strains are captured throughout the entire process using DIC and comprehensively analyzed in combination with the punch forces, outer contour and resulting defects.

4.6.1 Experimental test setup and procedure[4]

Experimental setup The platform developed for the experimental forming tests is presented in Figure 4.32. This platform consists of two modules: a mechanical module, housing the motion control system, punch, blankholder, and die for generating displacement and applying pressure; and an optical module, comprising cameras, a mirror and lights for measurements. The experimental set-up is placed on an electromechanical testing machine by ZwickRoell where the motion part is driven by the TestXpert^{II} software. The punch is connected to

[4] Extracts from Section 4.6 have been previously published in [208], i.e. B. Schäfer, R. Zheng, J. Colmars, A. Platzer, N. Naouar, P. Boisse, L. Kärger. Experimental analysis of the forming behavior of uni- and bidirectional non-crimp fabrics for different geometries. *[submitted for review]* | Sections 4.6.1-4.6.3 reproduce Sections 3-5 of [208].

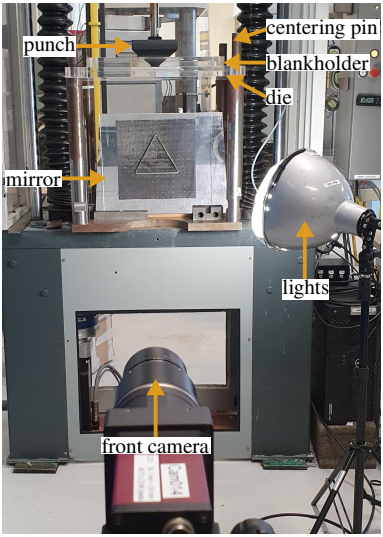

Figure 4.32: Experimental system setup of forming tests.

the motion part in order to deform the materials during the draping process. The blankholder and die are made transparent using methyl methacrylate (PMMA) material to allow for the acquisition of digital images by the optical module. The mirror is positioned at a $45°$ angle at the base, allowing the camera to capture images from its reflection. A top-mounted camera is connected to the horizontal beam on the machine to capture images of the rear side.

Three types of punches (hemisphere, tetrahedron, and square box) along with their corresponding shapes of blank holder and die are utilized in this study. Their dimensions and schematic are displayed in Figure 4.33. The forming depths are $75\,\mathrm{mm}$, $95\,\mathrm{mm}$, and $85\,\mathrm{mm}$ with blankholder weights of $1.7\,\mathrm{kg}$, $6.0\,\mathrm{kg}$, and $1.7\,\mathrm{kg}$ for the hemisphere, tetrahedron, and square box punches, respectively. The thickness of the transparent lower dies is $30\,\mathrm{mm}$.

The utilized specimens of UD- and Biax-NCF have dimensions of $300\,\mathrm{mm} \times 300\,\mathrm{mm}$. To investigate the impact of roving orientation and multiple layers on the material's deformation, three types of single-layer ($[0°_{\mathrm{U}}]$, $[45°_{\mathrm{U}}]$, $[90°_{\mathrm{U}}]$)

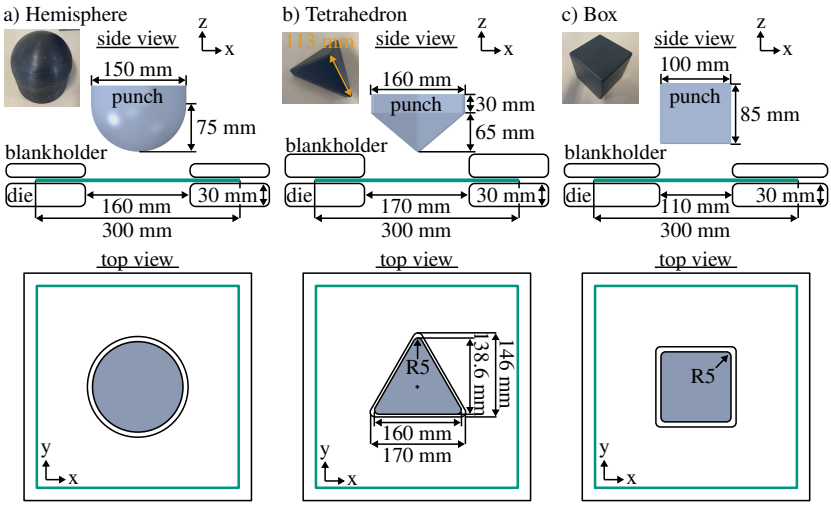

Figure 4.33: Schematics and dimensions of the utilized shapes: a) Hemisphere, b) tetrahedron and c) box [208].

and two types of double-layer($[0^\circ_\mathrm{U}/45^\circ_\mathrm{U}]$, $[0^\circ_\mathrm{U}/90^\circ_\mathrm{U}]$) configurations of UD-NCF and two types of single layer ($[(0°/90°)_\mathrm{B}]$, $[(\pm45°)_\mathrm{B}]$) and one type of double-layer $[(0°/90°)_\mathrm{B}/(\pm45°)_\mathrm{B}]$ configurations of Biax-NCF were used in the forming tests. This naming convention was chosen to better distinguish double-layer tests with UD-NCF ($[0^\circ_\mathrm{U}/90^\circ_\mathrm{U}]$) from single-layer tests with Biax-NCF ($[(0°/90°)_\mathrm{B}]$). They were then captured by the optical module at a rate of one per second to measure the strains throughout the entire forming process, which will be discussed in the next paragraph.

Macroscopic strain measurement method The deformation is measured via Digital Image Correlation (DIC) with the same method used for the investigation of the membrane behavior, which is described in Section 4.2.1. A regular grid of white dots is applied to half of the specimen using a stencil with a distance of $l_\mathrm{e} = 10\,\mathrm{mm}$, as shown in Figure 4.34 a.

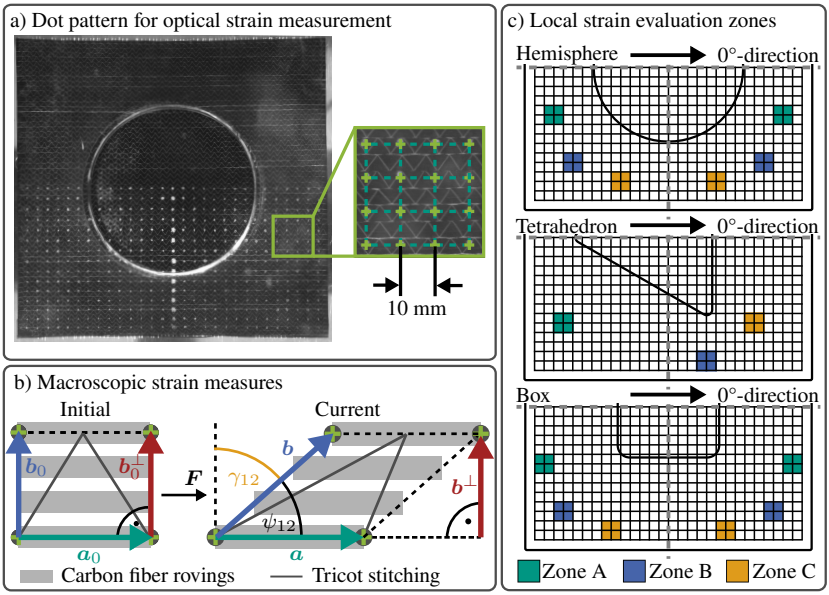

Figure 4.34: (a) Dot pattern utilized during 2D-DIC to measure (b) macroscopic strains as well as (c) local evaluation zones for average strains [208].

The E_{11}-, E_{22}-, $E_{\perp}$- and γ_{12}-strains are again calculated, cf. Figure 4.34 b, to differentiate between the different membrane deformation modes defined in Section 4.2.1. In many deformation modes observed during the forming tests of this study, the perpendicular $E_{\perp}$ and transverse E_{22} strains have the same sign and allow similar conclusions to be drawn. Thus, the analysis focuses on $E_{\perp}$ due to its stronger correlation with gapping as well as the fiber volume content, while E_{22} is used to identify zones with significant roving slippage and in-plane compaction (mixed-mode 2).

For a quantitative evaluation of the strain development during the tests, the strains are averaged over three local zones for each shape, cf. Figure 4.34 c. The locations of the zones were chosen to reflect the symmetry of each shape, remain in the flat part after the maximum punch displacement, and be positioned in areas of high deformation during forming.

4.6.2 Results & discussion[4]

4.6.2.1 Punch forces

The punch force f is a direct measure of the required energy to accomplish the draping process and indirectly indicates the drapability of a fabric. A material that conforms more easily to a geometry usually requires less energy [72]. Since the Biax-NCF has approximately twice the areal weight per textile layer ($602.24\,\mathrm{g\,m^{-2}}$) as the UD-NCF ($328.86\,\mathrm{g\,m^{-2}}$), the punch force was normalized by the total mass m of the formed fabric during each test, cf. Figure 4.35. This also indirectly normalizes the punch force by the number of layers, facilitating the comparison of single- and double-layer tests.

The **hemisphere** has a constant curvature over its height, resulting in an almost linear increase of the required force over the punch's displacement, cf. Figure 4.35 a) and b). The double-layer tests require minimally more force per layer compared to the single-layer tests but with often overlapping experimental scatter. The required forces per fabric mass for the UD-NCF are slightly lower than those for the Biax-NCF, indicating a simpler draping to the hemispherical geometry. In the single-layer tests, the stitching of the UD-NCF requires only relatively small forces for notable transverse strains, while this deformation mode is prevented for the Biax-NCF by the second fiber direction. That is also the reason that the double-layer [$0^\circ_\mathrm{U}/90^\circ_\mathrm{U}$]-test of the UD-NCF requires nearly equivalent force as the single-layer [$(0^\circ/90^\circ)_\mathrm{B}$]test of the Biax-NCF.

The **tetrahedron** geometry changes from its slanted surfaces to a constant cross-section at a height of $65\,\mathrm{mm}$, as indicated by the vertical dashed line in Figures 4.35 c) and d). This results in a higher slope for all tests after this point, since the vertical surfaces are more challenging to form and more friction occurs in the now constant gap between the textile and blankholder. In the [0°_U]- and [90°_U]-single-layer tests of the UD-NCF, the textile partially got caught in some

[4] Reproduced section from [208], cf. footnote p. 110 for details.

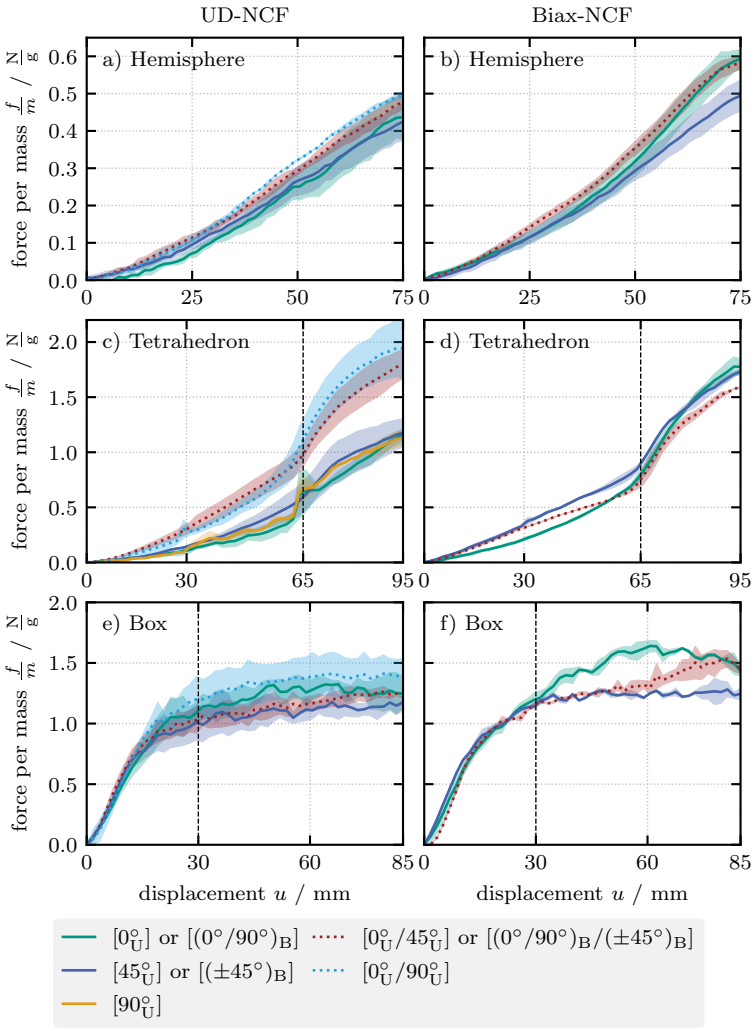

Figure 4.35: Punch forces normalized by the total mass of the fabric layers for the different geometries for Biax- and UD-NCF in single- (solid) or double-layer (dotted) configurations [208].

corners of the tetrahedron at this transition, forming larger gaps and resulting in a sudden spike in the punch forces. The double-layer tests of UD-NCF require notable higher forces because the layers interact with each other and influence their mutual deformation, which will be discussed in more detail in the next Sections. Thus, the forces per mass are in the same range as for the Biax-NCF where the stitching enforces the interaction between the two fiber directions within a single layer.

The **square box** geometry has a constant cross-section but the lower die only has a thickness of $30\,\mathrm{mm}$, as indicated by the vertical dashed line in Figures 4.35 e) and f). This results in a lower slope for all tests after this point, as the punch exits the lower die and part of the textile no longer has frictional contact. The forming tests on the square box show a more pronounced influence of the ply orientation on the punch forces compared to the other shapes. Both materials follow the same relative sequence of the resulting forces depending on the orientation of fibers within the stack of textile layers: only 0° or 90° fibers > mixed 0° and 45° fibers > only 45° fibers. This indicates that the $\pm 45°$-layers of both materials conform easier to the geometry compared to the 0°-layers. However, similar to the hemisphere tests, the influence of the number of layers is less pronounced, indicating less interaction between the textile layers.

In summary, the forces in the tests with lower blankholder weights on the hemisphere and box shape are slightly smaller for the same weight of textile (i.e. number of fibers) for single layers of UD-NCF. However, interactions between layers of UD-NCF result in comparable forces to tests with Biax-NCF. The influence of a layer's orientation on the required forces is relatively small and is only consistently identified for the square box shape.

4.6.2.2 Outer contours

The resulting outer contours of all tests are shown in Figures 4.36 & 4.37. The contours can be used to evaluate the overall deformation [72] and often represent a validation for forming simulation approaches based on the material

draw-in [136, 213, 229]. Furthermore, the fabric after forming consists of one effective zone that represents the desired shape and one non-effective zone that needs to be removed in the subsequent process. Analyzing the outer contour after forming helps in minimizing material waste and production costs during manufacturing.

Single-layer tests The contour after forming of fabrics usually reflects the symmetry of the utilized shape and material. This results in an orthotropic deformation pattern with fewer symmetries for unbalanced textiles [72, 136] compared to balanced fabrics [217, 229]. Similar behavior can also be observed for the investigated UD- and Biax-NCF in the single-layer tests shown in the first columns of the respective material in Figures 4.36 & 4.37. The Biax-NCF exhibits a nearly balanced architecture with a symmetrical stitching pattern and a similar number of carbon fibers in both reinforcement directions. Therefore, its highest material draw-in in both fiber directions is close to symmetrical for the point symmetrical hemisphere and box shape, resulting in a quarter-symmetrical contour. In contrast, the highest material draw-in of the very unbalanced UD-NCF has a single preferred direction along the carbon fibers, resulting in a half-symmetrical contour for the hemisphere and box. The tetrahedron is only axisymmetric, so the contours of the Biax-NCF are only half-symmetrical, which is also the case for the UD-NCF in the $[0^\circ_\mathrm{U}]$- and $[90^\circ_\mathrm{U}]$-tests. The contour of the $[45^\circ_\mathrm{U}]$-test of the UD-NCF no longer exhibits any symmetry, because no material axis coincides with a geometric axis of symmetry.

Double-layer tests The contours of the double-layer tests are shown in the second column of the respective material in Figures 4.36 & 4.37. They are investigated for a better understanding of the interactions between layers. Significant slippage between the layers can be observed in all tests.

In the **hemisphere** tests, the differences between the individual layers and the respective single-layer tests are quite small, cf. Figure 4.36 a). Only in the $[0^\circ_\mathrm{U}/45^\circ_\mathrm{U}]$-test of UD-NCF the direction of the maximum material draw-in in

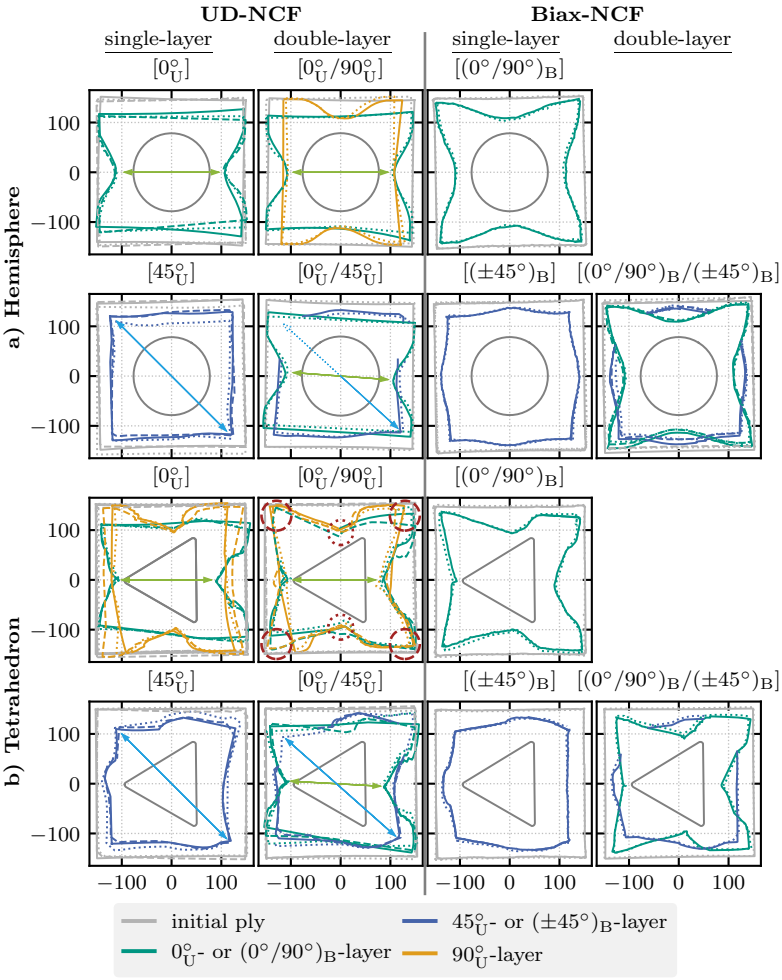

Figure 4.36: Outer contours (all in mm) of single- and double-layer configurations in the a) hemisphere and b) tetrahedron forming tests. Annotations for interactions between layers with arrows and red circles [208].

the fiber direction of both layers tilts slightly (green and cyan arrows) due to the superposition of their mutual deformation. For the Biax-NCF, this rotation

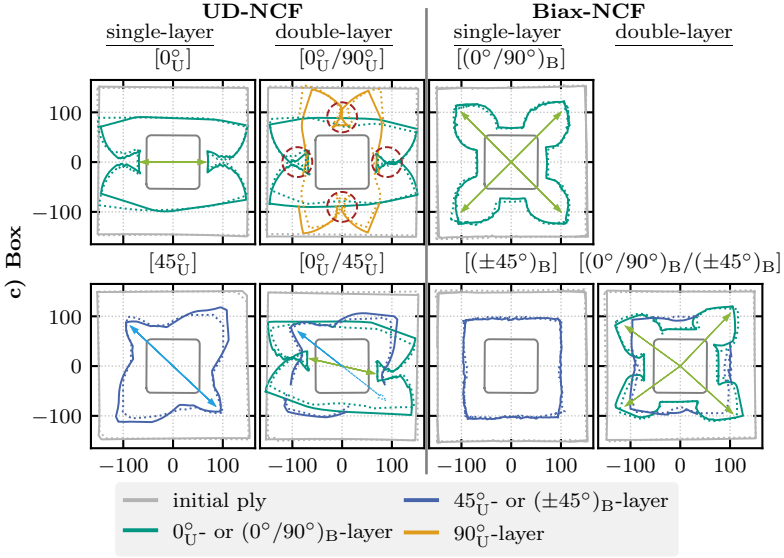

Figure 4.37: Outer contours (all in mm) of single- and double-layer configurations in the box forming tests. Annotations for interactions between layers with arrows and red circles [208].

is not observed because the deformation of the 45°-layer does not have a single preferred direction. In general, the absence of a binder and relatively low blankholder weight limit the interactions between layers for the hemisphere geometry.

In the $[0°_U/45°_U]$-test on the **tetrahedron** shape, a similar tilt of the draw-in (green and cyan arrows) is observed again only for the UD-NCF, cf. Figure 4.36 b). In the $[0°_U/90°_U]$-test more pronounced interactions between the UD-NCF layers are observed from the contour analysis. The superimposed draw-in of the 90°-layer leads to a stronger draw-in of the 0°-layer as indicated by the dotted red circles. Additionally, the corners of the 0°- and 90°-layer remain superposed during some tests (dashed red circles), resulting in a joint deformation of both layers and producing a similar contour to the $[(0°/90°)_B]$-test of the Biax-NCF. The fact that this joint deformation does not always occur is probably caused

by the blankholder forces not being large enough to invariably prevent mutual slippage.

For the **square box** shape notable interactions in the double-layer test are observed, cf. Figure 4.37 c), despite a lower blankholder weight similar to the hemisphere with few significant interactions. The material draw-in of the UD-NCF perpendicular to the fiber direction in the $[0^\circ_\mathrm{U}/90^\circ_\mathrm{U}]$-test is increased due to the second layer, resulting in partly overlapping flaps of textile (dashed red circles). In the $[(0^\circ/90^\circ)_\mathrm{B}/(\pm 45^\circ)_\mathrm{B}]$-test a notable tilt of diagonals of the $(0^\circ/90^\circ)_\mathrm{B}$-layer due to interaction with the $(\pm 45^\circ)_\mathrm{B}$-layer is observed for the Biax-NCF. The increase in interactions for the box shape compared to the hemisphere, despite similar blankholder weights, highlights the impact of the more challenging geometry in the context of forming due to the sharp edges and corners instead of a smooth curvature.

Summary Overall, a significantly larger experimental scatter is observed for the UD-NCF, especially in the direction transverse to the fibers. The deformation in the transverse direction of the UD-NCF is governed by the stitching, which is more compliant and permits larger strains compared to the second fiber direction of the Biax-NCF. Additionally, the stitching pattern is not manufactured perfectly homogeneous across each sample, from which some variation in the material properties is suspected.

In summary, the contours of the single-layer tests are a quantitative measure of the overall deformation of the material. The unidirectional high stiffness of the single fiber direction in a UD-NCF layer is reflected in the resulting contours. In contrast, the Biax-NCF has a more symmetrical behavior due to the stitching that couples the deformation of both fiber directions within a layer. The double-layer tests provide insights into the possible interactions between the layers, which depend on the relative orientation between two textile layers, the blankholder weight and the shape of the punch. The magnitude of the observed interactions between the layers for each punch shape is similar to the relative influences that have been identified based on the required forces, cf.

Section 4.6.2.1. The double-layer tests of UD-NCF show more signs of mutual interactions in their contour than the tests with Biax-NCF, presumably because of their easier deformability and the more asymmetrical deformation due to the lack of a second fiber direction.

Comparing the $[0^\circ_U/90^\circ_U]$- and $[(0^\circ/90^\circ)_B]$-setup as configurations with an initial 0°- and 90°-fiber layer for both materials, the differences are most evident. In the hemisphere- and box-test of the UD-NCF, the resulting fiber orientation after forming remains nearly 0°/90° as evident from the outer edges which stay comparably straight due to the independent deformation of the layers. In contrast, the fibers of the Biax-NCF undergo more rotation due to shear in the areas between the bidirectional high material draw-in, because of the coupled deformation of both fiber layers due to the stitching. Only in the tetrahedron test, the stronger interaction between UD-NCF layers due to the higher blankholder forces can result in a joint deformation and the resulting contours are comparable to the Biax-NCF.

4.6.2.3 Macroscopic strains

The strains during the tests were measured with DIC based on the method described in Section 4.2.1. The edges of the openings of the lower dies appear white on the images, with a similar contrast to the white dots of the applied pattern. This results in a loss of correlation for points passing over these edges, which become obvious as strongly deformed elements. The 2D measurement method has the disadvantage that only the strains in the flat area can be measured accurately. In return, the strains can be determined over the entire punch displacement. Furthermore, there is no need for a specialized 3D measuring system, which often requires a way to remove the textile from the mold and is more often used for fabrics with a binder [213, 232, 297]. The measurements in the punch areas can be qualitatively compared to each other despite the 3D-distortion assuming full contact with the fabric, which was observed for the closed configurations.

The strains for the different shapes are presented separately in Figures 4.38 & A.7 for the hemisphere, Figures 4.40 & A.8 for the tetrahedron and Figures 4.41 & A.9 for the square box. The development of the local shear angles in the three areas highlighted in Figure 4.34 c) for all three shapes is summarized in Figure 4.39.

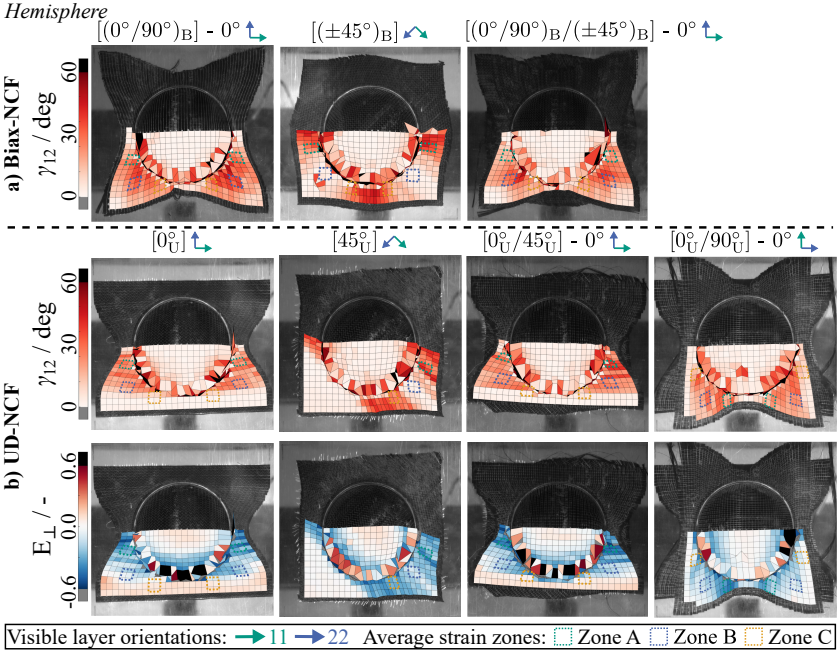

Figure 4.38: Relevant DIC-strains in the hemisphere shape forming test with different layup orientations at a maximum tool displacement of 75 mm [208].

First, the most relevant strains for the **hemisphere** are analyzed, which are shown in Figure 4.38. The remaining strains less relevant within the scope of this work are shown in Figure A.7. As discussed in Section 4.6.1, the shear angle γ_{12}, transverse strain E_{22} and perpendicular strain $E_{\perp}$ can be evaluated to distinguish between different membrane deformation modes, cf. Figure 4.2. For the Biax-NCF, only γ_{12} is presented because mainly shear was observed.

The observed $E_\perp$-strains result from pure shear according to Equation 4.2, cf. Figure A.7 a. For the UD-NCF, mainly the mixed deformation modes 1 and 3 are observed for the hemisphere shape, cf. Figure 4.2, thus a detailed analysis of E_{22} is omitted as it would allow the same conclusions as $E_\perp$. The development of the local shear angles during the hemisphere tests are shown in Figure 4.39 a).

Both the single- and the double-layer tests with Biax-NCF show a symmetrical shear deformation, cf. Figure 4.38 a), as also evident by the local shear angles in Zones A and B, cf. Figure 4.2. The behavior is similar to the results observed for balanced woven fabrics [217, 350]. The additional $\pm 45°$-layer in the $[(0°/90°)_\mathrm{B}/(\pm 45°)_\mathrm{B}]$-tests slightly reduces the shear deformation in the visible 0°-layer.

The UD-NCF has an asymmetric shear behavior with the main deformation due to shear parallel to the fiber direction, cf. Figure 4.38 b). In the $[0°_\mathrm{U}]$-test, positive perpendicular strains are measured in the lower edge regions. Slight gaps between the rovings are visible there and the stitching is under high tension. This stitching tension is reduced for the $[0°_\mathrm{U}/45°_\mathrm{U}]$-test and vanishes in the $[0°_\mathrm{U}/90°_\mathrm{U}]$-test, because of the superimposed material draw-in of the second layer. Similarly, positive perpendicular strains are measured for $[0°_\mathrm{U}]$and $[45°_\mathrm{U}]$in the hemisphere's center despite the distortion caused by the 3D-curvature, but they are reduced in the double-layer tests. The interaction with the superimposed layers increases shear deformation in the areas around zones B and especially C compared to the $[0°_\mathrm{U}]$-test, cf. Figure 4.39 a). In zone A, a superposed 90°-layer reduces the shear angle, while a 45°-layer leads to higher shear angles due to the tilted material draw-in, cf. Section 4.6.2.2.

Second, the most relevant strains for the **tetrahedron** are analyzed, which are shown in Figure 4.40 and in Figure 4.39 b). The remaining strains less relevant within the scope of this work are shown in Figure A.8. The main deformation due to shear of the UD-NCF is again observed parallel to the fiber direction, compared to the more symmetrical deformation dominated by pure shear of the Biax-NCF similar to the behavior observed for woven fabrics [217]. The shear

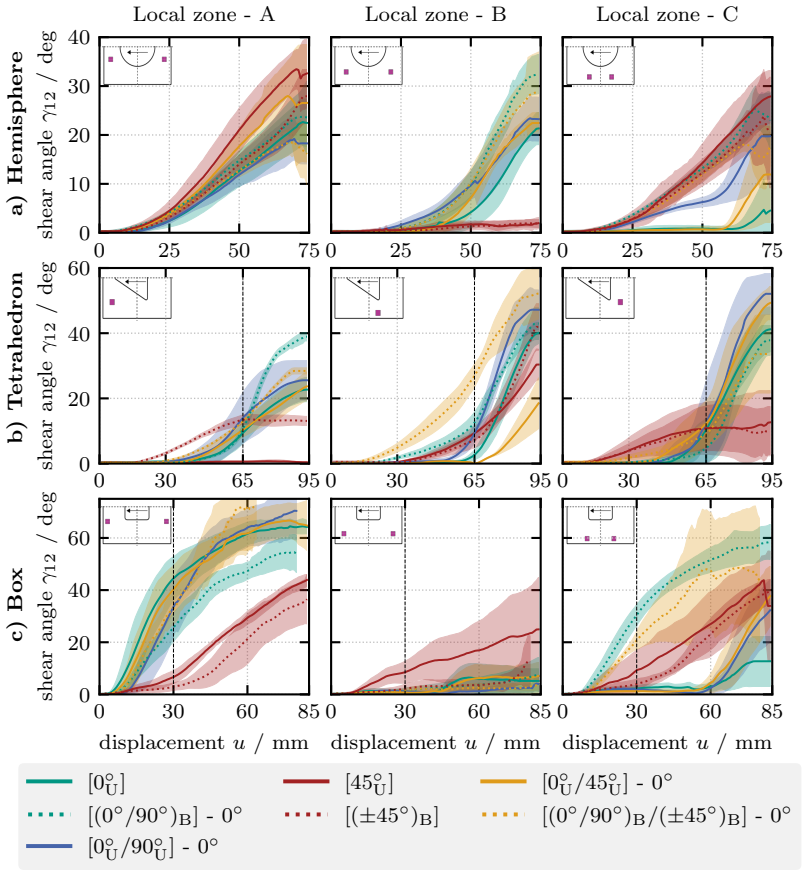

Figure 4.39: Local shear angles γ_{12} for the a) hemisphere, b) tetrahedron and c) box punch shapes. The shear is measured on the visible 0°-fiber layer in double-layer setups. Vertical dashed lines indicate geometrical changes in the box and tetrahedron experimental setups [208].

angles close to the corners of the punch are higher than for the hemisphere tests, due to the small radius of curvature of the tetrahedron in this area. This is especially evident in zones B and C of the 0°-layers in all tests, cf. Figure 4.39 b). Furthermore, comparing the signs of $E_\perp$ with E_{22}, in the region around zone

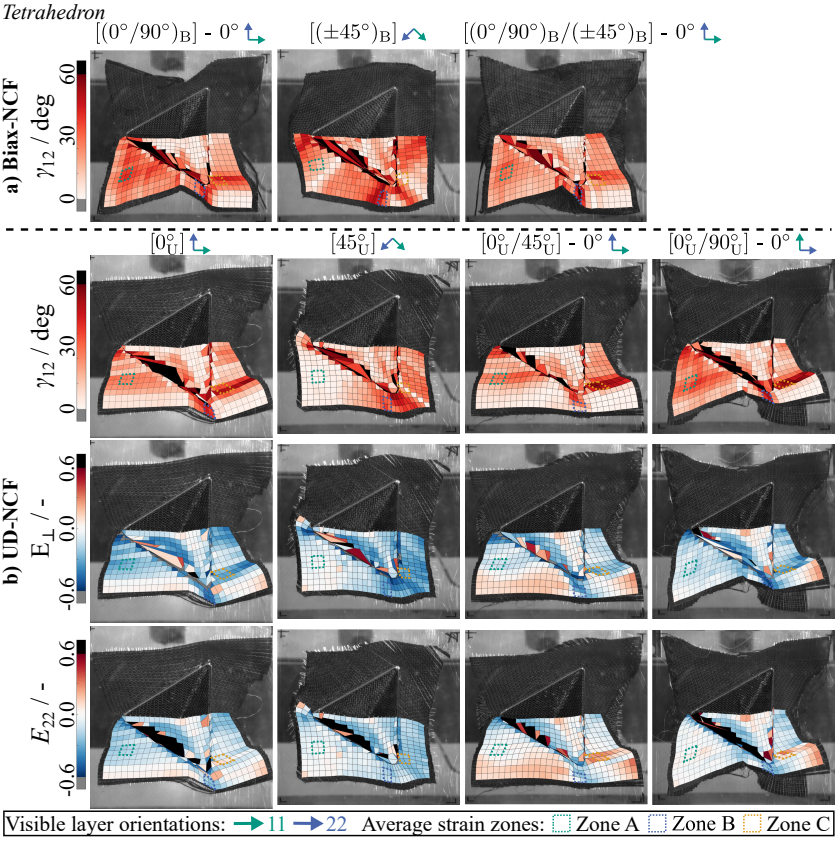

Figure 4.40: Relevant DIC-strains in the tetrahedron shape forming test with different layup orientations at a maximum tool displacement of 95 mm [208].

C the mixed deformation mode 2 is observed for the UD-NCF, cf. Figure 4.2. Notable shear-induced slippage between the fiber rovings occurs in this area, especially in the double-layer tests. The additional 90°-layer induces a more symmetrical shear behavior in the parts of the 0°-layer remaining superposed during the test, like the lower left half in the $[0°_U/90°_U]$-test in Figure 4.40 b). This results in a behavior similar to the Biax-NCF and higher shear angles, cf. Figure 4.39 b). In the $[0°_U/45°_U]$-test, positive perpendicular strains are

measured in the lower left edge regions, similar to the observations in the $[0°_U]$-test of the hemisphere. The 45°-layer prevents some of the material draw-in of the 0°-layer resulting in small gaps between the fiber rovings and tension in the stitching.

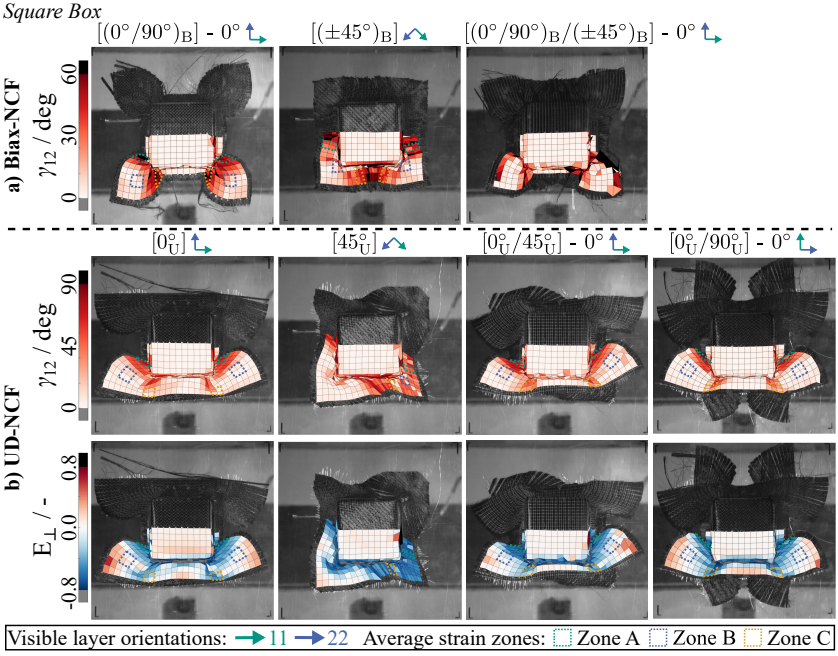

Figure 4.41: Relevant DIC-strains in the square box shape forming test with different layup orientations at a maximum tool displacement of 85 mm [208].

Third, the most relevant strains for the **square box** are analyzed, which are shown in Figure 4.41 and in Figure 4.39 c). The remaining strains less relevant within the scope of this work are shown in Figure A.9. The small radius of the corners and significant depth lead to even higher shear angles than for the tetrahedron shape. The relative observations regarding the measured strains for the tests with the square box shape are similar to those for the hemisphere due to the comparable blankholder weight. The symmetrical shear-dominated

deformation without notable roving slippage of the Biax-NCF is again similar to the behavior observed for balanced woven fabrics [68, 211, 223]. The UD-NCF mainly deforms under shear (mixed-mode 1, cf. Figure 4.2) parallel to the fiber rovings with strong strain concentrations around the corners of the box. The interactions in double layer tests observed based on the contour, cf. Section 4.6.2.2, are only slightly reflected in the locally measured strains. In the area around zone C of the 0°-layers, an increase in the shear angle due to the superimposed layers is measured in the double-layer tests for the UD-NCF, cf. Figure 4.39 c).

In summary, the general difference between the deformation behavior of the nearly balanced Biax-NCF and the highly unbalanced UD-NCF already discussed for the outer contours (cf. Section 4.6.2.2) is also reflected in the macroscopic strains for all shapes. Thereby, a clear influence of the geometry on the magnitude of measured strains is obvious. As the complexity and curvature of the geometry increase from the hemisphere to the tetrahedron to the box, so the measured strains increase too. Especially the forming of the corners of the tetrahedron and box requires a significant material draw-in in those areas, resulting in high strain concentrations.

4.6.2.4 Forming defects

Defects may occur during the forming process due to variations in part geometry, reinforcement type, and experimental setup. A summary of the most relevant forming defects and their location during the tests is shown in Figure 4.42.

In the tests for **Biax-NCF**, the structural integrity is enhanced through the two fiber orientations. Only highly localized mesoscopic defects were observed for the Biax-NCF for all investigated shapes. These defects involve isolated gaps and small wrinkles in highly curved areas, such as the corners of the square box shape, as illustrated in Figure 4.42 d).

For the **UD-NCF**, significantly larger and more systematic defects are detected due to the lower stiffness of the stitching compared to the second fiber direction

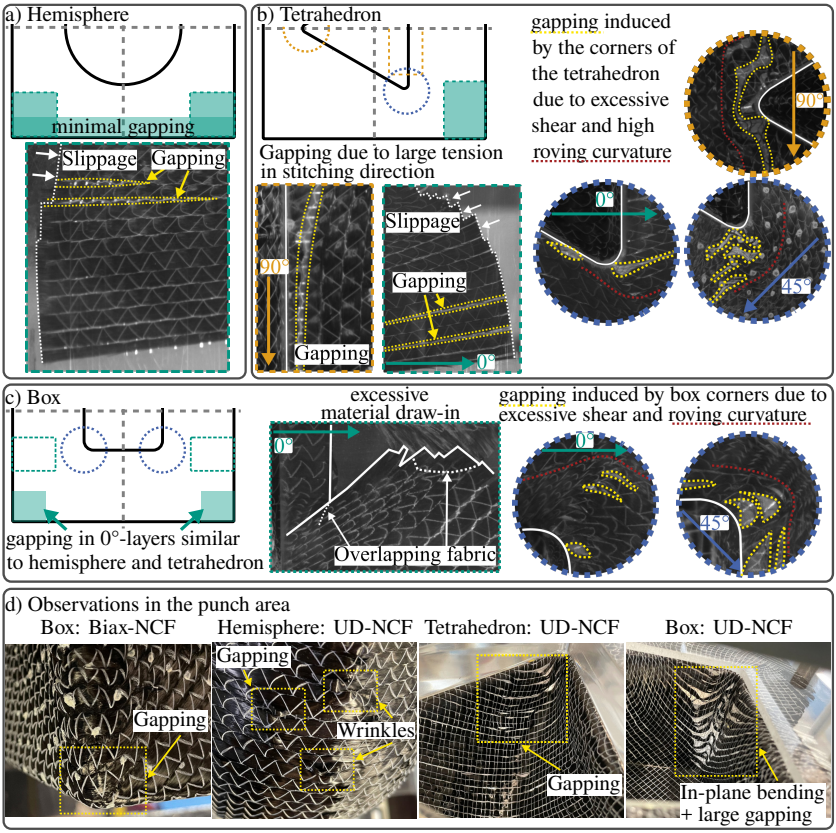

Figure 4.42: Schematic overview of the location and type of observed forming effects for the UD-NCF in the planar region for the a) hemisphere, b) tetrahedron and c) square box tests. d) Additional defects of UD- and Biax-NCF observed in the punch region [208].

of the Biax-NCF, cf. Figure 4.42. Relative slippage and small gapping between the carbon fiber rovings are visible in the corner areas of the 0°-layers for all shapes (shaded green areas). These areas coincide with regions of positive perpendicular strains $E_{\perp}$, cf. Section 4.6.2.3. Those result from the high tension in the stitching direction induced by friction with the tools, as well as the largest relative displacements that occur in these areas due to the material draw-in.

Larger gapping is observed near the corners of the punch in the single-layer tests of both the tetrahedron and box shape, cf. circles in Figure 4.42 b) and c). The localized strong material draw-in in those areas results in high shear deformation, cf. Section 4.6.2.3. In cases where the shear cannot propagate parallel to the carbon fibers, the rovings undergo strong in-plane bending deformation (indicated by the red dotted lines). This results in the formation of gaps, which increase in size as the deformation progresses and are also drawn from the flat outer area into the 3D regions, cf. Figure 4.42 d). These gaps develop to a much smaller extent in the double-layer tests, because the superposed layer acts as a reinforcement in the transverse direction and distributes the deformation more evenly.

4.6.3 Summary and discussion[4]

The forming behavior of a UD- and a Biax-NCF is investigated for different double-curved punch shapes (hemisphere, tetrahedron and square box) for different initial fiber orientations in single- and double-layer configurations. The application of planar blankholders enables strains measurements via DIC in the flat areas, but also results in a membrane-dominated behavior without notable influence of the bending behavior or wrinkling. A comprehensive analysis is conducted based on the required punch forces, outer contours, macroscopic strains and observed forming defects.

The punch forces for both textiles in configurations with similar total fabric weights are comparable and only weakly influenced by the relative layer orientation. Early indications of inter-layer interactions in the double-layer tests can be derived from the forces: The normalized punch forces are significantly increased due to a second ply for UD-NCF in the tetrahedron test, since the two plies remain partially superposed. In all other double-layer tests, the friction between layers is too small to provoke significant interactions.

[4] Reproduced section from [208], cf. footnote p. 110 for details.

The analysis of the contours and macroscopic strains clearly shows fundamental differences in the general deformation behavior of the UD- and Biax-NCF. The Biax-NCF mainly deforms under symmetrical shear with limited roving slippage and defects. The stitching couples the deformation of both fiber layers. Therefore, the fibers of the Biax-NCF undergo rotation due to the nearly pure shear in the areas between the high material draw-ins in the two fiber directions.

The UD-NCF has an asymmetrical behavior with the main deformation due to shear parallel to the fiber rovings superimposed with significant perpendicular and transverse strains ($E_{\perp}$ and E_{22}) in different deformation modes. The fiber orientation after forming often remains similar to the initial orientation, because the shear results from parallel roving slippage instead of rotation in most deformation modes, cf. Figure 4.2. In addition, the lower stiffness in the transverse direction results in positive perpendicular strains due to gapping as well as more defects. In the single-layer tests in particular, gapping occurs due to large tension in the stitching direction or strong in-plane bending of the rovings since shear transverse to the fiber direction is not possible. Especially larger areas with gapping can be identified by positive perpendicular strains $E_{\perp}$. Fewer defects were observed in double-layer tests due to the interaction between the superimposed high stiffness of the differently oriented layers. However, the magnitude of interactions was limited because of the relatively low blankholder weights. Future studies should therefore focus on the influence of the blankholder force, which is expected to increase the magnitude of interactions. The presented results constitute an extensive database to validate forming simulation approaches for UD- and Biax-NCF, which was not yet available for UD-NCF in particular.

4.7 Discussion and conclusion

The experimental characterization of the relevant intra- and inter-ply deformation mechanisms as well as a comprehensive analysis of different forming tests are presented and investigated in this chapter. The mesoscopic structure of the constituents of the NCFs leads to a specific macroscopic behavior, which is largely influenced by the interaction of the stitching and the rovings. Therefore, all experiments must take into account the orientation and resulting load of the stitching, in addition to the rovings. The membrane behavior in particular does not adhere to theoretical models and must be specifically evaluated using optical methods. The observed similarities as well as unique characteristics of the investigated UD- and Biax-NCF are summarized in Figure 4.43.

In many experiments, the Biax-NCF behaves very similarly to the well-understood behavior of woven textiles. A strongly shear-dominated and nearly symmetrical membrane behavior is observed during characterization as well as forming tests. Instances of observed roving slippage are very limited and occurring defects are mainly mesoscopic. The bending behavior is only slightly anisotropic, which can be mainly attributed to the different architecture of the rovings on the front and back sides of the fabric. The main difference to woven fabrics due to the stitching is observed during the characterization of the compaction and inter-ply behavior.

The characterization of the UD-NCF exhibits many similar phenomena but also fundamental differences to the Biax-NCF. In particular, the membrane and bending behavior of the UD-NCF are significantly different from that of the Biax-NCF and consequently also from other balanced textiles. A strongly anisotropic and asymmetric behavior is observed, since the transverse behavior is determined by the stitching instead of a second fiber orientation. Therefore, a description of the membrane behavior solely based on shear is not sufficient and superimposed transverse tensile as well as perpendicular compressive strains must be considered. In the forming tests, this results in many areas with different membrane deformation modes as well as gapping and roving slippage. For

Characterization on coupon level - Chapter 4

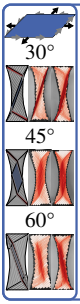

Membrane behavior - Section 4.2

- Off-axis tension tests (OATs) impose different ratios of superimposed shear, transverse tension and in-plane roving compaction
- DIC to measure combined membrane deformation modes
- New method to quantify in-plane roving curvature (κ_{11})

UD-NCF	Biax-NCF
• Strongly asymmetric shear behavior	• Shear-dominated with minor asymmetry
• Superimposed E_{22} & $E_{\perp}$ strains	• Limited slippage in all OATs
• Large slippage in all OATs	• 45°-OAT: Sufficient for shear behavior
• 45°-OAT: Shear-dominated	• 30°-OAT: Roving bending & slippage
• 30°-OAT: Highest shear & slippage	
• 60°-OAT: Stitching tension limits shear	

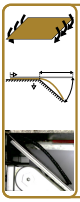

Bending behavior - Section 4.3

- Cantilever tests to investigate different fiber & stitching orientations
- Higher bending stiffness in configurations with stitching under tension
- M-κ-curves: Non-linear behavior for higher curvatures
- Peirce bending stiffness good approximation for small curvatures

UD-NCF	Biax-NCF
• Strongly anisotropic behavior	• Slight anisotropy due to roving sizes
• 45°: significant twist of the specimen	• 45°: slight sagging in specimen center

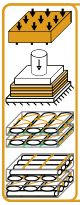

Compaction behavior - Section 4.4

- Punch-to-plate setup to investigate number of layers n_{L} & relative orientation $\Delta\Theta$
- Analytical p-model $\Phi^{\mathrm{p}}(p)$ for pressure-dependent FVC suitable for individual tests
- Increasing n_{L}: Superimposed stitching and roving nesting for both materials

UD-NCF	Biax-NCF
• Small influence of $\Delta\Theta$	• Notable influence of $\Delta\Theta$
• Only nesting during compaction	• Initial FVC depends on n_{L} + nesting
• Good approximation by $\Phi^{\mathrm{pn}}(p, n_{\mathrm{L}})$	• $\Phi^{\mathrm{pn}}(p, n_{\mathrm{L}})$ fits only for medium n_{L}

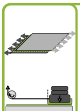

Inter-ply behavior - Section 4.5

- Sled pull-over setup to investigate tool-ply and ply-ply contact
- CoF independent of sled velocity and relative roving orientation
- TP: $\mu_{\mathrm{d}} < 0.17$, increases for higher normal pressure
- PP: $\mu_{\mathrm{d}} > 0.3$, decreases for higher normal pressure, higher for zigzag stitching side

UD-NCF: Lower CoF	Biax-NCF: Higher CoF

Forming behavior - Section 4.6

- Different double-curved punch shapes (hemisphere, tetrahedron, square box)
- Comprehensive analysis of forces, outer contour, macroscopic strains & defects

UD-NCF	Biax-NCF
• Asymmetrical behavior	• Nearly symmetrical behavior
• Shear parallel to rovings superimposed with significant E_{22} & $E_{\perp}$ strains	• Mainly shear & limited roving slippage
• Gapping & slippage (not in double layer)	• Only mesoscopic defects

Figure 4.43: Summary of all similarities and unique characteristics of the investigated UD- and Biax-NCF that were determined in the experimental investigations in Chapter 4.

the bending behavior, the stitching-dominated behavior in transverse direction yields a very different bending stiffness, which deviates from the roving direction by several orders of magnitude. This results in a strong twist deformation for off-axis bending loads as demonstrated by the 45°-cantilever tests.

Requirements for macroscopic approach The profound understanding and characterization of the macroscopic deformation mechanisms during forming is essential for the development of suitable simulation approaches in the following chapters. The focus is on UD-NCF, since there is a lack of suitable simulation models and the specific behavior compared to Biax-NCF requires specialized approaches. On the basis of the experimental results in Sections 4.2-4.6 and the above outlined discussion, the following main requirements for a macroscopic simulation approach for NCF are proposed:

- Development of a membrane constitutive model suitable for large superimposed shear, transverse tensile and in-plane perpendicular compressive behavior
  - Capability to model large in-plane roving slippage
  - Quantitative validation based on the forming test results
  - Ensure transferability to other UD-NCFs and, in principle, to Biax-NCFs
- Parameterization of a suitable bending constitutive model accounting for strongly anisotropic behavior
- Layer-by-layer approach of the forming processes to take into account inter-ply behavior and slipping
- Development of an efficient 3D element formulation that considers compaction during forming and fulfills the necessary numerical as well as CoFRP specific requirements

5 Hyperelastic modeling of non-crimp fabrics

Outline

The following chapter presents the development of a new hyperelastic modeling approach for the membrane behavior of unidirectional non-crimp fabrics. First, existing modeling approaches in literature are analyzed and compared to a strongly simplified approach based on decoupled deformation modes in Section 5.1. The objective is to identify the minimum required level of complexity and necessary couplings between deformation modes to describe the membrane behavior of UD-NCF. Second, a new hyperelastic membrane modeling approach with a moderate number of parameters for the strain energy density and coupling is proposed in Section 5.2. All functions are based on generalized formulations to simplify the parameterization process and facilitate the transfer to new materials. The new modeling approach is parameterized based on off-axis tension tests with bias angles of $30°$, $45°$ and $60°$. Third, a suitable bending approach is parameterized to describe the strongly anisotropic behavior observed during cantilever tests with different orientations in Section 5.3. Fourth, the proposed membrane and bending approaches are validated with forming simulations of a hemisphere, tetrahedron and square box shape in Section 5.4. The proposed model achieves good results in quantitative comparisons of the outer contour after forming as well as measured global and local strains. Subsequently, the transferability of the new model is demonstrated by an application to forming of Biax-NCF in Section 5.5.

5.1 Preliminary investigation of the state of research[6]

In Chapter 4, requirements for a membrane modeling approach of UD-NCF were derived based on the experimental investigations. In the current state of research outlined in Section 2.3.3, both very simple shear-based approaches and highly complex approaches based on superimposed strains exist to model this behavior. Based on the results of Krogh et al. [139], it can be concluded that a purely shear-focused approach does not suffice, because pure shear is not an intrinsic deformation mode of UD-NCF and poor results are already achieved for coupon tests. In contrast, the comprehensive approach of Schirmaier et al. [137] is highly tailored to the specific architecture of the investigated UD-NCF. It describes the behavior based on superimposed shear, transverse tension and in-plane compaction perpendicular to the CF rovings, by parameterization of different strain states and interpolating between them. In addition, multiple couplings between the deformation modes are introduced. This results in a complex approach with a large number of parameters that make modification and transferability to other materials difficult.

A preliminary study is conducted to investigate which level of complexity is necessary to describe a UD-NCF with sufficient accuracy. Therefore, a simple approach is proposed with decoupled non-linear stiffnesses for each membrane deformation mode of superimposed shear, transverse tension and in-plane compression perpendicular to the CF rovings. The approach is parameterized with the experimental results of Schirmaier et al. [137] to facilitate a direct comparison to their simulation approach. The most relevant mechanisms are identified and the final requirements for a new membrane model are derived.

[6] Extracts from Section 5.1 have been previously published in [140], i.e. B. Schäfer, S. Haas, P. Boisse, L. Kärger. Investigation of the membrane behavior of UD-NCF in macroscopic forming simulations. *Key Engineering Materials*, 926:1413–1422, 2022. | Reproduced paragraphs and subsections are marked with [6].

5.1.1 Modeling approaches

Schirmaier et al.[6] In this section the key mechanisms of the membrane model relevant for this work are summarized. A comprehensive description can be found in [86, 137]. The model consists of a non-orthogonal elastic-plastic material behavior based on a custom linear strain measure ($\underline{\varepsilon}$) superimposed by an orthogonal compressive stress based on an introduced perpendicular strain component $\varepsilon_\perp$. The strain components are defined in an alternative configuration described by decomposition of the deformation gradient according to

$$\boldsymbol{F} = \boldsymbol{A} \cdot \boldsymbol{B}, \tag{5.1}$$

where $\boldsymbol{A}$ is the alternative stretch tensor and $\boldsymbol{B}$ the individual rotation tensor, cf. Figure 5.1. The material formulation uses the principle material strain ε_1 in fiber direction $\boldsymbol{t}_1^*$, the non-orthogonal transverse strain ε_2 contributing only under tensile loading in the stitching direction $\boldsymbol{t}_2^*$, the shear angle γ_{12} and the perpendicular strain $\varepsilon_\perp$ superimposed only for in-plane compression in $\boldsymbol{t}_\perp^*$ direction. This approach yields a co-rotational Cauchy stress $\boldsymbol{\sigma}$ consisting of a stress $\boldsymbol{\sigma}_{\mathrm{pm}}$ in the principal material directions and a stress $\boldsymbol{\sigma}_\perp$ perpendicular to the fiber direction according to

$$\boldsymbol{\sigma} = \boldsymbol{\sigma}_{\mathrm{pm}}(\varepsilon_1, \varepsilon_2, \gamma_{12}) + \boldsymbol{\sigma}_\perp(\varepsilon_\perp, \gamma_{12}) \quad \text{with} \quad \boldsymbol{\sigma}_\perp = \boldsymbol{0} \ \text{ for } \ \varepsilon_\perp > 0. \tag{5.2}$$

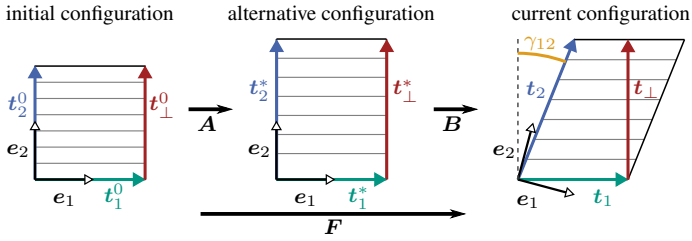

Figure 5.1: Schematic illustration of the principal material directions and intermediate configuration proposed for UD-NCF by Schirmaier et al. [86, 137].

[6] Reproduced subsection from [140], cf. footnote p. 136 for details.

Elastic-plastic behavior is introduced by splitting the total tensile strain ε_2 and shear angle γ_{12} into elastic $(\cdot)_{,\mathrm{e}}$ and hardening plastic parts $(\cdot)_{,\mathrm{p}}$. A yield surface $R_{2,\Gamma}(\varepsilon_{2,\mathrm{p}}, \gamma_{12})$ and a yield curve $R_{12,\Gamma}(\gamma_{12,\mathrm{p}})$ define the transition from a purely elastic to an elastic-plastic deformation, thus coupling the transverse deformation to the total shear angle γ_{12}. The yield surface $R_{2,\Gamma}(\varepsilon_{2,\mathrm{p}}, \gamma_{12})$ consists of a yield curve for low $(\bullet)^{,\mathrm{s}}$ and high $(\bullet)^{,\mathrm{e}}$ shear angles with continuous interpolation between them. The perpendicular compressive stress $\boldsymbol{\sigma}_\perp$ is additively superimposed as a 2D non-linear elastic material law depending on $\varepsilon_\perp$ and γ_{12}. Similar to the transverse yield surface, the perpendicular compression is parameterized for low $(\cdot)^{,\mathrm{a}}$ and high $(\cdot)^{,\mathrm{b}}$ shear angles with continuous interpolation between them. The final membrane model requires a total of over 40 material parameters (cf. Table A.4) and utilizes two different couplings between deformation modes.

Decoupled approach[6] A simple decoupled approach is utilized to investigate which mechanisms and couplings are necessary to model the membrane behavior of UD-NCF. A hyperelastic St.Venant-Kirchhoff material formulation is applied, thus intrinsically capturing rotations due to large shear, cf. Section 2.3.1. The material behavior is assumed to be non-linear elastic without any couplings

$$\boldsymbol{S} = \mathbb{C} : \boldsymbol{E} \overset{\text{2D-Voigt}}{\underset{\text{notation}}{=}} \begin{bmatrix} C_1 & 0 & 0 \\ 0 & C_2(E_{22}) & 0 \\ 0 & 0 & C_\gamma(E_{12}) \end{bmatrix} \begin{bmatrix} E_{11} \\ E_{22} \\ E_{12} \end{bmatrix}. \tag{5.3}$$

The co-rotational Cauchy stress is calculated by

$$\boldsymbol{\sigma}_{\mathrm{pm}} = J^{-1} \boldsymbol{U} \boldsymbol{S} \boldsymbol{U}, \tag{5.4}$$

where $\boldsymbol{U}$ the right stretch tensor of the polar decomposition $\boldsymbol{F} = \boldsymbol{R}\boldsymbol{U}$.

[6] Reproduced subsection from [140], cf. footnote p. 136 for details.

Additionally, a stress $\boldsymbol{\sigma}_\perp$ is superimposed based on the perpendicular strain $E_\perp$ introduced in Equation 4.2. This results in the perpendicular stress

$$\boldsymbol{\sigma}_\perp(E_\perp) = \boldsymbol{R}^\mathsf{T}\left(\boldsymbol{R}_\perp{}^\mathsf{T}\begin{bmatrix}0 & 0\\ 0 & \frac{C_\perp(E_\perp)}{\sqrt{C_{11}}}\end{bmatrix}\boldsymbol{R}_\perp\right)\boldsymbol{R} \tag{5.5}$$

with

$$\boldsymbol{R}_\perp = \frac{1}{\sqrt{C_{11}}}\begin{bmatrix}F_{11} & -F_{21}\\ F_{21} & F_{11}\end{bmatrix}. \tag{5.6}$$

The non-linear stiffnesses $(C_2, C_\gamma, C_\perp)$ are modeled as functions of their respective strains $(E_{22}, E_{12}, E_\perp)$ according to

$$C_i(E_i) = \begin{cases} C_i^\mathrm{i} & ,0 \le |E_i| \le E_i^\mathrm{i} \\ k_i^\mathrm{m}(|E_i - E_i^\mathrm{m}|)^{e_i^\mathrm{m}} + C_i^\mathrm{m} & ,E_i^\mathrm{i} < |E_i| \le E_i^\mathrm{m} \\ C_i^\mathrm{m} & ,E_i^\mathrm{m} < |E_i| \le E_i^\mathrm{l} \\ k_i^\mathrm{l}(|E_i - E_i^\mathrm{l}|)^{e_i^\mathrm{l}} + C_i^\mathrm{m} & ,E_i^\mathrm{l} < |E_i|, \end{cases} \tag{5.7}$$

with $k_i^\mathrm{m} = \frac{C_i^\mathrm{i} - C_i^\mathrm{m}}{E_i^\mathrm{i} - E_i^\mathrm{m}}$ and $i \in [2, \gamma, \perp]$, cf. Figure 5.2.

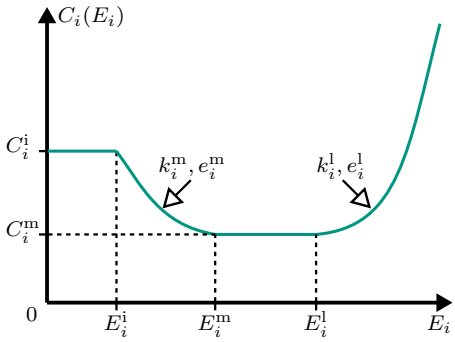

Figure 5.2: Modeling approach for the decoupled non-linear stiffness (adapted from [140]).

The formulation was chosen based on its high adaptability with relatively few, easy to physically interpret parameters and good results for woven fabrics [64]. It consists of an initial modulus C_i^{i}, which decreases to a middle modulus C_i^{m} over a strain range from E_i^{i} to E_i^{m} and increases again after E_i^{l}. This approach requires a total of seven material parameters for each stiffness. Additionally, to ensure disjunction between the perpendicular compressive and transverse tensile behavior in case of equal sign, the following auxiliary conditions are introduced:

$$C_{\perp}(E_{\perp}) = 0 \text{ for } E_{\perp} > 0 \quad \text{and} \quad C_2(E_{22}) = 0 \text{ for } E_{22} < 0. \tag{5.8}$$

In summary, the new membrane approach is based on similar superimposed stresses as the model proposed by Schirmaier et al. [137], but common strain measures (mostly quadratic instead of linear) are used, plasticity and couplings of deformation mechanisms are neglected and a simple approach for the non-linear stiffnesses is introduced. Nevertheless, for a more straightforward comparison of the results, the linear strain measures are additionally calculated and utilized during the evaluation.

5.1.2 Numerical studies

The presented decoupled membrane approach is implemented as a subroutine for user-defined material behavior (VUMAT) in ABAQUS/Explicit and compared to the existing approach of Schirmaier et al [86, 137] in two numerical studies. First, their behavior on coupon level is discussed based on their parameterization with off-axis tension tests. Second, they are applied to hemisphere forming tests to investigate the effects on part level.

5.1.2.1 Coupon tests

The UD-NCF material investigated by Schirmaier et al. [86, 110, 137] was very similar to the UD-NCF of this work (cf. Section 4.1), except for a more loose

stitching combining a tricot and chain pattern. OATs with similar experimental results to the tests described in Section 4.2 but lower forces due to the different stitching pattern are used to parameterize the membrane model.

The OATs were conducted at two velocities of 20 and 100 mm/min, but no rate-dependent behavior was observed. The macroscopic strains were only measured during the tests with 20 mm/min with a similar method as described in Section 4.2. Unfortunately, during the strain measurement of the 30°-OATs, the CF rovings in the top right and bottom left edges of the specimens were slipping out of the clamping area. This resulted in significantly lower forces and presumably also smaller strains. The utilized simulation models with their respective boundary conditions are shown in Figure 5.3. Two sets of boundary conditions (BC) are used: BC 1 with all nodes in the clamping region fixed for simulation of the 30°-OATs without slipping CF; BC 2 with three free nodes in the clamping region to emulate the slipping of CF rovings during the 30°-OATs with strain measurement [137]. The numerical results of Schirmaier et al. [137] are compared to two parameterizations of the decoupled approach in the following.[6]

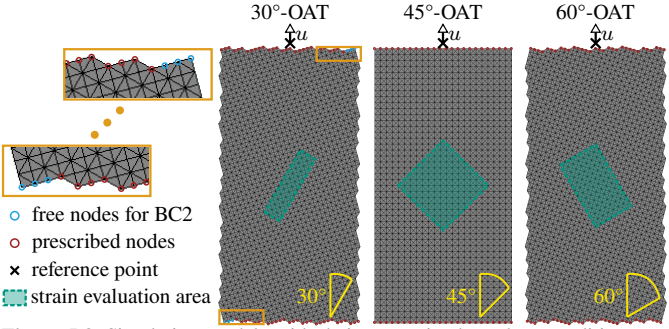

Figure 5.3: Simulation models with their respective boundary conditions to simulate slip in the clamping area during the 30°-OAT (boundary condition BC 2) and highlighted areas (green) for an averaging of the strain components (adapted from [140]).

6 Reproduced paragraph from [140], cf. footnote p. 136 for details.

Schirmaier et al. The modeling approach is referred to as Sch17 in the following. The material parameters for their modeling approach were inversely identified based on a best-fit to the forces and strains of the three OATs simultaneously. The resulting forces are shown in Figure 5.4. An acceptable overall approximation is achieved in particular for the 30°-OAT with both boundary conditions as well as the 45°-OAT. The initial steep force increase in the 60°-

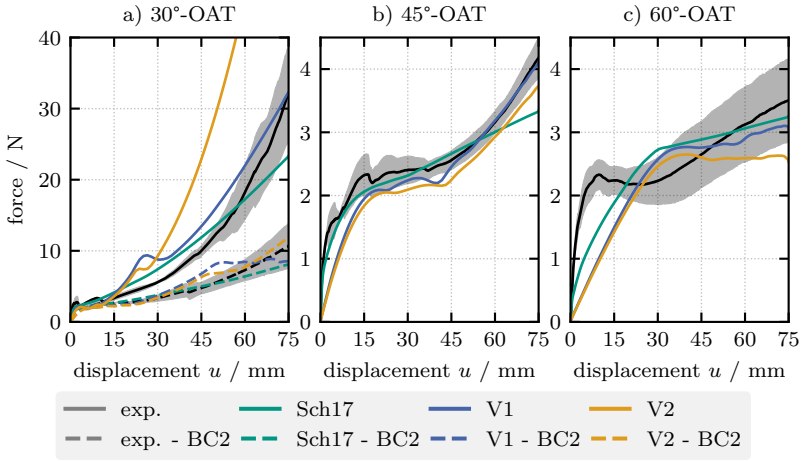

Figure 5.4: Experimental and simulative force-displacement-curves for different fiber orientations (a) 30°, (b) 45° and (c) 60° (exp. curves based on [86], figure adapted from [140]).

OAT is not described by the model and the forces for large displacements are slightly underestimated for all tests. The global strain contours are shown in Figure 5.5 b. The predicted shear γ_{12} deformation behavior in the main and secondary deformation zones of each test is in good agreement with the experiments. However, the transverse tensile strains ε_{22} are much more homogeneous in the simulation model compared to the experimental observations, which is a general limitation of the macroscopic approach that cannot describe the complex mesoscopic deformation of the stitching. Additionally, the perpendicular compression $\varepsilon_{\perp}$ in the main deformation zone (MDZ) of the 45°-OAT is

underestimated by the simulation and completely missing in the center of the 60°-OAT. The observations for the global strains are also reflected in the quantitative comparison of the averaged strain in the MDZ in Figure 5.6. Especially γ_{12} and $\varepsilon_\perp$ are underestimated by the simulation in the 45°- and 60°-OAT, while the strains in the 30°-OAT are predicted well.

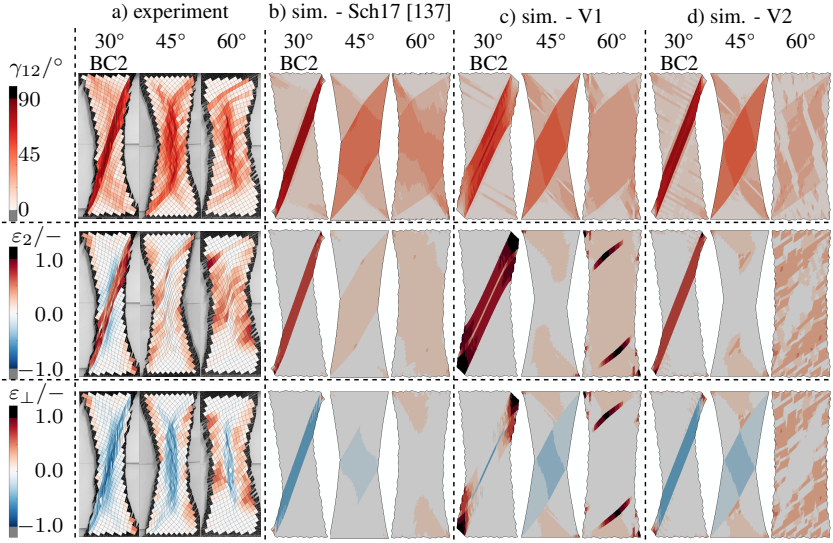

Figure 5.5: Strain distributions of OATs with different orientations from (a) the experimental measurements (based on [137]), (b) the macroscopic model proposed by Schirmaier et al. [137] and (c-d) different parameterizations of the new membrane model (adapted from [140]).

Decoupled approach Achieving an overall fit to all OATs with the decoupled membrane model is difficult, because of the different multiaxial strain conditions induced by the three bias angles. Therefore, only the results for two sets of parameters (V1 and V2) are discussed in the following to highlight some of the key findings relevant to this work. Both parameter sets utilize a perpendicular compressive locking to prevent a collapse of highly sheared elements,

but differ in their shear and transverse tensile stiffness. Additional information on the parameterization is detailed in [140] but not repeated here, as it will be described in more detail for the final membrane approach in Section 5.2.6.

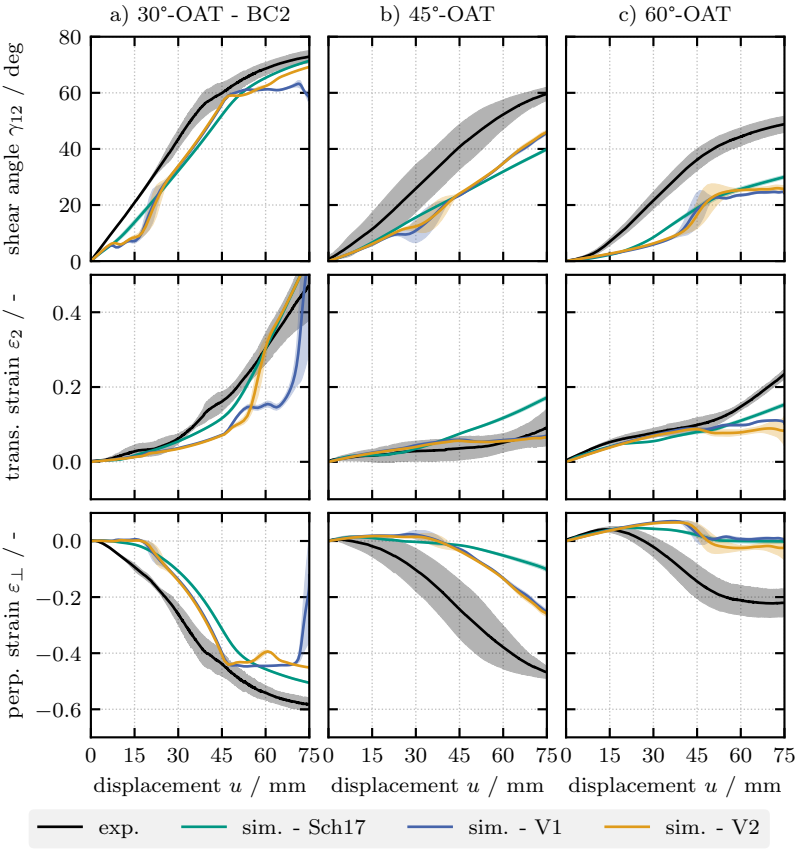

Figure 5.6: Experimental and simulative strains in the specimen's center for different fiber orientations (a) 30° with slipping CF rovings in the clamping region - BC2, (b) 45° and (c) 60° (exp. curves based on [86], figure adapted from [140]).

Parameter set V1 was determined with the objective to achieve a good agreement for the force-displacement relation of the 30°-OAT without slipping rovings (BC 1) as well as the 45°- and 60°-OAT, cf. Figure 5.4). The initial steep force increase during the 45°- and 60°-OAT was slightly underestimated compared to Sch17, but the steeper force increase during the 45°-OAT at a displacement $u > 40$ mm was better predicted by the decoupled model. However, the predicted force for the 30°-OAT was much higher compared to the experiments in the middle of the test. A local maximum is observed for a displacement between $23 - 32$ mm, which is caused by a steep decrease in the C_2-stiffness. This decrease is necessary because a high initial stiffness C_2^{i} is required in the 45°- and 60°-OATs, but a significantly lower middle modulus C_2^{m} is required to not severely overestimate the forces in the 30°-OAT.[6]

The pure consideration of the force-displacement relation during parameterization leads to some problems with highly localized deformations when analyzing the strain distributions in Figure 5.5 c. Strongly localized tensile strains ε_2 occur at the edge of the MDZ during the 60°-OAT and a general non-physical deformation of the central area is observed in the 30°-OAT with BC2. The strain distributions of γ_{12} and $\varepsilon_\perp$ for the 45°-OAT tests seem comparable to the results from Sch17 and the experimental results. The averaged strains in the MDZ (cf. Figure 5.6) are underestimated in the 30°- and 60°- OAT compared to the results from Sch17, but closer to the experimental results for larger displacements during the 45°-OAT. A better overall agreement with the results of the 45°-OAT is achieved, because the deformation behavior is shear-dominated and only smaller tensile strains occur compared to the 30°- and 60°-OAT.[6]

Parameter set V2 was adapted from parameter set V1 with the objective of alleviating the localized deformation during the 60°-OAT and 30°-BC2-OAT. The strain range over which the tensile stiffness C_2 decreases was shortened (lower E_2^{m}) and the middle modulus C_2^{m} increased, while the shear stiffness

[6] Reproduced paragraph from [140], cf. footnote p. 136 for details.

C_γ was only slightly reduced. The perpendicular compressive stiffness was not adjusted compared to parameter set V1.[6]

The adaptations resulted in a similar overall fit to the forces in the 45°-OAT as for set V1 and only a small underestimation of the forces for higher displacements (> 45 mm) in the 60°-OAT, cf. Figure 5.4. The predicted forces in the 30°-OAT are close to the experimental results for BC2, but significantly overestimated compared to the experimental results for clamped CF rovings with BC1. The localized high tensile deformations ε_2 in the 30°- and 60°-OAT are prevented, cf. Figure 5.5. Overall, the strains during the 30°- and 45°-OAT are similar to the experimental as well as simulative results of Sch17. However, the strains in the 60°-OAT show some irregular patterns. They are significantly different from the simulative results of Sch17, but closer to the experimental results in some regions. The shear angle γ_{12} is more localized in a delimited area in the specimen's center and positive tensile ε_2 as well as perpendicular $\varepsilon_\perp$ strains are located around the MDZ. This is similar to the experimental distribution in the lateral areas, but overestimated in the areas near the clamping. The averaged strains in the MDZ show an acceptable agreement with the results of Sch17, cf. Figure 5.6.[6]

In the next Section, both parameterizations of the decoupled approach as well as the model of Schirmaier et al [137] are applied to a hemisphere forming test to investigate the behavior on part level before a conclusive comparison.

5.1.2.2 Forming tests

Forming simulations of single UD-NCF ply with an initial fiber orientation of 0° are performed in ABAQUS/Explicit. The tools are modeled as discrete rigid surfaces based on the dimensions shown in Figure 4.33. The tool-ply contact is modeled via the built-in general contact algorithm, using a constant friction coefficient of $\mu^{\text{tool-ply}} = 0.3$. Bending behavior is described with the

[6] Reproduced paragraph from [140], cf. footnote p. 136 for details.

approach proposed by Schirmaier et al. [137]. It is modeled linear elastic within a non-orthogonal material frame to account for fiber rotation and the strongly anisotropic bending stiffness of UD-NCF. It is implemented in a VUGENS subroutine for a user-defined integration scheme over the thickness of S3 shell elements, which are superposed to the membrane elements via shared nodes for a membrane-bending decoupling. The results of the forming simulations are shown in Figure 5.7. Despite the different architecture of the UD-NCF, similar qualitative behavior to the results presented in Section 4.6 are expected because of similar experimental tests presented by Schirmaier et al. [110].

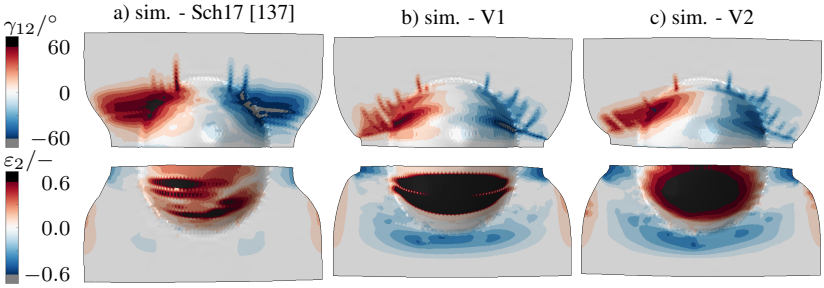

Figure 5.7: Strain distributions of OATs with different orientations from (a) the experimental measurements (based on [137]), (b) the macroscopic model proposed by Schirmaier et al. [137] and (c-d) different parameterizations of the new membrane model.

The outer contour of all modeling approaches is similar and indicates the general suitability to describe the strongly asymmetrical behavior of UD-NCF. However, the shear angle distribution of the decoupled approach is notably different from the results of Schirmaier et al [137] with strongly localized shear bands for both parameter sets. These shear bands occur only sporadically in the Sch17-model and result from a fundamental limitation of macroscopic approaches: The macroscopic approach cannot distinguish between shear deformation parallel to the CF rovings (21-shear) or transverse to the CF-rovings (12-shear), which will be further discussed in Section 5.4.2. However, the prevalence of these strain localizations indicates the instability of the decoupled approach during forming. This is similar to the observations made in the coupon tests. The instabilities are more noticeable for parameter set V1 and can also be seen in

the excessive tensile strains ε_2 in the hemisphere center. The tensile strains for parameter set V2 are also very large but more homogeneous. These instabilities presumably result from the chosen stiffness-based approach, cf. Figure 5.2. The stiffnesses are reduced over a small strain range from C_i^{i} to C_i^{m}, resulting in not monotonically increasing stress curves with local minima of the individual components. This is exemplified for both parameter sets and compared to Sch17 in Figure A.10. The local minima lead to instabilities and provoke localizations of excessive strains.

Spurious tensile strains also occur in the model of Sch17, indicated by significantly larger ε_2 in individual elements compared to their surrounding area, cf. Figure 5.7 a. This also indicates some instability for planar blankholders, which were never applied in studies by Schirmaier et al. [137]. An investigation of the origin of these slight instabilities is difficult due to the large number of parameters and complex constitutive equations.

5.1.3 Summary and requirements for the development of a new approach

Summary The modeling of the membrane behavior of UD-NCF during OATs requires the consideration of different ratios of superimposed strains. The comprehensive approach by Schirmaier et al. [86, 137] utilizes complex elastic-plastic constitutive equations to describe this behavior. A good agreement with the general deformation behavior is observed during coupon and forming tests. However, the shear angle and perpendicular compression in the MDZ of the 45°- and 60°-OATs are still severely underestimated. Additionally, some spurious deformations are observed during hemisphere forming tests with planar blankholders.

The results of the decoupled model suggest that a less complex modeling approach is possible to describe the behavior. Similar results were partially achieved on coupon level despite significant simplifications. Additionally, the strongly asymmetrical behavior during hemisphere forming was also predicted

in principle. A disadvantage due to the purely elastic approach compared to the elastic-plastic approach of the Sch17-model cannot be determined, which is similar to the results found by Ghafour et al. [292]. However, several fundamental shortcomings of a decoupled model are evident from the investigations of the OATs and forming simulations. First, the stiffness-based approach is susceptible to numerical instabilities resulting in localized deformations or excessive tensile strains ε_2. This was observed during parameterization in particular for parameter sets with a high ratio of shear to transverse tensile stiffness ($C_\gamma/C_2 > 1$). During forming, these instabilities manifest in a large number of local shear bands. Second, an uncoupled transverse tensile behavior is not sufficient to achieve a satisfactory overall fit for different OATs. The modeling of high tensile strains due to roving slippage in the 30°-OAT requires a smaller C_2 with a steep decrease compared to the 45°- and 60°-OAT. As a result, C_2 is too small and excessive tensile strains occur during forming.

Requirements for the development of a new approach On the basis of the preliminary investigation of the state of research, the following requirements for the development of a new membrane approach for UD-NCF are proposed:

- Membrane modeling needs to account for large superimposed shear, transverse tensile and in-plane perpendicular compressive strains
- Coupling of the transverse tensile behavior with the perpendicular roving compaction to model large tensile strains due to roving slippage
- Complexity of the individual constitutive equations similar to the proposed approach in Equation 5.7 of the preliminary investigation
- Strictly monotonically increasing constitutive equations for the stresses to reduce numerical instabilities
- Decoupled description of shear and in-plane perpendicular compression
- Perpendicular compressive locking to prevent a collapse of highly sheared elements

5.2 Intra-ply modeling - Membrane behavior[5]

Modeling the membrane behavior of UD-NCF is challenging as evident from the specific characteristics derived in Section 4.7 and the preliminary investigation in Section 5.1. In this work, a new hyperelastic macroscopic forming model for UD-NCF is proposed. A strain energy density is introduced instead of non-linear stiffnesses. The strain energy density is additively decomposed into individual contributions that are associated with different deformation modes, which is often assumed for engineering textiles [64, 106, 239, 244, 246, 247]. For UD-NCF these are tension in fiber direction, transverse tension, shear deformation and in-plane compression perpendicular to the rovings. A coupling between transverse tension and perpendicular compression is proposed to model large roving slippage if the rovings are under compression. A new generalized approach with relatively few material parameters for the strain energy density and possible couplings between the deformation modes is used. The objective is to minimize the complexity of the model and thus facilitate its application to other materials. The model is parameterized using the forces and strains measured in different multiaxial deformation states obtained in OATs.

5.2.1 Fundamentals of hyperelasticity adopted for UD-NCF[5]

Hyperelastic approaches are defined by a total strain energy density function W_{tot} as a potential for the resulting stress [244]

$$\boldsymbol{S} = 2\frac{\partial W_{\mathrm{tot}}(\boldsymbol{C})}{\partial \boldsymbol{C}}, \tag{5.9}$$

[5] Extracts from Section 5.2 have been previously published in [180], i.e. B. Schäfer, D. Dörr, R. Zheng, N. Naouar, L. Kärger. A hyperelastic approach for modeling the membrane behavior in finite element forming simulation of unidirectional non-crimp fabrics (UD-NCF). *[submitted for review]*. | Sections 5.2.1-5.2.4 reproduce Sections 3.1-3.4 of [180]; Section 5.2.6 reproduces excerpts from Sections 3.5 & 4 of [180]; Section 5.2.7 reproduces excerpts from Section 6 of [180].

where $\boldsymbol{S}$ is the second Piola-Kirchhoff stress tensor and $\boldsymbol{C}$ is the right Cauchy-Green deformation tensor. To account for anisotropic behavior, W_{tot} can alternatively be expressed by a set of directional pseudo-invariants I_i of the strain by

$$\boldsymbol{S} = 2\sum_{i}^{N} \frac{\partial W_{\mathrm{tot}}}{\partial I_i} \frac{\partial I_i}{\partial \boldsymbol{C}}. \tag{5.10}$$

Thereby, physically interpretable pseudo-invariants are commonly chosen based on the principal orientations $\boldsymbol{a}_0$ and $\boldsymbol{b}_0$, cf. Figure 5.8 a, to relate them to the observed deformation modes of the material. The directional pseudo-invariants [245] are introduced:

$$I_4 = \boldsymbol{a}_0 \cdot \boldsymbol{C} \cdot \boldsymbol{a}_0 \qquad \text{with} \quad I_4^0 = 1, \tag{5.11}$$

$$I_6 = \boldsymbol{a}_0 \cdot \boldsymbol{C} \cdot \boldsymbol{b}_0 \qquad \text{with} \quad I_6^0 = 0, \tag{5.12}$$

$$I_8 = \boldsymbol{b}_0 \cdot \boldsymbol{C} \cdot \boldsymbol{b}_0 \qquad \text{with} \quad I_8^0 = 1, \tag{5.13}$$

$$I_{10} = \arccos\left(\boldsymbol{a}_0 \cdot \boldsymbol{b}_0\right) - \arccos\left(\frac{I_6}{\sqrt{I_4 I_8}}\right) \qquad \text{with} \quad I_{10}^0 = 0, \tag{5.14}$$

$$I_{11} = \sqrt{I_8}\sin\left(\arccos\left(\frac{I_6}{\sqrt{I_4 I_8}}\right)\right) \qquad \text{with} \quad I_{11}^0 = 1, \tag{5.15}$$

where I_4 and I_8 are the quadratic stretches along $\boldsymbol{a}_0$ and $\boldsymbol{b}_0$ respectively, I_6 is the shear strain, I_{10} is the shear angle γ_{12} and I_{11} is the stretch in the derived direction $\mathbf{b}^{\perp}$ which is the component of $\mathbf{b}$ that remains perpendicular to the carbon fiber direction $\mathbf{a}$. For UD-NCF these are related to tension in fiber direction (I_4), transverse tension (I_8), shear deformation (I_6) and in-plane compression perpendicular to the fiber rovings (I_{11}). The values of the invariants in the undeformed configuration are denoted as I_i^0. The shear strain (I_6) is chosen instead of the shear angle (I_{10}), to ensure independence of the shear deformation from the stitching strains, cf. Equation 5.14.

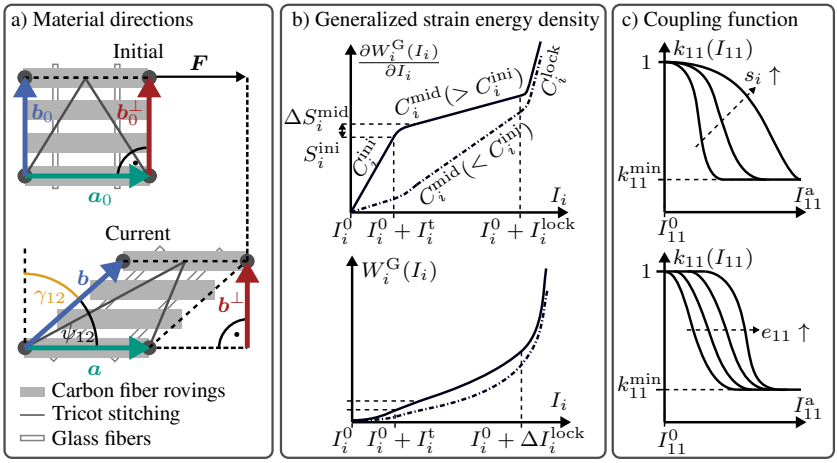

	initial	pure shear	simple shear	mixed-mode 1	mixed-mode 2	mixed-mode 3
I_4^0	$I_4^0 = 1$	$= 1$	$= 1$	$= 1$	$= 1$	$= 1$
I_6^0	$I_6^0 = 0$	> 0	> 0	> 0	> 0	> 0
I_8^0	$I_8^0 = 1$	$= 1$	> 1	< 1	> 1	> 1
I_{11}^0	$I_{11}^0 = 1$	< 1	$= 1$	< 1	< 1	> 1

Figure 5.8: a) Schematic illustration of the orientation of pseudo-invariants in the initial and current configuration; b) Generalized hyperelastic energy and its derivative; c) Coupling functions with schematic illustrations of its parameters influence; d) Schematic representation of different deformation modes (adapted from [102]) and the corresponding resulting pseudo-invariants. [180]

Combining Equation 2.9 with the invariants (Equation 5.11-5.15) and their partial derivatives (Appendix A.2.3) yields the expression

$$\boldsymbol{S} = 2\left(\frac{\partial W_{\text{tot}}}{\partial I_4}\frac{\partial I_4}{\partial \boldsymbol{C}} + \frac{\partial W_{\text{tot}}}{\partial I_6}\frac{\partial I_6}{\partial \boldsymbol{C}} + \frac{\partial W_{\text{tot}}}{\partial I_8 4}\frac{\partial I_8}{\partial \boldsymbol{C}} + \frac{\partial W_{\text{tot}}}{\partial I_{11}}\frac{\partial I_{11}}{\partial \boldsymbol{C}}\right) \tag{5.16}$$

$$= 2\left(\frac{\partial W_{\text{tot}}}{\partial I_4}\frac{\partial I_4}{\partial \boldsymbol{C}} + \frac{\partial W_{\text{tot}}}{\partial I_6}\frac{\partial I_6}{\partial \boldsymbol{C}} + \frac{\partial W_{\text{tot}}}{\partial I_8}\frac{\partial I_8}{\partial \boldsymbol{C}}\right) \tag{5.17}$$

$$+ 2\left(\frac{\partial W_{\text{tot}}}{\partial I_{11}}\left(\frac{\partial I_{11}}{\partial I_4}\frac{\partial I_4}{\partial \boldsymbol{C}} + \frac{\partial I_{11}}{\partial I_6}\frac{\partial I_6}{\partial \boldsymbol{C}} + \frac{\partial I_{11}}{\partial I_8}\frac{\partial I_8}{\partial \boldsymbol{C}}\right)\right)$$

$$
\begin{aligned}
&= 2\left(\frac{\partial W_{\mathrm{tot}}}{\partial I_4}\boldsymbol{a}_0 \otimes \boldsymbol{a}_0 + \frac{\partial W_{\mathrm{tot}}}{\partial I_8}\boldsymbol{b}_0 \otimes \boldsymbol{b}_0\right) \\
&+ \frac{\partial W_{\mathrm{tot}}}{\partial I_6}\left(\boldsymbol{a}_0 \otimes \boldsymbol{b}_0 + \boldsymbol{b}_0 \otimes \boldsymbol{a}_0\right) \\
&+ \frac{2}{\sqrt{I_4 I_8 - I_6^2}}\frac{\partial W_{\mathrm{tot}}}{\partial I_{11}}\left(\frac{I_6^2}{2I_4^{3/2}}\boldsymbol{a}_0 \otimes \boldsymbol{a}_0 + \frac{-I_6}{\sqrt{I_4}}\boldsymbol{a}_0 \otimes \boldsymbol{b}_0 + \frac{\sqrt{I_4}}{2}\boldsymbol{b}_0 \otimes \boldsymbol{b}_0\right).
\end{aligned}
\tag{5.18}
$$

The next step is the definition of the total strain energy density function W_{tot} based on the observed deformation behavior of the UD-NCF.

5.2.2 General assumptions[5]

UD-NCFs deform under large shear strains superimposed with transverse tensile deformation and in-plane compression perpendicular to the carbon fiber rovings. This behavior was experimentally observed during the characterization of the membrane behavior described in Section 4.2 as well as similar studies [109, 137, 138] and during the forming tests described in Section 4.6 as well as similar studies [128, 137, 230]. Therefore, UD-NCF undergoes not only pure or simple shear, but also mixed deformation modes with different amplitudes of multiaxial strains, cf. Figure 5.8 d.

The deformation of individual components is assumed to be directly related to the proposed invariants:

- Roving slippage parallel to the fiber direction results in shear I_6 as well as increased transverse tensile deformation I_8, as demonstrated during simple shear or the mixed-modes 2 & 3 in Figure 5.8 d.
- Transverse tensile deformation $I_8 > I_8^0 = 1$ additionally indicates tension in the stitching pattern (initially aligned with $\boldsymbol{b}_0$), assuming limited slippage between stitching and rovings.

[5] Reproduced section from [180], cf. footnote p. 150 for details.

- It is assumed that the stitching only bears tensile stresses $I_8 > I_8^0$, while in-plane compaction takes place via the rovings and is perpendicularly oriented to them $I_{11} < I_{11}^0$.
- The perpendicular invariant I_{11} quantifies the distance between fiber rovings, indicating their compression $I_{11} < I_{11}^0$ as well as their widening or gap formation $I_{11} > I_{11}^0$.

In the preliminary study in Section 5.1 it was demonstrated that a decoupled consideration of the deformation modes is not sufficient to model the membrane behavior during OATs (to be discussed further in Section 5.2.6). As concluded in Section 4.2, significant roving slippage (high I_6 and I_8) occurs in areas of high roving compression (mixed-mode 2, cf. Fig. 5.8 d), compared to cases where tensioning of the stitching limits the shear deformation (mixed-mode 3, cf. Fig. 5.8 d). A coupling between the transverse tensile (I_8) and perpendicular compressive behavior (I_{11}) is introduced to model this interaction.

Based on the above assumption, it is proposed that the total strain energy density W_{tot} can be decomposed additively into tension of the rovings $W_4(I_4)$, shear deformation $W_6(I_6)$, transverse in-plane tension coupled to perpendicular compression $W_8(I_8, I_{11})$ and in-plane compaction perpendicular to the fiber rovings $W_{11}(I_{11})$ according to:

$$W_{\mathrm{tot}}(I_4, I_6, I_8, I_{11}) = W_4(I_4) + W_6(I_6) + W_8(I_8, I_{11}) + W_{11}(I_{11}) \quad (5.19)$$

The constitutive equations for the individual energy contributions and coupling are formulated in a parameterized way in the following, to simplify the parameterization process.

5.2.3 Generalized strain energy density function[5]

Piecewise functions [64, 140] or polynomial functions [244, 247, 295] are usually chosen to define the strain energy density and subsequently stress-strain relation. Polynomial functions are highly adaptable and commonly fitted to analytical models that directly derive the stress-strain relation from experimental tests. Piecewise functions prescribe a characteristic curve, whereby the parameters have a localized impact on the trend and are thus often easier to interpret physically. Since the typical deformation modes of UD-NCF consist of superimposed strains, cf. Section 5.2.2, the respective contributions to the total energy cannot necessarily be identified individually during the characterization. Therefore, previous studies [137, 140] have shown that an inverse parameterization process is required to simultaneously consider the force- and strain-displacement results of different characterization tests.

Based on the above assumptions, a generalized, piecewise function for the derivative of the strain energy density is proposed as basis for the individual contributions in Equation 5.19

$$\frac{\partial W_i^{\mathrm{G}}(I_i)}{\partial I_i} = \begin{cases} C_i^{\mathrm{ini}} I_i^{\mathrm{a}} & ,[0 \leq I_i^{\mathrm{a}} < I_i^{\mathrm{t}}] \\ S_i^{\mathrm{ini}} + \left(C_i^{\mathrm{mid}}(I_i^{\mathrm{a}} - I_i^{\mathrm{t}}) + \Delta S_i^{\mathrm{mid}}\right) \\ \quad \cdot \left(1 - e^{-c_i^{\mathrm{t}}(I_i^{\mathrm{a}} - I_i^{\mathrm{t}})}\right) & ,[I_i^{\mathrm{t}} \leq I_i^{\mathrm{a}} < I_i^{\mathrm{lock}}] \\ S_i^{\mathrm{ini}} + \left(C_i^{\mathrm{mid}}(I_i^{\mathrm{a}} - I_i^{\mathrm{t}}) + \Delta S_i^{\mathrm{mid}}\right) \\ \quad \cdot \left(1 - e^{-c_i^{\mathrm{t}}(I_i^{\mathrm{a}} - I_i^{\mathrm{t}})}\right) & ,[I_i^{\mathrm{lock}} \leq I_i^{\mathrm{a}}] \\ \quad + C_i^{\mathrm{lock}}(I_i^{\mathrm{a}} - I_i^{\mathrm{lock}})^2 \end{cases} \tag{5.20}$$

with $I_i^{\mathrm{a}} = |I_i - I_i^0|$, $I_i^{\mathrm{t}} = \frac{S_i^{\mathrm{ini}}}{C_i^{\mathrm{ini}}}$ and $c_i^{\mathrm{t}} = \frac{C_i^{\mathrm{ini}}}{\Delta S_i^{\mathrm{mid}}}$. The corresponding generalized strain energy density $W_i^{\mathrm{G}}(I_i)$ is listed in Appendix A.2.4 and the generalized curves are shown in Figure 5.8 b. The formulation was chosen based on its high adaptability with six, easy to physically interpret parameters. It consists of

[5] Reproduced section from [180], cf. footnote p. 150 for details.

an initial stress limit S_i^{ini} and initial modulus C_i^{ini}. The modulus increases or decreases to a middle modulus C_i^{mid} over a stress range $\Delta S_i^{\mathrm{mid}}$ and increases again with C_i^{lock} after I_i^{lock}. The transition invariant I_i^{t} and exponent c_i^{t} are determined to achieve an overall $\mathcal{C}^1$-smooth function.

This generalized approach can represent the typical three-stage response ($C_i^{\mathrm{mid}} < C_i^{\mathrm{ini}}$) during shear or elongation [64, 244, 295] as well as the exponential character ($C_i^{\mathrm{mid}} > C_i^{\mathrm{ini}}$) typically obtained during compaction of fabrics [137, 167], cf. Figure 5.8 b. The approach is based on the absolute invariant I_i^{a} due to the exponential function, and the sign for tension and shear must be considered separately by

$$W_4(I_4) = \operatorname{sgn}\left(I_4 - I_4^0\right) \cdot W_4^{\mathrm{G}}(I_4) \tag{5.21}$$

and

$$W_6(I_6) = \operatorname{sgn}\left(I_6 - I_6^0\right) \cdot W_6^{\mathrm{G}}(I_6). \tag{5.22}$$

The strain energy contribution due to the perpendicular invariant I_{11} only accounts for in-plane perpendicular compression

$$W_{11}(I_{11}) = \begin{cases} -W_{11}^{\mathrm{G}}(I_{11}) & ,[I_{11} < I_{11}^0] \\ 0 & ,[I_{11}^0 \leq I_{11}]. \end{cases} \tag{5.23}$$

The transverse strain energy density contribution $W_8(I_8, I_{11})$ is detailed separately in the following section due to the coupling to the perpendicular invariant I_{11}.

5.2.4 Transverse tension - in-plane compression coupling[5]

In-plane compression in the perpendicular direction ($I_{11} < I_{11}^0$) facilitates large roving slippage (large I_8), as concluded in Section 4.2. A coupling function is introduced to model this behavior:

$$k_{11}(I_{11}) = \begin{cases} \left(1 - k_{11}^{\min}\right) e^{-s_{11}(I_{11}^{\mathrm{a}})^{e_{11}}} + k_{11}^{\min} & ,[I_{11} \leq I_{11}^0] \\ 1 & ,[I_{11}^0 \leq I_{11}]. \end{cases} \tag{5.24}$$

and the impact of its parameters on the characteristic trend is shown in Figure 5.8 c. The threshold slippage–compression-parameter $k_{11}^{\min}$ is only allowed to attain values between 1 and 0, representing a maximum reduction of the strain energy density W_8 for large in-plane compression. The coefficient s_{11} characterizes the intensity of the coupling and the exponent e_{11} controls the onset of the coupling. The transverse strain energy density contribution is given by

$$W_8(I_8, I_{11}) = \begin{cases} 0 & ,[I_8 < I_8^0] \\ k_{11}(I_{11}) \cdot W_8^{\mathrm{G}}(I_8) & ,[I_8^0 \leq I_8]. \end{cases} \tag{5.25}$$

A multiplicative coupling was chosen to take advantage of the generalized strain energy density function (Equation 5.20) and simplify the transferability to new materials or couplings in the future.

5.2.5 Total membrane behavior

The total membrane behavior is obtained by combining the general formulation of $\boldsymbol{S}$ in Equation 5.18 with the partial derivatives of the pseudo invariants in Appendix A.2.3, the assumed decomposition of the total strain energy density

[5] Reproduced section from [180], cf. footnote p. 150 for details.

in Equation 5.19 and the generalized energy function from Equation 5.20 as well as the coupling function from Equation 5.24

$$\begin{aligned}\boldsymbol{S} &= 2\left(\frac{\partial W_4^{\mathrm{G}}(I_4)}{\partial I_4}\frac{\partial I_4}{\partial \boldsymbol{C}} + \frac{\partial W_6^{\mathrm{G}}(I_6)}{\partial I_6}\frac{\partial I_6}{\partial \boldsymbol{C}} + k_{11}(I_{11})\frac{\partial W_8^{\mathrm{G}}(I_8)}{\partial I_8}\frac{\partial I_8}{\partial \boldsymbol{C}}\right) \\ &\quad + 2\left(\frac{\partial W_{11}^{\mathrm{G}}(I_{11})}{\partial I_{11}} + \frac{\partial k_{11}(I_{11})}{\partial I_{11}}\cdot W_8^{\mathrm{G}}(I_8)\right) \\ &\quad \cdot\left(\frac{\partial I_{11}}{\partial I_4}\frac{\partial I_4}{\partial \boldsymbol{C}} + \frac{\partial I_{11}}{\partial I_6}\frac{\partial I_6}{\partial \boldsymbol{C}} + \frac{\partial I_{11}}{\partial I_8}\frac{\partial I_8}{\partial \boldsymbol{C}}\right). \qquad (5.26) \\ &= 2\left(\frac{\partial W_4^{\mathrm{G}}(I_4)}{\partial I_4}\boldsymbol{a}_0\otimes\boldsymbol{a}_0 + k_{11}(I_{11})\frac{\partial W_8^{\mathrm{G}}(I_8)}{\partial I_8}\boldsymbol{b}_0\otimes\boldsymbol{b}_0\right) \\ &\quad + \frac{\partial W_6^{\mathrm{G}}(I_6)}{\partial I_6}\left(\boldsymbol{a}_0\otimes\boldsymbol{b}_0 + \boldsymbol{b}_0\otimes\boldsymbol{a}_0\right) \\ &\quad + \frac{2}{\sqrt{I_4 I_8 - I_6^2}}\left(\frac{\partial W_{11}^{\mathrm{G}}(I_{11})}{\partial I_{11}} + \frac{\partial k_{11}(I_{11})}{\partial I_{11}}\cdot W_8^{\mathrm{G}}(I_8)\right) \\ &\quad \cdot\left(\frac{I_6^2}{2I_4^{3/2}}\boldsymbol{a}_0\otimes\boldsymbol{a}_0 + \frac{-I_6}{\sqrt{I_4}}\boldsymbol{a}_0\otimes\boldsymbol{b}_0 + \frac{\sqrt{I_4}}{2}\boldsymbol{b}_0\otimes\boldsymbol{b}_0\right). \qquad (5.27)\end{aligned}$$

A major advantage of this formulation is that $W_i^{\mathrm{G}}(I_i)$ and $k_i(I_i)$ can be changed modularly if more complex constitutive equations for the deformation modes or couplings are required for other materials.

5.2.6 Parameterisation of the membrane model with off-axis tension tests[5]

The proposed hyperelastic model is implemented by means of a user-defined material behavior (VUMAT) and applied to M3D3 membrane elements with their edges aligned in fiber direction to avoid numerical intra-ply locking [287, 288]. The tensile modulus C_4^{ini} is assumed to be a sufficiently high constant value because no significant tensile strains were measured experimentally, as an alternative to a numerically complex inextensibility condition. The identification of

[5] Reproduced section from [180], cf. footnote p. 150 for details.

the remaining material parameters is performed manually, by gradually introducing the parameters impacting the initial (C_i^{ini}, S_i^{ini}), middle ($\Delta S_i^{\mathrm{mid}}$, C_i^{mid}) and locking sections (I_i^{lock}, C_i^{lock}) of the generalized approach as well as the coupling function (k_{11}^{min}, s_{11}, e_{11}), cf. Figure 5.8 b and c. The results of the off-axis-tension tests (OATs) with three different bias angles (30°, 45° and 60°) described in Section 4.2 are used to parameterize the membrane behavior. The utilized simulation models are shown in Figure 5.9.

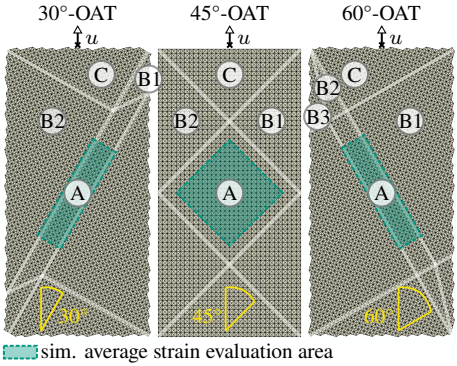

Figure 5.9: Simulation models for the parameterization with off-axis-tension tests (OATs) and highlighted areas (green) for an averaging of the strain components (adapted from [180]).

Observations during the parameterization process Parameter studies were performed, aiming at the best overall agreement of forces and local strains in the MDZ (cf. Figure 5.12) as well as global strains (cf. Figure 5.11) for the three OATs simultaneously. Therefore, equivalent strain measures to the pseudo-invariants were calculated by $E_{22} = I_8 - I_8^0$, $\gamma = I_{10}$ and $E_\perp = I_{11} - I_{11}^0$. Each energy contribution influences the resulting forces and strains with varying intensity during different displacement ranges of the different OATs. In general, W_{11} mainly influences the overall relative necking of the specimens and the compressive strain distribution, while only slightly impacting the forces. Transverse tension W_8 and shear W_6 on the other hand have a decisive influence on the force-displacement relation for all OATs, while

establishing the order of magnitude for the strains depending on their relative ratio. The behavior during the 45°-OAT is mostly dominated by shear deformation, compared to the 30°- and 60°-OAT in which proportionally a higher amount of transverse tensile deformation occurs. Therefore, initial parameters for W_6 are determined based on the 45°-OAT and then W_8 is used to adapt the membrane model to the other orientations in the 30°- and 60°-OAT. The locking parts of W_6 and W_8 are not utilized in this work, since their introduction always led to a clear overestimation of the forces. However, the perpendicular compressive locking of W_{11} is crucial to prevent a collapse of highly sheared elements and therefore acts as an alternative to the shear locking mechanism for unidirectional fabrics.

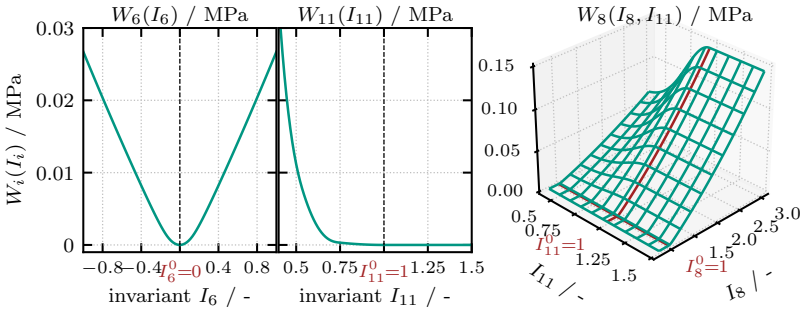

Figure 5.10: Contributions to the strain energy density [180].

The contributions to the total strain energy density due to shear W_6, perpendicular in-plane compression W_{11} and transverse tension W_8 are shown in Figure 5.10. The identified material parameters are listed in Appendix A.2.5 in Table A.5. An additional parameter study based on the final parameterization was conducted to demonstrate the observations described above, which is described in Appendix A.2.6.

Final parameterized membrane behavior in the OATs The general deformation behavior corresponds well between the simulations and experiments as evident from Figure 5.11. The resulting forces and averaged shear angles over the MDZ are also in good agreement with the experimental results, cf. Figure 5.12. During the 30°-OAT (cf. Figure 5.12 a), the slope of the forces is too high at a displacement of $25\,\mathrm{mm}$ and flattens out again from $30\,\mathrm{mm}$ because at this point the coupling strongly reduces W_8. The transverse tensile strains E_{22} in the MDZ of the 30°-OAT are overestimated for large displacements because the specimen's main deformation concentrates in this zone and is homogeneously distributed during simulation. In the experiments, the large transverse tensile strains are more inhomogeneous and limited to slippage at the transition between zones A and B2, cf. Figure 5.11 a. Additionally, notable shear and compressive strains also occur outside the MDZ due to the lateral contraction of the stitching during the experiments. Both of these effects cannot be modeled with a local macroscopic approach that assumes homogeneous material properties over the whole specimen. To demonstrate these observations, the strains in the experiments and simulation were averaged over areas of different sizes and compared in Appendix A.2.7.

The perpendicular compressive strains are slightly underestimated in the MDZ for all OATs. However, a further reduction of W_{11} resulted in an overestimated necking of the outer contours, so a compromise of both objectives was chosen. Nevertheless, the simulation approach was able to model the perpendicular compression in the MDZ of the 60°-OAT, which has not been achieved by previous modeling approaches [137, 140]. In the experiments of the 45°- and 60°-OAT, positive E_{22}- and $E_{\perp}$-strains occur along the outer edges of the specimens, cf. Figure 5.11. The stitching has slipped inward along the rovings in these areas during the tests, resulting in a reduced transverse stiffness and small gapping. This effect cannot be reproduced by the macroscopic approach.

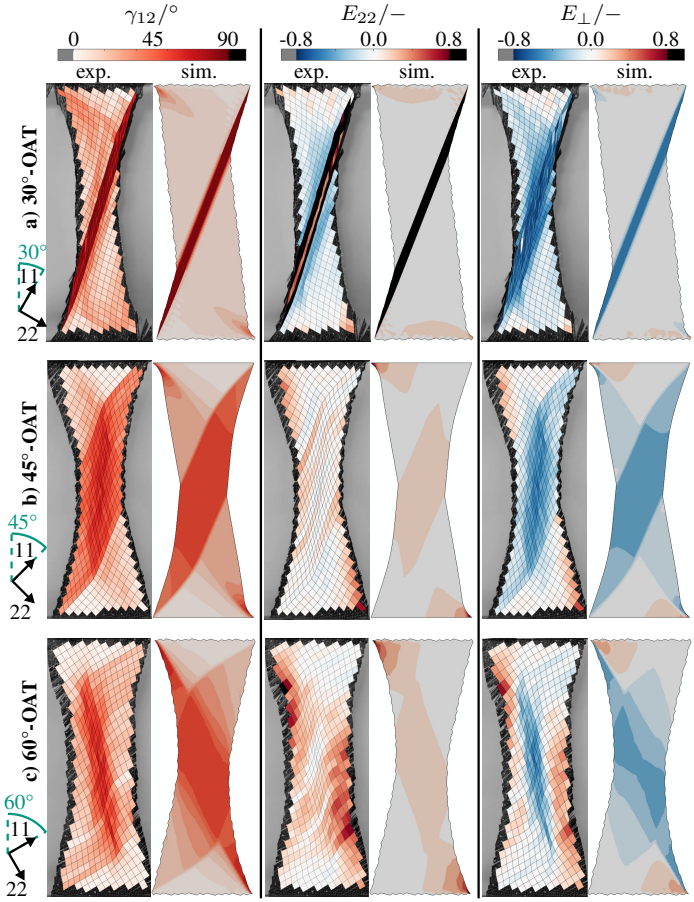

Figure 5.11: Comparison of the experimentally measured (left) and predicted (right) contour plots of the a) 30°-, b) 45°- and c) 60°-OAT at a displacement of 80 mm [180].

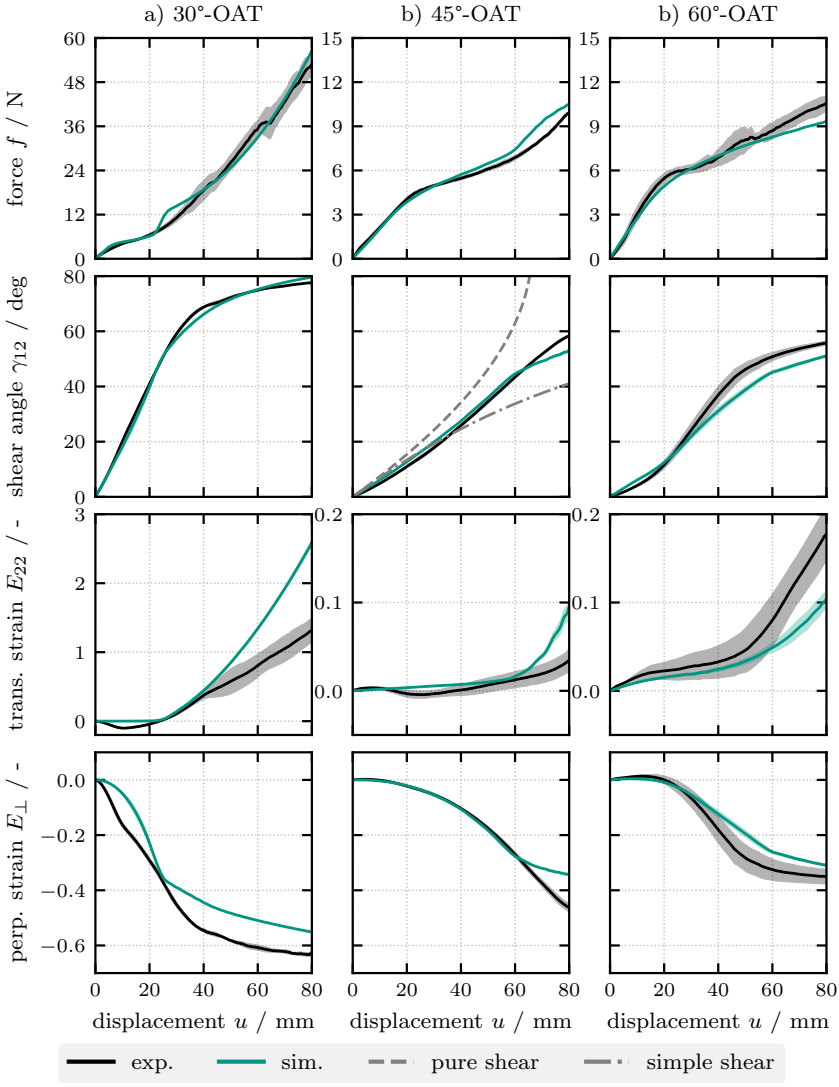

Figure 5.12: Overview of forces and strains in the MDZ of the off-axis-tension tests (OATs) with a bias direction of a) 30°, b) 45° and c) 60° [180].

5.2.7 Summary and conclusion[5]

Unidirectional non-crimp fabrics deform not only under pure or simple shear, but under mixed deformation modes. These consist of different ratios of large shear superimposed with transverse tensile deformation due to roving slippage and stitching extension as well as in-plane compression perpendicular to the carbon fibers. To describe this complex membrane behavior, a new hyperelastic approach is presented and implemented in the FE solver ABAQUS/Explicit. Suitable directional pseudo-invariants are introduced and related to the different deformation modes. Generalized formulations based on piecewise functions with physically interpretable parameters for the strain energy density contributions and coupling function are proposed to simplify the parameterization process and transferability to other materials. The transverse tensile energy is coupled to the perpendicular compression, to consider large roving slippage under stitching and roving compression.

The proposed hyperelastic approach is successfully parameterized based on the forces and different ratios of superimposed strains during off-axis tension tests with bias angles of 30°, 45° and 60°. Good overall agreement is achieved and the location as well as orientation of the different deformation zones observed in the experiments are well captured. The deformation behavior is better predicted within the main deformation zone compared to the secondary deformation zones. This is mainly due to the complex behavior of the stitching during the experiments, as it can slip relative to the rovings and distribute loads over large areas due to lateral contraction. This behavior cannot be modeled with the proposed approach due to the limitations of a local macroscopic approach. It was found that a perpendicular compressive locking is essential to prevent a collapse of highly sheared elements, while a traditional shear locking and a transverse tensile locking are not necessary. The perpendicular locking acts as an alternative shear locking mechanism for unidirectional fabrics.

[5] Reproduced section from [180], cf. footnote p. 150 for details.

5.3 Intra-ply modeling - Bending behavior

The bending behavior of UD-NCF needs to be considered in a decoupled fashion during forming due to the fabric's low transverse shear stiffness [137]. An existing approach for the bending behavior is used that was previously developed for thermoplastic tapes [28] and already successfully applied for UD-NCF [137] as well as woven fabrics [64]. Bending is modeled with a hypoelastic approach, that accounts for large shear deformation. It considers an orthotropic elastic bending stiffness in the resulting non-orthogonal material frame. The cantilever tests presented in Section 4.3 are used for the parameterization of the approach.

5.3.1 Hypoelastic constitutive equations for the bending behavior

The elastic part of the hypo-viscoelastic approach developed by Dörr et al. [17, 28] for thermoplastic UD-tapes is adopted for UD-NCF in this work. The approach is implemented in a VUGENS subroutine for a user-defined shell-section integration scheme over the initial thickness t_0 in ABAQUS/Explicit. This user interface provides the incremental membrane strain $\Delta\boldsymbol{\varepsilon}^0$, the incremental curvature $\Delta\boldsymbol{\kappa}$ and the membrane deformation gradient $\boldsymbol{F}^0$ as input. The fundamentals of hypoelastic material modeling within the fiber-parallel frame were already outlined in Section 2.3.1. The fiber-parallel frame $\{\boldsymbol{g}^{*i}\}$ is calculated based on the membrane deformation gradient according to Equation 2.5. This enables the calculation of the respective covariant strain increment over the thickness direction ζ by

$$[\Delta\boldsymbol{\varepsilon}(\zeta)]_{\{\boldsymbol{g}^{*i}\otimes\boldsymbol{g}^{*j}\}} = [\Delta\boldsymbol{\varepsilon}^0]_{\{\boldsymbol{g}^{*i}\otimes\boldsymbol{g}^{*j}\}} + \zeta F^0_{33}[\Delta\boldsymbol{\kappa}]_{\{\boldsymbol{g}^{*i}\otimes\boldsymbol{g}^{*j}\}}. \tag{5.28}$$

The incremental stress from Equation 2.6 is integrated over the thickness to determine the incremental contravariant section moments by

$$[\boldsymbol{M}^{n+1}]_{\{\boldsymbol{g}_i^* \otimes \boldsymbol{g}_j^*\}} = [\boldsymbol{M}^{n}]_{\{\boldsymbol{g}_i^* \otimes \boldsymbol{g}_j^*\}} + \int_{t_0} [\Delta\boldsymbol{\sigma}(\zeta)]_{\{\boldsymbol{g}^{*i} \otimes \boldsymbol{g}^{*j}\}} (F_{33}^0)^2 \zeta \mathrm{d}\zeta. \tag{5.29}$$

Membrane strains are omitted and section forces are neglected ($\boldsymbol{N} = \boldsymbol{0}$) to suppress the membrane part within the shell element for a complete membrane-bending decoupling. A closed form solution for the integrand in Equation 5.29 in the linear-elastic case is thus given by

$$[\Delta\boldsymbol{M}^{n+1}]_{\{\boldsymbol{g}_i^* \otimes \boldsymbol{g}_j^*\}} = [\mathbb{C}^{\mathrm{bend}}]_{\{\boldsymbol{g}_i^* \otimes \boldsymbol{g}_j^* \otimes \boldsymbol{g}_k^* \otimes \boldsymbol{g}_l^*\}} : [\Delta\boldsymbol{\kappa}]_{\{\boldsymbol{g}^{*k} \otimes \boldsymbol{g}^{*l}\}} \frac{(t_0 F_{33}^0)^3}{12}. \tag{5.30}$$

The bending moments are finally transformed to the Green-Naghdi's frame based on Equation 2.5.

5.3.2 Parameterisation of the bending model with cantilever tests

The results of the cantilever tests described in Section 4.3 are used to parameterize the bending model. The configurations with the front and back of the fabric facing up are parameterized separately. Since this work focuses on the membrane behavior and no significant out-of-plane deformation was observed in the forming tests presented in Section 4.6 due to the planar blankholders, only a constant bending stiffness $\mathbb{C}^{\mathrm{bend}}$ is used. Therefore, only the bending stiffnesses in the principal material directions (C_{11}^{bend} and C_{22}^{bend}) and the shear component (C_{12}^{bend}) are required for 2D shell elements. Similar to previous studies [28, 65, 137], the material stiffness of the bending model is inversely identified by modeling of relevant tests in combination with a gradient based Nelder-Mead algorithm [351]. The overhang length l_{bend} of the individual configurations is chosen as the optimization goal, cf. Figure 4.13. After analysis of the resulting stiffnesses in the 0°- and 90°-directions, it turns out that these

can alternatively be determined directly from the Peirce bending stiffness $G_{\mathrm{w}}^{\mathrm{P}}$ from Equation 4.5 by

$$C_i^{\mathrm{bend}} = 0.944 \cdot G_{\mathrm{w}}^{\mathrm{P}} \frac{w_0}{I} = 0.944 \cdot G_{\mathrm{w}}^{\mathrm{P}} \frac{12}{t_0^3} \quad \text{with} \quad i \in [11, 22], \tag{5.31}$$

with the moment of inertia I based on the initial thickness t_0 and an additional correction factor of 0.944. The correction factor was consistent for both directions and fabric sides. It presumably results from the logarithmic strain measure in ABAQUS/Explicit in combination with large deformations. The resulting deflections curves are shown in Figure 5.13.

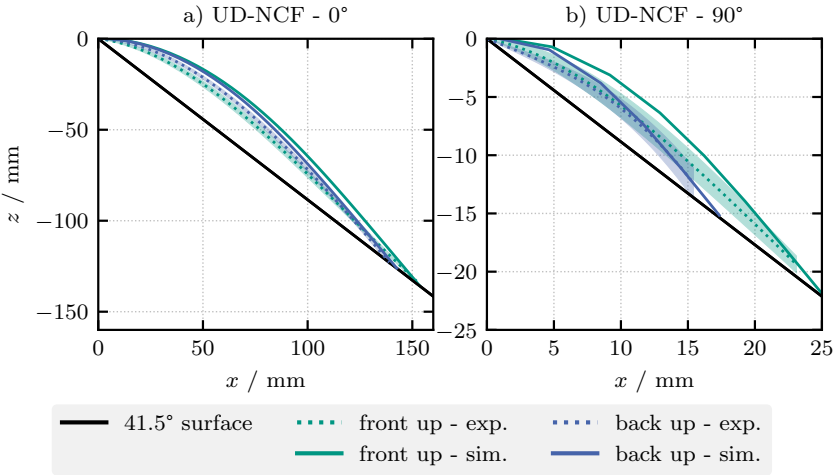

Figure 5.13: Simulated deflections curves during the cantilever tests of UD-NCF with the front and back of the fabric facing up.

It should be noted that the average overhang length of the optically measured deflection curve during the experiments in Figure 5.13 is smaller due to the averaging over the lowest common l_{bend} of all individual tests. The predicted deflection curves deviate slightly from the experimental results. The constant bending stiffness neglects the decrease for large curvatures measured during the optical evaluation in Section 4.3.2.

In the 45°-cantilever test, a significant twist of the specimens was observed due to the strong anisotropy of UD-NCF, cf. Figure 5.14 a. To model this behavior, the bending shear component C_{12}^{bend} is inversely determined to achieve a similar first contact with the inclined surface. The shear component is often neglected in literature or just assumed as a sufficiently small value [65, 86]. The result for the configuration with the front facing up is shown in Figure 5.14 b. The deformation during the simulation is qualitatively in good agreement with the observed deformation during the experiment. The final material parameters for the respective configurations with the front or back of the fabric facing up are given in Appendix A.2.8 in Table A.6.

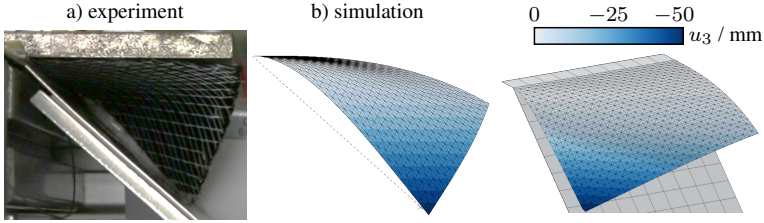

Figure 5.14: Simulation of twist deformation during the 45°-cantilever tests with the stitching side facing up.

5.3.3 Summary and conclusion

A hypoelastic bending model was parameterized to describe the strongly anisotropic deformation of UD-NCF. The bending stiffnesses in the principal material directions can be directly derived from the Peirce cantilever tests. Inverse parameter identification is only necessary for the shear component to describe the twist deformation during 45°-cantilever tests. However, the impact of the shear parameterization on the forming behavior has never been investigated and requires further analysis to assess its relevance. The results for the three investigated fiber orientations during cantilever tests are in good agreement with the experimental observations.

5.4 Validation of the forming simulation[5]

The proposed hyperelastic membrane approach (cf. Section 5.2) and hypoelastic bending approach (cf. Section 5.3) are applied to forming simulations of different punch shapes in this section. The results are compared to experimental forming tests described in Section 4.6, whose setup was previously used by researchers at at INSA Lyon for the validation of simulation approaches for woven fabrics [211, 216, 217, 223] or biaxial NCF [136]. The hemisphere, tetrahedron and square box punch shapes are applied to evaluate the validity of the approach for different geometrically challenging features.

5.4.1 Setup of forming simulations

The details of the experimental setup and procedure are described in detail in Section 4.6.1. The setup of the corresponding forming simulations is implemented in the commercially available FE solver ABAQUS/Explicit and shown in Figure 5.15. The tools are modeled as discrete rigid surfaces based on the dimensions shown in Figure 4.33. The tool stroke is implemented via a displacement boundary condition and the blankholder weights are implemented via an equivalent pressure boundary condition. The blankholder is placed on centering pins during the experiments (cf. Figure 4.32), which prevents upward movement due to counterpressure caused by the deformation of the textile. However, Dirichlet- and Neumann-boundary conditions cannot be applied simultaneously in the simulation. Therefore, an additional fixed surface above the blankholder is modeled which prevents upward movement due to a contact boundary condition.

[5] Extracts from Section 5.4 have been previously published in [180], i.e. B. Schäfer, D. Dörr, R. Zheng, N. Naouar, L. Kärger. A hyperelastic approach for modeling the membrane behavior in finite element forming simulation of unidirectional non-crimp fabrics (UD-NCF). *[submitted for review]*. | Section 5.4.2 and Section 5.4.3.1 reproduce Sections 5.2 & 5.3 of [180].

The membrane approach described in Section 5.2 is applied to M3D3 membrane elements with their edges aligned in fiber direction to avoid numerical intra-ply locking. The bending approach described in Section 5.3 is applied to S3 shell elements, which are superposed to the membrane elements via shared nodes to ensure a membrane-bending decoupling. The bending parameterization for the front of the fabric facing up was used for all simulations, because no differences between the two configurations were found in preliminary investigations due to the planar blankholders. The superimposed membrane and shell elements represent each individual layer of the textile layup. For a quantitative comparison of the strain development during the tests, the three local zones in areas of high deformation for each shape are defined, which correspond to the experimental evaluation, cf. Figure 5.15. All single-layer configurations described in Section 4.6 are investigated for the validation of the forming approach. Additionally, the $[0°/90°]$-configuration is analyzed to represent the double-layer tests.

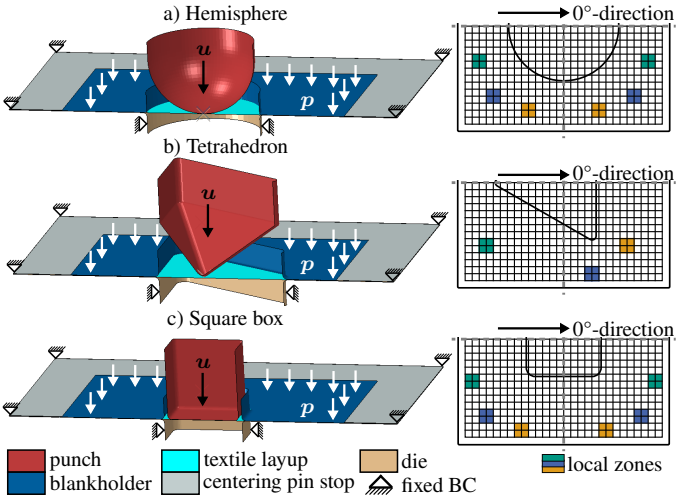

Figure 5.15: Forming simulation setup and local evaluation zones for average strains for the a) hemisphere, b) tetrahedron and c) square box.

Inter-ply behavior Tool-ply and ply-ply contact are modeled via the built-in general contact algorithm in ABAQUS/Explicit. The dynamic friction coefficients are selected based on average values of the measured configurations in Section 4.5 as $\mu^{\mathrm{tool-ply}} = 0.147$ and $\mu^{\mathrm{ply-ply}} = 0.336$. A more complex modeling of the inter-ply behavior was omitted. In preliminary investigations, the friction coefficients in the forming simulations were varied between the maximum and minimum experimentally measured CoF. No notable influence on the forming behavior was observed. This observation is consistent with the conclusions of Poppe et al. [56, 186]. They developed a pressure-, rate- and orientation-dependent contact formulation for woven fabrics with CoF in a similar order of magnitude to the investigated UD-NCF. The predicted tangential stresses were almost always sufficiently low enough to allow for a nearly independent deformation of each ply. Even for studies on thermoplastic UD-tapes with one or two orders of magnitude higher tangential stresses, only small effects on the overall draping results are reported for variations within the order of magnitude [17, 21]. Therefore, the expected benefit of a more complex contact formulation based on the detected influences on the CoF in Section 4.5 would be small.

5.4.2 Hemisphere forming[5]

The outer contours of the fabric layers for a displacement of $u = 75\,\mathrm{mm}$ of the hemispherical punch are shown in Figure 5.16. The contour is used to evaluate the overall deformation and often represents a first validation step for simulation approaches based on the material draw-in [113, 136, 213]. A strongly anisotropic behavior specific to UD-NCF is observed, compared to the typically more symmetrical behavior previously reported for biaxial fabrics [136, 216]. The results of the proposed approach are in good agreement with the experiments for the [0°]- and [45°]-test. The simulative contours of the double-layer tests nearly match the results of two superposed single-layer contours, because the individual layers deform mostly unconstrained due to the low blankholder weight. Similar behavior is observed during the experimental tests in Section 4.6.

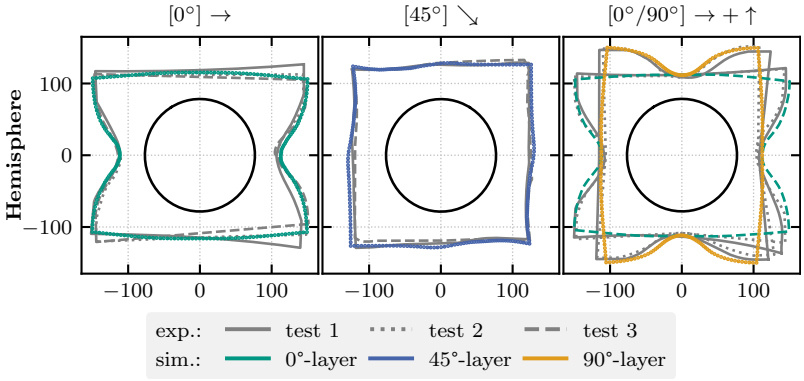

Figure 5.16: Outer contours (all in mm) of the hemisphere forming simulations (adapted from [180]).

The experimental and simulative strains are shown in Figure 5.17 for a more detailed comparison. The general orientation and location of areas with high

[5] Reproduced section from [180], cf. footnote p. 169 for details.

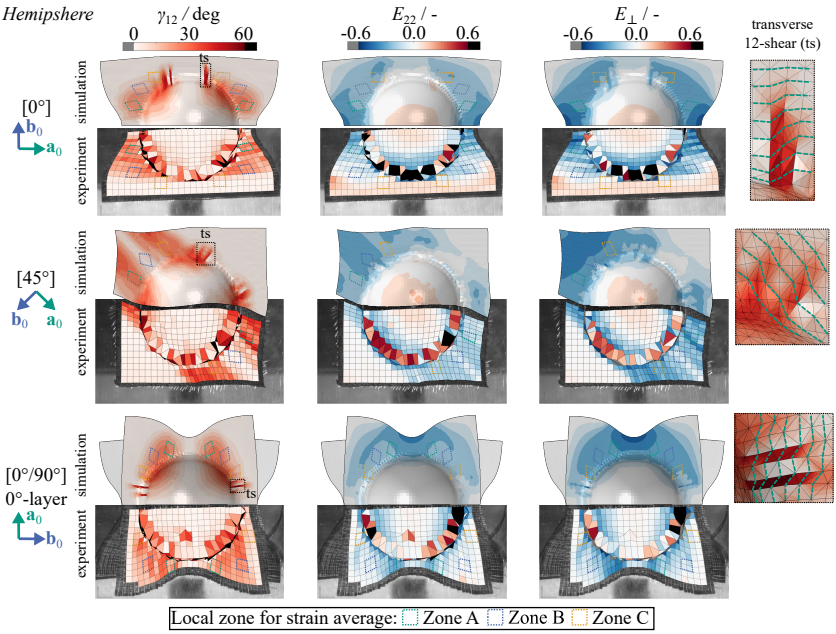

Figure 5.17: Comparison of experimental and simulative strains for [0°] and [45°] single-layer as well as [0°/90°] double-layer setups in the hemisphere forming tests for a punch displacement of $u = 75\,\mathrm{mm}$ with a zoom on local shear bands due to transverse 12-shear (ts) [180].

shear deformation γ_{12} are predicted well for all investigated setups. Considering the local shear angles in zones A, B and C, the magnitudes are also quantitatively in good agreement but with a tendency to be slightly underestimated, cf. Figure 5.18. Comparing the [0°]-test and the 0°-layer in the [0°/90°]-test, the superposed 90°-layer reduces shear in zone A and increases it towards zones B and C both in simulation and experiment.

Local shear bands in the transverse direction (12-shear) are observed in Figure 5.17 for all setups at the boundaries of the high shear area starting at the radius of the hemisphere, similar to those already reported for the model proposed by Schirmaier et al. [137]. In the experiments, shear deformation primarily occurs parallel to the carbon fiber rovings (21-shear), cf. Figure 5.8 d,

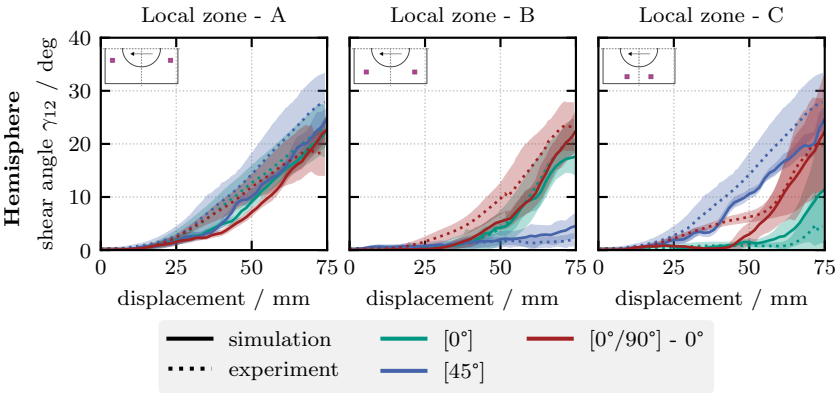

Figure 5.18: Shear angle in local zones of the hemisphere forming tests (adapted from [180]).

since the in-plane bending stiffness of the rovings prevents transverse in-plane shear. This distinction of the asymmetrical shear behavior cannot be achieved with the proposed macroscopic approach based on Cauchy mechanics. The introduction of an in-plane fiber bending stiffness could account for this phenomenon, but would require the calculation of higher strain gradients based on generalized continua approaches [97, 301] which are not yet realized for ABAQUS/Explicit.

The negative transverse and perpendicular strains are well predicted within the areas of high shear deformation but overestimated in the outer areas. Especially in the [0°]-setup, positive strains in combination with small gaps between the rovings are observed along the lower edge during the experiments, which is similar to the observations during the 45°- and 60°-OATs and cannot be reproduced by the macroscopic simulation approach (cf. Section 5.2.6). The positive E_{22}- and $E_{\perp}$-strains in the center of the hemisphere during both single-layer tests are predicted well by the simulation. In the double-layer test, the additional superposed layer prevents positive strains in the center, which is captured by the model.

5.4.3 Tetrahedron forming

The results of the tetrahedron tests are divided into two groups. First, the single-layer tests are investigated to analyze the performance of the new simulation approach for a more complex shape compared to the hemisphere tests. Second, the double-layer [0°/90°]-configuration is investigated in more detail due to the distinct interactions described in Section 4.6.2.

5.4.3.1 Single-layer tests[5]

The outer contours of the fabric layers for a displacement of $u = 95\,\mathrm{mm}$ of the tetrahedral punch are shown in Figure 5.19. The general shapes of the

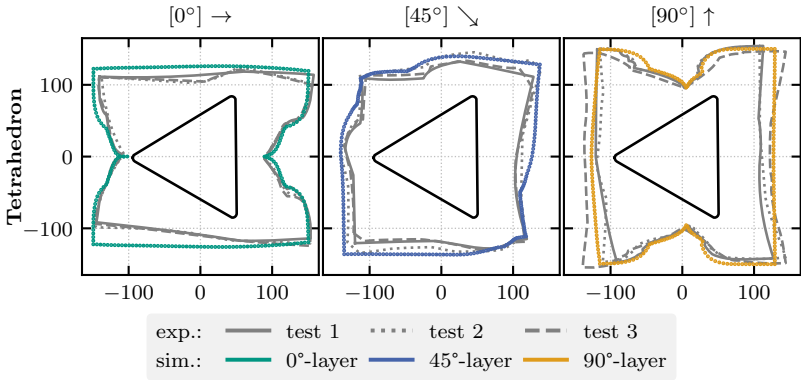

Figure 5.19: Outer contours (all in mm) of the single-layer tetrahedron forming simulations (adapted from [180]).

simulative contours are in good agreement with the experiments. However, the material draw-in transverse to the initial fiber orientation is underestimated for all investigated setups. Additionally, large positive E_{22}- and $E_{\perp}$-strains

[5] Reproduced section from [180], cf. footnote p. 169 for details.

are predicted in the tetrahedron's center during the simulation compared to the experimental measurement, cf. Figure 5.20.

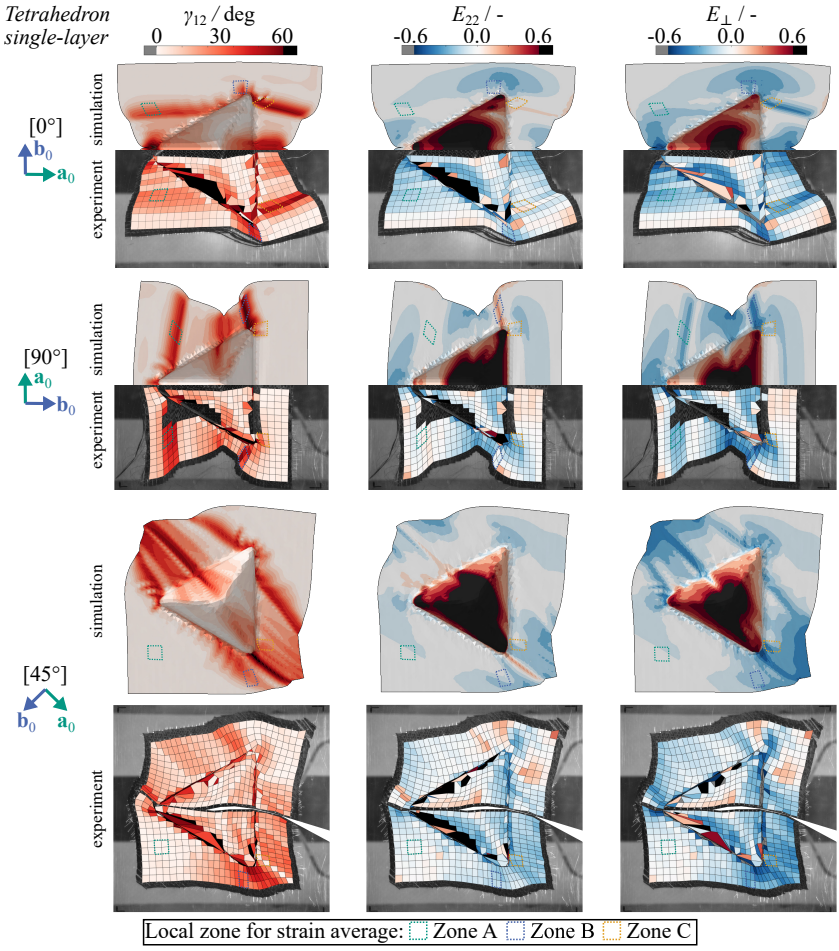

Figure 5.20: Comparison of experimental and simulative strains for [0°], [45°] and [90°] single-layer setups in the tetrahedron forming tests for a punch displacement of $u = 95\,\mathrm{mm}$ [180].

This observation can be attributed to two reasons. First, the 2D-DIC method significantly underestimates the strains in the three-dimensional regions of the shape (demonstrated in Figure A.14 in Appendix A.2.9). Second, the pressure due to the blankholder increases friction between the glass fibers, rovings and stitching, which results in a higher stiffness in the transverse direction [110]. This effect is not accounted for during the parameterization based on OATs and would also require considering the impact of the pressure on the transverse behavior along the glass-fiber direction, which is not possible with the current plane-stress approach. Both effects are more pronounced for the tetrahedron test compared to the hemisphere test, due to the stronger distortion in the DIC results and the higher blankholder weight.

The general shear behavior and location of areas with high deformation are predicted well for the investigated setups, except for the area around zone B in the [0°]-setup, cf. Figure 5.20. The high shear is localized around the tetrahedron's corner and does not extend towards the edges due to the underestimated material draw-in in the transverse direction. This is also reflected in the quantitative comparison of the local strains, cf. Figure 5.21. The local shear angles in all zones and configurations are in acceptable agreement between the simulation and experiment, except for zone B in the [0°]-test. However, the onset of transverse shear bands is again noticeable in multiple areas, especially in the corners and close to the transition from the flat parts to the tetrahedron.

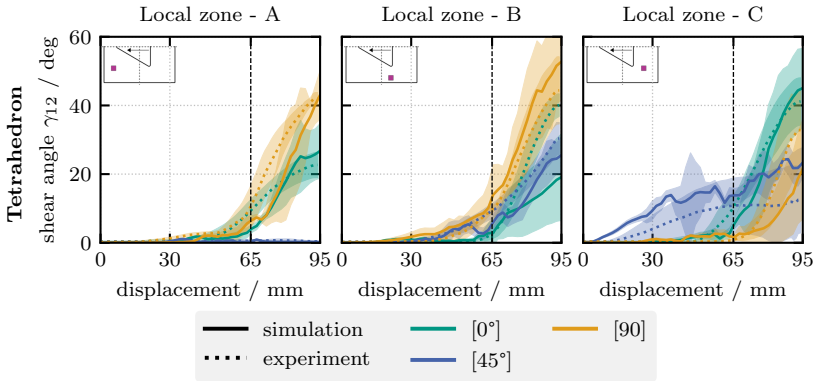

Figure 5.21: Shear angle in local zones of the tetrahedron forming tests (adapted from [180]).

While mixed-mode 1 ($I_8, I_{11} < 1$, cf. Figure 5.8 d) was the main deformation mode in the hemisphere-test, mixed-mode 2 ($I_{11} < 1$, $I_8 > 1$) additionally occurs during tetrahedron forming near zone C in the [0°]-, zone B in the [90°]- and between zones B & C in the [45°]-setup. This deformation mode indicates significant roving slippage which is more pronounced in the simulation than in the experiments ($E_{22}^{\mathrm{sim}} > E_{22}^{\mathrm{exp}}$). However, it highlights the necessity to take into account the different deformation modes during characterization.

5.4.3.2 Double-layer tests

The double-layer [0°/90°]-configuration of the tetrahedron tests is investigated separately due to the distinct interactions observed during the experiments described in Section 4.6.2. In the experiments, the superposed 90°-layer leads to a stronger material draw-in of the 0°-layer in transverse direction compared to the single-layer tests, and the the corners of the 0°- and 90°-layer remain completely or partially superposed during some tests.

The results for the simulation with the assumed CoF for ply-ply contact of $\mu^{\mathrm{ply-ply}} = 0.336$ are shown in the top row of Figure 5.22. A notable impact of the additional 90°-layer on the deformation of the 0°-layer is observed in comparison to the single-layer tests, cf. Figure 5.20. The location and general orientation of zones with significant shear deformation are similar to the [0°]-configuration, but the material draw-in in the transverse direction is higher. Thus, the upper edge remains less straight and the positive E_{22}- and $E_{\perp}$-strains in the center are significantly smaller compared to the simulation of the single-layer tests, cf. Section 5.4.3.1. Additionally, the high shear deformation around zone B extends further towards the layer's edge. The higher material draw-in and extended shear zone are similar to the experiment.

The predicted strains of the right half of the tetrahedron are in reasonable agreement with the lower right half of the experiments, cf. Figure 5.22, in which the corners of both layers did not remain superimposed. Only the positive transverse strains around zone C and the lower right corner of the 0°-layer are

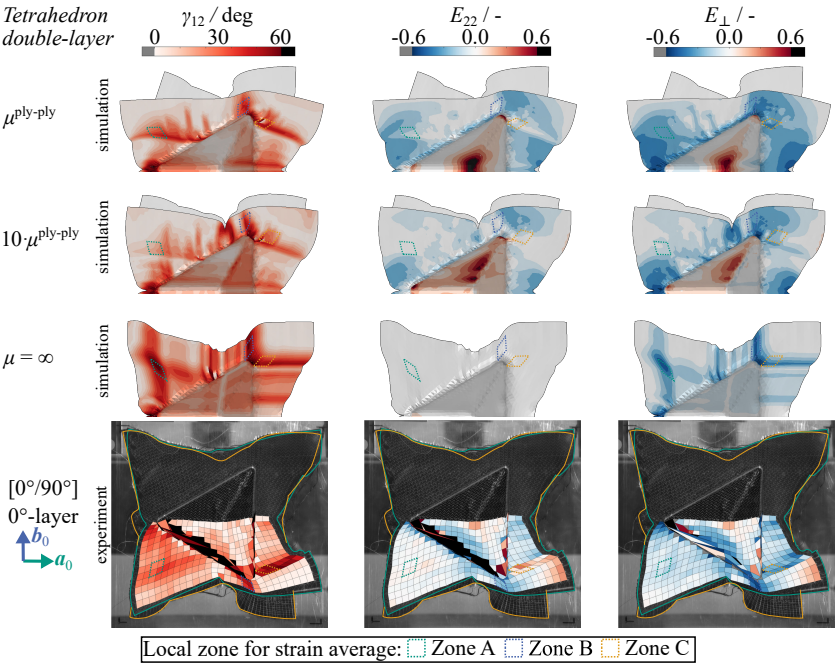

Figure 5.22: Comparison of experimental and simulative strains for [0°/90°] double-layer setups with different ply-ply CoF in the tetrahedron forming tests for a punch displacement of $u = 95\,\mathrm{mm}$

underestimated. The different sign of E_{22}- and $E_{\perp}$ in zone C is still discernible, indicating mixed-mode 2 ($I_{11} < 1$, $I_8 > 1$, cf. Figure 5.8 d) with relative roving slippage. However, compared to the single-layer tests it is more pronounced in the experimental tests than in the simulation.

The predicted deformation in the left half of the 0°-layer is very different from the experimental results. The layers deform relatively unconstrained during the simulation and do not remain superimposed in contrast to the experiment. This indicates that the tangential stresses are underestimated by the simulation. The CoF was gradually increased to further investigate this effect. The results for a high CoF with $10 \cdot \mu^{\mathrm{ply-ply}}$ as well as a sticking contact formulation to suppress relative movement between the plies (equivalent to $\mu^{\mathrm{ply-ply}} = \infty$) are

shown in Figure 5.22. The corners still do not remain completely superimposed during the simulation with the CoF increased by an order of magnitude, which is significantly higher than any experimentally measured dynamic or static CoF, cf. Section 4.5. For the sticking contact formulation, a joint deformation of both layers is observed. Thus, transverse E_{22}-strains are suppressed by the second layer and a pure shear deformation is enforced, similar to the results of the Biax-NCF in Figure 4.40 a. The experimental results fall somewhere between both simulations with significantly increased CoFs. This suggests that there must have been interlocking effects between the mesoscopic constituents of both layers in the experiments, that prevent relative slippage and were not detected during characterization. However, since the joint deformation of both layers did not occur for all repetitions in the experimental tests, no conclusive claim can be made on the basis of the available results. More detailed experimental as well as numerical investigations would be necessary.

5.4.4 Square box forming

The square box is a geometrically very challenging shape with significant forming depth, to test the forming behavior of a fabric for an extreme case. The outer contours of the fabric layers for a displacement of $u = 85\,\mathrm{mm}$ of the square box punch are shown in Figure 5.23. The general shapes of the simulative contours are in reasonable agreement with the experiments, especially for the [0°]-test. In the [45°]-test, the material draw-in in the transverse direction is underestimated. In the analysis of the experimental [0°/90°]-tests in Section 4.6.2.2, an increased material draw-in transverse to the fiber direction is observed due to the second layer resulting in slightly overlapping flaps of textile. The additional draw-in is notable but underestimated in the simulation, resulting in deviations of the outer contours.

The experimental and simulative strains are shown in Figure 5.24 for a more detailed comparison. The general orientation and location of areas with high shear deformation γ_{12} are predicted well for all investigated setups. Considering

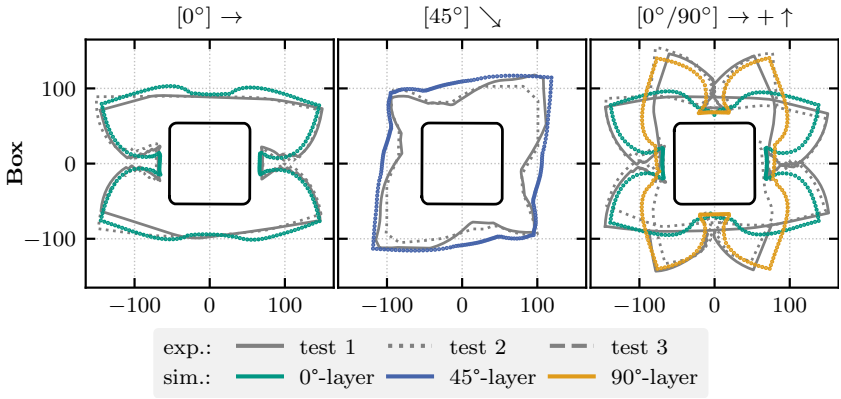

Figure 5.23: Outer contours (all in mm) of the square box forming simulations.

the local shear angles in zones A and C, the magnitudes are also quantitatively in good agreement but with a tendency to be slightly underestimated, cf. Figure 5.25. In zone B, the shear angle for the [45°]-test is overestimated, but it is close to the upper limit of the measured strong scattering in the experiments. Comparing the [0°]-test and the 0°-layer in the [0°/90°]-test, the superposed 90°-layer increases shear in zone C both in the simulation and experiment.

The strongly negative $E_{\perp}$- and close to positive E_{22}-strains in zone A of the 0°-layers are well predicted by the simulation. However, the positive perpendicular strains in combination with small gaps between the rovings in the corners during the experiments cannot be predicted by the model. This observation is similar to the hemisphere tests, cf. Section 5.4.2. The positive E_{22}- and $E_{\perp}$-strains in the center of the box during both single-layer tests are significantly overestimated by the simulation. This observation is similar to the results for the tetrahedron tests despite a smaller blankholder weight. The overestimated tensile strains are presumably caused by the challenging geometry of the box with a large forming depth. In the double-layer test, the additional superposed layer reduces these positive strains in the center of the 0°-layer during the experiments. This tendency is captured by the model, but E_{22} remains overestimated. The

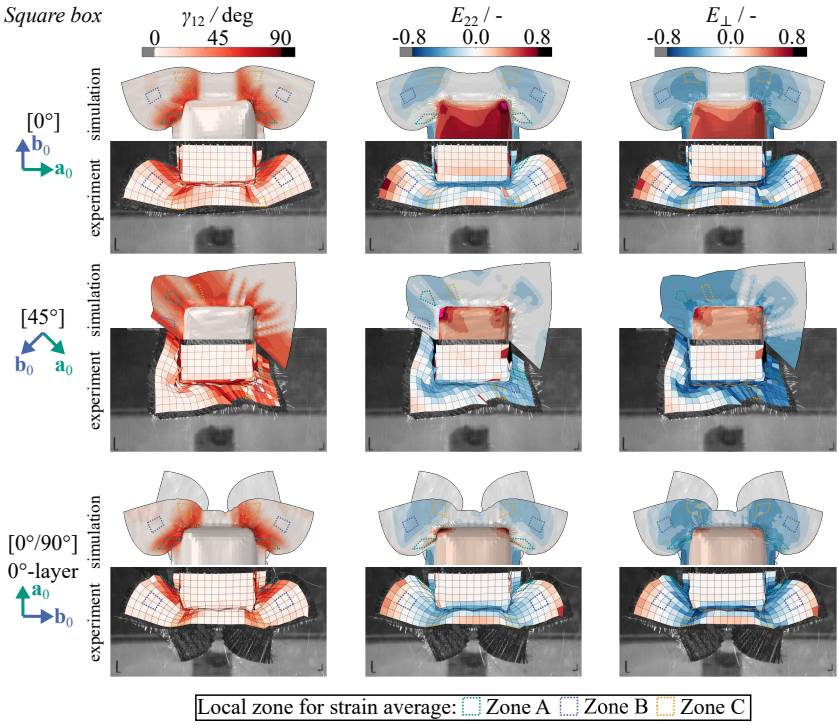

Figure 5.24: Comparison of experimental and simulative strains for [0°] and [45°] single-layer as well as [0°/90°] double-layer setups in the square box forming tests for a punch displacement of $u = 85\,\mathrm{mm}$.

predicted peaks of $E_{\perp}$ in the corners of the box for all orientations coincide with observed gapping during the tests, cf. Section 4.6.2.4.

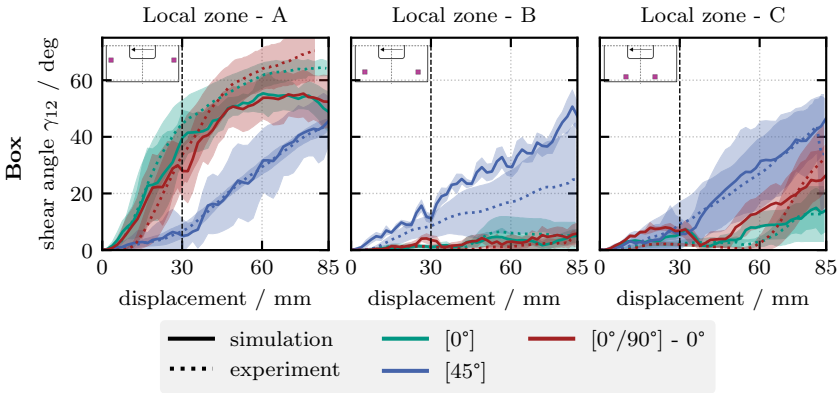

Figure 5.25: Shear angle in local zones of the square box forming tests.

5.4.5 Summary and conclusion

The proposed hyperelastic membrane approach combined with a parameterized hypoelastic bending approach is validated with forming simulations of hemisphere, tetrahedron and square box punch shapes. The specific behavior of UD-NCF with an asymmetric deformation consisting of superimposed shear, transverse tension as well as perpendicular compression is predicted well in all configurations. For the hemisphere tests, all resulting contours, the global strain distributions as well as the local strains are in particular good quantitative agreement with the experiments. For the single-layer tetrahedron tests and square box tests, the orientation, location as well as magnitude of areas with high deformation are well predicted despite the challenging corners and large forming depth. The shear and compressive strains are in good agreement with the experiments, but the transverse strains are overestimated. This presumably results in increased friction between the glass fibers, rovings and stitching due to normal pressure of the planar blankholder. The pressure-dependent transverse behavior is not accounted for during the parameterization based on OATs and cannot be modeled based on plane-stress. In the double-layer tests, the superimposed layer strongly reduces the impact of this effect and the transverse strains were only slightly overestimated.

Local shear bands transverse to the roving direction (12-shear) occur for all investigated shapes and configurations. In the hemisphere forming simulations, they are observed at the boundaries of high shear areas close to the transition from the flat parts to the curved hemisphere. In the tetrahedron and square box forming simulations, they occur especially around the corners, where gaps are observed in the experiments due to excessive shear and high roving curvature, cf. Figure 4.42. These local shear bands do not significantly affect the global forming behavior, but prevent a better prediction of local effects like gapping. They result from the limitation to a symmetric shear behavior of the proposed macroscopic approach based on Cauchy mechanics. Experimentally, an asymmetrical shear behavior is observed mainly parallel to the rovings (21-shear), while shear transverse to the rovings (12-shear) is prevented due to their in-plane bending stiffness. The introduction of an in-plane fiber bending stiffness based on generalized continua approaches could account for this phenomenon [97,301]. However, this would require the calculation of higher strain gradients which are not yet realized for ABAQUS/Explicit.

Lastly, the strong interactions and partially joint deformation of both layers during the experimental double-layer tetrahedron tests are not predicted by the model. To reproduce similar interactions, a significantly higher CoF than experimentally measured for any configuration during inter-ply characterization would be necessary, cf. Section 4.5. In addition, the interactions were not equally pronounced in all repetitions of the experimental tests, cf. Section 4.6. This suggests local interlocking of the mesoscopic constituents of both layers, but requires further investigation for a conclusive assertion and before a suitable model can be developed.

5.5 Transfer and validation for Biax-NCF

This section demonstrates the general transferability of the proposed modeling approaches and outlined parameterization strategies to Biax-NCF. The proposed hyperelastic membrane model can be conveniently adapted to Biax-NCF due to the modularity of the individual energy contributions and the selected generalized approaches. The observation of a shear-dominated behavior in Section 4.2 is used to derive the necessary parameters analytically from the 45°-OAT. For the bending behavior, only the inverse determination of the shear component is necessary. The bending stiffnesses in the fiber direction are calculated analytically based on the Peirce bending stiffness analogous to UD-NCF. Finally, forming simulations of the hemisphere, tetrahedron and box are used for validation.

5.5.1 Membrane modeling of Biax-NCF

The characterization in Section 4.2 revealed a shear-dominated and almost symmetrical membrane behavior of the investigated Biax-NCF. Based on this observation a simplified approach is proposed based on pure shear. Thus, relative roving slippage is neglected and only tension in both roving directions as well as pure shear are considered by

$$W_{\mathrm{tot}}^{\mathrm{Biax}}(I_4, I_6, I_8) = W_4^{\mathrm{Biax}}(I_4) + W_6^{\mathrm{Biax}}(I_6) + W_8^{\mathrm{Biax}}(I_8). \tag{5.32}$$

The generalized approach for the strain energy density $W_i^{\mathrm{G}}(I_i)$ from Equation 5.20 is applied for all contributions with respect to their sign by

$$W_i^{\mathrm{Biax}}(I_i) = \mathrm{sgn}\left(I_i - I_i^0\right) \cdot W_i^{\mathrm{G}}(I_i) \quad \text{with} \quad i \in [4, 6, 8]. \tag{5.33}$$

The moduli C_4^{ini} and C_8^{ini} in both roving directions are assumed to be sufficiently high constant values, as an alternative to a numerically complex inextensibility

condition. This assumption of a very high fiber stiffness prevents consideration of roving slippage in a single-layer approach, since slippage manifests numerically by positive tensile strains in macroscopic approaches.

Shear parameterization To parameterize the contribution due to shear, the energetic approach proposed by Boisse et al. [114] to incrementally calculate the second Piola-Kirchhoff shear stress S_{12} during the 45°-OAT is applied

$$S_{12}(\gamma) = f(\gamma)\frac{(l_0 - w_0)\left(\cos\left(\frac{\gamma}{2}\right) - \sin\left(\frac{\gamma}{2}\right)\right)}{w_0^2 t_0 \cos(\gamma)} - \frac{\cos\left(\frac{\gamma}{2}\right)}{2\cos(\gamma)} S_{12}\left(\frac{\gamma}{2}\right), \quad (5.34)$$

where f is the machine force, l_0 is the initial specimen length, w_0 is the initial specimen width, t_0 is the initial thickness and γ is the optically measured shear angle. The resulting analytical shear stress based on the experimental results presented in Section 4.2 is shown in Figure 5.26. Two different parameter sets

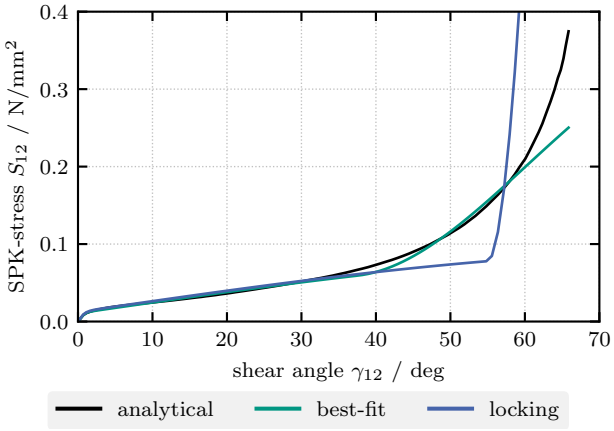

Figure 5.26: Parameterization of the shear behavior of Biax-NCF based on the energetic approach by Boisse et al. [114] for the 45°-OAT.

are considered in the following. First, the optimization procedure presented by Nelder and Mead [351] is applied to determine a 'best-fit' of the generalized approach to Equation 5.34. For this purpose, I_6 is converted to the shear angle

using Equation 5.14, whereby $I_4 = I_8 = 1$ applies for pure shear. A good agreement until medium shear angles is achieved, but the intentionally limited complexity of the approach underestimates the locking behavior for very large shear angles. Second, a 'locking' parameter set was determined to prevent a complete collapse of highly sheared elements during the OATs and forming tests. The locking invariant I_i^{lock} and stiffness C_i^{lock} are adjusted to induce a significant locking after a shear angle of 57°.

Results during the OATs The simulation models of the 30°- and 45°-OAT previously introduced for UD-NCF are applied, cf. Figure 5.9. The resulting forces and strains in the MDZ during the 30°- and 45°-OAT for both parameter sets are shown in Figure 5.27.

The predicted shear angle for both parameter sets in the 45°-OAT closely follows the pure shear assumption. However, since the experimental shear angle is smaller due to relative roving slippage, the force is significantly overestimated for higher displacements. Similar behavior is observed in the 30°-OAT for even lower displacements. In simulations with the "best-fit" parameter set, the elements in the MDZ completely collapse at a shear angle of 90°. This results in a termination of the simulation of the 30°-OAT at $u \approx 30$ mm. The earlier and stronger onset of 'locking' in the second parameter sets limits the shear angle in the 45°-OAT and delays a complete collapse of the elements in the 30°-OAT until $u \approx 58$ mm. In the following, only the 'locking' parameter set (cf. Table A.7) is considered due to the better agreement with the experimental shear angle and higher stability for large displacements.

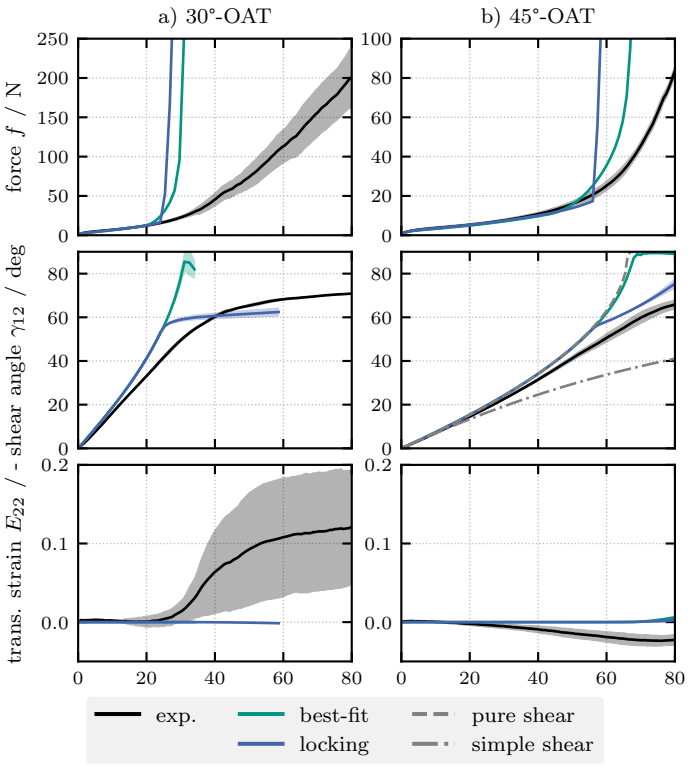

Figure 5.27: Overview of forces and strains in the MDZ of the off-axis-tension tests (OATs) with Biax-NCF with a bias direction of a) 30° and b) 45°-OAT.

The strain contours for the 30°- and 45°-OAT at the displacements where the predicted forces start to deviate from the experiments and the maximum displacement are shown in Figure 5.28. The orientation and location of the different shear zones are in good agreement for lower displacements. The neglect of roving slippage ($E_{22} \neq 0$ in the experiment) prevents a better agreement for higher displacements.

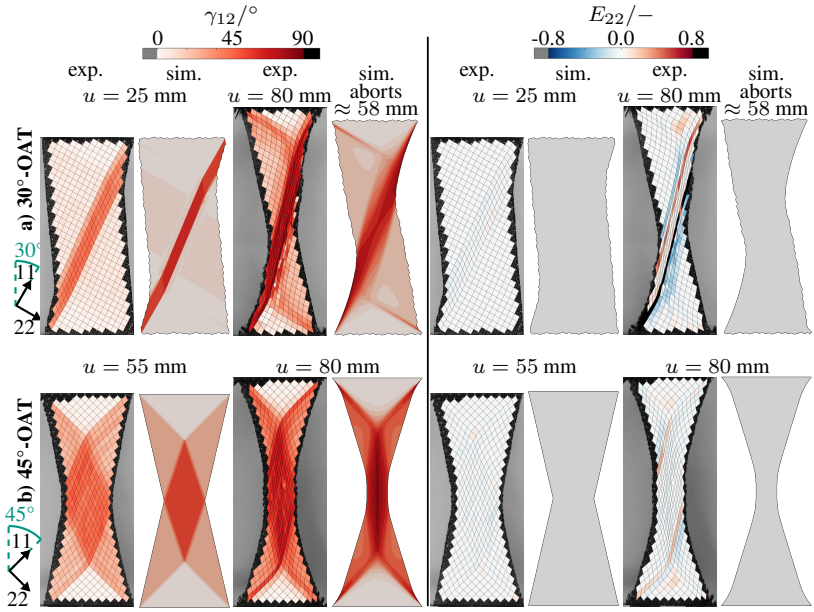

Figure 5.28: Comparison of the experimentally measured (left) and for the 'locking' parameter set predicted (right) contour plots of the a) 30°- and b) 45°-OAT at a displacement of 80 mm.

5.5.2 Bending modeling of Biax-NCF

The hypoelastic bending approach [28] utilized for UD-NCF in Section 5.3 is parameterized for Biax-NCF based on the experimental results presented in Section 4.3. First, the bending stiffnesses (C_{11}^{bend}, C_{22}^{bend}) for both fiber directions and both fabric sides are determined based on the experimentally measured Peirce bending stiffness with the approximation proposed in Equation 5.31. Second, the shear component C_{12}^{bend} is inversely adjusted to achieve a similar bending length l_{bend} in simulations of the 45°-cantilever tests. In agreement with the experimental observations shown in Figure 4.14, a slight sagging of the specimen in the center is predicted by the model in the 45°-tests. The final material parameters are given in Table A.8 and the resulting deflection curves are shown in Figure 5.29.

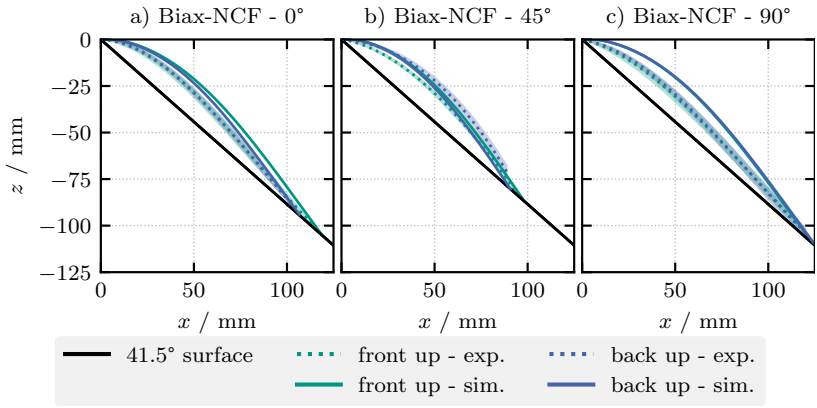

Figure 5.29: Simulated deflections curves during the cantilever tests of Biax-NCF with the front and back of the fabric facing up.

The predicted deflection curves for all tests deviate slightly from the experimental results. This is similar to the observations for UD-NCF in Section 5.3 and can be attributed to the neglected decrease of the bending stiffness for large curvatures which is measured during the optical evaluation in Section 4.3.2.

5.5.3 Validation of the forming simulation of Biax-NCF

The membrane and bending modeling approaches outlined above are applied to forming simulations of different punch shapes in this section. The hemisphere, tetrahedron and square box punch shapes are investigated to evaluate the validity of the proposed approach for different geometrically challenging features and identify the limitations of a pure shear based model. The same setups introduced for UD-NCF in Section 5.4.1 are utilized and the results are compared to experimental forming tests described in Section 4.6. Two single-layer ($[(0°/90°)_B]$ and $[(\pm45°)_B]$) layups and one double-layer ($[(0°/90°)_B/(\pm45°)_B]$) layup are considered. Tool-ply and ply-ply contact are modeled via the built-in general contact algorithm in ABAQUS/Explicit. The dynamic friction coefficients are selected based on average values of the measured configurations in Section 4.5

as $\mu^{\text{tool-ply}} = 0.157$ and $\mu^{\text{ply-ply}} = 0.449$. The experimental and simulative shear strain distribution for the three punch shapes are shown in Figure 5.30.

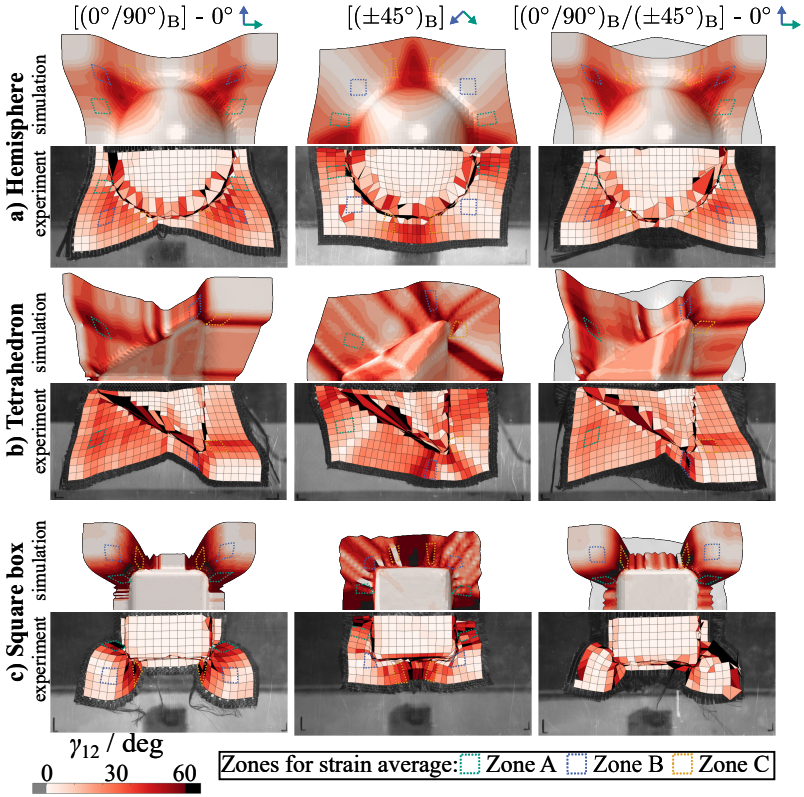

Figure 5.30: Comparison of experimental and simulative strains for [0°] and [45°] single-layer as well as [0°/90°] double-layer setups in the hemisphere, tetrahedron and square box forming tests of Biax-NCF.

The simulative outer contours are in good quantitative agreement with the experiments for the hemisphere and tetrahedron punch, with slight deviations for the square box (cf. Figure A.15 in Appendix A.2.11 for an isolated comparison of the contours). The general orientation and location of areas with high shear

deformation are predicted well for all investigated setups. However, the peak shear angles in high deformation areas are overestimated. This is also reflected in the detailed analysis of the strains in the local zones A, B and C shown in Figure 5.31.

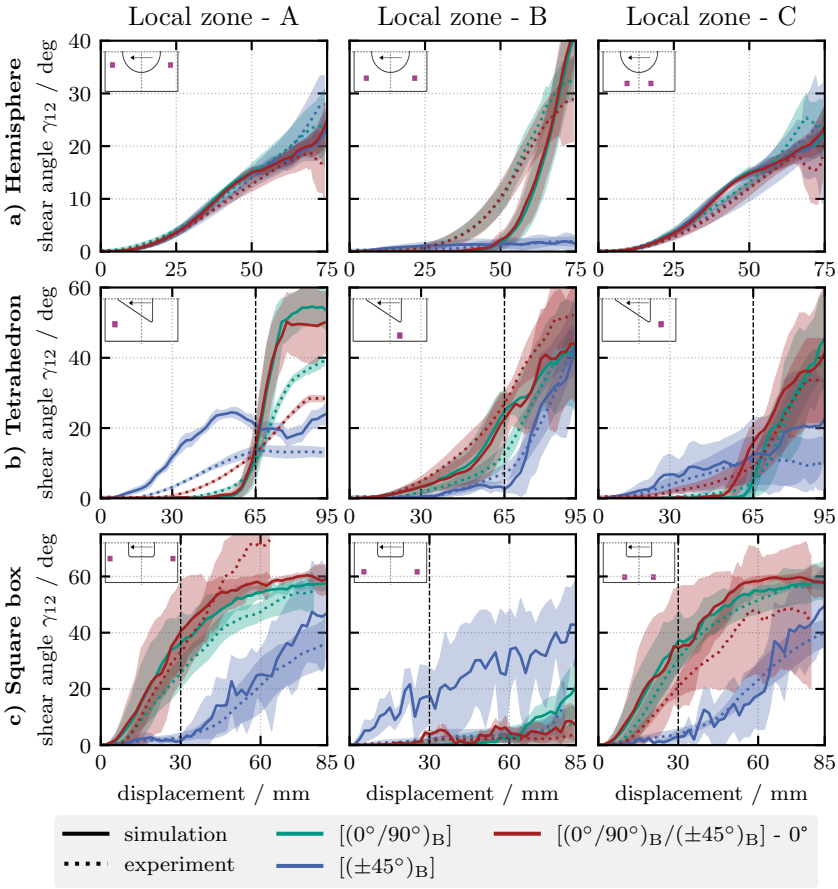

Figure 5.31: Shear angle in local zones of the a) hemisphere, b) tetrahedron and c) square box forming tests.

The local shear angle in zones further away from the punch area, i. e. zone B for the hemisphere and box as well as zone A for the tetrahedron, is notably overestimated by the simulation. This is attributable to relative roving slippage within the fiber layer and between both fiber layers of the Biax-NCF during the experiments in these areas, cf. Appendix A.1.5. The local shear angles in the other zones are in good quantitative agreement with the experiments.

In the square box simulations local shear bands occur in the areas between the flaps in the $(0°/90°)_{\mathrm{B}}$-layers as well as the diagonal areas of the $(\pm 45°)_{\mathrm{B}}$-layers, cf. Figure 5.30 c. These result from small out-of plane wrinkling between the die and punch These wrinkles are difficult to identify in the images of the experiments due to the camera angle, but they are consistently observed in box forming studies of materials with comparable forming properties presented by Wang et al. [223] as well as Bai et al. [68].

5.5.4 Summary and conclusion

The general transferability of the developed modeling approach and outlined parameterization strategies from UD-NCF to Biax-NCF is demonstrated in this section. The hyperelastic membrane model is easily adapted for Biax-NCF based on a pure shear assumption due to the modularity of the energy contributions. This simplifying assumption in combination with the generalized strain energy function enables an analytical determination of the material parameters from the 45°-OAT. A modified locking is introduced to prevent a collapse of highly shear elements. Good agreement with the experimental results is obtained for medium displacements, but the forces are overestimated for large deformations, especially for the 30°-OAT. This results from neglected roving slippage, which cannot be modeled with the current single-layer approach.

The parameterization strategy of the bending approach is directly transferable to Biax-NCF and only requires the inverse determination of the shear bending properties to model the 45°-cantilever test. However, similar to UD-NCF,

the impact of the shear parameterization on the forming behavior cannot be conclusively evaluated and requires further analysis to assess its relevance.

The general forming behavior of Biax-NCF is adequately described despite the highly simplified approaches. The location and orientation of areas with high shear angles are predicted well, but the peak shear angles are overestimated due to the neglected roving slippage.

In summary, the developed methods can be utilized for a decent approximation of the forming behavior of Biax-NCF without notable modifications to the implementation itself. The majority of the required material parameters can be determined analytically, enabling a quick and simple parameterization process. However, the shear-based approach for Biax-NCF reveals a limitation at high deformations, as the specific deformation of NCFs requires the modeling of relative roving slippage compared to woven fabrics.

5.6 Discussion and conclusion

In the scope of this chapter, a new hyperelastic membrane modeling approach for UD-NCF is developed based on the experimental characterization of the forming behavior and a preliminary investigation of existing approaches. The new approach is combined with a hypoelastic bending model to accurately predict the forming behavior for different geometries. The general transferability of the proposed modeling approach and parameterization strategies is demonstrated by an application to forming of Biax-NCF.

Preliminary investigation Initially, existing approaches for macroscopic modeling of UD-NCF are analyzed and compared to a proposed approach based on the decoupled description of the shear, transverse tensile and perpendicular compressive behavior. Shear-focused approaches are not suitable [139], because pure shear is not an intrinsic deformation mode of UD-NCF. Similarly, a simple decoupled model is not able to describe the different ratios of superimposed strains during off-axis-tension tests (OATs) simultaneously. This reveals the necessity of a coupled transverse tensile behavior to model large roving slippage. Additionally, a stiffness-based approach is prone to numerical instabilities, which result in localized deformations or excessive tensile strains.

The comprehensive approach by Schirmaier et al. [86, 137] utilizes individual elastic and elastic-plastic constitutive equations based on custom strain measures with multiple couplings to model UD-NCF. Despite an acceptable overall approximation of the behavior, three weaknesses of this approach have been identified. First, parameterization, transferability to other materials, and extension of the approach are hampered by the complex constitutive equations with a high number of material parameters. Second, the shear angle and perpendicular compression in the main deformation zone (MDZ) of the OATs are significantly underestimated. Third, spurious tensile strains occur during forming simulations, indicating some instability of unidentifiable origin.

Membrane modeling Based on the experimental characterization of the forming behavior and the analysis of the state of research, a new hyperelastic membrane approach is developed with the objective of minimizing the complexity of the model while achieving adequate accuracy. Suitable pseudo-invariants are introduced and related to the different deformation modes of UD-NCF concluded from the experimental analysis in Chapter 4. Generalized formulations based on piecewise functions with physically interpretable parameters are chosen for the strain energy density contributions and coupling. A coupling between the transverse tensile and perpendicular compressive behavior is necessary to model significant roving slippage. An uncoupled shear behavior was found to be sufficient. The above features simplify the parameterization and allows a modular implementation of the approach to facilitate transferability to other materials and future modifications. The model is parameterized using the measured forces and strains in different multiaxial deformation states obtained from 30°-, 45°- and 60°-OATs. It turned out that a perpendicular compressive locking is essential to prevent a collapse of highly sheared elements, while a traditional shear locking and a transverse tensile locking are not necessary. The perpendicular locking acts as an alternative shear locking mechanism for unidirectional fabrics. Excellent quantitative agreement is achieved for all OATs despite less than half the required material parameters compared to the approach of Schirmaier et al. [86, 137]. However, three aspects of the proposed approach could be improved further.

First, roving slippage is modeled homogenized over the entire main deformation zone due to the limitations of a macroscopic approach that assumes homogeneous material properties over the whole specimen. In the experiments, roving slippage is limited to the area between the main and secondary deformation zones. These areas could be identified during the simulation by calculating strain gradients within each element based on information of neighboring elements. Subsequently, the shear gradient could be used as an additional coupling for the transverse tensile behavior to localize the modeling of slippage.

Second, significant in-plane bending is observed in the transition zones of the OATs as described in Section 4.2. This is not considered in the current approach

due to the limitations of classical Cauchy continuum theory. Therefore, generalized continua approaches are required [145,259,299], which have not yet been realized for ABAQUS/Explicit. Alternatively, the curvature of the rovings could be calculated based on neighboring elements similar to the approach proposed by Steer et al. [301] for woven fabrics. An additional in-plane bending stiffness of the roving is expected to model the asymmetrical shear behavior of UD-NCF that primarily occurs parallel to the rovings in the experiments (21-shear) by preventing excessive shear transverse to the rovings (12-shear).

Third, the parameterization of the transverse tensile behavior based on OATs neglects the influence of pressure in thickness-direction. This would increase the friction between the glass fibers, rovings and stitching, thus increasing the resulting transverse stiffness. Furthermore, if pressure is applied to the glass fibers at two points, the stiffness in the areas in between would need to be increased, as the glass fibers are nearly inextensible after an initial decrimping. The upper and lower limits of this effect were demonstrated by Schirmaier et al. [110] in transverse tensile tests with either fully slipping or clamped glass fibers for a similar UD-NCF. However, the consideration of this effect would require a three-dimensional approach combined with a non-local method to propagate the impact of the pressure on the transverse behavior along the elements in glass-fiber direction.

Bending modeling A hypoelastic bending approach is parameterized to model the strongly anisotropic behavior of UD-NCF decoupled from the membrane behavior. Since this work focuses on membrane behavior, a simplified linear-elastic bending behavior is assumed. This simplification enables an analytical calculation of the stiffnesses in the principal directions from the experimentally measured Peirce bending stiffness. The shear component is determined by modeling the twist deformation during 45°-cantilever tests. The predicted deflection curves of all cantilever tests are in good agreement with the experimental measurements. However, the influence of the shear component and the neglected decrease in bending stiffness for higher curvatures on the forming behavior cannot be assessed based on the available experimental

results due to the planar blankholders. Additional tests without blankholders are desirable to evaluate the accurate approximation of the bending behavior.

Forming simulation The hyperelastic membrane approach and hypoelastic bending approach are applied to forming simulations of hemisphere, tetrahedron and square box punch shapes for different layups. The predicted forming behavior is comprehensively evaluated qualitatively and quantitatively based on the experimental tests presented in Section 4.6. The specific deformation behavior of UD-NCF with an asymmetric deformation in different modes is well predicted in all configurations. The outer contours and strains for the hemisphere tests are in particularly good quantitative agreement with the experiments. In the square box and tetrahedron single-layer configurations, the outer contours and areas of high deformation are predicted well. The shear and compressive strains are in good agreement, but the transverse strains are overestimated. This results from the above outlined limitations of the membrane approach, which become more notable in those setups due to the geometrically challenging corners and large forming depth. However, this effect is already significantly reduced in the double-layer tests.

In the experimental double-layer tests for the tetrahedron punch strong interactions are observed, which were not predicted by the model. To further investigate this effect, a variation of the ply-ply coefficient of friction is used. The CoF required to reproduce the observed interactions would be of a higher order of magnitude than that measured during characterization in Section 4.5. This indicates the existence of interlocking effects between the mesoscopic constituents of both layers, which were not detected during characterization. However, more detailed experiments are needed to make a conclusive claim, especially since the interactions are not reproducible in every test. Forming tests with different blankholder pressures for the tetrahedron in particular as well as the other punch shapes would be necessary to identify triggers for their consistent occurrence. Subsequently, a new interface model needs to be developed.

In all simulations local transverse shear bands are observed, which are prevented during experiments due to the in-plane bending stiffness of the rovings. They do not significantly affect the overall forming behavior, but emphasis the above outlined need for generalized continua approaches for membrane modeling of UD-NCF.

Biax-NCF The general transferability of the developed approaches to Biax-NCF is demonstrated. The hyperelastic membrane model is adapted based on a pure shear assumption without notable modifications to the implementation itself due to the modularity of the approach. A direct analytical determination of the membrane material parameters from the 45°-OAT is possible due to the pure shear assumption. The parameterization strategy of the bending approach is directly transferable to Biax-NCF and only requires the inverse determination of the shear bending properties to model the 45°-cantilever test. The general forming behavior of Biax-NCF is adequately described despite the highly simplified approach until medium deformations. However, the shear-based approach for Biax-NCF reveals an expected limitation at high deformations, as the specific deformation of NCFs requires the modeling of relative roving slippage compared to woven fabrics. Since slippage manifests numerically by positive tensile strains, this cannot be modeled in a single-layer approach without artificial strains in fiber direction. A possible remedy to this limitation is proposed by Bel et al. [132] by individually modeling the fiber layers connected by bar elements. A specific contact formulation is applied to restrict sliding between the layers and bar elements to the fiber direction. Subsequently, the membrane model of UD-NCF could be applied to the individual fiber layers without simplifying assumptions.

6 Three-dimensional solid-shell element formulation for forming simulations[7,8]

Outline

The following chapter presents the development of a three-dimensional solid-shell element formulation for forming of engineering textiles. First, the fundamentals of the element formulation are outlined in Section 6.1. For a locking-free behavior, a selective reduced integration scheme (SRI) is combined with the assumed natural strain (ANS) and enhanced assumed strain (EAS) method. To account for the specific requirements of CoFRP forming, a membrane-bending decoupling is introduced based on a Taylor series approximation of the strains and combined with a specific stabilization technique. Second, the locking-free behavior in general is demonstrated and validated by comparison to conventional three-dimensional elements in forming simulations of isotropic as well as anisotropic materials in Section 6.2. Third, the solid-shell element is directly applied to forming of engineering textiles in Section 6.3 to highlight the potential of the developed formulation.

[7] Extracts from Chapter 6 have been previously published in [352], i. e. B. Schäfer, D. Dörr, and L. Kärger. Reduced-Integrated 8-Node Hexahedral Solid-Shell Element for the Macroscopic Forming Simulation of Continuous Fibre-Reinforced Polymers. *Procedia Manufacturing*,47:pp. 134–139,2020 | Sections 6.1.1 and 6.2.1 have been revised and adapted from Sections 2 & 3 of [352].

[8] Extracts from Chapter 6 have been previously published in [353], i. e. B. Schäfer, D. Dörr, and L. Kärger. Potential and challenges of a solid-shell element for the macroscopic forming simulation of engineering textiles. *PoPuPS of ULiège Library*, DOI: 10.25518/esaform21.883, ESAFORM 2021, Liège/Belgium, 2021 | Sections 6.1.2, 6.2.2 and 6.3.1 have been revised and adapted from Sections 2 & 3 of [353].

6.1 Solid-shell element formulation

The consideration of compaction during forming is necessary to predict the final thickness of a component and requires a three-dimensional material behavior in an appropriate element formulation. The individual plies within a composite layup are usually modeled as single element layers within layer-by-layer approaches to account for the intra- and inter-ply mechanisms, cf. Section 2.3.3. Conventional three-dimensional solid elements are prone to numerical locking effects during bending deformation of thin structures, cf. Section 2.4.1. Additionally, their implementation in commercial FE solvers usually does not allow for a membrane-bending decoupling. Thus, they are not suitable for a direct application in forming simulations of engineering textiles. Therefore, a solid-shell element formulation based on the methods to prevent locking outlined in Section 2.4.1 is proposed in this section with specific modifications to account for the requirements of CoFRP forming. The objective is a representation of each ply in a layup with a single element layer to ensure direct transferability of methods developed for 2D approaches.

6.1.1 Fundamental solid-shell element formulation[7]

The fundamental solid-shell element formulation applied in this work was originally proposed by Schwarze and Reese [314, 332] and denoted as Q1STs. The formulation is based on a selective reduced integration scheme (SRI), the assumed natural strain method (ANS) with four collocation points and the enhanced assumed strain method (EAS) with a single EAS-DOF. The original notation is adopted for its derivation in the following.

The Q1STs formulation is derived from the standard isoparametric 8-node hexahedral brick-element with tri-linear shape functions [240, pp. 188-190].

[7] Adapted and revised from [352], cf. footnote p. 201 for details.

To enable modifications of the strains, it is based on the two-field form of the Hu-Washizu variational principle initially proposed by Simo and Rifai [312]

$$\delta g_1(\boldsymbol{u}, \boldsymbol{\alpha}) = \int_{V_0} \boldsymbol{S}(\boldsymbol{E}) \colon \delta \boldsymbol{E}_{\mathrm{c}} \mathrm{d}V + \int_{V_0} \rho \ddot{\boldsymbol{u}} \colon \delta \boldsymbol{u} \mathrm{d}V - \delta g^{\mathrm{ext}} = 0, \tag{6.1}$$

in combination with the orthogonality condition

$$\delta g_2(\boldsymbol{u}, \boldsymbol{\alpha}) = \int_{V_0} \boldsymbol{S}(\boldsymbol{E}) \colon \delta \boldsymbol{E}_{\mathrm{e}} \mathrm{d}V = 0, \tag{6.2}$$

where ρ is the density, V is the volume, δg^{ext} is the virtual work of external loads and $\boldsymbol{S}(\boldsymbol{E})$ is the second Piola-Kirchhoff stress depending on the total strain. According to the enhanced assumed strain (EAS) method introduced in Section 2.4.1, the Green-Lagrange strain tensor $\boldsymbol{E}$ is additively split

$$\boldsymbol{E} = \boldsymbol{E}_{\mathrm{c}}(\boldsymbol{u}) + \boldsymbol{E}_{\mathrm{e}}(\alpha_{\mathrm{e}}), \tag{6.3}$$

into a compatible part $\boldsymbol{E}_{\mathrm{c}}$ depending solely on the displacements $\boldsymbol{u}$, and an enhanced part $\boldsymbol{E}_{\mathrm{e}}$ depending on a single additional enhanced DOF α_{e}.

The *kinematics* of the element formulation are described by tri-linear shape functions. The material coordinates $\boldsymbol{X}$ and the displacement vector $\boldsymbol{u}$ in isoparametric coordinates $\boldsymbol{\xi}$ ($\xi_1 = \xi$, $\xi_2 = \eta$ and $\xi_3 = \zeta$) are calculated from

$$\boldsymbol{X}(\boldsymbol{\xi}) = \sum_{I=1}^{8} N_I \boldsymbol{X}_I^{\mathrm{node}} \quad \text{and} \quad \boldsymbol{u}(\boldsymbol{\xi}) = \sum_{I=1}^{8} N_I \boldsymbol{u}_I^{\mathrm{node}} \tag{6.4}$$

$$\text{with} \quad N_I = \frac{1}{8}(1 + \xi_I \xi)(1 + \eta_I \eta)(1 + \zeta_I \zeta), \tag{6.5}$$

where index I refers to the nodes, shown in Figure 6.1 a. The modifications of the Green-Lagrange strain require a description in the in the isoparametric domain. Therefore, the covariant base vectors of the initial configuration $\boldsymbol{J}_i$

and current configuration $\tilde{\boldsymbol{J}}_i$ result from the columns of the respective Jacobian matrices and displacement gradient $\boldsymbol{D}$ by

$$\boldsymbol{J} = \frac{\partial \boldsymbol{X}}{\partial \boldsymbol{\xi}} = [\boldsymbol{J}_1, \boldsymbol{J}_2, \boldsymbol{J}_3] \quad \text{and} \quad \tilde{\boldsymbol{J}} = \boldsymbol{J} + \frac{\partial \boldsymbol{u}}{\partial \boldsymbol{\xi}} = \boldsymbol{J} + \boldsymbol{D} = [\tilde{\boldsymbol{J}}_1, \tilde{\boldsymbol{J}}_2, \tilde{\boldsymbol{J}}_3]. \tag{6.6}$$

The corresponding contravariant base vectors of the initial configuration $\boldsymbol{H}_i$ and current configuration $\tilde{\boldsymbol{H}}_i$ result from the rows of the inverse Jacobian matrices by

$$\boldsymbol{H}_i = \frac{\partial \xi_i}{\partial X_j} \boldsymbol{e}_j = j_{ij} \boldsymbol{e}_j = (\boldsymbol{J}^{-1})_{ij} \boldsymbol{e}_j \quad \text{and} \quad \tilde{\boldsymbol{H}}_i = (\tilde{\boldsymbol{J}}^{-1})_{ij} \boldsymbol{e}_j. \tag{6.7}$$

The deformation gradient $\boldsymbol{F}$ based on Equations 6.6 and 6.7 has the following form:

$$\boldsymbol{F} = \frac{\partial \boldsymbol{x}}{\partial \boldsymbol{X}} = \frac{\partial x_i}{\partial \xi_k} \frac{\partial \xi_k}{\partial X_j} \boldsymbol{e}_i \otimes \boldsymbol{e}_j = \tilde{J}_k \otimes \boldsymbol{H}_k. \tag{6.8}$$

Thus, the Green-Lagrange strain tensor is derived in its cartesian components E_{ij} and its covariant components $\bar{E}_{ij} = E_{\xi_i \xi_j}$ by

$$\boldsymbol{E}_{\mathrm{c}} = \frac{1}{2}(\boldsymbol{F}^{\mathsf{T}} \cdot \boldsymbol{F} - \boldsymbol{I}) = \frac{1}{2} \left(\frac{\partial \boldsymbol{u}}{\partial \boldsymbol{X}} + \frac{\partial \boldsymbol{u}^{\mathsf{T}}}{\partial \boldsymbol{X}} + \frac{\partial \boldsymbol{u}^{\mathsf{T}}}{\partial \boldsymbol{X}} \frac{\partial \boldsymbol{u}}{\partial \boldsymbol{X}} \right) = E_{ij} \boldsymbol{e}_i \otimes \boldsymbol{e}_j \tag{6.9}$$

$$= \frac{1}{2}(\boldsymbol{J}_i^{\mathsf{T}} \cdot \boldsymbol{D}_j + \boldsymbol{J}_j^{\mathsf{T}} \cdot \boldsymbol{D}_i + \boldsymbol{D}_i^{\mathsf{T}} \cdot \boldsymbol{D}_j) \boldsymbol{H}_i \otimes \boldsymbol{H}_j = \bar{E}_{ij} \boldsymbol{H}_i \otimes \boldsymbol{H}_j \tag{6.10}$$

To simplify the derivation of the necessary modifications to prevent locking in the following, the Voigt matrix notation ($\hat{\bullet}$) is adopted by

$$\hat{\boldsymbol{E}} = [E_{11}, E_{22}, E_{33}, \Gamma_{12}, \Gamma_{23}, \Gamma_{13}]^{\mathsf{T}} \quad \text{with} \quad \Gamma_{ij} = 2E_{ij} \tag{6.11}$$

$$\text{and} \quad \hat{\tilde{\boldsymbol{E}}} = [E_{\xi\xi}, E_{\eta\eta}, E_{\zeta\zeta}, \Gamma_{\xi\eta}, \Gamma_{\eta\zeta}, \Gamma_{\xi\zeta}]^{\mathsf{T}} \quad \text{with} \quad \Gamma_{\xi_i \xi_j} = 2E_{\xi_i \xi_j}. \tag{6.12}$$

The direct transformation between the contravariant and cartesian matrices is achieved by $\hat{\boldsymbol{E}} = \boldsymbol{T} \hat{\tilde{\boldsymbol{E}}}$ with the transformation matrix $\boldsymbol{T}$ based on Equation 6.9 and detailed in Appendix A.3.1.

A *selective reduced integration scheme (SRI)* is applied with a reduced in-plane integration to prevent in-plane shear locking. In thickness-direction a variable number of integration points (IP) are used for a full integration. The resulting integration points are located along the normal through the center of the element, defined by $\boldsymbol{\xi}^{\star} = \{0, 0, \zeta\}^{\mathsf{T}}$ as illustrated in Figure 6.1 a. The efficiency and suitability of this integration scheme for explicit dynamic simulations was demonstrated by Pagani et al. [333]. It captures nonlinear behavior in the thickness direction better compared to commercially available explicit reduced-integration elements, which typically use a single IP in the element center.

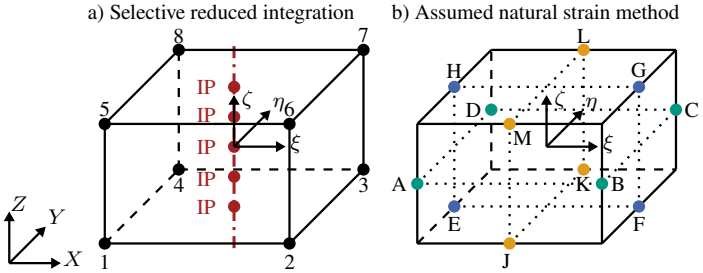

Figure 6.1: Isoparametric solid-shell element | (a) Conventions for the element nodes 1-8 and integration points (IP), (b) Collocation points for the ANS method [352].

The *assumed natural strain method (ANS)* is applied to the compatible strain components in the isoparametric domain $\hat{\hat{\boldsymbol{E}}}_{\mathrm{c}}$. To prevent locking, collocation points are selected within the elements at known zero points of the specific parasitic stresses and the strains are re-interpolated over the element with bi-linear shape functions. The locations of the collocation points in the isoparametric domain are shown in Figure 6.1 b. It is applied to the transverse normal component $E_{\mathrm{c},\zeta\zeta}$ based on Betsch and Stein [354] to prevent curvature-thickness locking (collocation points $P_{\zeta\zeta} \in \{\mathrm{A,B,C,D}\}$). Transverse shear locking is prevented by application to $\Gamma_{\mathrm{c},\eta\zeta}$ (collocation points $P_{\eta\zeta} \in \{\mathrm{E,F,G,H}\}$) and

$\Gamma_{\mathrm{c},\xi\zeta}$ (collocation points $P_{\xi\zeta} \in \{\mathrm{J,K,L,M}\}$), as first proposed by Bathe and Dvorkin [311]. The application of ANS results in:

$$E_{\mathrm{c}\zeta\zeta}^{\mathrm{ANS}}(\xi,\eta) = \sum_{P_{\zeta\zeta}=\mathrm{A}}^{\mathrm{D}} \frac{1}{4}(1+\xi_{P_{\zeta\zeta}}\xi)(1+\eta_{P_{\zeta\zeta}}\eta)E_{\mathrm{c},\zeta\zeta}(\boldsymbol{\xi}_{P_{\zeta\zeta}}), \tag{6.13}$$

$$\Gamma_{\mathrm{c}\eta\zeta}^{\mathrm{ANS}}(\xi,\zeta) = \sum_{P_{\eta\zeta}=\mathrm{E}}^{\mathrm{H}} \frac{1}{4}(1+\xi_{P_{\eta\zeta}}\xi)(1+\zeta_{P_{\eta\zeta}}\zeta)\Gamma_{\mathrm{c},\eta\zeta}(\boldsymbol{\xi}_{P_{\eta\zeta}}), \tag{6.14}$$

$$\Gamma_{\mathrm{c}\xi\zeta}^{\mathrm{ANS}}(\eta,\zeta) = \sum_{P_{\xi\zeta}=\mathrm{J}}^{\mathrm{M}} \frac{1}{4}(1+\eta_{P_{\xi\zeta}}\eta)(1+\zeta_{P_{\xi\zeta}}\zeta)\Gamma_{\mathrm{c},\xi\zeta}(\boldsymbol{\xi}_{P_{\xi\zeta}}). \tag{6.15}$$

The *enhanced assumed strain method (EAS)* is applied to prevent volumetric locking. The ANS method results in a constant transverse normal strain in the out-of-plane direction $\bar{E}_{\mathrm{c}\zeta\zeta}^{\mathrm{ANS}}$. Thus, the enhanced strain tensor $\boldsymbol{E}_{\mathrm{e}}$ is constructed to extend $\bar{E}_{\zeta\zeta}$ by a linear component with a single enhanced DOF α_{e} by

$$\hat{\boldsymbol{E}}_{\mathrm{e}} = \hat{\boldsymbol{B}}_{\mathrm{e}}\alpha_{\mathrm{e}} \quad \text{with} \quad \hat{\boldsymbol{B}}_{\mathrm{e}} = [0,0,\zeta,0,0,0]^{\mathsf{T}}. \tag{6.16}$$

A main advantage of this simple formulation for $\hat{\boldsymbol{E}}_{\mathrm{e}}$ is the later estimation of α_{e} within a single iteration of an explicit dynamic integration scheme, due to the small explicit time step size, as demonstrated by Pagani et al. [333].

A *Taylor expansion of the compatible Green-Lagrange strains* with respect to the element center $\boldsymbol{\xi} = \mathbf{0}$ is carried out to introduce an hourglass stabilization for the SRI and enable later adaptations for engineering textiles

$$\hat{\boldsymbol{E}}_{\mathrm{c}} \approx \underbrace{\hat{\boldsymbol{E}}_{\mathrm{c}}^{0} + \zeta\hat{\boldsymbol{E}}_{\mathrm{c}}^{\zeta} + \zeta^2\hat{\boldsymbol{E}}_{\mathrm{c}}^{\zeta\zeta}}_{\hat{\boldsymbol{E}}_{\mathrm{c}}^{\star}} + \underbrace{\xi\hat{\boldsymbol{E}}_{\mathrm{c}}^{\xi} + \eta\hat{\boldsymbol{E}}_{\mathrm{c}}^{\eta} + \xi\eta\hat{\boldsymbol{E}}_{\mathrm{c}}^{\xi\eta} + \eta\zeta\hat{\boldsymbol{E}}_{\mathrm{c}}^{\eta\zeta} + \xi\zeta\hat{\boldsymbol{E}}_{\mathrm{c}}^{\xi\zeta}}_{\hat{\boldsymbol{E}}_{\mathrm{c}}^{\mathrm{hg}}}, \tag{6.17}$$

where $\hat{\boldsymbol{E}}_{\mathrm{c}}^{\xi_i} = \left.\dfrac{\partial\hat{\boldsymbol{E}}_{\mathrm{c}}}{\partial\xi_i}\right|_{\boldsymbol{\xi}=\mathbf{0}}$ are constant matrices, listed in Section A.3.1. The compatible strain is separated into a part $\hat{\boldsymbol{E}}_{\mathrm{c}}^{\star}$ related to the full integration in thickness direction and a part $\hat{\boldsymbol{E}}_{\mathrm{c}}^{\mathrm{hg}}$ unaffected by the SRI. The strain part

$\hat{\boldsymbol{E}}_{\mathrm{c}}^{\mathrm{hg}}$ is essential for an hourglass stabilization to achieve a full rank of the element stiffness matrix despite the reduced in-plane integration. A similar Taylor expansion of the second Piola-Kirchhoff stress along the element normal through the center $\boldsymbol{\xi}^\star$ is carried out

$$\hat{\boldsymbol{S}} \approx \underbrace{\hat{\boldsymbol{S}}(\hat{\boldsymbol{E}}^\star)}_{\hat{\boldsymbol{S}}^\star} + \underbrace{\overbrace{\left.\frac{\partial \hat{\boldsymbol{S}}(\hat{\boldsymbol{E}})}{\partial \hat{\boldsymbol{E}}}\right|_{\boldsymbol{\xi}=\boldsymbol{\xi}^\star}}^{\hat{\mathbb{C}}^\star} : \left(\xi \hat{\boldsymbol{E}}_{\mathrm{c}}^{\xi} + \eta \hat{\boldsymbol{E}}_{\mathrm{c}}^{\eta} + \xi\zeta \hat{\boldsymbol{E}}_{\mathrm{c}}^{\xi\zeta} + \eta\zeta \hat{\boldsymbol{E}}_{\mathrm{c}}^{\eta\zeta}\right)}_{\boldsymbol{S}^{\mathrm{hg}}}, \tag{6.18}$$

where again the stress is separated into a part related to the full integration in thickness direction $\hat{\boldsymbol{S}}^\star$ and hourglass stabilization $\boldsymbol{S}^{\mathrm{hg}}$. The material stiffness tangent $\hat{\mathbb{C}}^\star$ in general can be material- and deformation-dependent in thickness direction. To simplify the hourglass stabilization, it is replaced by an approximation based on a constant linear-elastic material tangent $\hat{\mathbb{C}}^{\mathrm{hg}}$. The specific choice of $\hat{\mathbb{C}}^{\mathrm{hg}}$ in the context of engineering textiles will be discussed in Section 6.1.2. This method allows for efficient analytical integration of the hourglassing terms to ensure a full rank of the element stiffness matrix.

Finally, the *discretization and integration* of Equations 6.1 and 6.2 is carried out on element level. Thereby, the infinitesimal volume on element level is approximated with the Jacobian determinant at the center $J^0 = \det(J)|_{\boldsymbol{\xi}=0}$ by $\mathrm{d}V^{\mathrm{e}} = J^0 \mathrm{d}\Omega^{\mathrm{e}} = J^0 \mathrm{d}\xi \mathrm{d}\eta \mathrm{d}\zeta$. The discretized weak element formulation corresponding to Equations 6.1 and 6.2 combined with Equations 6.18 and 6.16 results in:

$$\boldsymbol{G}_1 = \boldsymbol{R}_{\mathrm{u}}^\star + \boldsymbol{R}_{\mathrm{u}}^{\mathrm{hg}} + \boldsymbol{M}\ddot{\boldsymbol{u}} - \boldsymbol{G}_{\mathrm{ext}} = \boldsymbol{0} \quad \text{and} \tag{6.19}$$

$$G_2 = R_\alpha^\star = 4J^0 \int_{-1}^{1} \hat{\boldsymbol{B}}_{\mathrm{e}}^{\mathsf{T}} \cdot \hat{\boldsymbol{S}}^\star \mathrm{d}\zeta = 0, \tag{6.20}$$

where $\boldsymbol{M}$ is the element mass matrix and $\boldsymbol{G}_{\mathrm{ext}}$ the external element force vector.

The internal forces related to the out-of-plane integration $\boldsymbol{R}_{\mathrm{u}}^{\star}$ and hourglass stabilization are derived as

$$\begin{aligned}
\boldsymbol{R}_{\mathrm{u}}^{\star} &= \int_{\Omega^{\mathrm{e}}} \hat{\boldsymbol{B}}_{\mathrm{c}}^{\star\mathsf{T}} \cdot \hat{\boldsymbol{S}}^{\star} J^0 \mathrm{d}\Omega^{\mathrm{e}} \\
&= 4J^0 \int_{-1}^{1} \left(\hat{\boldsymbol{B}}_{\mathrm{c}}^{0} + \zeta \hat{\boldsymbol{B}}_{\mathrm{c}}^{\zeta} + \zeta^2 \hat{\boldsymbol{B}}_{\mathrm{c}}^{\zeta\zeta} \right)^{\mathsf{T}} \cdot \hat{\boldsymbol{S}}^{\star} \mathrm{d}\zeta, \qquad (6.21) \\
\boldsymbol{R}_{\mathrm{u}}^{\mathrm{hg}} &= \int_{\Omega^{\mathrm{e}}} \hat{\boldsymbol{B}}_{\mathrm{c}}^{\mathrm{hg}\mathsf{T}} \cdot \hat{\boldsymbol{S}}^{\mathrm{hg}} J^0 \mathrm{d}\Omega^{\mathrm{e}} \\
&= \frac{8}{3} J^0 \left(\hat{\boldsymbol{B}}_{\mathrm{c}}^{\xi\mathsf{T}} \cdot \left(\hat{\mathbb{C}}^{\mathrm{hg}} : \hat{\boldsymbol{E}}_{\mathrm{c}}^{\xi} \right) + \hat{\boldsymbol{B}}_{\mathrm{c}}^{\eta\mathsf{T}} \cdot \left(\hat{\mathbb{C}}^{\mathrm{hg}} : \hat{\boldsymbol{E}}_{\mathrm{c}}^{\eta} \right) \right) \\
&\quad + \frac{8}{9} J^0 \left(\hat{\boldsymbol{B}}_{\mathrm{c}}^{\eta\zeta\mathsf{T}} \cdot \left(\hat{\mathbb{C}}^{\mathrm{hg}} : \hat{\boldsymbol{E}}_{\mathrm{c}}^{\eta\zeta} \right) + \hat{\boldsymbol{B}}_{\mathrm{c}}^{\xi\zeta\mathsf{T}} \cdot \left(\hat{\mathbb{C}}^{\mathrm{hg}} : \hat{\boldsymbol{E}}_{\mathrm{c}}^{\xi\zeta} \right) \right), \qquad (6.22)
\end{aligned}$$

where the $\hat{\boldsymbol{B}}_{\mathrm{c}}^{(\bullet)}$ matrices represent the relation between the respective virtual compatible strains $\delta\hat{\boldsymbol{E}}_{\mathrm{c}}^{(\bullet)}$ and displacements according to $\delta\hat{\boldsymbol{E}}_{\mathrm{c}}^{(\bullet)} = \hat{\boldsymbol{B}}_{\mathrm{c}}^{(\bullet)} \delta\boldsymbol{u}$. The discretized weak from of the orthogonality condition G_2 in Equation 6.20 is used to iteratively update the enhanced DoF α_{e} based on static condensation at the element level as proposed by Simo et al. [355]. In the context of explicit simulations Pagani et al. [333] showed that an accurate approximation of this procedure can be achieved within one iteration due to the small time step size. Therefore, G_2 is linearized with respect to α_{e} and an explicit estimate of $\Delta\alpha_{\mathrm{e}}$ calculated

$$\Delta\alpha_{\mathrm{e}} = -S_{\alpha\alpha}^{-1} R_{\alpha}^{\star} \quad \text{with} \quad S_{\alpha\alpha} = 4J^0 \int_{-1}^{1} \hat{\boldsymbol{B}}_{\mathrm{e}}^{\star\mathsf{T}} \cdot \left(\hat{\mathbb{C}}^{\star} : \hat{\boldsymbol{B}}_{\mathrm{e}}^{\star} \right) \mathrm{d}\zeta \qquad (6.23)$$

6.1.2 Modifications for forming of engineering textiles[8]

The locking-free behavior of the above outlined Q1STs solid-shell element has been shown by Schwarze and Reese for small [314] as well as large [332] deformations in several well-known benchmarks. It showed promising results for structural simulations of consolidated fiber-reinforced composites [334, 335], deep drawing of sheet metals [333, 336] as well as packaging simulation of cardboard [337]. However, some modifications are necessary to adapt it for forming simulations of engineering textiles.

First, the *hourglass stabilization* must be adapted by selecting a suitable approximation of the hourglass stiffness $\hat{\mathbb{C}}^{\mathrm{hg}}$ based on Equation 6.18. For the Q1STs solid-shell, Schwarze and Resse [314, 332] proposed a constant deviatoric matrix $\hat{\mathbb{C}}^{\mathrm{hg}} = \mu_{\mathrm{eff}}^{\mathrm{hg}} \mathbb{I}^{\mathrm{dev}}$ based on an effective shear modulus and the deviatoric part of the fourth-order identity tensor. A deviatoric hourglassing stiffness prevents volumetric locking for the stabilization term, according to the B-Bar method developed by Hughes [356]. However, this approximation is based on isotropic effective shear modulus and underestimates the hourglass stresses for highly anisotropic materials resulting in instabilities. Thus, an alternative hourglass stiffness calculation based on the material tangent evaluated in the element center is proposed

$$\hat{\mathbb{C}}^{\mathrm{hg}} = \left. \frac{\partial \hat{\boldsymbol{S}}(\hat{\boldsymbol{E}})}{\partial \hat{\boldsymbol{E}}} \right|_{\boldsymbol{\xi}=\mathbf{0}} , \tag{6.24}$$

which accounts for the anisotropy of the material, while still allowing for an analytical integration in Equation 6.22. This approach is limited to compressible materials as it does not conform with the B-bar method. However, engineering textiles are in most cases compressible and the influence of a possible volumetric locking in the hourglass terms is assumed to be small.

[8] Adapted and revised from [353], cf. footnote p. 201 for details.

Second, a *membrane-bending decoupling* is a necessary requirement for CoFRP forming, cf. Section 2.3.3. This can be accomplished intrinsically or extrinsically with different methods. The intrinsic methods for individual elements are based on modifications to the out-of-plane integration scheme [219, 281], variable stiffness over the thickness [283, 285] or generalized continua approaches [162, 239, 282]. Based on these ideas and in combination with the Taylor approximation of the strains in Equation 6.17, the following split is introduced to the stress $\hat{\boldsymbol{S}}^{\star}$ during the integration in Equation 6.21

$$\hat{\boldsymbol{S}}^{\star} = \hat{\boldsymbol{S}}^{\mathrm{mem}} + \hat{\boldsymbol{S}}^{\mathrm{bend}} = \hat{\mathbb{C}}^{\mathrm{mem}} : (\hat{\boldsymbol{E}}_{\mathrm{c}}^{0} + \hat{\boldsymbol{E}}_{\mathrm{e}}) + \hat{\mathbb{C}}^{\mathrm{bend}} : \left(\zeta \hat{\boldsymbol{E}}_{\mathrm{c}}^{\zeta} + \zeta^{2} \hat{\boldsymbol{E}}_{\mathrm{c}}^{\zeta\zeta}\right). \tag{6.25}$$

The membrane part $\hat{\boldsymbol{S}}^{\mathrm{mem}}$ is related to the constant compatible strain in the element center $\hat{\boldsymbol{E}}_{\mathrm{c}}^{0}$ as well as the enhanced strains $\hat{\boldsymbol{E}}_{\mathrm{e}}$ by a membrane stiffness $\hat{\mathbb{C}}^{\mathrm{mem}}$. The bending part $\hat{\boldsymbol{S}}^{\mathrm{bend}}$ is related to the out-of-plane components of the compatible strain $\hat{\boldsymbol{E}}_{\mathrm{c}}^{\zeta}$ and $\hat{\boldsymbol{E}}_{\mathrm{c}}^{\zeta\zeta}$ by a bending stiffness $\hat{\mathbb{C}}^{\mathrm{bend}}$. A major advantage of this solid-shell formulation is that there are no restrictions on the three-dimensional stiffnesses $\hat{\mathbb{C}}^{(\bullet)}$ and that more complex formulations for $\hat{\boldsymbol{S}}^{\star}$ can be introduced based on the same split.

6.1.3 Implementation

The modified solid-shell is implemented within a VUEL user-defined element formulation in ABAQUS/Explicit. To ensure a computationally efficient implementation, a MATHEMATICA-based programming environment called AceGEN [307] is used. It provides symbolic and algebraic capabilities, combined with a simultaneous runtime-optimization. Figure 6.2 illustrates an implementation concept by means of a flowchart. The matrices corresponding to the expressions in Section 6.1.1 are given in their implemented form in Appendix A.3.1. In addition, the utilized solid-shell element formulation requires a specific coordinate system (COS) and node convention to ensure the thickness integration in the thinnest direction, cf. Figure 6.1. However, automatic meshing algorithms do not necessarily comply with these conventions. Therefore,

the COS is temporarily rotated and an internal renumbering of the nodes is applied if required. The method is detailed in Appendix A.3.2

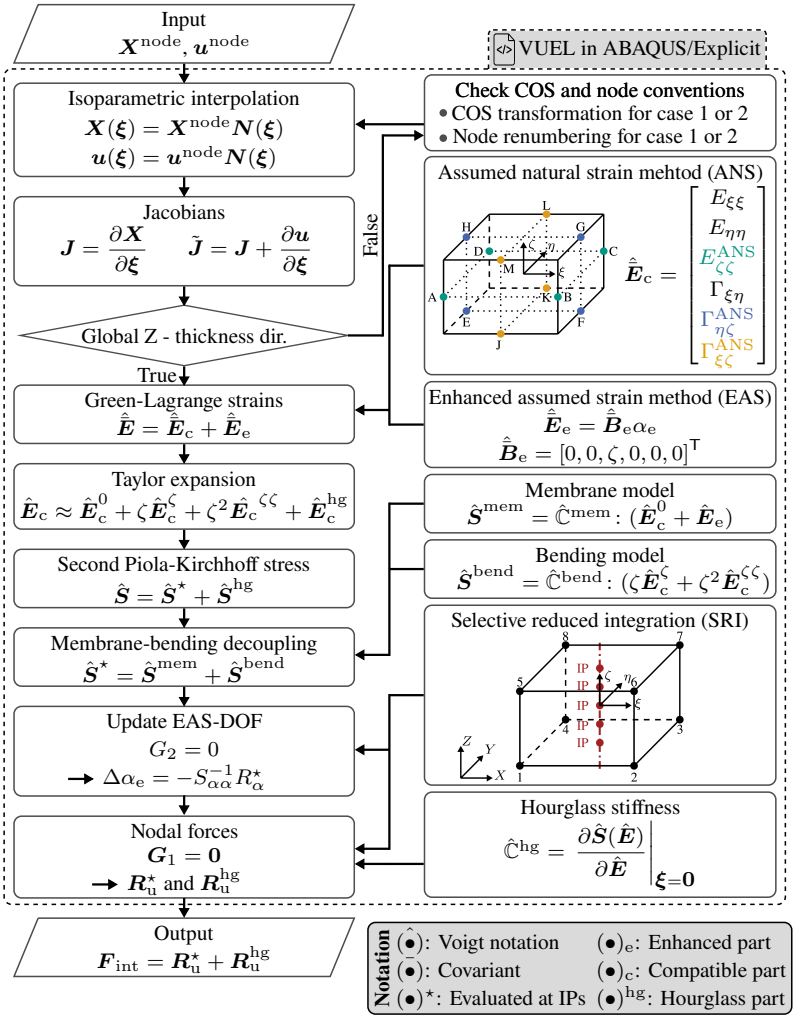

Figure 6.2: Flowchart of the solid-shell implemented as a VUEL in ABAQUS/Explicit.

6.2 Validation of locking-free behavior in forming simulations

The locking-free behavior of the Q1STs solid-shell element has been shown by Schwarze and Reese in several well-known benchmarks for small [314] as well as large [332] deformations. These benchmarks mainly focus on prescribed deformations and loads for different scenarios. In order to investigate the advantages of a locking-free behavior in the context of macroscopic forming simulations, the proposed solid-shell element is compared to commercially available three-dimensional elements in ABAQUS/Explicit. For computationally efficient forming simulations, high aspect ratios and a representation of each layer within a single element layer are desirable. The relevant aspect ratio for thin engineering textiles is the ratio of an element's in-plane edge length to thickness $a = l_\mathrm{e}/t_0$.

The behavior of thin engineering textiles is often characterized by a high in-plane stiffness in fiber direction combined with a low bending stiffness. However, the commercially available elements do not offer a direct possibility of decoupling the membrane bending behavior. Therefore, the forming behavior is initially assessed for standard material models and different aspect ratios. Thus, $\mathbb{C}^\mathrm{mem} = \mathbb{C}^\mathrm{bend}$ applies in Equation 6.25 for the solid-shell element in this section. First, the behavior for simple elastic isotropic materials is presented in Section 6.2.1. Cantilever bending tests are utilized to estimate how well locking is prevented for a single layer of thin elements. Hemisphere forming tests without blankholders are applied to evaluate the influence of numerical locking on the forming behavior. Second, the behavior for highly anisotropic materials is presented in Section 6.2.2.

Compared element formulations The convergence behavior of the solid-shell element with $n_\mathrm{IP} = 3$ integration points over the thickness is compared to in ABAQUS/Explicit available elements. The reduced integrated 2D shell element (S4R) is used as a reference for a locking-free bending behavior. For comparison to other 3D element formulations without adaptations to prevent

locking, the standard fully-integrated (C3D8 with $n_{\mathrm{IP}} = 8$) and reduced-integrated (C3D8R with $n_{\mathrm{IP}} = 1$) elements are utilized. Different elements in ABAQUS/Explicit are recommended for bending-dominated problems [357]. The C3D8R-Enh element introduces up to six additional internal degrees of freedom based on the EAS method, to augment the hourglass stabilization forces of the C3D8R element to prevent locking [358]. The fully integrated solid element C3D8I is enhanced by incompatible modes (cf. Section 2.4.1) to prevent parasitic locking stresses in bending deformations. The reduced-integrated continuum shell element SC8R utilizes a kinematic and constitutive behavior similar to conventional shells, but derives them from a three-dimensional shape with displacement DOF to allow linear compaction [357].

6.2.1 Isotropic materials[7]

To isolate the influence of the element formulation as much as possible a simple isotropic material behavior is utilized. A Young's modulus of $E = 100$ MPa and Poisson ratio of $\nu = 0.3$ is chosen to test the behavior for low stiffness.

Cantilever test Potential locking phenomena are prevalent in bending-dominated deformations and increase for higher aspect ratios, cf. Section 2.4.1. A cantilever test is used to estimate how well locking is prevented in the element formulations. The beam has a width of $w_0 = 10$ mm, a length of $l_0 = 60$ mm, a thickness of $t_0 = 0.3$ mm and a tip load of $f = 0.4$ mN is applied. The setup is shown in Figure 6.3.

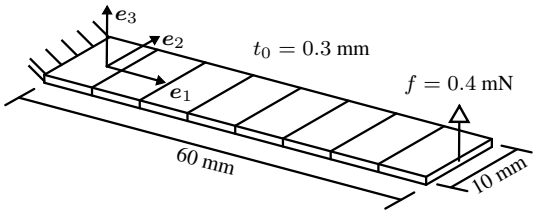

Figure 6.3: Cantilever test setup | Geometry and applied tip load (adapted from [352]).

[7] Adapted and revised from [352], cf. footnote p. 201 for details.

A single element over the width of the beam and a variable number of elements along the length are applied to achieve aspect ratios in bending direction of $a \in [2.5, 5, 10, 20, 40]$. The results for the element formulations outlined in Section 6.2 are shown in Figure 6.4.

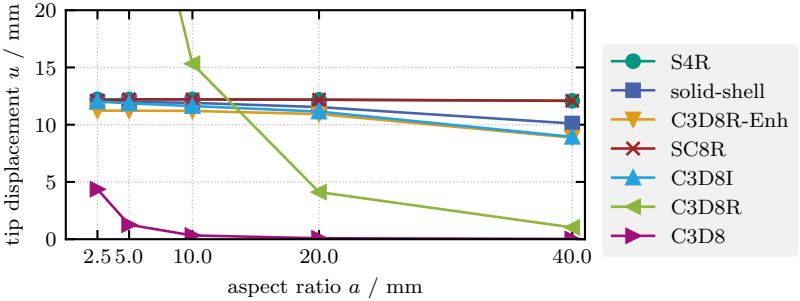

Figure 6.4: Cantilever-bending test | Results for the conventional shell (S4R), solid-shell and different commercially available three-dimensional (C3D8R-Enh, SC8R, C3D8I, C3D8R and C3D8) elements (adapted from [352]).

The S4R reduced-integrated shell element predicts a nearly constant tip displacement for the investigated aspect ratio and is therefore used as the reference solution based on the observed locking-free out-of-plane bending behavior. Similar results are achieved by the continuum shell as its behavior is directly based on a pure shell theory.

First, the elements applying methods to prevent locking are compared to the reference. The solid-shell solution is close to the reference of S4R for $a <= 20$ and converges towards it for $a <= 5$. The deviations increase for higher aspect ratios, but $a <= 20$ should be sufficient for efficient simulations as is a frequently used range macroscopic forming [17, 56, 86, 298]. Similar results to the solid-shell are achieved by the incompatible mode (C3D8I) and enhanced (C3D8R-Enh) formulation. The results of the C3D8R-Enh element with enhanced hourglass stabilization deviate slightly more from the reference, presumably because it applies only one IP over the thickness.

Second, the conventional solid elements are evaluated. The fully-integrated C3D8 element behaves too stiff due to locking effects and even for an aspect ratio as low as 2.5 is unsuited for this bending problem. The reduced-integrated C3D8R element achieves a slightly better solution for high aspect ratios. However, for low aspect ratios a single element over the thickness with only one IP is unable to account for bending deformations and as a result behaves completely compliant. Therefore, the C3D8R element is subjected to locking phenomena for high aspect ratios and is not suitable to model bending for low aspect ratios.

Hemisphere forming The influence of a locking-free element formulation is investigated in numerical hemisphere tests similar to the studies of Haanappel [21] or Dörr [17]. The ratio of shear-to-bending stiffness is one of the key factors influencing the wrinkling behavior during forming [67, 68]. Since locking phenomena mainly affect the bending behavior, a significant effect on the forming behavior with a tendency to larger wrinkles can be expected. The hemisphere has a radius of 90 mm and a height of 35 mm. Forming simulations are conducted without blankholders to provoke significant wrinkling. A single layer with a thickness of $t = 0.3$ mm is formed with aspect ratios of 10 and 20. Figure 6.5 shows the results for a remaining tool stroke of $\Delta u = 7.0$ mm, because at this stage the differences in the forming behavior can be better highlighted than for a completely closed tool.

A significant influence on the distinct wrinkling pattern for the different element types is observed and directly rated in comparison to the S4R results (green: good agreement; orange: slightly too stiff; red: notable differences). A strong correlation between the locking behavior of the element formulations in the cantilever tests and their performance in the hemisphere test is observed. The most similar results for both aspect ratios in terms of size and location of wrinkling compared to the S4R element are observed for the solid-shell and C3D8R-Enh element. The behavior of the SC8R and C3D8I elements is slightly too stiff for an aspect ratio of $a = 20$, indicating some form of locking not detected in the unidirectional bending during the cantilever tests. The forming behavior of the elements without locking prevention (C3D8 and C3D8R) is notably too stiff and different from the reference.

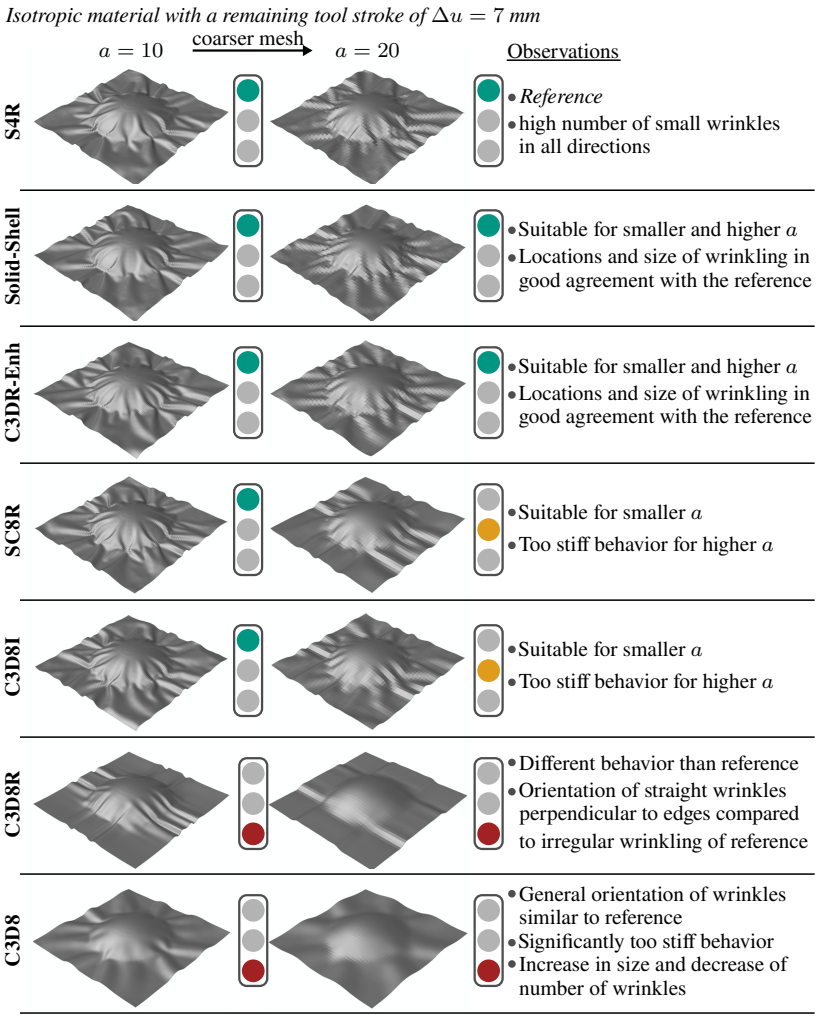

Figure 6.5: Hemisphere forming for isotropic materials | Results and observations for a remaining tool stroke $\Delta u = 7$ mm for the conventional shell (S4R), solid-shell and different commercially available three-dimensional (C3D8R-Enh, SC8R, C3D8I, C3D8R and C3D8) elements. Colors indicate comparison to S4R-results - green: good agreement; orange: slightly too stiff; red: notable differences (adapted from [352]).

6.2.2 Anisotropic materials[8]

The isotropic hemisphere tests show that the element formulation and thus locking-free bending behavior for larger aspect ratios has a significant influence on the macroscopic forming behavior even for a simple material model. In this section, the formulations are compared for highly anisotropic materials, to emulate a deformation behavior more similar to engineering textiles. Two different orthotropic stiffness matrices with high stiffness in one ($\hat{\mathbb{C}}_{\mathrm{UD}}$) or two ($\hat{\mathbb{C}}_{\mathrm{Biax}}$) principal material direction are applied. A sufficiently high stiffness of 1000 MPa in the principal directions is assumed to prevent notable strains in the respective directions instead of a numerically expensive inextensibility condition, similar to the assumption in Chapter 5. Comparatively low shear and compaction stiffnesses are applied to achieve a large anisotropy ratio for both cases:

$$\hat{\mathbb{C}}_i = \begin{bmatrix} 1000 & 0 & 0 & 0 & 0 & 0 \\ 0 & (C_{22})_i & 0 & 0 & 0 & 0 \\ 0 & 0 & 10 & 0 & 0 & 0 \\ 0 & 0 & 0 & 10 & 0 & 0 \\ 0 & 0 & 0 & 0 & 10 & 0 \\ 0 & 0 & 0 & 0 & 0 & 10 \end{bmatrix} \text{MPa} \quad \begin{matrix} \text{with :} \\ (C_{22})_{\mathrm{Biax}} = 1000 \\ (C_{22})_{\mathrm{UD}} = 10 \end{matrix} \tag{6.26}$$

Figure 6.6 shows the results for a remaining tool stroke of $\Delta u = 7.0$ mm. The reduced-integrated shell (S4R) predicts medium-sized wrinkles in all directions for the biaxial stiffness $\hat{\mathbb{C}}_{\mathrm{Biax}}$, and wrinkles mainly oriented along the axis of the highest stiffness and semi-circular runouts towards the edge for the unidirectional stiffness $\hat{\mathbb{C}}_{\mathrm{UD}}$. The results are consistent for both aspect ratios and therefore again used as a reference to compare the element formulations outlined in Section 6.2.

[8] Adapted and revised from [353], cf. footnote p. 201 for details.

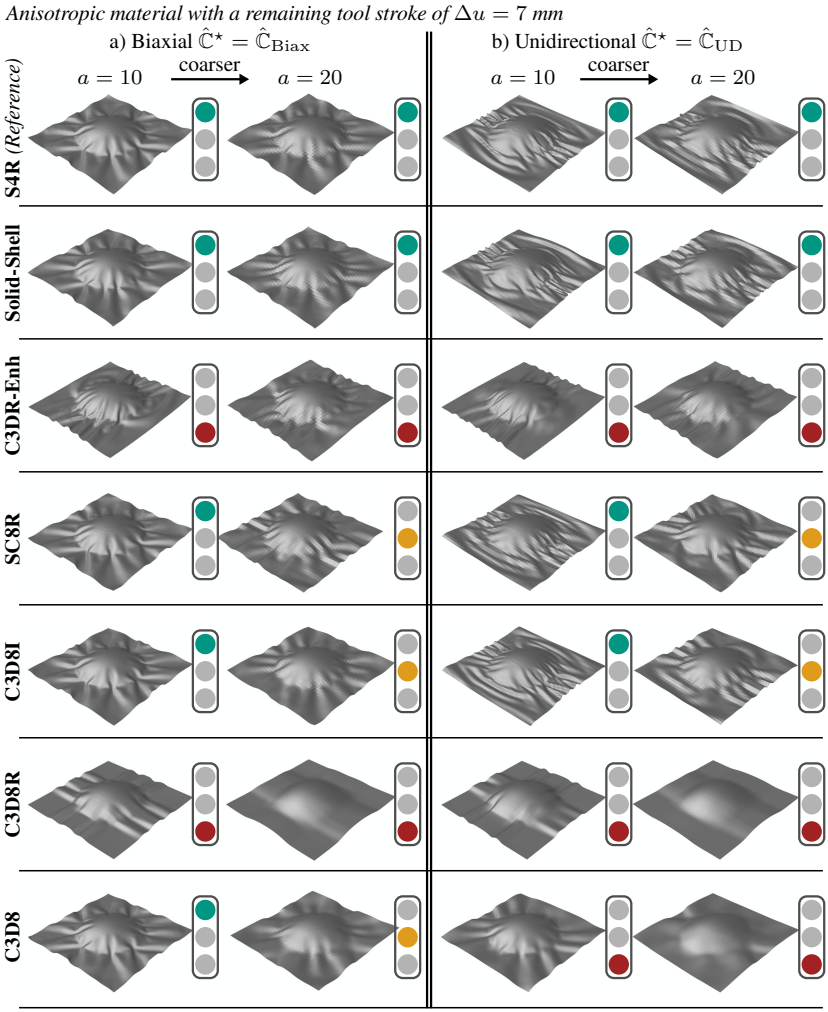

Figure 6.6: Hemisphere forming for anisotropic materials | Results for a remaining tool stroke $\Delta u = 7$ mm for the conventional shell (S4R), solid-shell and different commercially available three-dimensional (C3D8R-Enh, SC8R, C3D8I, C3D8R and C3D8) elements. Colors indicate comparison to S4R-results - Green: Good agreement; Orange: Slightly too stiff; Red: Notable differences (adapted from [353]).

The only element that can achieve a similar forming behavior to the S4R shell for both stiffnesses and aspect ratios is the solid-shell element. This further demonstrates the advantages of the applied methods for a locking-free behavior, as they are independent of material behavior.

The enhanced hourglass stabilization of the C3D8R-Enh element showed promising results for the isotropic material in Section 6.2.1, but the performance for highly anisotropic materials is significantly different. An unexpected unidirectional wrinkling is observed for $\hat{\mathbb{C}}_{\mathrm{Biax}}$ and wrinkles perpendicular to the direction of the highest stiffness for $\hat{\mathbb{C}}_{\mathrm{UD}}$. This is presumably caused by the initial development of the stabilization technique for isotropic materials as it is based on the works of Puso [358]. However, missing details on the exact implementation in ABAQUS/Explicit [357] prevent a conclusive claim.

The observations for the SC8R and C3D8I elements are similar to the results for the isotropic material, cf. Figure 6.5. The general orientation and size of wrinkles are similar to the S4R shell for $a = 10$, but larger wrinkles are observed for an increased aspect ratio of 20 indicating some form of locking.

The forming behavior of the reduced integrated solid element C3D8R is completely different compared to the other examined elements. The observed wrinkling is similar for both materials and close to the results for the isotropic material, cf. Figure 6.5. This further demonstrates its unsuitability for forming simulations. The results of the fully integrated solid element (C3D8) in the biaxial case for $a = 10$ are in good agreement with the reference and only slightly too stiff for the higher aspect ratio. In this case, the higher anisotropy ratio seems to be advantageous compared to isotropic material. However, the behavior for $\hat{\mathbb{C}}_{\mathrm{UD}}$ is notably too stiff for both aspect ratios.

Summary The observations for the hemisphere forming of an anisotropic material are similar to the isotropic material for most element formulations. However, the large deviations for the C3D8R-Enh element demonstrate the importance of considering material behavior when selecting methods to prevent locking. None of the available formulations in ABAQUS/Explicit is unconditionally suitable for forming highly anisotropic materials with a single element

layer, in addition to the lack of a direct membrane-bending decoupling capability. The developed solid-shell element has a similar behavior to the locking-free S4R shell in all investigated configurations.

6.3 Application for textile forming simulation

The general suitability of the developed solid-shell element for forming simulations was demonstrated for isotropic and strongly anisotropic materials in Section 6.2. Macroscopic modeling of forming processes for CoFRP additionally requires a decoupling of the membrane and bending behavior as outlined in Section 2.3.3. Therefore, a suitable modification of the solid-shell element was proposed in Section 6.1.2. First, the potential of the proposed decoupling method is demonstrated in Section 6.3.1 by application to numerical coupon tests and hemisphere forming tests. Second, the proposed solid-shell element is applied to forming of Biax-NCF and compared to the 2D approach presented in Section 5.5.

6.3.1 Membrane-bending decoupling[8]

Proof of concept The general suitability of the proposed membrane-bending decoupling is demonstrated in simple tensile and cantilever bending tests by variation of $\hat{\mathbb{C}}^{\mathrm{mem}}$ and $\hat{\mathbb{C}}^{\mathrm{bend}}$. The geometry as well as load conditions of the tensile test are shown in Figure 6.7. For the cantilever test, the setup already shown in Figure 6.3 is used again. In both tests, the beam is discretized with a single element in thickness and width direction as well as ten elements in length direction, resulting in $a = 20$. The membrane and the bending stiffness are varied between a medium stiffness and a low stiffness, respectively, resulting in a total of four combinations. The medium bending and membrane stiffnesses are chosen equal to Equation 6.26 with $\hat{\mathbb{C}}^{\mathrm{mem}} = \hat{\mathbb{C}}^{\mathrm{bend}} = \hat{\mathbb{C}}_{\mathrm{UD}}$.

[8] Adapted and revised from [353], cf. footnote p. 201 for details.

The low stiffnesses differ from the medium stiffness by a factor of 10 only in the 11-component by $(\hat{\mathbb{C}}^{\mathrm{bend,low}})_{11} = (\hat{\mathbb{C}}^{\mathrm{mem,low}})_{11} = 1/10(\hat{\mathbb{C}}_{\mathrm{UD}})_{11} = 100$ MPa, which determines the effective bending stiffness in beam direction.

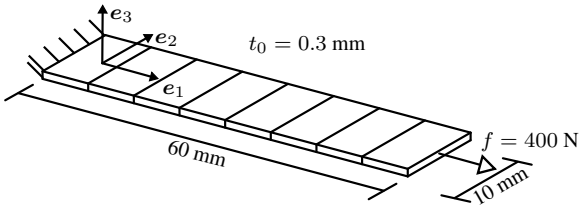

Figure 6.7: Tensile test setup | Geometry and applied tip load (adapted from [352]).

The results of the tensile and cantilever tests are shown in Table 6.1 a and b respectively. The tip displacement in the tensile test is only increased by decreasing the membrane stiffness, and independent of the bending stiffness. Analogously, the tip displacement in the cantilever tests is only depending on the bending stiffness. This indicates that the approach proposed in Equation 6.25 is generally suitable for a membrane-bending-decoupling.

Table 6.1: Resulting tip displacement for the a) tensile tests and b) cantilever tests [353].

a) Tensile test

tip disp. u / mm	$\hat{\mathbb{C}}^{\mathrm{bend}}$	$\hat{\mathbb{C}}^{\mathrm{bend,low}}$
$\hat{\mathbb{C}}^{\mathrm{mem}}$	6.8	6.8
$\hat{\mathbb{C}}^{\mathrm{mem,low}}$	37.5	37.5

b) Cantilever test

tip disp. u / mm	$\hat{\mathbb{C}}^{\mathrm{bend}}$	$\hat{\mathbb{C}}^{\mathrm{bend,low}}$
$\hat{\mathbb{C}}^{\mathrm{mem}}$	1.277	12.12
$\hat{\mathbb{C}}^{\mathrm{mem,low}}$	1.277	12.12

Influence on forming behavior The proposed membrane-bending decoupling is applied to the hemisphere forming tests with $a = 20$ and the same geometry described in Section 6.2.1. A constant unidirectional $\hat{\mathbb{C}}^{\mathrm{mem}}_{\mathrm{UD}} = \hat{\mathbb{C}}_{\mathrm{UD}}$ and biaxial $\hat{\mathbb{C}}^{\mathrm{mem}}_{\mathrm{Biax}} = \hat{\mathbb{C}}_{\mathrm{Biax}}$ membrane stiffness are utilized in all tests, cf. Equation 6.26. The bending stiffness is initially equal to the respective membrane stiffness ($\mathbb{C}^{\mathrm{bend}}_{\mathrm{UD}} = \mathbb{C}^{\mathrm{mem}}_{\mathrm{UD}}$ and $\hat{\mathbb{C}}^{\mathrm{bend}}_{\mathrm{Biax}} = \hat{\mathbb{C}}^{\mathrm{mem}}_{\mathrm{Biax}}$). Subsequently, the 11-component in the unidirectional, as well as additionally the 22-component in the biaxial case, is either increased ($\hat{\mathbb{C}}^{\mathrm{bend,high}}_{\mathrm{UD}}$ and $\hat{\mathbb{C}}^{\mathrm{bend,high}}_{\mathrm{Biax}}$) or decreased ($\hat{\mathbb{C}}^{\mathrm{bend,low}}_{\mathrm{UD}}$ and $\hat{\mathbb{C}}^{\mathrm{bend,low}}_{\mathrm{Biax}}$) by a factor of 10. The results for all combinations are shown in Figure 6.8.

In the biaxial case, the general orientation and position of the wrinkles remain similar for increasing bending stiffness. However, the number of wrinkles decreases while their size strongly increases. In the unidirectional case, the wrinkles straighten towards the edges for increasing bending stiffness. For the low bending stiffness, wrinkles also form perpendicular to the direction of the highest stiffness. The tendency of a decreased wrinkling for a higher membrane-to-bending stiffness ratio agrees with observations in literature [67, 68, 154].

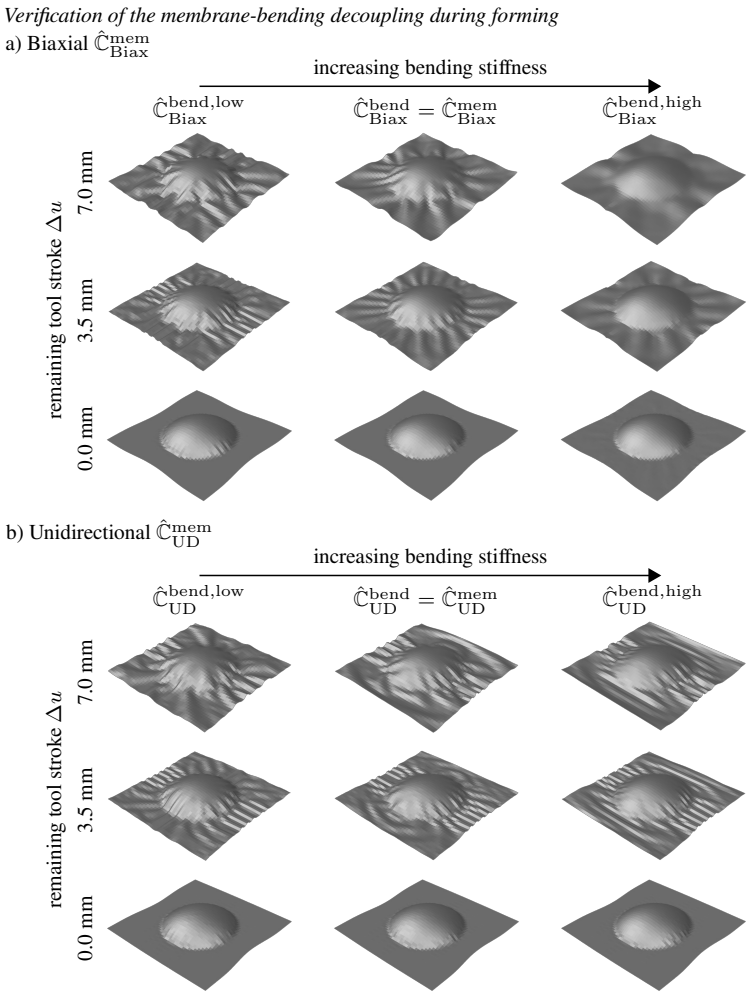

Figure 6.8: Hemisphere forming for different membrane to bending stiffness ratios | Results for a constant a) biaxial and b) unidirectional membrane stiffness with different bending stiffnesses at several remaining tool strokes Δu (adapted from [353]).

6.3.2 Double dome forming

Parameterization The developed solid-shell element is applied to textile forming simulation using Biax-NCF as an example and compared to the 2D approach presented in Section 5.5. This enables a direct transfer of the parameterization with only minor modifications to the membrane stiffness $\hat{\mathbb{C}}^{\mathrm{mem}}$ in Equation 6.25. The invariants introduced in Section 5.2.1 can be directly related to the components of the Green-Lagrange strain by

$$E_{11} \hat{=} I_4 - I_4^0 \quad , \quad E_{12} \hat{=} I_6 - I_6^0 = I_6 \quad \text{and} \quad E_{22} \hat{=} I_8 - I_8^0. \tag{6.27}$$

This allows an equivalent membrane stiffness matrix to be derived with the same shear parameters given in Table A.7 by

$$\hat{\mathbb{C}}^{\mathrm{mem}}_{\mathrm{Biax-NCF}} = \begin{bmatrix} 1000 & 0 & 0 & 0 & 0 & 0 \\ 0 & 1000 & 0 & 0 & 0 & 0 \\ 0 & 0 & 10 & 0 & 0 & 0 \\ 0 & 0 & 0 & \dfrac{\partial W_6^{\mathrm{Biax}}}{\partial I_6}(E_{12}) & 0 & 0 \\ 0 & 0 & 0 & 0 & 0.1 & 0 \\ 0 & 0 & 0 & 0 & 0 & 0.1 \end{bmatrix} \text{MPa}. \tag{6.28}$$

In numerical studies, no influence of the transverse shear components of the membrane stiffness was observed, because this deformation is modeled by the bending part. Therefore, they were assumed as very small. A relatively high compaction stiffness of $(\hat{C}^{\mathrm{mem}}_{\mathrm{Biax-NCF}})_{33} = 10$ MPa is used to reduce the impact of possible compaction during the comparison to the 2D approach.

The cantilever tests described in Section 5.5.2 are used to identify the bending stiffness $\hat{\mathbb{C}}^{\mathrm{bend}}_{\mathrm{Biax-NCF}}$. The stiffnesses already derived for the hypoelastic approach, cf. Table A.8, are also used for the solid-shell approach. Good agreement for the overhang lengths l_{bend} and simulative deflection curves are achieved between the solid-shell and 2D approach. This indicates a direct transferability of the identified parameters for a linear elastic behavior, despite the

hyperelastic approach in the solid-shell compared to the hypoelastic model in the 2D approach.

Double dome forming The developed solid-shell model is compared to the 2D approach in a forming simulation on a generic double dome geometry without a blankholder. The setup is shown in Figure 6.9 a. Only one quarter is simulated with corresponding symmetry boundary conditions, because of the double-symmetric shape of the geometry. A single ply with a $[(0°/90°)_{\mathrm{B}}]$ orientation that is slightly larger than the upper tool is utilized.

The global forming behavior for different relative tool strokes Δu_3 is shown in Figure 6.9 b. A good qualitative agreement is achieved for the location of out-of-plane deformations with slight deviations in magnitude. This indicates a correct description of the decoupled membrane and bending behavior by the solid-shell element. The predicted shear strains of 3D solid-element nearly match the results of the 2D approach after the tool is closed, cf. Figure 6.9 c. Minor deviations only occur along the upper edge of the ply that protrudes from the blankholder.

The final thickness of the ply can be evaluated for the solid-shell element and is shown in Figure 6.9 d. The assumed compacting stiffness $(\hat{C}^{\mathrm{mem}}_{\mathrm{Biax-NCF}})_{33}$ is significantly higher than the experimentally measured exponential stiffness for small deformations, cf. Section 4.4. As a result, the predicted thickness reduction is small and only notable along the radii of the tools. However, the general location of the reduced ply thickness is in qualitative agreement with the model of Poppe et al. [66] for double dome forming of a woven fabric.

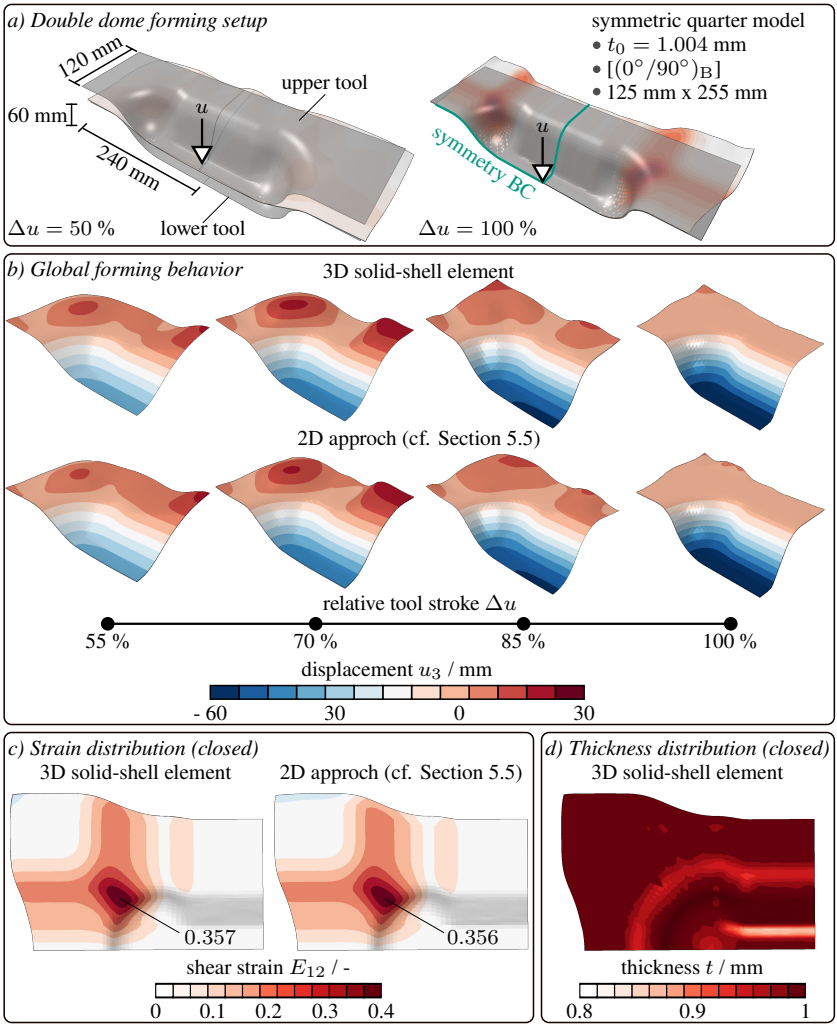

Figure 6.9: Comparison of the 3D solid-shell element and the 2D approach proposed in Section 5.5 for Biax-NCF during double dome forming |a) Setup of the model; b) global forming behavior represented by the out-of-plane displacements; c) shear strain distribution for closed tools (maximum values shown); d) thickness distribution for closed tools.

6.4 Conclusion and discussion

In the scope of this chapter, a three-dimensional solid-shell element for forming of engineering textiles is developed and implemented as a user-defined element formulation for the commercial solver ABAQUS/Explicit.

Element formulation Initially, the element formulation based on an isoparametric hexahedral element with linear shape functions and methods to prevent different locking phenomena are outlined. The assumed natural strain method is applied to alleviate curvature-thickness and transverse shear locking. A single internal DOF based on the enhanced assumed strain method is introduced to prevent volumetric locking. A variable number of integration points over the thickness are utilized to alleviate in-plane shear locking based on a selective reduced integration scheme.

Additional modifications are proposed to adapt the solid-shell element for textile forming. Taylor expansion of the strains and stresses are utilized to introduce a membrane-bending decoupling and an hourglass stabilization for strongly anisotropic materials. However, the proposed stabilization is only suitable for compressible materials such as engineering textiles because it does not result in a purely deviatoric stiffness [356]. Other than that, no further restrictions on the material model are necessary. A fully three-dimensional constitutive law can be used to model the intra-ply mechanisms, including compaction.

Locking-free forming behavior The influence of numerical locking on the forming behavior and the resulting need for a locking-free element was demonstrated by comparing the solid-shell to different three-dimensional elements in ABAQUS/Explicit. The objective is accurate modeling with a single element layer and high element aspect ratios. The standard solid elements without locking prevention (C3D8 & C3D8R) behave significantly too stiff during forming and are generally unsuitable even for isotropic materials. The elements incorporating methods to prevent locking showed promising results for

smaller aspect ratios. However, numerically too stiff behavior was observed for higher aspect ratios (SC8R & C3D8I) or the element formulation was found to be unsuitable for highly anisotropic materials (C3D8R-Enh). Thus, none of the available formulations in ABAQUS/Explicit is unconditionally suitable for forming highly anisotropic materials within a single element layer, in addition to the lack of a direct membrane-bending decoupling capability. This illustrates the complexity of locking phenomena during forming and the need to thoroughly evaluate the underlying element formulation. The only element that consistently achieves good results for larger aspect ratios and both isotropic and anisotropic material behavior with a single element over the thickness is the solid-shell.

Application for textile forming The proposed method for a membrane-bending decoupling in the solid-shell is required for an application to engineering textiles. The general suitability of the method is demonstrated on coupon level in tensile and cantilever bending tests. On part level, the impact of the decoupling on the wrinkling behavior is qualitatively well predicted in hemisphere forming tests. The solid-shell element thus fulfills all necessary prerequisites to model the deformation of thin engineering textiles efficiently in macroscopic forming simulations.

Finally, the solid-shell element is applied to forming simulation of a double dome geometry for Biax-NCF and compared to the approach for 2D elements presented in Section 5.5. The solid-shell can accurately model a fabric ply with a single element over the thickness. This facilitates the transferability of modeling approaches developed for approaches with 2D elements. The membrane and bending parameterizations of the 2D model could be transferred directly to the solid-shell element without significant modifications. Good agreement is achieved for the global forming behavior and shear strain distribution compared to the 2D approach.

The final thickness of the ply can be evaluated for the solid-shell and qualitatively plausible thinning of the ply is predicted for the radii of the double dome.

However, an upscaled compaction stiffness was applied for direct comparison to the 2D approach. A suitable model for the experimentally measured exponential compaction behavior has to be introduced and validated before the thickness prediction can be conclusively evaluated. Therefore, the analytical models proposed in Section 4.4 can be used as a starting point. The solid-shell element can then be used to examine effects in thickness direction in more detail.

The utilization of a fully three-dimensional approach should enable a better approximation of forming effects like the fiber volume content [66, 345]. This would also improve the prediction quality of subsequent process steps when embedded in a CAE chain [52]. Additionally, the three-dimensional constitutive law can be exploited to introduce relevant couplings for multi-axial stress states, which cannot be modeled with 2D approaches. This includes the shear-compaction coupling for woven fabrics [121] or the influence on the transverse tensile behavior of UD-NCF discussed in Section 5.6.

7 Conclusions and recommendations

The forming behavior of a unidirectional and a bidirectional non-crimp fabric (UD- and Biax-NCF) was investigated and suitable 2D as well as 3D modeling approaches for their textile forming simulations were developed. The results of this work contribute to the understanding of the relevant mechanisms for forming non-crimp fabrics and their efficient modeling. In this chapter, the main conclusions from these achievements are categorized by the proposed objectives (cf. Section 3.1) and recommendations to motivate future research are proposed.

Conclusions

Objective O-1. Systematic characterization of the inter- and intra-ply deformation mechanisms and quantitative analysis of the forming behavior of non-crimp fabrics with an emphasis on the specific challenges of unidirectional non-crimp fabrics (UD-NCF) to enable process modeling and its validation.✓

The mesoscopic structure of the constituents of NCFs results in a specific macroscopic behavior, which is largely influenced by the interaction of the stitching and the rovings. Therefore, all experiments must take into account the orientation and resulting load of the stitching, in addition to the rovings. A wide experimental database is established for the inter-ply as well intra-ply

mechanisms of the UD- and the Biax-NCF as a foundation for the development and quantitative validation of modeling approaches. A comprehensive analysis is presented in Chapter 4 and summarized in Figure 4.43. The membrane and bending behavior in particular are specific for the UD-NCF compared to the Biax-NCF, which behaves similar to woven fabrics in many aspects. The UD-NCF exhibits a strongly anisotropic and asymmetric behavior, since the transverse behavior is determined by the stitching instead of a second fiber orientation. Thus, a solely shear-focused description of the membrane behavior is insufficient. Different membrane deformation modes with superimposed shear, transverse tensile and perpendicular compressive strains are observed during membrane characterization as well as component forming. In addition, in-plane roving bending in transition zones is observed and quantified with a new curvature measurement method. The out-of-plane bending stiffness in transverse direction is stitching-dominated and significantly lower than the stiffness in the roving direction. This results in a strong twist deformation for off-axis bending loads.

Objective O-2. Development of a 2D macroscopic forming model for UD-NCF based on a hyperelastic approach with a sufficient complexity to accurately describe the relevant deformation modes, but still facilitate a simplified parameterization process and the transferability to other materials.✓

The most relevant mechanisms and necessary complexity of a suitable constitutive model for UD-NCF are identified in a preliminary investigation of existing methods. Subsequently, a new hyperelastic membrane approach for UD-NCF is developed, parameterized and validated in Chapter 5. The different membrane deformation modes of superimposed shear, transverse tension and perpendicular in-plane compression can be related to suitable pseudo-invariants. A coupling between the transverse tensile and perpendicular in-plane compressive behavior is required to model large roving slippage. An uncoupled shear behavior is sufficient. The number of material parameters is significantly reduced by introducing generalized formulations for the strain energy density contributions

and coupling. This simplifies the parameterization and enables a modular implementation of the approach to facilitate transferability to other materials and future modifications. High quantitative agreement between the simulation and experiments is achieved for all characterization tests. Furthermore, the forming behavior is accurately predicted for different geometrically challenging shapes and layup configurations. The developed approach and parameterization strategies can be directly transferred to Biax-NCF to adequately model its forming behavior up to medium deformations.

Objective O-3. Development of a 3D solid-shell element to account for compaction during the forming of engineering textiles, which exhibits locking-free behavior for slender structures and takes into account the specific requirements of continuous fiber-reinforced plastics (CoFRP).✓

A new 3D solid-shell formulation based on methods to avoid numerical locking and with necessary modifications for forming simulation of engineering textiles is presented in Chapter 6. A locking-free element formulation is required to accurately model forming processes due to the strong impact of numerical locking on the bending behavior in particular. Most commercially available 3D elements behave too stiff during forming for isotropic or anisotropic materials. In contrast, the proposed solid-shell is capable of modeling the forming behavior with a single element over the thickness for large aspect ratios independent of the material model. This increases the numerical efficiency and enables direct transferability of methods developed for 2D approaches. The solid-shell is also capable of decoupling the membrane and bending behavior required for engineering textiles. As a result, the developed 3D solid-shell element can model forming processes as accurately as 2D approaches with the same number of elements, but with the additional prediction of the behavior in thickness direction.

Recommendations for future research

- Macroscopic approaches consider the material as a homogenized continuum usually based on the limited information available within each element. Incorporating information from neighboring elements in a non-local approach would enable the modeling of several effects observed for UD-NCF due to its mesoscopic structure:
  - The in-plane curvature of the rovings could be calculated based on the displacements of neighboring elements to introduce an in-plane bending stiffness motivated by generalized continua approaches. This is expected to model the asymmetric shear behavior of UD-NCF that primarily occurs parallel to the rovings in the experiments (21-shear) by preventing excessive shear transverse to the rovings (12-shear).
  - Local shear gradients could be calculated and introduced as an additional coupling for the transverse tensile behavior. This could localize the predicted roving slippage to the experimentally observed transition zones.
  - The pressure-dependent transverse tensile behavior due to local clamping of glass fibers could be introduced by incorporating the UD-NCF model into the solid-shell element in combination with a non-local method to propagate the impact of local pressure along the elements in glass-fiber direction.
- The modeling approaches of this work are developed to describe the fundamental mechanisms of dry engineering textiles and could be enhanced to account for the influence of binders or infiltration.
- Forming tests without blankholders are desirable to investigate the impact and correct modeling of the observed twist during off-axis bending loads for UD-NCF. The proposed bending model could also be enhanced to

account for the non-linear bending behavior measured for high curvatures during characterization.

- Comprehensive experiments are needed to further investigate the cause of the observed interactions between layers during some forming tests and develop a suitable inter-ply modeling approach.
- The solid-shell element is developed for the requirements of textile forming without restrictions on the applied material model and could be utilized in future investigations of other engineering textiles or pre-infiltrated semi-finished products.
- A non-linear model to accurately describe compaction could be implemented within the solid-shell element formulation and validated. This would enable further investigations of forming effects in thickness direction during the process as well as their impact on subsequent process steps by application in the context of a CAE-chain.

A Appendix

A.1 Supplementary experimental results

A.1.1 Membrane behavior - Investigation of different specimen sizes in OATs[1]

The observed behavior in bias-extension tests ($45°$-OAT) can depend on the specimen size, as has been reported for unbalanced fabrics [111, 134] and Biax-NCF [119]. The influence of the specimen's size has not yet been investigated for UD-NCF. Therefore, additional tests with a bias angle of $45°$ were performed on smaller specimens for $a_2^{\text{small}} = {}^{160\,\text{mm}}/_{80\,\text{mm}}$ and on larger specimens for $a_3^{\text{large}} = {}^{480\,\text{mm}}/_{160\,\text{mm}}$. The larger specimens were only tested up to $\varepsilon = 16.6\%$, due to a limited clamping length of the tensile testing machine. The averaged strains in the MDZ and the average curvature are shown in Figure A.1 and the resulting strain distributions in Figure A.2. Additionally, the theoretical shear angles according to pure shear theory proposed by Cao et al. [111] and simple shear theory proposed by Pourtier et al. [119] are included for the averaged strains for both investigated aspect ratios.

The larger and smaller specimens of Biax-NCF show similar behavior to the medium specimen. The typical deformation zones, described in Section 4.2.2.1 are present with the highest deformation in the MDZ and measurable roving curvatures in the transition zones, cf. Figure A.1 a and A.2 a. The behavior in the MDZ is mostly shear-dominated and the measured shear angle for medium

[1] Reproduced section from [102], cf. footnote p. 61 for details.

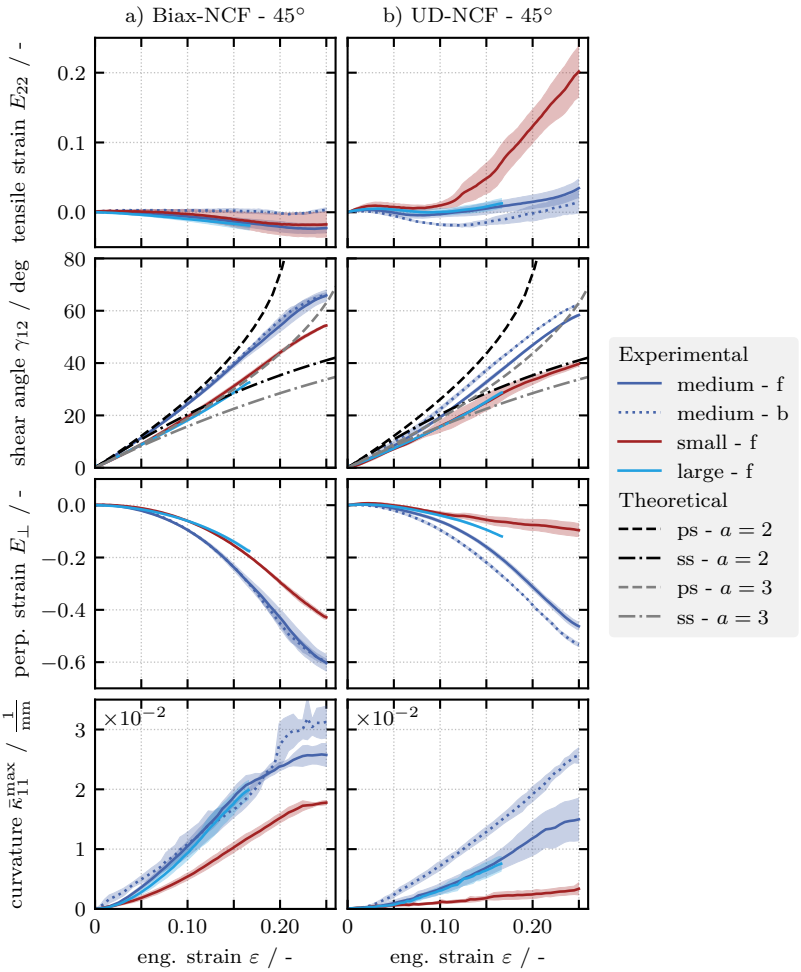

Figure A.1: Averaged strains in the MDZ and average roving curvature of the 45°-OAT for different specimen sizes of the a) Biax-NCF (MD600) and b) UD-NCF (UD300)

and large specimens corresponds to the prediction according to a pure shear assumption for lower strains $\varepsilon < 0.1$, cf. Figure A.1 a. However, the measured shear angle of the small specimen is below the simple and pure shear prediction. The deviations are caused by slippage between the rovings in the transition area

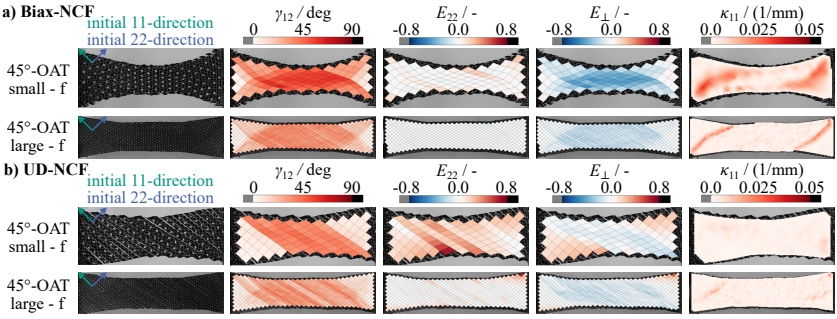

Figure A.2: Deformed specimens and strain distributions during Off-Axis-Tensions tests (OATs) (a) for Biax-NCF and (b) UD-NCF of different specimen sizes

between zones "A" to "B1" and "B2" to "C". The effect is stronger for a smaller specimen size due to the relative size of a roving compared to the area of the MDZ.

The specimen size has a more pronounced effect on the observed behavior for UD-NCF. The larger specimens show the typical deformation zones but have a more inhomogeneous strain field, cf. Figure A.2 b. Due to the relatively loose stitching and the mesoscopic nature of the fabric, the load is not evenly distributed in the specimen. However, compared to the medium specimen similar averaged strains relative to the simple shear theory of their respective aspect ratios as well as averaged curvatures are measured, cf. Figure A.1 b. In the smaller specimen, zones "B1" and "B2" are hardly pronounced and the fibers behave the same as in zones "A" and "C", respectively. The rovings bend significantly less and the stitching is strongly tensioned, resulting in visible gaps and high transverse tensile strains E_{22}, cf. Figure A.2 b. The effects described above are also reflected in the averaged strains in the MDZ, cf. Figure A.1 b. Generally, the measured shear angle of all sizes for small strains is close to or below the simple shear theory, starting to exceed it for $\varepsilon > 0.1 \,\text{to}\, 0.125$ for medium and large specimens. For small specimens, γ_{12} remains below both theories due to the large transverse tensile strains E_{22}.

A.1.2 Bending behavior - Peirce bending stiffness

Table A.1: Resulting bending stiffness of the cantilever tests in Section 4.3 according to Peirce.

		front facing up $G_{\mathrm{w}}^{\mathrm{P}}$ [N m]	back facing up $G_{\mathrm{w}}^{\mathrm{P}}$ [N m]
UD-NCF	0°	4.062 ± 0.119	3.260 ± 0.112
	45°	1.309 ± 0.241	2.094
	90°	0.018 ± 0.00244	0.00591 ± 0.000466
Biax-NCF	0°	3.403 ± 0.172	2.498 ± 0.122
	45°	1.979 ± 0.091	1.569 ± 0.101
	90°	3.863 ± 0.424	4.0460 ± 0.257

A.1.3 Compaction behavior - Analytical model

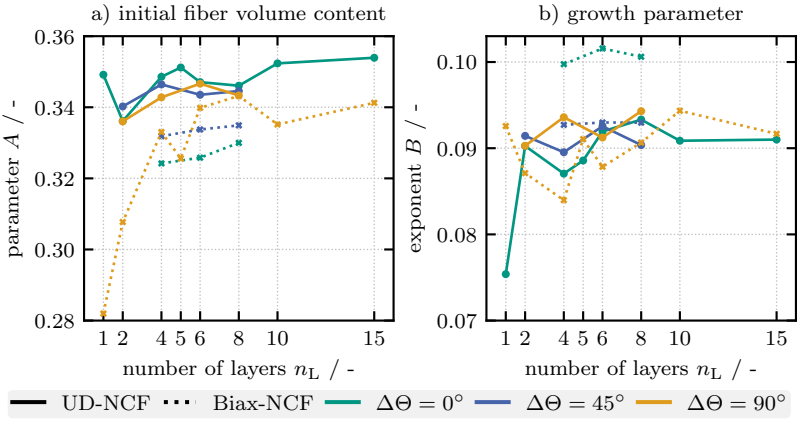

Figure A.3: Overview of the parameters for the 1D analytical model $\Phi(p)$ for compaction in Section 4.4.

Table A.2: Resulting parameters of the analytical p-model $\Phi(p)$ for the compaction test based on Equation 4.9 in Section 4.4.

UD-NCF					Biax-NCF				
$\Delta\Theta$	n_L	A	B	R^2	$\Delta\Theta$	n_L	A	B	R^2
0°	1	0.34916	0.07539	0.98754	0°	4	0.32421	0.09975	0.99838
	2	0.33613	0.09026	0.99958		6	0.32582	0.10157	0.99741
	4	0.34857	0.08705	0.99919		8	0.33	0.10061	0.99669
	5	0.35119	0.08857	0.99817	45°	4	0.33186	0.09271	0.9973
	6	0.34707	0.09194	0.99905		6	0.33375	0.09299	0.99693
	8	0.34607	0.09332	0.99919		8	0.33491	0.09297	0.9962
	10	0.35235	0.09087	0.99776	90°	1	0.28197	0.09257	0.99849
	15	0.35393	0.091	0.9973		2	0.30772	0.08711	0.99949
45°	2	0.34023	0.09143	0.99915		4	0.33304	0.08397	0.99848
	4	0.34642	0.08953	0.99964		5	0.32559	0.09105	0.99699
	6	0.34351	0.09255	0.99956		6	0.33984	0.08785	0.99673
	8	0.34457	0.09037	0.99895		8	0.34319	0.09065	0.99635
90°	2	0.33604	0.09028	0.99959		10	0.33517	0.09435	0.99668
	4	0.34279	0.09359	0.99975		15	0.34125	0.09167	0.99211
	6	0.34664	0.09124	0.99946					
	8	0.34333	0.0943	0.99936					

Table A.3: Resulting parameters of the analytical pn-model $\Phi(p, n_\mathrm{L})$ for the compaction tests based on Equation 4.10 in Section 4.4.

	$\Delta\Theta$	A	B	C	D	R^2
UD-NCF	0°	0.3452	0.10142	0.23821	0.54049	0.99417
	45°	0.34397	0.09138	0.92546	4.89785	0.99793
	90°	0.34165	0.09501	1.03257	3.44216	0.99838
Biax-NCF	0°	0.32579	0.10745	0.31078	0.97228	0.99705
	45°	0.33307	0.09528	0.21457	1.32509	0.99615
	90°	0.32688	0.11261	0.46652	0.56297	0.96447

A.1.4 Inter-ply behavior - Supplementary plots

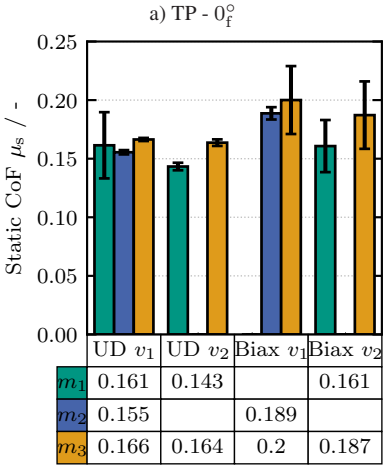

	UD v_1	UD v_2	Biax v_1	Biax v_2
m_1	0.161	0.143		0.161
m_2	0.155		0.189	
m_3	0.166	0.164	0.2	0.187

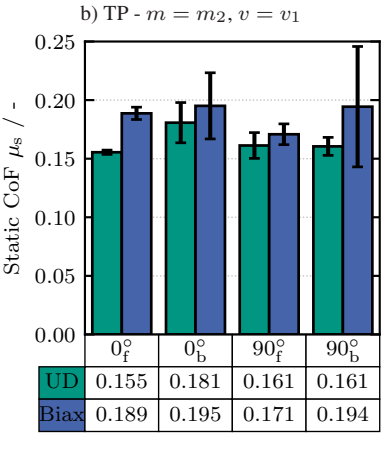

	0°_f	0°_b	90°_f	90°_b
UD	0.155	0.181	0.161	0.161
Biax	0.189	0.195	0.171	0.194

Figure A.4: Experimental results for the tool-ply (TP) static CoF from Section 4.5| (a) Influence of the applied mass m and velocity v in a 0°_f-configuration for both materials; (b)Influence of the relative interface orientations with an applied mass of $m = m_2$ and velocity $v = v_1$.

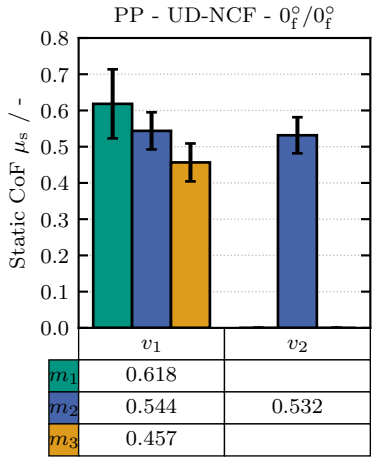

	v_1	v_2
m_1	0.618	
m_2	0.544	0.532
m_3	0.457	

Figure A.5: Influence of the applied mass m and velocity v on the static CoF for the ply-ply behavior of UD-NCF in a $0^\circ_f/0^\circ_f$-configuration from Section 4.5.

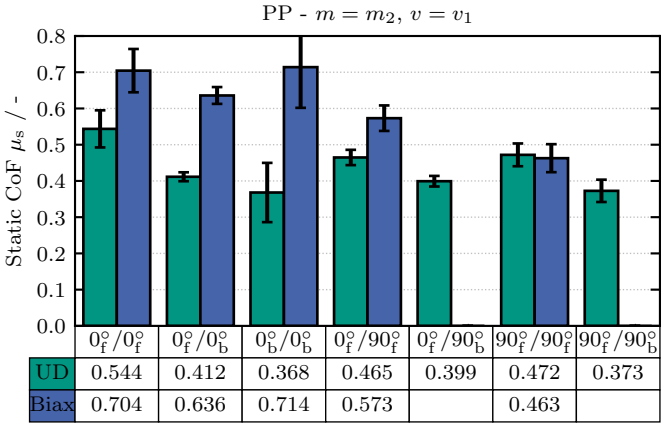

	$0^\circ_f/0^\circ_f$	$0^\circ_f/0^\circ_b$	$0^\circ_b/0^\circ_b$	$0^\circ_f/90^\circ_f$	$0^\circ_f/90^\circ_b$	$90^\circ_f/90^\circ_f$	$90^\circ_f/90^\circ_b$
UD	0.544	0.412	0.368	0.465	0.399	0.472	0.373
Biax	0.704	0.636	0.714	0.573		0.463	

Figure A.6: Influence of the relative interface orientations on the static CoF for the ply-ply behavior with an applied mass of $m = m_2$ and velocity $v = v_1$ from Section 4.5.

A.1.5 Forming behavior - Supplementary plots[3]

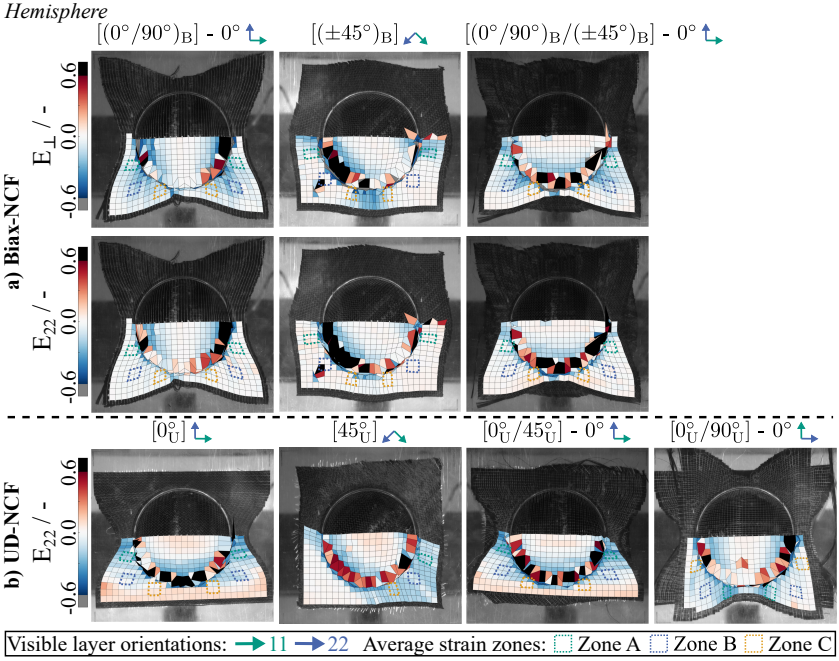

Figure A.7: Additional DIC-strains in the hemisphere shape forming test from Section 4.6 for UD- and Biax-NCF with different layup orientations at a tool displacement of 75 mm [208].

[3] Reproduced section from [208], cf. footnote p. 110 for details.

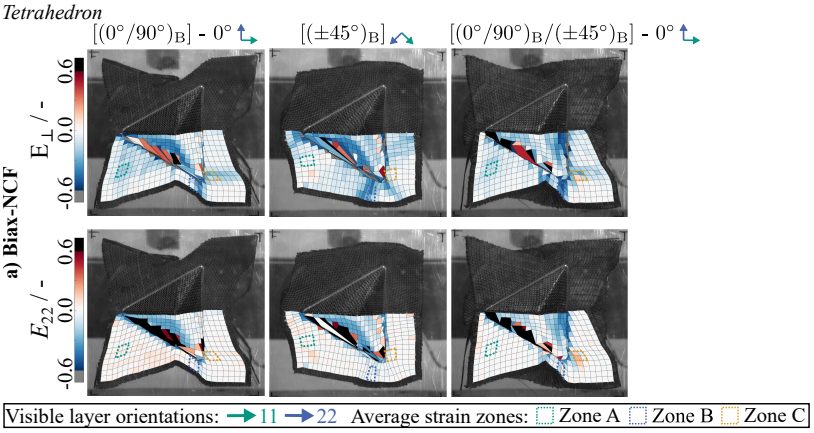

Figure A.8: Additional DIC-strains in the tetrahedron shape forming test from Section 4.6 for Biax-NCF with different layup orientations at a tool displacement of 95 mm [208].

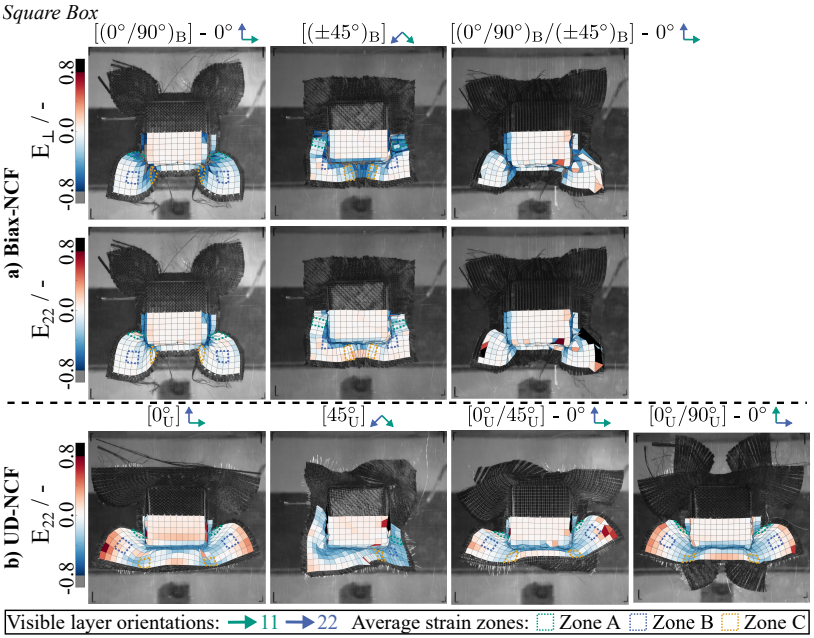

Figure A.9: Additional DIC-strains for the box shape forming test from Section 4.6 for UD- and Biax-NCF with different layup orientations at a tool displacement of 85 mm [208].

A.2 Supplementary simulative results for the hyperelastic modeling of non-crimp fabrics

A.2.1 Preliminary investigation - Material parameter for approach by Schirmaier et al.

Table A.4: Material parameters for the UD-NCF membrane model of Schirmaier et al. in Section 5.1 - nomenclature is comprehensibly outlined in [86].

E_{1t}	E_{1c}	E_{2t}	E_{2c}	γ_{12}^{s}	γ_{12}^{e}	$R_{2\Gamma,max}^{0,s}$
[MPa]	[MPa]	[MPa]	[MPa]	[-]	[-]	[MPa]
1000.0	1000.0	3.0	0.0	0.05	0.15	0.05
$R_{2\Gamma}^{0,e}$	H_{2p}^{c}	H_{2p}^{e}	$R_{2\Gamma}^{0,s}$	$R_{2\Gamma}^{0,e}$	k_{2p}^{c}	k_{2p}^{e}
[MPa]	[MPa]	[MPa]	[MPa]	[MPa]	[-]	[-]
0.02	0.25	0.07	0.005	0.002	15.0	40.0
$H_{2p,lock}^{c}$	$H_{2p,lock}^{e}$	$\varepsilon_{22,p,lock}^{c}$	$\varepsilon_{22,p,lock}^{e}$	$\Delta\varepsilon_{22,p,lock}$	$E_{\perp,0}$	γ_{12}^{a}
[MPa]	[MPa]	[-]	[-]	[-]	[MPa]	[-]
0.02	0.012	0.1	0.2	0.4	1.0	0.2
γ_{12}^{b}	$E_{\perp,off}^{a}$	$E_{\perp,off}^{b}$	$P_{\perp,off}^{a}$	$P_{\perp,off}^{b}$	$E_{\perp,lock}^{a}$	$E_{\perp,lock}^{b}$
[MPa]	[-]	[-]	[MPa]	[MPa]	[MPa]	[MPa]
1.0	0.08	0.01	0.008	0.004	10.0	5.0
$\lvert\varepsilon_{\perp,lock}^{a}\rvert$	$\lvert\varepsilon_{\perp,lock}^{b}\rvert$	$\lvert\Delta\varepsilon_{\perp,lock}\rvert$	G_{12}	$R_{12\Gamma}^{0}$	H_{12p}	k_{12p}
[-]	[-]	[-]	[MPa]	[MPa]	[MPa]	[-]
0.2	0.5	0.2	3.0	0.01	0.001	20.0
$R_{12\Gamma,max}^{0}$	n_{12p}	$R_{12\Gamma,sat}^{0}$	$\gamma_{12,p,lin}$	$H_{12,p,lock}$	$\gamma_{12,p,lock}$	$\Delta\gamma_{12,p,lock}$
[MPa]	[-]	[MPa]	[-]	[MPa]	[-]	[-]
0.028	10.0	0.018	-2.0	0.06	1.0	0.3
ν_{12}^{c}	ν_{12}^{e}	ν_{21}^{c}	ν_{12}^{e}	$E_{2,p,QK}$	η	$\eta_{\perp}$
[-]	[-]	[-]	[-]	[-]	[MPa s]	[MPa s]
0.0	0.0	0.0	0.0	0.0	0.001	0.001

A.2.2 Preliminary investigation - Non-monotonous stresses

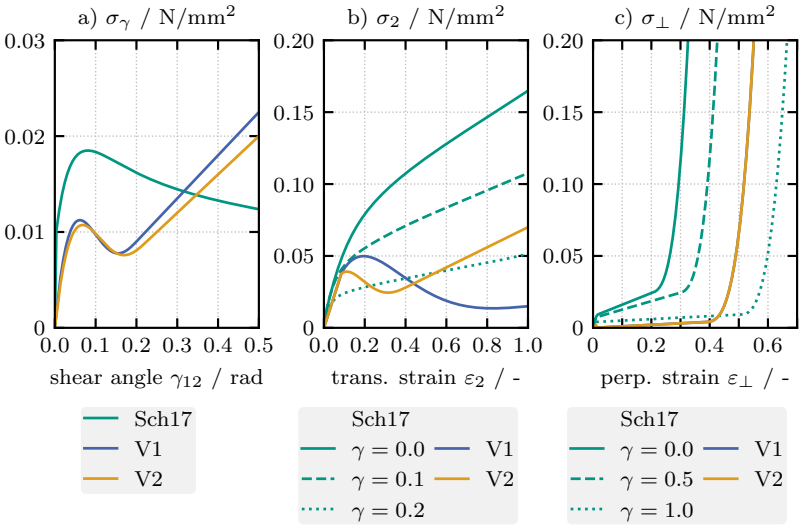

Figure A.10: Equivalent co-rotational stress contributions of the approach by Schirmaier et al. (Sch17) [137] and the decoupled approach from Section 5.1.

A.2.3 Membrane modeling - Derivatives of pseudo-invariants[5]

In the following, the relevant derivatives of the utilized pseudo-invariants in Section 5.2 are listed:

$$\frac{\partial I_4}{\partial \boldsymbol{C}} = \boldsymbol{a}_0 \otimes \boldsymbol{a}_0 \tag{A.1}$$

$$\frac{\partial I_6}{\partial \boldsymbol{C}} = \frac{1}{2}\left(\boldsymbol{a}_0 \otimes \boldsymbol{b}_0 + \boldsymbol{b}_0 \otimes \boldsymbol{a}_0\right) \tag{A.2}$$

$$\frac{\partial I_8}{\partial \boldsymbol{C}} = \boldsymbol{b}_0 \otimes \boldsymbol{b}_0 \tag{A.3}$$

$$\frac{\partial I_{11}}{\partial \boldsymbol{C}} = \frac{\partial I_{11}}{\partial I_4}\frac{\partial I_4}{\partial \boldsymbol{C}} + \frac{\partial I_{11}}{\partial I_6}\frac{\partial I_6}{\partial \boldsymbol{C}} + \frac{\partial I_{11}}{\partial I_8}\frac{\partial I_8}{\partial \boldsymbol{C}} \tag{A.4}$$

$$\frac{\partial I_{11}}{\partial I_4} = \frac{I_6^2}{2I_4^{/}}\frac{1}{\sqrt{I_4 I_8 - I_6^2}} \tag{A.5}$$

$$\frac{\partial I_{11}}{\partial I_6} = \frac{-I_6}{\sqrt{I_4}}\frac{1}{\sqrt{I_4 I_8 - I_6^2}} \tag{A.6}$$

$$\frac{\partial I_{11}}{\partial I_8} = \frac{\sqrt{I_4}}{2}\frac{1}{\sqrt{I_4 I_8 - I_6^2}} \tag{A.7}$$

[5] Reproduced section from [180], cf. footnote p. 150 for details.

A.2.4 Membrane modeling - Generalized strain energy density function[5]

Based on Equation 5.20 in Section 5.2, the generalized strain energy density function is given by

$$W_i^{\mathrm{G}}(I_i) = \begin{cases} \frac{1}{2} C_i^{\mathrm{ini}} I_i^{\mathrm{a}2} & , [0 \leq I_i^{\mathrm{a}} < I_i^t] \\ S_i^{\mathrm{ini}} I_i^{\mathrm{a}} + \frac{1}{cC} e^{-c(I-I)} \Big(C_i^{\mathrm{ini}} \left(\Delta S_i^{\mathrm{mid}} + C_i^{\mathrm{mid}} I_i^{\mathrm{a}} \right) \\ + C_i^{\mathrm{mid}} \left(\Delta S_i^{\mathrm{mid}} - S_i^{\mathrm{ini}} \right) \Big) + C_i^{\mathrm{ini}} I_i^{\mathrm{a}} \Big(2 C_i^{\mathrm{ini}} \Delta S_i^{\mathrm{mid}} & , [I_i^t \leq I_i^{\mathrm{a}} < I_i^{\mathrm{lock}}] \\ + C_i^{\mathrm{ini}} C_i^{\mathrm{mid}} I_i^{\mathrm{a}} - 2 C_i^{\mathrm{mid}} S_i^{\mathrm{ini}} \Big) - W_1 \\ S_i^{\mathrm{ini}} I_i^{\mathrm{a}} + \frac{1}{cC} e^{-c(I-I)} \Big(C_i^{\mathrm{ini}} \left(\Delta S_i^{\mathrm{mid}} + C_i^{\mathrm{mid}} I_i^{\mathrm{a}} \right) \\ + C_i^{\mathrm{mid}} \left(\Delta S_i^{\mathrm{mid}} - S_i^{\mathrm{ini}} \right) \Big) + C_i^{\mathrm{ini}} I_i^{\mathrm{a}} \Big(2 C_i^{\mathrm{ini}} \Delta S_i^{\mathrm{mid}} & , [I_i^{\mathrm{lock}} \leq I_i^{\mathrm{a}}] \\ + \quad C_i^{\mathrm{ini}} C_i^{\mathrm{mid}} I_i^{\mathrm{a}} \quad - \quad 2 C_i^{\mathrm{mid}} S_i^{\mathrm{ini}} \Big) \quad - \quad W_1 \quad + \\ \frac{1}{3} C_i^{\mathrm{lock}} \left(I_i^{\mathrm{a}} - \Delta I_i^{\mathrm{lock}} \right)^3 \end{cases} \tag{A.8}$$

with

$$W_1 = \frac{2(C_i^{\mathrm{ini}} + C_i^{\mathrm{mid}}) \Delta S_i^{\mathrm{mid}\,2} + 2 C_i^{\mathrm{ini}} \Delta S_i^{\mathrm{mid}} S_i^{\mathrm{ini}} - C_i^{\mathrm{mid}} S_i^{\mathrm{ini}\,2}}{2 C_i^{\mathrm{ini}\,2}} + \frac{1}{2} \frac{S_i^{\mathrm{ini}\,2}}{C_i^{\mathrm{ini}}} \tag{A.9}$$

A.2.5 Membrane modeling - Material parameters[5]

Table A.5: Material parameters of the hyperelastic membrane approach for UD-NCF.

UD-NCF	C_i^{ini} [MPa]	S_i^{ini} [MPa]	C_i^{mid} [MPa]	$\Delta S_i^{\mathrm{mid}}$ [MPa]	C_i^{lock} [MPa]	I_i^{lock} -
W_4	1000	-	-	-	-	-
W_6	0.14	0.018	0.01	0.005	-	-
W_8	1.1	0.025	0.03	0.02	-	-
W_{11}	0.01	0.0025	0.001	0.4	0.045	10.0
	k_{11}^{min} -	s_{11} -	e_{11} -			
k_{11}	0.4	10.0	2.0			

[5] Reproduced section from [180], cf. footnote p. 150 for details.

A.2.6 Membrane modeling - Parametric study

A parametric study on the final parameterization of the membrane model is conducted to illustrate the observations during the parameterization process described in Section 5.2.6. Therefore, the individual contributions to strain energy density due to shear W_6, transverse tension W_8, perpendicular compression W_{11} and the coupling k_{11} are scaled by $\pm 50\%$. The resulting forces and averaged strains in the main deformation zone (MDZ) are shown in Figure A.11. It has to be noted, that the scaling changes the magnitude of the respective contributions while the transition points between the different sections of the function remain at the same invariants (I_i^{t} and I_i^{lock}). This results in a stronger influence on the forces compared to the strains in the 30°- and 45°-OAT, which depend more on the location of the transition points.

The deformation in the MDZ of the 30°-OAT is strongly prescribed due to the boundary conditions, since all the strains necessary to allow the specimen to elongate are localized in this small area. The forces for small displacements are determined by the shear contribution W_6 since the transverse strains E_{22} remain close to zero. For $u > 25$ mm the contributions due to transverse tension W_8 and its coupling k_{11} have a decisive impact on the forces.

The deformation in the MDZ of the 45°-OAT is shear-dominated for $u < 60$ mm, after which notable E_{22} are predicted. The location of this transition point depends on the ratio of W_6/W_8. As a results, the forces strongly depend on the shear energy contribution W_6 in the early phase, while transverse tension W_8 and its coupling k_{11} impact the forces for larger displacements $u > 60$ mm.

The forces and strains in the 60°-OAT vary the most due to the scaling of the individual energy contributions, as positive shear and transverse strains occur together for small displacements. The deformation mode of the MDZ in the 60°-OAT strongly depends on the ratio of W_6/W_8. For the final parameterization, it consists of shear and transverse tension resulting in notable perpendicular compression. By reducing W_8 or increasing W_6 the shear and perpendicular

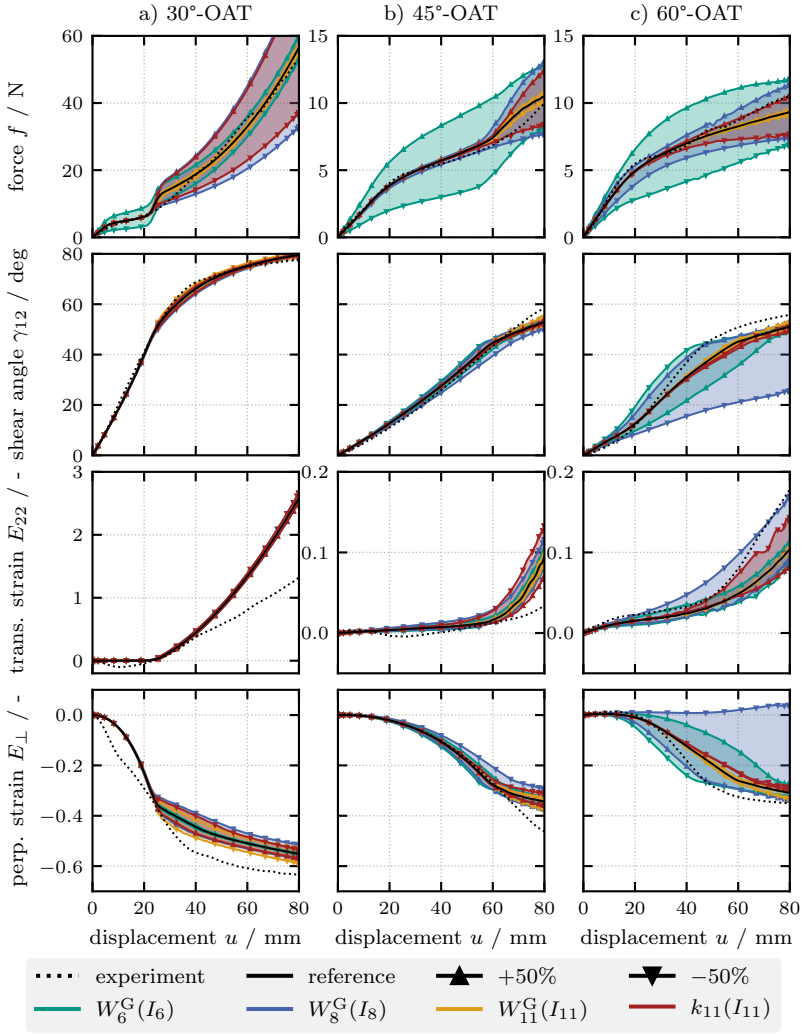

Figure A.11: Parametric study on the forces and strain in the MDZ of OATs | Variation of the individual contributions and coupling to the total strain energy density by ±50%.

compression in the MDZ are strongly reduced in favor of more transverse tension.

In summary, each energy contribution influences the resulting forces with varying intensity during different displacement ranges of the OATs. For the final parameterized model, the predicted deformation modes and strains during the 30°- and 45°-OAT are robust against scaling the individual contributions. In the 60°-OAT the deformation is highly sensitive to exact ratio between the individual energy contributions.

A.2.7 Membrane modeling - Local strains in different zones of OATs

The strains of the OATs are averaged over different areas to demonstrate differences between the experiments and simulation due to the continuous approach in Section 5.2.6. Zone B is selected to represent the deformation of the main deformation zone (MDZ) and is used during the evaluations of the experiments in Section 4.2. In addition, a smaller zone (A) and two larger zones (C and D) were evaluated to compare the homogenized description of the simulation to the experiments.

In the 30°-OAT experiment, the transverse tensile strains increase from zone A to B, but decrease from zone B to C to D. This indicates a strong localization of roving slippage to the difference area between zones A and B, which is the transition between the MDZ and secondary deformation zone. The measured perpendicular compression extends outside of the MDZ and $E_{\perp}$ is similar for all averaging areas at high displacements. The resulting shear angle is also similar for zones A, B and C at high displacements. This results from lateral contraction due to the stitching. Both of these effects cannot be modeled with a local macroscopic approach that assumes homogeneous material properties over the whole specimen. Thus, the same strains are predicted homogeneously by the simulation for zones A and B.

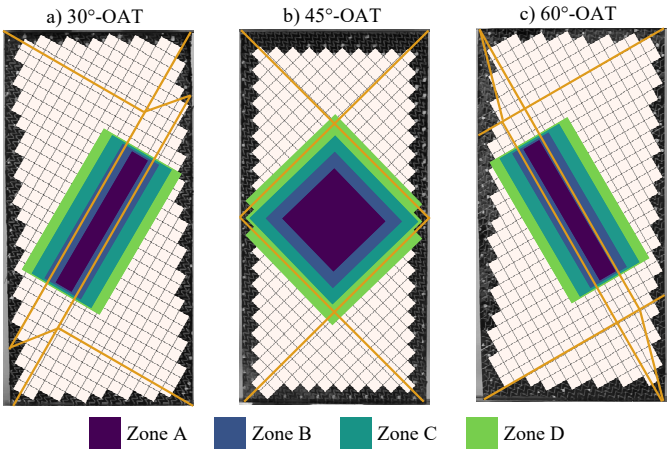

Figure A.12: Overview of different areas with increasing size for an averaging of the strain components | 30°- and 60°-OAT: Smallest zone with $130\,\mathrm{mm} \times 10\,\mathrm{mm}$ (A) whose width is increased symmetrically in increments of $20\,\mathrm{mm}$ | 45°-OAT: Smallest zone with $60\,\mathrm{mm} \times 60\,\mathrm{mm}$ (A) whose width and height is increased symmetrically in increments of $20\,\mathrm{mm}$.

In the 45°- and 60°-OAT experiments, γ_{12} decreases and E_{22} as well as $E_{\perp}$ increase from the smallest zone A to the biggest zone D. This indicates increasing roving slippage from the center outwards. In comparison, the strains in the simulation model are nearly homogeneous across all zones.

In summary, roving slippage is limited to the area between the main and secondary deformation zones during the experiments, while it is modeled homogenized over the entire main deformation zone. The deformation zones are clearly delimited in the simulation, while a softer transition takes place due to lateral contraction of the stitching in the experiments

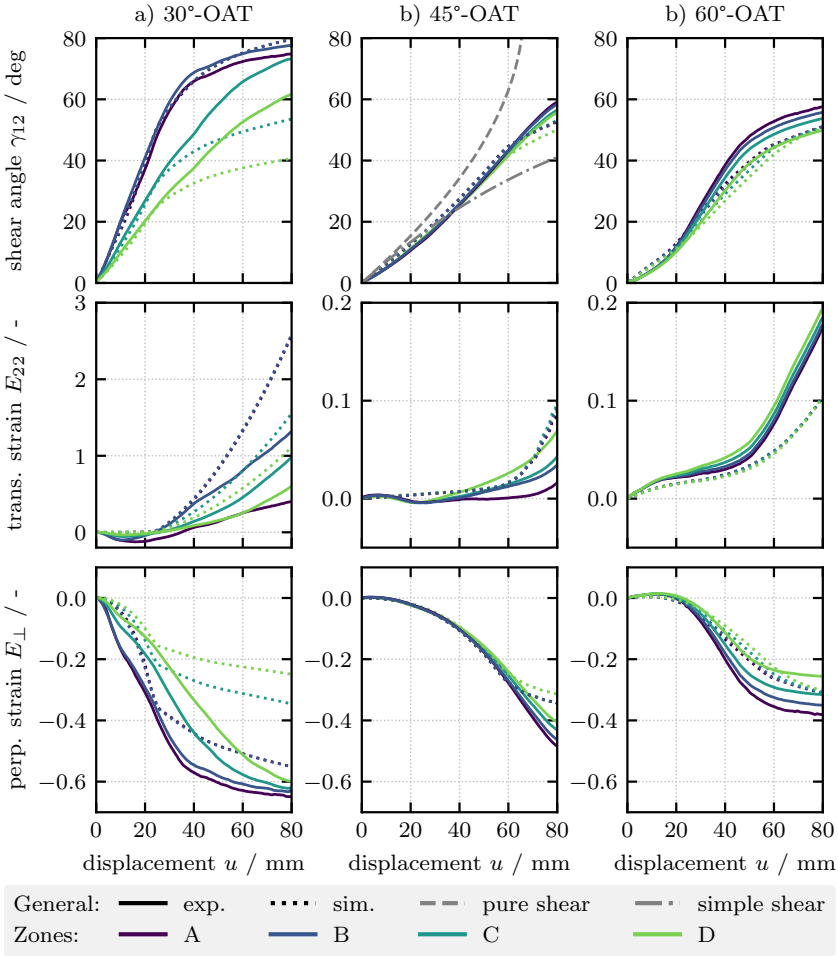

Figure A.13: Overview of strains in the different evaluation zones introduced in Figure A.13 of the off-axis-tension tests (OATs) for UD-NCF with a bias direction of a) 30°, b) 45° and c) 60°.

A.2.8 Bending modeling - Material parameters

Table A.6: Material parameters of the hypoelastic bending approach for UD-NCF in Section 5.3 | Additional necessary transverse shear stiffnesses $K_i^{\mathrm{bend,ts}}$ for the application of VUGENS subroutines to shell elements in ABAQUS/Explicit.

UD-NCF	C_{11}^{bend} [MPa]	C_{22}^{bend} [MPa]	C_{12}^{bend} [MPa]	$K_{11}^{\mathrm{bend,ts}}$ [MPa]	$K_{22}^{\mathrm{bend,ts}}$ [MPa]
front	377.385	1.65	8.688	3.590	0.341
back	302.814	0.548	1.624	0.671	0.113

A.2.9 Forming simulation - Distortion error of the 2D-DIC[5]

To demonstrate the significant distortion in the tetrahedron test due to the 2D-DIC, the resulting node coordinates of the simulation were parallel projected onto the xy-plane. Equivalent 2D-strains were calculated with the DIC algorithm used during the experimental tests [102]. The results for the perpendicular strain $E_{\perp}^{\mathrm{2D}}$ are shown in Figure A.14.

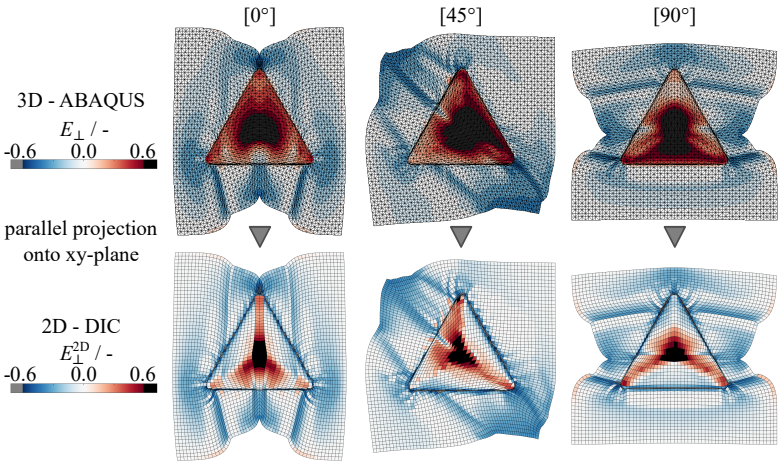

Figure A.14: Exemplary conversion from 3D strains to 2D-equivalent strains by planar projection for the tetrahedron forming simulation in Section 5.4.3.1. [180]

[5] Reproduced section from [180], cf. footnote p. 169 for details.

A.2.10 Biax-NCF - Material parameters

Table A.7: Material parameters of the hyperelastic membrane approach for Biax-NCF in Section 5.5.1.

Biax-NCF	C_i^{ini} [MPa]	S_i^{ini} [MPa]	C_i^{mid} [MPa]	$\Delta S_i^{\mathrm{mid}}$ [MPa]	C_i^{lock} [MPa]	I_i^{lock} -
W_4^{Biax}	1000	-	-	-	-	-
W_6^{Biax}	0.4	0.003	0.0035	0.04	1000	0.8192
W_8^{Biax}	1000	-	-	-	-	-

Table A.8: Material parameters of the hypoelastic bending approach for Biax-NCF in Section 5.5.2 | Additional necessary transverse shear stiffnesses $K_i^{\mathrm{bend,ts}}$ for the application of VUGENS subroutines to shell elements in ABAQUS/Explicit..

Biax-NCF	C_{11}^{bend} [MPa]	C_{22}^{bend} [MPa]	C_{12}^{bend} [MPa]	$K_{11}^{\mathrm{bend,ts}}$ [MPa]	$K_{22}^{\mathrm{bend,ts}}$ [MPa]
front	38.062	43.067	4.176	3.495	3.495
back	27.936	45.228	2.096	1.754	1.754

A.2.11 Biax-NCF - Outer contours after forming

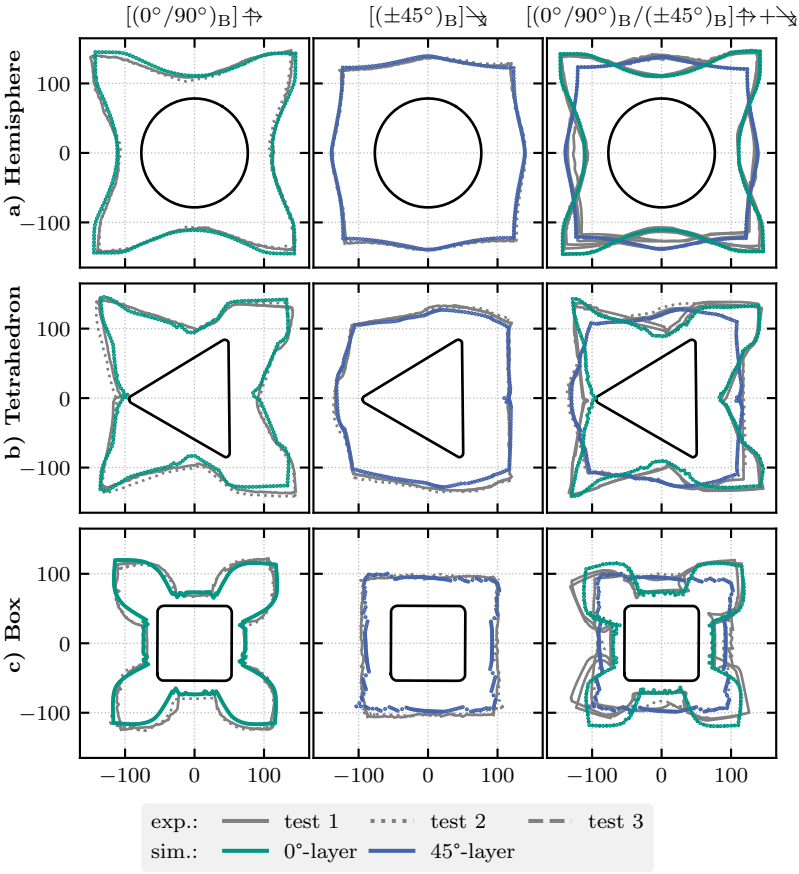

Figure A.15: Outer contours (all in mm) of the a) hemisphere, b) tetrahedron and c) square box forming simulation of Biax-NCF in Section 5.5.

A.3 Supplementary information for the solid-shell element formulation

A.3.1 Implemented solid-shell expressions

The following is a list of relevant expressions required for implementation of the solid-shell element derived in Section 6.1, that were originally published by Schwarze and Reese [314, 332]. The shape functions can alternatively be stored in a vector based on the location of the eight nodes in isoparametric coordinates

$$\boldsymbol{N}(\boldsymbol{\xi}) = \boldsymbol{r} + \xi\boldsymbol{g}_1 + \eta\boldsymbol{g}_2 + \zeta\boldsymbol{g}_3 + \xi\eta\boldsymbol{h}_1 + \eta\zeta\boldsymbol{h}_2 + \xi\zeta\boldsymbol{h}_3 + \xi\eta\zeta\boldsymbol{h}_4 \tag{A.10}$$

$$\boldsymbol{r} = 1/8[1,1,1,1,1,1,1,1]^{\mathsf{T}} \tag{A.11}$$

$$\boldsymbol{g}_1 = 1/8[-1,1,1,-1,-1,1,1,-1]^{\mathsf{T}} \tag{A.12}$$

$$\boldsymbol{g}_2 = 1/8[-1,-1,1,1,-1,-1,1,1]^{\mathsf{T}} \tag{A.13}$$

$$\boldsymbol{g}_3 = 1/8[-1,-1,-1,-1,1,1,1,1]^{\mathsf{T}} \tag{A.14}$$

$$\boldsymbol{h}_1 = 1/8[1,-1,1,-1,1,-1,1,-1]^{\mathsf{T}} \tag{A.15}$$

$$\boldsymbol{h}_2 = 1/8[1,1,-1,-1,-1,-1,1,1]^{\mathsf{T}} \tag{A.16}$$

$$\boldsymbol{h}_3 = 1/8[1,-1,-1,1,-1,1,1,-1]^{\mathsf{T}} \tag{A.17}$$

$$\boldsymbol{h}_4 = 1/8[-1,1,-1,1,1,-1,1,-1]^{\mathsf{T}} \tag{A.18}$$

The nodal coordinates and displacements in the cartesian domain are stored in 3×8 matrices

$$\boldsymbol{X}(\boldsymbol{\xi}) = \boldsymbol{X}^{\text{node}} \cdot \boldsymbol{N}(\boldsymbol{\xi}) \tag{A.19}$$

$$\boldsymbol{X}^{\text{node}} = [\boldsymbol{X}_{1e}, \boldsymbol{X}_{2e}, \boldsymbol{X}_{3e}]^{\mathsf{T}} \tag{A.20}$$

$$= \begin{bmatrix} X_{1,1} & X_{1,2} & X_{1,3} & X_{1,4} & X_{1,5} & X_{1,6} & X_{1,7} & X_{1,8} \\ X_{2,1} & X_{2,2} & X_{2,3} & X_{2,4} & X_{2,5} & X_{2,6} & X_{2,7} & X_{2,8} \\ X_{3,1} & X_{3,2} & X_{3,3} & X_{3,4} & X_{3,5} & X_{3,6} & X_{3,7} & X_{3,8} \end{bmatrix} \tag{A.21}$$

$$\boldsymbol{U}(\boldsymbol{\xi}) = \boldsymbol{U}^{\text{node}} \cdot \boldsymbol{N}(\boldsymbol{\xi}) \tag{A.22}$$

$$\boldsymbol{U}^{\text{node}} = [\boldsymbol{U}_{1e}, \boldsymbol{U}_{2e}, \boldsymbol{U}_{3e}]^{\mathsf{T}} \tag{A.23}$$

$$= \begin{bmatrix} U_{1,1} & U_{1,2} & U_{1,3} & U_{1,4} & U_{1,5} & U_{1,6} & U_{1,7} & U_{1,8} \\ U_{2,1} & U_{2,2} & U_{2,3} & U_{2,4} & U_{2,5} & U_{2,6} & U_{2,7} & U_{2,8} \\ U_{3,1} & U_{3,2} & U_{3,3} & U_{3,4} & U_{3,5} & U_{3,6} & U_{3,7} & U_{3,8} \end{bmatrix} \tag{A.24}$$

Taylor expansion of the Jacobian matrix $\boldsymbol{J}$

$$\boldsymbol{J} = \boldsymbol{J}^0 + \xi\boldsymbol{J}^\xi + \eta\boldsymbol{J}^\eta + \zeta\boldsymbol{J}^\zeta + \xi\eta\boldsymbol{J}^{\xi\eta} + \eta\zeta\boldsymbol{J}^{\eta\zeta} + \xi\zeta\boldsymbol{J}^{\xi\zeta} \tag{A.25}$$

$$\boldsymbol{J} = \frac{\partial \boldsymbol{X}}{\partial \boldsymbol{\xi}} = [\boldsymbol{J}_1\ ,\ \boldsymbol{J}_2\ ,\ \boldsymbol{J}_3] \tag{A.26}$$

$$\boldsymbol{J}_1 = \boldsymbol{X}^{\text{node}}(\boldsymbol{g}_1 + \eta\boldsymbol{h}_1 + \zeta\boldsymbol{h}_3 + \eta\zeta\boldsymbol{h}_4) = \boldsymbol{J}_1^0 + \eta\boldsymbol{J}_1^\eta + \zeta\boldsymbol{J}_1^\zeta + \eta\zeta\boldsymbol{J}_1^{\eta\zeta} \tag{A.27}$$

$$\boldsymbol{J}_2 = \boldsymbol{X}^{\text{node}}(\boldsymbol{g}_2 + \xi\boldsymbol{h}_1 + \zeta\boldsymbol{h}_2 + \xi\zeta\boldsymbol{h}_4) = \boldsymbol{J}_2^0 + \xi\boldsymbol{J}_2^\xi + \zeta\boldsymbol{J}_2^\zeta + \xi\zeta\boldsymbol{J}_1^{\xi\zeta} \tag{A.28}$$

$$\boldsymbol{J}_3 = \boldsymbol{X}^{\text{node}}(\boldsymbol{g}_3 + \xi\boldsymbol{h}_3 + \eta\boldsymbol{h}_3 + \xi\eta\boldsymbol{h}_4) = \boldsymbol{J}_3^0 + \xi\boldsymbol{J}_3^\xi + \eta\boldsymbol{J}_3^\eta + \xi\eta\boldsymbol{J}_3^{\xi\eta} \tag{A.29}$$

Taylor expansion of the displacement gradient $\boldsymbol{D}$

$$\boldsymbol{D} = \boldsymbol{D}^0 + \xi\boldsymbol{D}^\xi + \eta\boldsymbol{D}^\eta + \zeta\boldsymbol{D}^\zeta + \xi\eta\boldsymbol{D}^{\xi\eta} + \eta\zeta\boldsymbol{D}^{\eta\zeta} + \xi\zeta\boldsymbol{D}^{\xi\zeta} \tag{A.30}$$

$$\boldsymbol{D} = \frac{\partial \boldsymbol{u}}{\partial \boldsymbol{\xi}} = [\boldsymbol{D}_1\ ,\ \boldsymbol{D}_2\ ,\ \boldsymbol{D}_3] \tag{A.31}$$

$$\boldsymbol{D}_1 = \boldsymbol{U}^{\text{node}}(\boldsymbol{g}_1 + \eta\boldsymbol{h}_1 + \zeta\boldsymbol{h}_3 + \eta\zeta\boldsymbol{h}_4) = \boldsymbol{D}_1^0 + \eta\boldsymbol{D}_1^\eta + \zeta\boldsymbol{D}_1^\zeta + \eta\zeta\boldsymbol{D}_1^{\eta\zeta} \tag{A.32}$$

$$\boldsymbol{D}_2 = \boldsymbol{U}^{\text{node}}(\boldsymbol{g}_2 + \xi\boldsymbol{h}_1 + \zeta\boldsymbol{h}_2 + \xi\zeta\boldsymbol{h}_4) = \boldsymbol{D}_2^0 + \xi\boldsymbol{D}_2^\xi + \zeta\boldsymbol{D}_2^\zeta + \xi\zeta\boldsymbol{D}_1^{\xi\zeta} \tag{A.33}$$

$$\boldsymbol{D}_3 = \boldsymbol{U}^{\text{node}}(\boldsymbol{g}_3 + \xi\boldsymbol{h}_3 + \eta\boldsymbol{h}_3 + \xi\eta\boldsymbol{h}_4) = \boldsymbol{D}_3^0 + \xi\boldsymbol{D}_3^\xi + \eta\boldsymbol{D}_3^\eta + \xi\eta\boldsymbol{D}_3^{\xi\eta} \tag{A.34}$$

Taylor Approximation of the Transformation Matrix $\boldsymbol{T}$

$$\boldsymbol{T} = \boldsymbol{T}^0 + \boldsymbol{T}^\xi\xi + \boldsymbol{T}^\eta\eta + \boldsymbol{T}^\zeta\zeta \quad \text{and} \quad \boldsymbol{J}^{-1} = j_{ij}$$

with: $a^0_{ijkl} = (j_{ij})^0(j_{kl})^0$ and $a^{\xi,i}_{ijkl} = (j_{ij})^0(j_{kl})^{\xi,i} + (j_{ij})^{\xi,i}(j_{kl})^0$

$$\boldsymbol{T}^0 = \begin{bmatrix} a^0_{1111} & a^0_{2121} & a^0_{3131} & a^0_{1121} & a^0_{2131} & a^0_{1131} \\ a^0_{1212} & a^0_{2222} & a^0_{3232} & a^0_{1222} & a^0_{2232} & a^0_{1232} \\ a^0_{1313} & a^0_{2323} & a^0_{3333} & a^0_{1323} & a^0_{2333} & a^0_{1333} \\ 2a^0_{1112} & 2a^0_{2122} & 2a^0_{3132} & a^0_{2112} + a^0_{1122} & a^0_{2132} + a^0_{3122} & a^0_{1132} + a^0_{3112} \\ 2a^0_{1213} & 2a^0_{2223} & 2a^0_{3233} & a^0_{2213} + a^0_{1223} & a^0_{3223} + a^0_{2233} & a^0_{3213} + a^0_{1233} \\ 2a^0_{1113} & 2a^0_{2123} & 2a^0_{3133} & a^0_{2113} + a^0_{1123} & a^0_{3123} + a^0_{2133} & a^0_{3113} + a^0_{1133} \end{bmatrix}$$

$$\boldsymbol{T}^{\xi,i} = \begin{bmatrix} a^{\xi,i}_{1111} & a^{\xi,i}_{2121} & a^{\xi,i}_{3131} & a^{\xi,i}_{1121} & a^{\xi,i}_{2131} & a^{\xi,i}_{1131} \\ a^{\xi,i}_{1212} & a^{\xi,i}_{2222} & a^{\xi,i}_{3232} & a^{\xi,i}_{1222} & a^{\xi,i}_{2232} & a^{\xi,i}_{1232} \\ a^{\xi,i}_{1313} & a^{\xi,i}_{2323} & a^{\xi,i}_{3333} & a^{\xi,i}_{1323} & a^{\xi,i}_{2333} & a^{\xi,i}_{1333} \\ 2a^{\xi,i}_{1112} & 2a^{\xi,i}_{2122} & 2a^{\xi,i}_{3132} & a^{\xi,i}_{2112} + a^{\xi,i}_{1122} & a^{\xi,i}_{2132} + a^{\xi,i}_{3122} & a^{\xi,i}_{1132} + a^{\xi,i}_{3112} \\ 2a^{\xi,i}_{1213} & 2a^{\xi,i}_{2223} & 2a^{\xi,i}_{3233} & a^{\xi,i}_{2213} + a^{\xi,i}_{1223} & a^{\xi,i}_{3223} + a^{\xi,i}_{2233} & a^{\xi,i}_{3213} + a^{\xi,i}_{1233} \\ 2a^{\xi,i}_{1113} & 2a^{\xi,i}_{2123} & 2a^{\xi,i}_{3133} & a^{\xi,i}_{2113} + a^{\xi,i}_{1123} & a^{\xi,i}_{3123} + a^{\xi,i}_{2133} & a^{\xi,i}_{3113} + a^{\xi,i}_{1133} \end{bmatrix}$$

Taylor expansion of the Green-Lagrange strain $\hat{E}$

$$\hat{\boldsymbol{E}} = \hat{\boldsymbol{E}}^0 + \zeta\hat{\boldsymbol{E}}^\zeta + \zeta^2\hat{\boldsymbol{E}}^{\zeta\zeta} + \xi\hat{\boldsymbol{E}}^\xi + \eta\hat{\boldsymbol{E}}^\eta + \xi\eta\hat{\boldsymbol{E}}^{\xi\eta} + \eta\zeta\hat{\boldsymbol{E}}^{\eta\zeta} + \xi\zeta\hat{\boldsymbol{E}}^{\xi\zeta}$$

$$\hat{\boldsymbol{E}}^0 = \boldsymbol{T}^0 \cdot \hat{\bar{\boldsymbol{E}}}^0 \qquad \hat{\boldsymbol{E}}^\eta = \boldsymbol{T}^0 \cdot \hat{\bar{\boldsymbol{E}}}^\eta + \boldsymbol{T}^\eta \cdot \hat{\bar{\boldsymbol{E}}}^0$$

$$\hat{\boldsymbol{E}}^\zeta = \boldsymbol{T}^0 \cdot \hat{\bar{\boldsymbol{E}}}^\zeta + \boldsymbol{T}^\zeta \cdot \hat{\bar{\boldsymbol{E}}}^0 \qquad \hat{\boldsymbol{E}}^\xi = \boldsymbol{T}^0 \cdot \hat{\bar{\boldsymbol{E}}}^\xi + \boldsymbol{T}^\xi \cdot \hat{\bar{\boldsymbol{E}}}^0$$

$$\hat{\boldsymbol{E}}^{\zeta\zeta} = \boldsymbol{T}^0 \cdot \hat{\bar{\boldsymbol{E}}}^{\zeta\zeta} + \boldsymbol{T}^\zeta \cdot \hat{\bar{\boldsymbol{E}}}^\zeta \qquad \hat{\boldsymbol{E}}^{\xi\eta} = \boldsymbol{T}^0 \cdot \hat{\bar{\boldsymbol{E}}}^{\xi\eta} + \boldsymbol{T}^\xi \cdot \hat{\bar{\boldsymbol{E}}}^\eta + \boldsymbol{T}^\eta \cdot \hat{\bar{\boldsymbol{E}}}^\xi$$

$$\hat{\boldsymbol{E}}^{\eta\zeta} = \boldsymbol{T}^0 \cdot \hat{\bar{\boldsymbol{E}}}^{\eta\zeta} + \boldsymbol{T}^\eta \cdot \hat{\bar{\boldsymbol{E}}}^\zeta + \boldsymbol{T}^\zeta \cdot \hat{\bar{\boldsymbol{E}}}^\eta \qquad \hat{\boldsymbol{E}}^{\xi\zeta} = \boldsymbol{T}^0 \cdot \hat{\bar{\boldsymbol{E}}}^{\xi\zeta} + \boldsymbol{T}^\xi \cdot \hat{\bar{\boldsymbol{E}}}^\zeta + \boldsymbol{T}^\zeta \cdot \hat{\bar{\boldsymbol{E}}}^\xi$$

$$\hat{\bar{\boldsymbol{E}}}^0 = \begin{bmatrix} \boldsymbol{J}_1^{0\mathsf{T}} \cdot \boldsymbol{D}_1^0 + \frac{1}{2}\boldsymbol{D}_1^{0\mathsf{T}} \cdot \boldsymbol{D}_1^0 \\ \boldsymbol{J}_2^{0\mathsf{T}} \cdot \boldsymbol{D}_2^0 + \frac{1}{2}\boldsymbol{D}_2^{0\mathsf{T}} \cdot \boldsymbol{D}_2^0 \\ \frac{1}{4}\sum_{K=A}^{D}\left(\boldsymbol{J}_3^{K\mathsf{T}} \cdot \boldsymbol{D}_3^K + \frac{1}{2}\boldsymbol{D}_3^{K\mathsf{T}} \cdot \boldsymbol{D}_3^K\right) \\ \boldsymbol{J}_1^{0\mathsf{T}} \cdot \boldsymbol{D}_2^0 + \boldsymbol{J}_2^{0\mathsf{T}} \cdot \boldsymbol{D}_1^0 + \boldsymbol{D}_1^{0\mathsf{T}} \cdot \boldsymbol{D}_2^0 \\ \frac{1}{4}\sum_{K=E}^{H}\left(\boldsymbol{J}_2^{K\mathsf{T}} \cdot \boldsymbol{D}_3^K + \boldsymbol{J}_3^{K\mathsf{T}} \cdot \boldsymbol{D}_2^K + \boldsymbol{D}_2^{K\mathsf{T}} \cdot \boldsymbol{D}_3^K\right) \\ \frac{1}{4}\sum_{K=J}^{M}\left(\boldsymbol{J}_1^{K\mathsf{T}} \cdot \boldsymbol{D}_3^K + \boldsymbol{J}_3^{K\mathsf{T}} \cdot \boldsymbol{D}_1^K + \boldsymbol{D}_1^{K\mathsf{T}} \cdot \boldsymbol{D}_3^K\right) \end{bmatrix}$$

$$\hat{\bar{\boldsymbol{E}}}^\zeta = \begin{bmatrix} \boldsymbol{J}_1^{0\mathsf{T}} \cdot \boldsymbol{D}_1^\zeta + \boldsymbol{J}_1^{\zeta\mathsf{T}} \cdot \boldsymbol{D}_1^0 + \boldsymbol{D}_1^{0\mathsf{T}} \cdot \boldsymbol{D}_1^\zeta \\ \boldsymbol{J}_2^{0\mathsf{T}} \cdot \boldsymbol{D}_2^\zeta + \boldsymbol{J}_2^{\zeta\mathsf{T}} \cdot \boldsymbol{D}_2^0 + \boldsymbol{D}_2^{0\mathsf{T}} \cdot \boldsymbol{D}_2^\zeta \\ 0 \\ \boldsymbol{J}_1^{0\mathsf{T}} \cdot \boldsymbol{D}_2^\zeta + \boldsymbol{J}_1^{\zeta\mathsf{T}} \cdot \boldsymbol{D}_2^0 + \boldsymbol{J}_2^{0\mathsf{T}} \cdot \boldsymbol{D}_1^\zeta + \boldsymbol{J}_2^{\zeta\mathsf{T}} \cdot \boldsymbol{D}_1^0 + \boldsymbol{D}_1^{0\mathsf{T}} \cdot \boldsymbol{D}_2^\zeta + \boldsymbol{D}_1^{\zeta\mathsf{T}} \cdot \boldsymbol{D}_2^0 \\ \frac{1}{4}\sum_{K=E}^{H}\zeta^K\left(\boldsymbol{J}_2^{K\mathsf{T}} \cdot \boldsymbol{D}_3^K + \boldsymbol{J}_3^{K\mathsf{T}} \cdot \boldsymbol{D}_2^K + \boldsymbol{D}_2^{K\mathsf{T}} \cdot \boldsymbol{D}_3^K\right) \\ \frac{1}{4}\sum_{K=J}^{M}\zeta^K\left(\boldsymbol{J}_1^{K\mathsf{T}} \cdot \boldsymbol{D}_3^K + \boldsymbol{J}_3^{K\mathsf{T}} \cdot \boldsymbol{D}_1^K + \boldsymbol{D}_1^{K\mathsf{T}} \cdot \boldsymbol{D}_3^K\right) \end{bmatrix}$$

$$\hat{\bar{\boldsymbol{E}}}^{\zeta\zeta} = \begin{bmatrix} \boldsymbol{J}_1^{\zeta\mathsf{T}} \cdot \boldsymbol{D}_1^\zeta + \frac{1}{2}\boldsymbol{D}_1^{\zeta\mathsf{T}} \cdot \boldsymbol{D}_1^\zeta \\ \boldsymbol{J}_2^{\zeta\mathsf{T}} \cdot \boldsymbol{D}_2^\zeta + \frac{1}{2}\boldsymbol{D}_2^{\zeta\mathsf{T}} \cdot \boldsymbol{D}_2^\zeta \\ 0 \\ \boldsymbol{J}_1^{\zeta\mathsf{T}} \cdot \boldsymbol{D}_2^\zeta + \boldsymbol{J}_2^{\zeta\mathsf{T}} \cdot \boldsymbol{D}_1^\zeta + \boldsymbol{D}_1^{\zeta\mathsf{T}} \cdot \boldsymbol{D}_2^\zeta \\ 0 \\ 0 \end{bmatrix}$$

$$\hat{\hat{\boldsymbol{E}}}^{\xi} = \begin{bmatrix} 0 \\ \boldsymbol{J}_2^{0\mathsf{T}} \cdot \boldsymbol{D}_2^{\xi} + \boldsymbol{J}_2^{\xi\mathsf{T}} \cdot \boldsymbol{D}_2^{0} + \boldsymbol{D}_2^{0\mathsf{T}} \cdot \boldsymbol{D}_2^{\xi} \\ \frac{1}{4}\sum_{K=A}^{D} \xi^K \left(\boldsymbol{J}_3^{K\mathsf{T}} \cdot \boldsymbol{D}_3^{K} + \frac{1}{2} \boldsymbol{D}_3^{K\mathsf{T}} \cdot \boldsymbol{D}_3^{K} \right) \\ \boldsymbol{J}_1^{0\mathsf{T}} \cdot \boldsymbol{D}_2^{\xi} + \boldsymbol{J}_2^{\xi\mathsf{T}} \cdot \boldsymbol{D}_1^{0} + \boldsymbol{D}_1^{0\mathsf{T}} \cdot \boldsymbol{D}_2^{\xi} \\ \frac{1}{4}\sum_{K=E}^{H} \xi^K \left(\boldsymbol{J}_2^{K\mathsf{T}} \cdot \boldsymbol{D}_3^{K} + \boldsymbol{J}_3^{K\mathsf{T}} \cdot \boldsymbol{D}_2^{K} + \boldsymbol{D}_2^{K\mathsf{T}} \cdot \boldsymbol{D}_3^{K} \right) \\ 0 \end{bmatrix}$$

$$\hat{\hat{\boldsymbol{E}}}^{\eta} = \begin{bmatrix} \boldsymbol{J}_1^{0\mathsf{T}} \cdot \boldsymbol{D}_1^{\eta} + \boldsymbol{J}_1^{\eta\mathsf{T}} \cdot \boldsymbol{D}_1^{0} + \boldsymbol{D}_1^{0\mathsf{T}} \cdot \boldsymbol{D}_1^{\eta} \\ 0 \\ \frac{1}{4}\sum_{K=A}^{D} \eta^K \left(\boldsymbol{J}_3^{K\mathsf{T}} \cdot \boldsymbol{D}_3^{K} + \frac{1}{2} \boldsymbol{D}_3^{K\mathsf{T}} \cdot \boldsymbol{D}_3^{K} \right) \\ \boldsymbol{J}_2^{0\mathsf{T}} \cdot \boldsymbol{D}_1^{\eta} + \boldsymbol{J}_1^{\eta\mathsf{T}} \cdot \boldsymbol{D}_2^{0} + \boldsymbol{D}_2^{0\mathsf{T}} \cdot \boldsymbol{D}_1^{\eta} \\ 0 \\ \frac{1}{4}\sum_{K=J}^{M} \eta^K \left(\boldsymbol{J}_1^{K\mathsf{T}} \cdot \boldsymbol{D}_3^{K} + \boldsymbol{J}_3^{K\mathsf{T}} \cdot \boldsymbol{D}_1^{K} + \boldsymbol{D}_1^{K\mathsf{T}} \cdot \boldsymbol{D}_3^{K} \right) \end{bmatrix}$$

$$\hat{\hat{\boldsymbol{E}}}^{\eta\zeta} = \begin{bmatrix} \boldsymbol{J}_1^{0\mathsf{T}} \cdot \boldsymbol{D}_1^{\eta\zeta} + \boldsymbol{J}_1^{\eta\mathsf{T}} \cdot \boldsymbol{D}_1^{\zeta} + \boldsymbol{J}_1^{\zeta\mathsf{T}} \cdot \boldsymbol{D}_1^{\eta} + \boldsymbol{J}_1^{\eta\zeta\mathsf{T}} \cdot \boldsymbol{D}_1^{0} + \boldsymbol{D}_1^{0\mathsf{T}} \cdot \boldsymbol{D}_1^{\eta\zeta} + \boldsymbol{D}_1^{\eta\mathsf{T}} \cdot \boldsymbol{D}_1^{\zeta} \\ 0 \\ 0 \\ \boldsymbol{J}_2^{0\mathsf{T}} \cdot \boldsymbol{D}_1^{\eta\zeta} + \boldsymbol{J}_1^{\eta\mathsf{T}} \cdot \boldsymbol{D}_2^{\zeta} + \boldsymbol{J}_2^{\zeta\mathsf{T}} \cdot \boldsymbol{D}_1^{\eta} + \boldsymbol{J}_1^{\eta\zeta\mathsf{T}} \cdot \boldsymbol{D}_2^{0} + \boldsymbol{D}_2^{0\mathsf{T}} \cdot \boldsymbol{D}_1^{\eta\zeta} + \boldsymbol{D}_1^{\eta\mathsf{T}} \cdot \boldsymbol{D}_2^{\zeta} \\ 0 \\ \frac{1}{4}\sum_{K=J}^{M} \eta^K \zeta^K \left(\boldsymbol{J}_1^{K\mathsf{T}} \cdot \boldsymbol{D}_3^{K} + \boldsymbol{J}_3^{K\mathsf{T}} \cdot \boldsymbol{D}_1^{K} + \boldsymbol{D}_1^{K\mathsf{T}} \cdot \boldsymbol{D}_3^{K} \right) \end{bmatrix}$$

$$\hat{\hat{\boldsymbol{E}}}^{\xi\zeta} = \begin{bmatrix} 0 \\ \boldsymbol{J}_2^{0\mathsf{T}} \cdot \boldsymbol{D}_2^{\xi\zeta} + \boldsymbol{J}_2^{\xi\mathsf{T}} \cdot \boldsymbol{D}_2^{\zeta} + \boldsymbol{J}_2^{\zeta\mathsf{T}} \cdot \boldsymbol{D}_2^{\xi} + \boldsymbol{J}_2^{\xi\zeta\mathsf{T}} \cdot \boldsymbol{D}_2^{0} + \boldsymbol{D}_2^{0\mathsf{T}} \cdot \boldsymbol{D}_2^{\xi\zeta} + \boldsymbol{D}_2^{\xi\mathsf{T}} \cdot \boldsymbol{D}_2^{\zeta} \\ 0 \\ \boldsymbol{J}_1^{0\mathsf{T}} \cdot \boldsymbol{D}_2^{\xi\zeta} + \boldsymbol{J}_2^{\xi\mathsf{T}} \cdot \boldsymbol{D}_1^{\zeta} + \boldsymbol{J}_1^{\zeta\mathsf{T}} \cdot \boldsymbol{D}_2^{\xi} + \boldsymbol{J}_2^{\xi\zeta\mathsf{T}} \cdot \boldsymbol{D}_1^{0} + \boldsymbol{D}_1^{0\mathsf{T}} \cdot \boldsymbol{D}_2^{\xi\zeta} + \boldsymbol{D}_2^{\xi\mathsf{T}} \cdot \boldsymbol{D}_1^{\zeta} \\ \frac{1}{4}\sum_{K=E}^{H} \xi^K \zeta^K \left(\boldsymbol{J}_2^{K\mathsf{T}} \cdot \boldsymbol{D}_3^{K} + \boldsymbol{J}_3^{K\mathsf{T}} \cdot \boldsymbol{D}_2^{K} + \boldsymbol{D}_2^{K\mathsf{T}} \cdot \boldsymbol{D}_3^{K} \right) \\ 0 \end{bmatrix}$$

Taylor expansion of the B-matrices

$$\hat{\boldsymbol{B}} = \hat{\boldsymbol{B}}^0 + \zeta\hat{\boldsymbol{B}}^\zeta + \zeta^2\hat{\boldsymbol{B}}^{\zeta\zeta} + \xi\hat{\boldsymbol{B}}^\xi + \eta\hat{\boldsymbol{B}}^\eta + \xi\eta\hat{\boldsymbol{B}}^{\xi\eta} + \eta\zeta\hat{\boldsymbol{B}}^{\eta\zeta} + \xi\zeta\hat{\boldsymbol{B}}^{\xi\zeta}$$

Introducing the following split

$$\hat{\boldsymbol{B}}^0 = \left[\hat{\boldsymbol{B}}^0_1, \ldots, \hat{\boldsymbol{B}}^0_I, \ldots, \hat{\boldsymbol{B}}^0_8\right]$$

$$\hat{\boldsymbol{B}}^\xi = \left[\hat{\boldsymbol{B}}^\xi_1, \ldots, \hat{\boldsymbol{B}}^\xi_I, \ldots, \hat{\boldsymbol{B}}^\xi_8\right]$$

$$\hat{\boldsymbol{B}}^{\xi\xi} = \left[\hat{\boldsymbol{B}}^{\xi\xi}_1, \ldots, \hat{\boldsymbol{B}}^{\xi\xi}_I, \ldots, \hat{\boldsymbol{B}}^{\xi\xi}_8\right]$$

with $(\xi_1, \xi_2, \xi_3) = (\xi, \eta, \zeta)$ and $I = 1, \ldots, 8$

$$\hat{\boldsymbol{B}}^0_I = \boldsymbol{T}^0 \cdot \hat{\tilde{\boldsymbol{B}}}^0_I \qquad \hat{\boldsymbol{B}}^\xi_I = \boldsymbol{T}^0 \cdot \hat{\tilde{\boldsymbol{B}}}^\xi_I + \boldsymbol{T}^\xi \cdot \hat{\tilde{\boldsymbol{B}}}^0_I$$

$$\hat{\boldsymbol{B}}^\zeta_I = \boldsymbol{T}^0 \cdot \hat{\tilde{\boldsymbol{B}}}^\zeta_I + \boldsymbol{T}^\zeta \cdot \hat{\tilde{\boldsymbol{B}}}^0_I \qquad \hat{\boldsymbol{B}}^\eta_I = \boldsymbol{T}^0 \cdot \hat{\tilde{\boldsymbol{B}}}^\eta_I + \boldsymbol{T}^\eta \cdot \hat{\tilde{\boldsymbol{B}}}^0_I$$

$$\hat{\boldsymbol{B}}^{\zeta\zeta}_I = \boldsymbol{T}^0 \cdot \hat{\tilde{\boldsymbol{B}}}^{\zeta\zeta}_I + \boldsymbol{T}^\zeta \cdot \hat{\tilde{\boldsymbol{B}}}^\zeta_I \qquad \hat{\boldsymbol{B}}^{\xi\eta}_I = \boldsymbol{T}^0 \cdot \hat{\tilde{\boldsymbol{B}}}^{\xi\eta}_I + \boldsymbol{T}^\xi \cdot \hat{\tilde{\boldsymbol{B}}}^\eta_I + \boldsymbol{T}^\eta \cdot \hat{\tilde{\boldsymbol{B}}}^\xi_I$$

$$\hat{\boldsymbol{B}}^{\eta\zeta}_I = \boldsymbol{T}^0 \cdot \hat{\tilde{\boldsymbol{B}}}^{\eta\zeta}_I + \boldsymbol{T}^\eta \cdot \hat{\tilde{\boldsymbol{B}}}^\zeta_I + \boldsymbol{T}^\zeta \cdot \hat{\tilde{\boldsymbol{B}}}^\eta_I$$

$$\hat{\tilde{\boldsymbol{B}}}^0_I = \begin{bmatrix} g_{1I}\tilde{\boldsymbol{J}}^{0\mathsf{T}}_1 \\ g_{2I}\tilde{\boldsymbol{J}}^{0\mathsf{T}}_2 \\ \frac{1}{4}\sum_{K=A}^{D} N^K_{I,\zeta}\tilde{\boldsymbol{J}}^{K\mathsf{T}}_3 \\ g_{1I}\tilde{\boldsymbol{J}}^{0\mathsf{T}}_2 + g_{2I}\tilde{\boldsymbol{J}}^{0\mathsf{T}}_1 \\ \frac{1}{4}\sum_{K=E}^{H}\left(N^K_{I,\eta}\tilde{\boldsymbol{J}}^{K\mathsf{T}}_3 + N^K_{I,\zeta}\tilde{\boldsymbol{J}}^{K\mathsf{T}}_2\right) \\ \frac{1}{4}\sum_{K=J}^{M}\left(N^K_{I,\xi}\tilde{\boldsymbol{J}}^{K\mathsf{T}}_3 + N^K_{I,\zeta}\tilde{\boldsymbol{J}}^{K\mathsf{T}}_1\right) \end{bmatrix}$$

$$\hat{\tilde{\boldsymbol{B}}}^\zeta_I = \begin{bmatrix} h_{3I}\tilde{\boldsymbol{J}}^{0\mathsf{T}}_1 + g_{1I}\tilde{\boldsymbol{J}}^{\zeta\mathsf{T}}_1 \\ h_{2I}\tilde{\boldsymbol{J}}^{0\mathsf{T}}_2 + g_{2I}\tilde{\boldsymbol{J}}^{\zeta\mathsf{T}}_2 \\ \boldsymbol{0}^\mathsf{T} \\ h_{2I}\tilde{\boldsymbol{J}}^{0\mathsf{T}}_1 + h_{3I}\tilde{\boldsymbol{J}}^{0\mathsf{T}}_2 + g_{2I}\tilde{\boldsymbol{J}}^{\zeta\mathsf{T}}_1 + g_{1I}\tilde{\boldsymbol{J}}^{\zeta\mathsf{T}}_2 \\ \frac{1}{4}\sum_{K=E}^{H}\zeta^K\left(N^K_{I,\eta}\tilde{\boldsymbol{J}}^{K\mathsf{T}}_3 + N^K_{I,\zeta}\tilde{\boldsymbol{J}}^{K\mathsf{T}}_2\right) \\ \frac{1}{4}\sum_{K=J}^{M}\zeta^K\left(N^K_{I,\xi}\tilde{\boldsymbol{J}}^{K\mathsf{T}}_3 + N^K_{I,\zeta}\tilde{\boldsymbol{J}}^{K\mathsf{T}}_1\right) \end{bmatrix} \quad \hat{\tilde{\boldsymbol{B}}}^{\zeta\zeta}_I = \begin{bmatrix} h_{3I}\tilde{\boldsymbol{J}}^{\zeta\mathsf{T}}_1 \\ h_{2I}\tilde{\boldsymbol{J}}^{\zeta\mathsf{T}}_2 \\ \boldsymbol{0}^\mathsf{T} \\ h_{2I}\tilde{\boldsymbol{J}}^{\zeta\mathsf{T}}_1 + h_{3I}\tilde{\boldsymbol{J}}^{\zeta\mathsf{T}}_2 \\ \boldsymbol{0}^\mathsf{T} \\ \boldsymbol{0}^\mathsf{T} \end{bmatrix}$$

$$\hat{\tilde{\boldsymbol{B}}}_I^{\xi} = \begin{bmatrix} \mathbf{0}^{\mathsf{T}} \\ h_{1I}\tilde{\boldsymbol{J}}_2^{0\mathsf{T}} + g_{2I}\tilde{\boldsymbol{J}}_2^{\xi\mathsf{T}} \\ \frac{1}{4}\sum_{K=A}^{D} \xi^K N_{I,\zeta}^K \tilde{\boldsymbol{J}}_3^{K\mathsf{T}} \\ h_{1I}\tilde{\boldsymbol{J}}_1^{0\mathsf{T}} + g_{1I}\tilde{\boldsymbol{J}}_2^{\xi\mathsf{T}} \\ \frac{1}{4}\sum_{K=E}^{H} \xi^K \left(N_{I,\eta}^K \tilde{\boldsymbol{J}}_3^{K\mathsf{T}} + N_{I,\zeta}^K \tilde{\boldsymbol{J}}_2^{K\mathsf{T}} \right) \\ \mathbf{0}^{\mathsf{T}} \end{bmatrix}$$

$$\hat{\tilde{\boldsymbol{B}}}_I^{\eta} = \begin{bmatrix} h_{1I}\tilde{\boldsymbol{J}}_1^{0\mathsf{T}} + g_{1I}\tilde{\boldsymbol{J}}_1^{\eta\mathsf{T}} \\ \mathbf{0}^{\mathsf{T}} \\ \frac{1}{4}\sum_{K=A}^{D} \eta^K N_{I,\zeta}^K \tilde{\boldsymbol{J}}_3^{K\mathsf{T}} \\ h_{1I}\tilde{\boldsymbol{J}}_2^{0\mathsf{T}} + g_{2I}\tilde{\boldsymbol{J}}_1^{\eta\mathsf{T}} \\ \mathbf{0}^{\mathsf{T}} \\ \frac{1}{4}\sum_{K=J}^{M} \eta^K \left(N_{I,\xi}^K \tilde{\boldsymbol{J}}_3^{K\mathsf{T}} + N_{I,\zeta}^K \tilde{\boldsymbol{J}}_1^{K\mathsf{T}} \right) \end{bmatrix}$$

$$\hat{\tilde{\boldsymbol{B}}}_I^{\eta\zeta} = \begin{bmatrix} h_{4I}\tilde{\boldsymbol{J}}_1^{0\mathsf{T}} + h_{3I}\tilde{\boldsymbol{J}}_1^{\eta\mathsf{T}} + h_{1I}\tilde{\boldsymbol{J}}_1^{\zeta\mathsf{T}} + g_{1I}\tilde{\boldsymbol{J}}_1^{\eta\zeta\mathsf{T}} \\ \mathbf{0}^{\mathsf{T}} \\ \mathbf{0}^{\mathsf{T}} \\ h_{4I}\tilde{\boldsymbol{J}}_2^{0\mathsf{T}} + h_{2I}\tilde{\boldsymbol{J}}_1^{\eta\mathsf{T}} + h_{1I}\tilde{\boldsymbol{J}}_2^{\zeta\mathsf{T}} + g_{2I}\tilde{\boldsymbol{J}}_1^{\eta\zeta\mathsf{T}} \\ \mathbf{0}^{\mathsf{T}} \\ \frac{1}{4}\sum_{K=J}^{M} \eta^K \zeta^K \left(N_{I,\xi}^K \tilde{\boldsymbol{J}}_3^{K\mathsf{T}} + N_{I,\zeta}^K \tilde{\boldsymbol{J}}_1^{K\mathsf{T}} \right) \end{bmatrix}$$

$$\hat{\tilde{\boldsymbol{B}}}_I^{\xi\zeta} = \begin{bmatrix} \mathbf{0}^{\mathsf{T}} \\ h_{4I}\tilde{\boldsymbol{J}}_2^{0\mathsf{T}} + h_{2I}\tilde{\boldsymbol{J}}_2^{\xi\mathsf{T}} + h_{1I}\tilde{\boldsymbol{J}}_2^{\zeta\mathsf{T}} + g_{2I}\tilde{\boldsymbol{J}}_2^{\xi\zeta\mathsf{T}} \\ \mathbf{0}^{\mathsf{T}} \\ h_{4I}\tilde{\boldsymbol{J}}_1^{0\mathsf{T}} + h_{3I}\tilde{\boldsymbol{J}}_2^{\xi\mathsf{T}} + h_{1I}\tilde{\boldsymbol{J}}_1^{\zeta\mathsf{T}} + g_{1I}\tilde{\boldsymbol{J}}_2^{\xi\zeta\mathsf{T}} \\ \frac{1}{4}\sum_{K=E}^{H} \xi^K \zeta^K \left(N_{I,\eta}^K \tilde{\boldsymbol{J}}_3^{K\mathsf{T}} + N_{I,\zeta}^K \tilde{\boldsymbol{J}}_2^{K\mathsf{T}} \right) \\ \mathbf{0}^{\mathsf{T}} \end{bmatrix}$$

A.3.2 Coordinate transformation and node renumbering

The utilized solid-shell element formulation requires a specific COS and node convention to ensure the thickness integration in the thinnest direction, cf. Figure 6.1. The global Z-direction is assumed to be aligned with the thinnest edge length of the element and node numbering conventions are assumed for the upper surface (nodes 1-4) and lower surface (nodes 5-8) of the element. However, automatic meshing algorithms do not automatically identify a thickness-direction. Therefore, the strategy proposed by Reese [359] is adopted to temporarily rotate the COS and apply an internal renumbering of the nodes.

First, the initial thickness direction is determined based on the rows of the Jacobian matrix evaluated in the element center $\boldsymbol{J}^0$.

Rotation - Case 1:

$\left\| \sum_{i=1}^{1} J_{1i}^0 \right\| < \left\| \sum_{i=1}^{1} J_{2i}^0 \right\|$ and $\left\| \sum_{i=1}^{1} J_{1i}^0 \right\| < \left\| \sum_{i=1}^{1} J_{3i}^0 \right\|$ indicates that the global X-direction equals the thinnest direction and rotation is necessary, cf. Figure A.16.

$$\begin{bmatrix} X & \rightarrow & \xi & \rightarrow & \tilde{\eta} & \rightarrow & Index\ 12 \\ Y & \rightarrow & \eta & \rightarrow & \tilde{\zeta} & \rightarrow & Index\ 23 \\ Z & \rightarrow & \zeta & \rightarrow & \tilde{\xi} & \rightarrow & Index\ 31 \end{bmatrix} \rightarrow \boldsymbol{R}_{\mathrm{C1}}^{\mathrm{COS}} = \begin{bmatrix} 0 & 1 & 0 \\ 0 & 0 & 1 \\ 1 & 0 & 0 \end{bmatrix}$$

$$\boldsymbol{X}^{\mathrm{node}} = \boldsymbol{R}_{\mathrm{C1}}^{\mathrm{COS}} \cdot \boldsymbol{X}^{\mathrm{node}}, \boldsymbol{U}^{\mathrm{node}} = \boldsymbol{R}_{\mathrm{C1}}^{\mathrm{COS}} \cdot \boldsymbol{U}^{\mathrm{node}} \text{ and } \boldsymbol{J}^0 = \boldsymbol{R}_{\mathrm{C1}}^{\mathrm{COS}} \cdot \boldsymbol{J}^0$$

Rotation - Case 2:

$\left\| \sum_{i=1}^{1} J_{2i}^0 \right\| < \left\| \sum_{i=1}^{1} J_{1i}^0 \right\|$ and $\left\| \sum_{i=1}^{1} J_{2i}^0 \right\| < \left\| \sum_{i=1}^{1} J_{3i}^0 \right\|$ indicates that the global Y-direction equals the thinnest direction and rotation is necessary, cf. Figure A.17.

$$\begin{bmatrix} X & \rightarrow & \xi & \rightarrow & \tilde{\zeta} & \rightarrow & Index\ 13 \\ Y & \rightarrow & \eta & \rightarrow & \tilde{\xi} & \rightarrow & Index\ 21 \\ Z & \rightarrow & \zeta & \rightarrow & \tilde{\eta} & \rightarrow & Index\ 32 \end{bmatrix} \rightarrow \boldsymbol{R}_{\mathrm{C2}}^{\mathrm{COS}} = \begin{bmatrix} 0 & 0 & 1 \\ 1 & 0 & 0 \\ 0 & 1 & 0 \end{bmatrix}$$

$$\boldsymbol{X}^{\mathrm{node}} = \boldsymbol{R}_{\mathrm{C2}}^{\mathrm{COS}} \cdot \boldsymbol{X}^{\mathrm{node}} \quad , \quad \boldsymbol{U}^{\mathrm{node}} = \boldsymbol{R}_{\mathrm{C2}}^{\mathrm{COS}} \cdot \boldsymbol{U}^{\mathrm{node}} \quad \text{and} \quad \boldsymbol{J}^0 = \boldsymbol{R}_{\mathrm{C2}}^{\mathrm{COS}} \cdot \boldsymbol{J}^0$$

Second, it is determined based on the columns of the Jacobian matrix evaluated in the element $\boldsymbol{J}_i^0$ center if a node renumbering is necessary. $\boldsymbol{J}_1^0, \boldsymbol{J}_2^0$ and $\boldsymbol{J}_3^0$ represent the stretch of ξ, η and ζ between the isoparametric and cartesian domain.

Renumbering - Case 1:

$\|\boldsymbol{J}_1^0\| < \|\boldsymbol{J}_2^0\|$ and $\|\boldsymbol{J}_1^0\| < \|\boldsymbol{J}_3^0\|$:

$$\begin{bmatrix} 1 & \rightarrow & 1 & \rightarrow & Index\ 11 \\ 2 & \rightarrow & 4 & \rightarrow & Index\ 42 \\ 3 & \rightarrow & 8 & \rightarrow & Index\ 83 \\ 4 & \rightarrow & 5 & \rightarrow & Index\ 54 \\ 5 & \rightarrow & 2 & \rightarrow & Index\ 25 \\ 6 & \rightarrow & 3 & \rightarrow & Index\ 36 \\ 7 & \rightarrow & 7 & \rightarrow & Index\ 77 \\ 8 & \rightarrow & 6 & \rightarrow & Index\ 68 \end{bmatrix} \rightarrow \boldsymbol{R}_{\mathrm{C1}}^{\mathrm{N}} = \begin{bmatrix} 1 & 0 & 0 & 0 & 0 & 0 & 0 & 0 \\ 0 & 0 & 0 & 0 & 1 & 0 & 0 & 0 \\ 0 & 0 & 0 & 0 & 0 & 1 & 0 & 0 \\ 0 & 1 & 0 & 0 & 0 & 0 & 0 & 0 \\ 0 & 0 & 0 & 1 & 0 & 0 & 0 & 0 \\ 0 & 0 & 0 & 0 & 0 & 0 & 0 & 1 \\ 0 & 0 & 0 & 0 & 0 & 0 & 1 & 0 \\ 0 & 0 & 1 & 0 & 0 & 0 & 0 & 0 \end{bmatrix}$$

$$\boldsymbol{X}^{\mathrm{node}} = \boldsymbol{X}^{\mathrm{node}} \cdot \boldsymbol{R}_{\mathrm{C1}}^{\mathrm{N}} \quad , \quad \boldsymbol{U}^{\mathrm{node}} = \boldsymbol{U}^{\mathrm{node}} \cdot \boldsymbol{R}_{\mathrm{C1}}^{\mathrm{N}} \quad \text{and} \quad \boldsymbol{J}^0 = \boldsymbol{J}^0 \cdot \boldsymbol{R}_{\mathrm{C1}}^{\mathrm{COS}^{\mathrm{T}}}$$

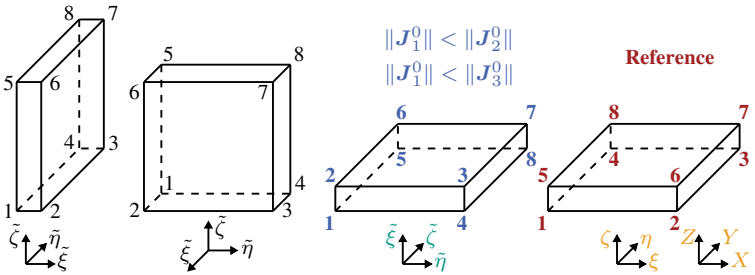

Figure A.16: Schematic illustration of the case 1 for a necessary rotation of the COS or node renumbering - First three illustrations represent the initial configuration and necessary rotations - Last illustration represents the desired reference configuration and global COS.

Renumbering - Case 2:

$\|\boldsymbol{J}_2^0\| < \|\boldsymbol{J}_3^0\|$ and $\|\boldsymbol{J}_2^0\| < \|\boldsymbol{J}_1^0\|$:

$$\begin{bmatrix} \mathbf{1} & \rightarrow & \mathbf{1} & \rightarrow & Index\ 11 \\ \mathbf{2} & \rightarrow & \mathbf{5} & \rightarrow & Index\ 52 \\ \mathbf{3} & \rightarrow & \mathbf{6} & \rightarrow & Index\ 63 \\ \mathbf{4} & \rightarrow & \mathbf{2} & \rightarrow & Index\ 24 \\ \mathbf{5} & \rightarrow & \mathbf{4} & \rightarrow & Index\ 45 \\ \mathbf{6} & \rightarrow & \mathbf{8} & \rightarrow & Index\ 86 \\ \mathbf{7} & \rightarrow & \mathbf{7} & \rightarrow & Index\ 77 \\ \mathbf{8} & \rightarrow & \mathbf{3} & \rightarrow & Index\ 38 \end{bmatrix} \rightarrow \boldsymbol{R}_{\mathrm{C2}}^{\mathrm{N}} = \begin{bmatrix} 1 & 0 & 0 & 0 & 0 & 0 & 0 & 0 \\ 0 & 0 & 0 & 1 & 0 & 0 & 0 & 0 \\ 0 & 0 & 0 & 0 & 0 & 0 & 0 & 1 \\ 0 & 0 & 0 & 0 & 1 & 0 & 0 & 0 \\ 0 & 1 & 0 & 0 & 0 & 0 & 0 & 0 \\ 0 & 0 & 1 & 0 & 0 & 0 & 0 & 0 \\ 0 & 0 & 0 & 0 & 0 & 0 & 1 & 0 \\ 0 & 0 & 0 & 0 & 0 & 1 & 0 & 0 \end{bmatrix}$$

$$\boldsymbol{X}^{\mathrm{node}} = \boldsymbol{X}^{\mathrm{node}} \cdot \boldsymbol{R}_{\mathrm{C2}}^{\mathrm{N}} \quad , \quad \boldsymbol{U}^{\mathrm{node}} = \boldsymbol{U}^{\mathrm{node}} \cdot \boldsymbol{R}_{\mathrm{C2}}^{\mathrm{N}} \quad \text{and} \quad \boldsymbol{J}^{0} = \boldsymbol{J}^{0} \cdot \boldsymbol{R}_{\mathrm{C2}}^{\mathrm{COS}^{\mathsf{T}}}$$

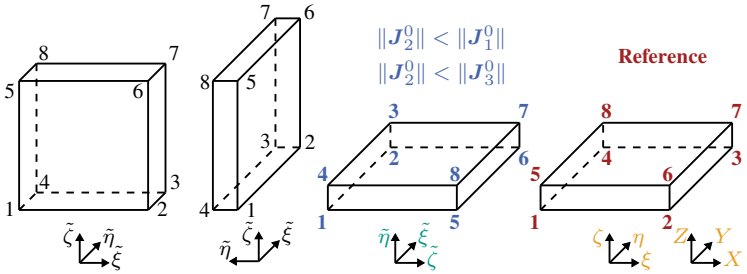

Figure A.17: Schematic illustration of the case 2 for a necessary rotation of the COS or node renumbering - First three illustrations represent the initial configuration and necessary rotations - Last illustration represents the desired reference configuration and global COS.

List of Figures

List of Tables

Bibliography

[1] F. Henning and E. Moeller, editors. *Handbuch Leichtbau: Methoden, Werkstoffe, Fertigung*. Carl Hanser Verlag, Munich, Germany, 2011.

[2] F. Henning, L. Kärger, D. Dörr, F. J. Schirmaier, J. Seuffert, and A. Bernath. Fast processing and continuous simulation of automotive structural composite components. *Composites Science and Technology*, 171:261–279, 2019.

[3] A. Hrymak, T. Böhlke, F. Henning, J. T. Wood, K. A. Weidenmann, and L. Kärger. *Continuous–Discontinuous Fiber-Reinforced Polymers; An Integrated Engineering Approach.* Carl Hanser Verlag, Munich, Germany, 2019.

[4] L. Zhu, N. Li, and P. Childs. Light-weighting in aerospace component and system design. *Propulsion and Power Research*, 7(2):103–119, 2018.

[5] K. Friedrich and A. A. Almajid. Manufacturing Aspects of Advanced Polymer Composites for Automotive Applications. *Applied Composite Materials*, 20(2):107–128, 2013.

[6] J. Zhang, G. Lin, U. Vaidya, and H. Wang. Past, present and future prospective of global carbon fibre composite developments and applications. *Composites Part B: Engineering*, 250:110463, 2023.

[7] E. Witten and M. Volker. *Der europäische Markt für Faserverstärkte Kunststoffe / Composites 2022: Marktentwicklungen, Trends, Herausforderungen und Ausblicke*. AVK – Industrievereinigung Verstärkte Kunststoffe e.V., Frankfurt, Germany, Industry report (in German) - available online: `https://www.avk-tv.de/news.php?id=455`, 04.2023.

[8] Y. Yang, R. Boom, B. Irion, D.-J. van Heerden, P. Kuiper, and H. d. Wit. Recycling of composite materials. *Chemical Engineering and Processing: Process Intensification*, 51:53–68, 2012.

[9] A. E. Krauklis, C. W. Karl, A. I. Gagani, and J. K. Jørgensen. Composite Material Recycling Technology—State-of-the-Art and Sustainable Development for the 2020s. *Journal of Composites Science*, 5(1):28, 2021.

[10] H. Voggenreiter. *Werkstoffinnovationen für nachhaltige Mobilität und Energieversorgung*. VDI - Society Materials Engineering e.V., Düsseldorf , Germany, VDI-GME-study (in German) - available online: `https://www.vdi.de/ueber-uns/presse/publikationen/details/werkstoffinnovationen-fuer-nachhaltige-mobilitaet-und-energieversorgung`, 03.2014.

[11] L. Kärger, A. Bernath, F. Fritz, S. Galkin, D. Magagnato, A. Oeckerath, A. Schön, and F. Henning. Development and validation of a CAE chain for unidirectional fibre reinforced composite components. *Composite Structures*, 132:350–358, 2015.

[12] H. Schürmann. *Konstruieren mit Faser-Kunststoff-Verbunden*. VDI. Springer-Verlag Berlin Heidelberg, Berlin, Germany, 2. edition, 2007.

[13] P. J. Halley and M. E. Mackay. Chemorheology of thermosets—an overview. *Polymer Engineering & Science*, 36(5):593–609, 1996.

[14] A. Bernath. *Numerical prediction of curing and process-induced distortion of composite structures*. Dissertation, Karlsruher Institute for Technology, Karlsruhe, Germany, 2019.

[15] G. Oliveux, L. O. Dandy, and G. A. Leeke. Current status of recycling of fibre reinforced polymers: Review of technologies, reuse and resulting properties. *Progress in Materials Science*, 72:61–99, 2015.

[16] R. Akkerman and S. P. Haanappel. Thermoplastic composites manufacturing by thermoforming. In P. Boisse, editor, *Advances in composites manufacturing and process design*, Woodhead publishing series in composites science and engineering, pages 111–129. Woodhead Publishing, Cambridge, UK, 2015.

[17] D. Dörr. *Simulation of the thermoforming process of UD fiber-reinforced thermoplastic tape laminates*. Dissertation, Karlsruher Institute for Technology, Karlsruhe, Germany, 2019.

[18] T. D. Joppich. *Beitrag zum Umformverhalten von PA6/CF Gelegelaminaten im nicht-isothermen Stempelumformprozess*. Dissertation (in German), Karlsruher Institute for Technology, Karlsruhe, Germany, 2019.

[19] K. Vanclooster. *Forming of multilayerd fabric reinforced thermoplastic composites*. Dissertation, KU Leuven, Leuven, Belgien, 2009.

[20] P. Harrison, R. Gomes, and N. Curado-Correia. Press forming a 0/90 cross-ply advanced thermoplastic composite using the double-dome benchmark geometry. *Composites Part A: Applied Science and Manufacturing*, 54:56–69, 2013.

[21] S. Haanappel. *Forming of UD fibre reinforced thermoplastics: A critical evaluation of intra-ply shear*. Dissertation, University of Twente, Enschede, Netherlands, 2013.

[22] U. Sachs. *Friction and bending in thermoplastic composites forming processes*. Dissertation, Universiteit Twente, Twente, Enschede, Netheralands, 2014.

[23] E. Guzman-Maldonado, N. Hamila, P. Boisse, and J. Bikard. Thermomechanical analysis, modelling and simulation of the forming of pre-impregnated thermoplastics composites. *Composites Part A: Applied Science and Manufacturing*, 78:211–222, 2015.

[24] A. Schug, J. Winkelbauer, R. Hinterhölzl, and K. Drechsler. Thermoforming of glass fibre reinforced polypropylene: A study on the influence of different process parameters. *AIP Conference Proceedings*, 1896(1):030010, 2017.

[25] H. Chen, A. Ding, S. Li, and J. Wang. A focused review on the thermo-stamping process and simulation progresses of continuous fibre reinforced thermoplastic composites. *Composites Part B: Engineering*, 224:109196, 2021.

[26] R. A. Brooks, H. Wang, Z. Ding, J. Xu, Q. Song, H. Liu, J. P. Dear, and N. Li. A review on stamp forming of continuous fibre-reinforced thermoplastics. *International Journal of Lightweight Materials and Manufacture*, 47(1):15, 2022.

[27] E. Guzman-Maldonado, N. Hamila, N. Naouar, G. Moulin, and P. Boisse. Simulation of thermoplastic prepreg thermoforming based on a visco-hyperelastic model and a thermal homogenization. *Materials & Design*, 93:431–442, 2016.

[28] D. Dörr, F. J. Schirmaier, F. Henning, and L. Kärger. A viscoelastic approach for modeling bending behavior in finite element forming simulation of continuously fiber reinforced composites. *Composites Part A: Applied Science and Manufacturing*, 94:113–123, 2017.

[29] D. Dörr, F. Henning, and L. Kärger. Nonlinear hyperviscoelastic modelling of intra-ply deformation behaviour in finite element forming simulation of continuously fibre-reinforced thermoplastics. *Composites Part A: Applied Science and Manufacturing*, 109:585–596, 2018.

[30] H. Xiong, E. Guzman Maldonado, N. Hamila, and P. Boisse. A prismatic solid-shell finite element based on a DKT approach with efficient calculation of through the thickness deformation. *Finite Elements in Analysis and Design*, 151:18–33, 2018.

[31] H. Xiong, N. Hamila, and P. Boisse. Consolidation Modeling during Thermoforming of Thermoplastic Composite Prepregs. *Materials*, 12(18):2853, 2019.

[32] P. D. Mulye, L. Morançay, C. Binetruy, S. Comas-Cardona, A. Leygue, and D. Guillon. Unified numerical process modeling of forming and consolidation for thermoplastic composites with prepreg patches. *Frontiers in Materials*, 10:211, 2023.

[33] C. Cherif, editor. *Textile Werkstoffe für den Leichtbau: Techniken - Verfahren - Materialien - Eigenschaften*. Springer-Verlag Berlin Heidelberg, Berlin, Germany, 2011.

[34] S. Chen, O. McGregor, A. Endruweit, M. T. Elsmore, D. d. Focatiis, L. T. Harper, and N. A. Warrior. Double diaphragm forming simulation for complex composite structures. *Composites Part A: Applied Science and Manufacturing*, 95:346–358, 2017.

[35] A. J. Thompson, J. P.-H. Belnoue, and S. R. Hallett. Modelling defect formation in textiles during the double diaphragm forming process. *Composites Part B: Engineering*, 202(3):108357, 2020.

[36] F. Yu, S. Chen, L. T. Harper, and N. A. Warrior. Investigation into the effects of inter-ply sliding during double diaphragm forming for multi-layered biaxial

non-crimp fabrics. *Composites Part A: Applied Science and Manufacturing*, 150(4):106611, 2021.

[37] F. Kruse and T. Gries. 2 - Standardisation of production technologies for non-crimp fabric composites. In Stepan V. Lomov, editor, *Non-Crimp Fabric Composites*, Woodhead publishing series in composites science and engineering, pages 42–66. Woodhead Publishing, Cambridge, UK, 2011.

[38] A. Schnabel and T. Gries. 1 - Production of non-crimp fabrics for composites. In Stepan V. Lomov, editor, *Non-Crimp Fabric Composites*, Woodhead publishing series in composites science and engineering, pages 3–41. Woodhead Publishing, Cambridge, UK, 2011.

[39] S.V. Lomov. 6 - Deformability of textile performs in the manufacture of non-crimp fabric composites. In Stepan V. Lomov, editor, *Non-Crimp Fabric Composites*, Woodhead publishing series in composites science and engineering, pages 117–144. Woodhead Publishing, 2011.

[40] A. Bernath, L. Kärger, and F. Henning. Accurate Cure Modeling for Isothermal Processing of Fast Curing Epoxy Resins. *Polymers*, 8(11):390, 2016.

[41] M. Deléglise, P. Le Grognec, C. Binetruy, P. Krawczak, and B. Claude. Modeling of high speed rtm injection with highly reactive resin with on-line mixing. *Composites Part A: Applied Science and Manufacturing*, 42(10):1390–1397, 2011.

[42] C. Fais. Lightweight automotive design with HP-RTM. *Reinforced Plastics*, 55(5):29–31, 2011.

[43] M. A. Siddiqui, H. Koelman, and P. S. Shembekar. High Pressure RTM Process Modeling for Automotive Composite Product Development. In *Symposium on International Automotive Technology 2017*. SAE International, 2017.

[44] J. Merotte, P. Simacek, and S. G. Advani. Resin flow analysis with fiber preform deformation in through thickness direction during compression resin transfer molding. *Composites Part A: Applied Science and Manufacturing*, 41(7):881–887, 2010.

[45] J. Seuffert, P. Rosenberg, L. Kärger, F. Henning, M. H. Kothmann, and G. Deinzer. Experimental and numerical investigations of pressure-controlled resin transfer

molding (PC-RTM). *Advanced Manufacturing: Polymer & Composites Science*, 6(3):154–163, 2020.

[46] P. Rosenberg. *Entwicklung einer RTM Prozessvariante zur kavitätsdruckgeregelten Herstellung von Faserverbundstrukturbauteilen*. Dissertation (in German), Karlsruher Institute for Technology, Karlsruhe, Germany, 2018.

[47] R. Azzouz, S. Allaoui, and R. Moulart. Composite preforming defects: a review and a classification. *International Journal of Material Forming*, 48(3):177, 2021.

[48] P. Boisse, N. Hamila, and A. Madeo. Modelling the development of defects during composite reinforcements and prepreg forming. *Philosophical transactions. Series A, Mathematical, physical, and engineering sciences*, 374(2071):20150269, 2016.

[49] E. Capelle, P. Ouagne, D. Soulat, and D. Duriatti. Complex shape forming of flax woven fabrics: Design of specific blank-holder shapes to prevent defects. *Composites Part B: Engineering*, 62:29–36, 2014.

[50] F. N. Nezami, T. Gereke, and C. Cherif. Active forming manipulation of composite reinforcements for the suppression of forming defects. *Composites Part A: Applied Science and Manufacturing*, 99:94–101, 2017.

[51] M. R. Piggott. The effect of fibre waviness on the mechanical properties of unidirectional fibre composites: A review. *Composites Science and Technology*, 53(2):201–205, 1995.

[52] S. Galkin. *Modeling structural behavior of fiber reinforced composite parts by considering draping effects*. Dissertation, Karlsruher Institute for Technology, Karlsruhe, Germany, 2022.

[53] A. Hautefeuille, S. Comas-Cardona, and C. Binetruy. Mechanical signature and full-field measurement of flow-induced large in-plane deformation of fibrous reinforcements in composite processing. *Composites Part A: Applied Science and Manufacturing*, 118:213–222, 2019.

[54] A. Hautefeuille, S. Comas-Cardona, and C. Binetruy. Consolidation and compression of deformable impregnated fibrous reinforcements: Experimental study and modeling of flow-induced deformations. *Composites Part A: Applied Science and Manufacturing*, 131:105768, 2020.

[55] M. Bodaghi, P. Simacek, N. Correia, and S. G. Advani. Experimental parametric study of flow–induced fiber washout during high–injection–pressure resin transfer molding. *Polymer Composites*, 41(3):1053–1065, 2020.

[56] C. T. Poppe. *Process simulation of wet compression moulding for continuous fibre-reinforced polymers*. Dissertation, Karlsruher Institute for Technology, Karlsruhe, Germany, 2021.

[57] T.S. Mesogitis, A.A. Skordos, and A.C. Long. Uncertainty in the manufacturing of fibrous thermosetting composites: A review. *Composites Part A: Applied Science and Manufacturing*, 57:67–75, 2014.

[58] T. Senner. *Methodik zur virtuellen Absicherung der formgebenden Operation des Nasspressprozesses von Gelege-Mehrschichtverbunden*. Dissertation (in German), Friedrich-Alexander-Universität Erlangen-Nürnberg, Erlangen, Germany, 2016.

[59] J. Bergmann, H. Do rmann, and R. Lange. Interpreting process data of wet pressing process. Part 1: Theoretical approach. *Journal of Composite Materials*, 50(17):2399–2407, 2016.

[60] J. Bergmann, H. Do rmann, and R. Lange. Interpreting process data of wet pressing process. Part 2: Verification with real values. *Journal of Composite Materials*, 50(17):2409–2419, 2016.

[61] S. J. Stanglmaier. *Empirische Charakterisierung und Modellierung des Imprägnierprozesses lokal verstärkter Kohlenstofffaserhalbzeuge im RTM- und Nasspress-Verfahren für die Großserie*. Dissertation (in German), Karlsruhe Institute of Technology, Karlsruhe, Germany, 2017.

[62] F. Albrecht. *Experimentelle Untersuchungen zur Fluid-Struktur-Interaktion im Wet Compression Molding Prozess*. Dissertation (in German), Karlsruhe Institute of Technology, Karlsruhe, Germany, 2022.

[63] F. Albrecht, C. Poppe, T. Tiemann, V. Sauerwein, P. Rosenberg, and F. Henning. Flow-induced fiber displacement in non-bindered UD-NCF during Wet Compression Molding – Analysis and implications for process control. *Composites Science and Technology*, 228:109574, 2022.

[64] C. Poppe, D. Dörr, F. Henning, and L. Kärger. Experimental and numerical investigation of the shear behaviour of infiltrated woven fabrics. *Composites Part A: Applied Science and Manufacturing*, 114:327–337, 2018.

[65] C. Poppe, T. Rosenkranz, D. Dörr, and L. Kärger. Comparative experimental and numerical analysis of bending behaviour of dry and low viscous infiltrated woven fabrics. *Composites Part A: Applied Science and Manufacturing*, 124:105466, 2019.

[66] C. T. Poppe, C. Krauß, F. Albrecht, and L. Kärger. A 3D process simulation model for wet compression moulding. *Composites Part A: Applied Science and Manufacturing*, 50(17):106379, 2021.

[67] P. Boisse, J. Colmars, N. Hamila, N. Naouar, and Q. Steer. Bending and wrinkling of composite fiber preforms and prepregs. A review and new developments in the draping simulations. *Composites Part B: Engineering*, 141:234–249, 2018.

[68] R. Bai, B. Chen, J. Colmars, and P. Boisse. Physics-based evaluation of the drapability of textile composite reinforcements. *Composites Part B: Engineering*, 242(7):110089, 2022.

[69] U. Mohammed, C. Lekakou, and M. G. Bader. Experimental studies and analysis of the draping of woven fabrics. *Composites Part A: Applied Science and Manufacturing*, 31(12):1409–1420, 2000.

[70] S. V. Lomov, I. Verpoest, M. Barburski, and J. Laperre. Carbon composites based on multiaxial multiply stitched preforms. Part 2. KES-F characterisation of the deformability of the preforms at low loads. *Composites Part A: Applied Science and Manufacturing*, 34(4):359–370, 2003.

[71] H. Krieger, T. Gries, and S. E. Stapleton. Design of Tailored Non-Crimp Fabrics Based on Stitching Geometry. *Applied Composite Materials*, 25(1):113–127, 2018.

[72] Y. P. Chuves, M. Pitanga, I. Grether, M. O. Cioffi, and F. Monticeli. The Influence of Several Carbon Fiber Architecture on the Drapability Effect. *Textiles*, 2(3):486–498, 2022.

[73] S. Allaoui, C. Cellard, and G. Hivet. Effect of inter-ply sliding on the quality of multilayer interlock dry fabric preforms. *Composites Part A: Applied Science and Manufacturing*, 68:336–345, 2015.

[74] S. Allaoui, G. Hivet, D. Soulat, A. Wendling, P. Ouagne, and S. Chatel. Experimental preforming of highly double curved shapes with a case corner using an interlock reinforcement. *International Journal of Material Forming*, 7(2):155–165, 2014.

[75] H. Lin, J. Wang, A. C. Long, M. J. Clifford, and P. Harrison. Predictive modelling for optimization of textile composite forming. *Composites Science and Technology*, 67(15–16):3242–3252, 2007.

[76] J. S. Lee, S. J. Hong, W.-R. Yu, and T. J. Kang. The effect of blank holder force on the stamp forming behavior of non-crimp fabric with a chain stitch. *Composites Science and Technology*, 67(3–4):357–366, 2007.

[77] F. N. Nezami, T. Gereke, and C. Cherif. Analyses of interaction mechanisms during forming of multilayer carbon woven fabrics for composite applications. *Composites Part A: Applied Science and Manufacturing*, 84:406–416, 2016.

[78] C. Tephany, J. Gillibert, P. Ouagne, G. Hivet, S. Allaoui, and D. Soulat. Development of an experimental bench to reproduce the tow buckling defect appearing during the complex shape forming of structural flax based woven composite reinforcements. *Composites Part A: Applied Science and Manufacturing*, 81:22–33, 2016.

[79] J. V. Viisainen, A. Hosseini, and M. Sutcliffe. Experimental investigation, using 3D digital image correlation, into the effect of component geometry on the wrinkling behaviour and the wrinkling mechanisms of a biaxial NCF during preforming. *Composites Part A: Applied Science and Manufacturing*, 142(5):106248, 2021.

[80] R. Jagpal, E. Evangelou, R. Butler, and E. G. Loukaides. Preforming of non-crimp fabrics with distributed magnetic clamping and Bayesian optimisation. *Journal of Composite Materials*, 56(18):2835–2854, 2022.

[81] L. Kärger, S. Galkin, C. Zimmerling, D. Dörr, J. Linden, A. Oeckerath, and K. Wolf. Forming optimisation embedded in a CAE chain to assess and enhance

the structural performance of composite components. *Composite Structures*, 192:143–152, 2018.

[82] C. Poppe, T. Joppich, D. Dörr, L. Kärger, and F. Henning. Modeling and validation of gripper induced membrane forces in finite element forming simulation of continuously reinforced composites. *AIP Conference Proceedings*, 1896:030002, 2017.

[83] C. R. Zimmerling. *Machine learning algorithms for efficient process optimisation of variable geometries at the example of fabric forming*. Dissertation, Karlsruher Institute for Technology, Karlsruhe, Germany, 2023.

[84] C. Krogh, J. A. Glud, and J. Jakobsen. Modeling the robotic manipulation of woven carbon fiber prepreg plies onto double curved molds: A path-dependent problem. *Journal of Composite Materials*, 53(15):2149–2164, 2019.

[85] S. Coutandin, D. Brandt, P. Heinemann, P. Ruhland, and J. Fleischer. Influence of punch sequence and prediction of wrinkling in textile forming with a multi-punch tool. *Production Engineering*, 12(6):779–788, 2018.

[86] F. Schirmaier. *Experimentelle Untersuchung und Simulation des Umformverhaltens nähgewirkter unidirektionaler Kohlenstofffasergelege*. Dissertation (in German), Karlsruher Institute for Technology, Karlsruhe, Germany, 2017.

[87] P. Boisse, N. Naouar, and A. Charmetant. Finite element analysis of composite forming at macroscopic and mesoscopic scale. In Philippe Boisse, editor, *Advances in Composites Manufacturing and Process Design*, pages 297–315. Woodhead Publishing, 2015.

[88] E. Syerko, S. Comas-Cardona, and C. Binetruy. Models for shear properties/behavior of dry fibrous materials at various scales: a review. *International Journal of Material Forming*, 8:1–23, 2015.

[89] P. Bussetta and N. Correia. Numerical forming of continuous fibre reinforced composite material: A review. *Composites Part A: Applied Science and Manufacturing*, 113:12–31, 2018.

[90] B. Liang and P. Boisse. A review of numerical analyses and experimental characterization methods for forming of textile reinforcements. *Chinese Journal of Aeronautics*, 34(8):143–163, 2021.

[91] P. Boisse, R. Akkerman, P. Carlone, L. Kärger, S. V. Lomov, and J. A. Sherwood. Advances in composite forming through 25 years of ESAFORM. *International Journal of Material Forming*, 15(3):99, 2022.

[92] M. Tourlonias, M.-A. Bueno, and D. Poquillon. Friction of carbon tows and fine single fibres. *Composites Part A: Applied Science and Manufacturing*, 98(20):116–123, 2017.

[93] M. Engelfried, B. Aichele, and P. Middendorf. Investigation of the Friction between Dry and Wetted Carbon Filaments. *Procedia Manufacturing*, 47:60–64, 2020.

[94] G. Creech and A. Pickett. Meso-modelling of Non-Crimp Fabric composites for coupled drape and failure analysis. *Journal of Materials Science*, 41(20):6725–6736, 2006.

[95] F. Härtel, P. Böhler, and P. Middendorf. An Integral Mesoscopic Material Characterization Approach. *Key Engineering Materials*, 611-612:280–291, 2014.

[96] S. Allaoui, G. Hivet, A. Wendling, P. Ouagne, and D. Soulat. Influence of the dry woven fabrics meso-structure on fabric/fabric contact behavior. *Journal of Composite Materials*, 46(6):627–639, 2012.

[97] P. Boisse, N. Hamila, and A. Madeo. The difficulties in modeling the mechanical behavior of textile composite reinforcements with standard continuum mechanics of Cauchy. Some possible remedies. *International Journal of Solids and Structures*, 154:55–65, 2018.

[98] P. A. Kelly, R. Umer, and S. Bickerton. Viscoelastic response of dry and wet fibrous materials during infusion processes. *Composites Part A: Applied Science and Manufacturing*, 37(6):868–873, 2006.

[99] R. Arbter, J. M. Beraud, C. Binetruy, L. Bizet, J. Bréard, S. Comas-Cardona, C. Demaria, A. Endruweit, P. Ermanni, F. Gommer, S. Hasanovic, P. Henrat, F. Klunker, B. Laine, S. Lavanchy, S. V. Lomov, A. Long, V. Michaud, G. Morren, . . . , and G. Ziegmann. Experimental determination of the permeability of textiles: A benchmark exercise. *Composites Part A: Applied Science and Manufacturing*, 42(9):1157–1168, 2011.

[100] N. Vernet, E. Ruiz, S. Advani, J. B. Alms, M. Aubert, M. Barburski, B. Barari, J. M. Beraud, D. C. Berg, N. Correia, M. Danzi, T. Delavière, M. Dickert, C. Di Fratta, A. Endruweit, P. Ermanni, G. Francucci, J. A. Garcia, A. George, . . . , and G. Ziegmann. Experimental determination of the permeability of engineering textiles: Benchmark II. *Composites Part A: Applied Science and Manufacturing*, 61:172–184, 2014.

[101] M. Kruse, H. O. Werner, H. Chen, T. Mennecart, W. V. Liebig, K. A. Weidenmann, and N. Ben Khalifa. Investigation of the friction behavior between dry/infiltrated glass fiber fabric and metal sheet during deep drawing of fiber metal laminates. *Production Engineering*, 33:1292, 2022.

[102] B. Schäfer, R. Zheng, N. Naouar, and L. Kärger. Membrane behavior of uni- and bidirectional non-crimp fabrics in off-axis-tension tests. *International Journal of Material Forming*, 16(6):68, 2023.

[103] K. Buet-Gautier and P. Boisse. Experimental analysis and modeling of biaxial mechanical behavior of woven composite reinforcements. *Experimental Mechanics*, 41(3):260–269, 2001.

[104] P. Boisse, A. Gasser, and G. Hivet. Analyses of fabric tensile behaviour: determination of the biaxial tension–strain surfaces and their use in forming simulations. *Composites Part A: Applied Science and Manufacturing*, 32(10):1395–1414, 2001.

[105] W. Lee, J.-H. Byun, M. K. Um, J. Cao, and P. Boisse. Coupled non-orthogonal constitutive model for woven fabric composites. In *Proceedings of the 17th International Conference on Composite Materials (ICCM17)*, 2009.

[106] Y. Yao, X. Huang, X. Peng, P. Liu, and G. Youkun. An anisotropic hyperelastic constitutive model for plain weave fabric considering biaxial tension coupling. *Textile Research Journal*, 89(3):434–444, 2019.

[107] S. V. Lomov, M. Barburski, T. Stoilova, I. Verpoest, R. Akkerman, R. Loendersloot, and Ten Thije, R. H. W. Carbon composites based on multiaxial multiply stitched preforms. Part 3: Biaxial tension, picture frame and compression tests of the preforms. *Composites Part A: Applied Science and Manufacturing*, 36(9):1188–1206, 2005.

[108] P. Quenzel, H. Kröger, B. Manin, K. Ngoc Vu, T. X. Duong, T. Gries, M. Itskov, and R. A. Sauer. Material characterisation of biaxial glass-fibre non-crimp fabrics as a function of ply orientation, stitch pattern, stitch length and stitch tension. *Journal of Composite Materials*, 56(26):3971–3991, 2022.

[109] M. Ghazimoradi, E. A. Trejo, C. Butcher, and J. Montesano. Characterizing the macroscopic response and local deformation mechanisms of a unidirectional non-crimp fabric. *Composites Part A: Applied Science and Manufacturing*, 156(9):106857, 2022.

[110] F. J. Schirmaier, K. A. Weidenmann, L. Kärger, and F. Henning. Characterisation of the draping behaviour of unidirectional non-crimp fabrics (UD-NCF). *Composites Part A: Applied Science and Manufacturing*, 80:28–38, 2016.

[111] J. Cao, R. Akkerman, P. Boisse, J. Chen, H. S. Cheng, E. F. d. Graaf, J. L. Gorczyca, P. Harrison, G. Hivet, J. Launay, W. Lee, L. Liu, S. V. Lomov, A. Long, E. d. Luycker, F. Morestin, J. Padvoiskis, X. Q. Peng, J. Sherwood, Tz. Stoilova, . . . , and B. Zhu. Characterization of mechanical behavior of woven fabrics: Experimental methods and benchmark results. *Composites Part A: Applied Science and Manufacturing*, 39(6):1037–1053, 2008.

[112] P. Boisse, editor. *Advances in composites manufacturing and process design*, volume 56 of *Woodhead publishing series in composites science and engineering*. Woodhead Publishing, Cambridge, UK, 2015.

[113] S. Chen, O. McGregor, L. T. Harper, A. Endruweit, and N. A. Warrior. Defect formation during preforming of a bi-axial non-crimp fabric with a pillar stitch pattern. *Composites Part A: Applied Science and Manufacturing*, 91:156–167, 2016.

[114] P. Boisse, N. Hamila, E. Guzman-Maldonado, A. Madeo, G. Hivet, and F. dell'Isola. The bias-extension test for the analysis of in-plane shear properties of textile composite reinforcements and prepregs: a review. *International Journal of Material Forming*, 10(4):473–492, 2016.

[115] P. Harrison, J. Wiggers, and A. C. Long. Normalization of Shear Test Data for Rate-independent Compressible Fabrics. *Journal of Composite Materials*, 42(22):2315–2344, 2008.

[116] S. V. Lomov, P. Boisse, E. Deluycker, F. Morestin, K. Vanclooster, D. Vandepitte, I. Verpoest, and A. Willems. Full-field strain measurements in textile deformability studies. *Composites Part A: Applied Science and Manufacturing*, 39(8):1232–1244, 2008.

[117] M. Mei, Y. He, X. Yang, K. Wei, Z. Qu, and D. Fang. Shear deformation characteristics and defect evolution of the biaxial ±45° and 0/90° glass non-crimp fabrics. *Composites Science and Technology*, 193(3–4):108137, 2020.

[118] F. N. Nezami, T. Gereke, C. Eberdt, and C. Cherif. Characterisation of the shear–tension coupling of carbon-fibre fabric under controlled membrane tensions for precise simulative predictions of industrial preforming processes. *Composites Part A: Applied Science and Manufacturing*, 67:131–139, 2014.

[119] J. Pourtier, B. Duchamp, M. Kowalski, P. Wang, X. Legrand, and D. Soulat. Two-way approach for deformation analysis of non-crimp fabrics in uniaxial bias extension tests based on pure and simple shear assumption. *International Journal of Material Forming*, 12(6):995–1008, 2019.

[120] M. H. Kashani, A. Rashidi, B. J. Crawford, and A. S. Milani. Analysis of a two-way tension-shear coupling in woven fabrics under combined loading tests: Global to local transformation of non-orthogonal normalized forces and displacements. *Composites Part A: Applied Science and Manufacturing*, 88:272–285, 2016.

[121] M. Graf. *Entwicklung und Validierung einer neuen Methode zur Charakterisierung des Scherverhaltens von Carbonfasergewebe mit Binderauftrag unter Normalkraft und viskoser Reibung bei hohen Prozesstemperaturen.* Dissertation (in German), Karlsruher Institute for Technology, Karlsruhe, Germany, 2018.

[122] G. Lebrun, M. N. Bureau, and J. Denault. Evaluation of bias-extension and picture-frame test methods for the measurement of intraply shear properties of pp/glass commingled fabrics. *Composite Structures*, 61(4):341–352, 2003.

[123] P. Harrison, M. J. Clifford, and A. C. Long. Shear characterisation of viscous woven textile composites: a comparison between picture frame and bias extension experiments. *Composites Science and Technology*, 64(10–11):1453–1465, 2004.

[124] P. Harrison, M. K. Tan, and A. C. Long. Kinematics of Intra-Ply Slip in Textile Composites during Bias Extension Tests. In *Proceedings of the 8th International ESAFORM Conference on Material Forming*, 2005.

[125] J. Launay, G. Hivet, A. V. Duong, and P. Boisse. Experimental analysis of the influence of tensions on in plane shear behaviour of woven composite reinforcements. *Composites Science and Technology*, 68(2):506–515, 2008.

[126] G. Hivet and A. V. Duong. A contribution to the analysis of the intrinsic shear behavior of fabrics. *Journal of Composite Materials*, 45(6):695–716, 2011.

[127] L. Li, Y. Zhao, H.-g.-n. Vuong, Y. Chen, J. Yang, and Y. Duan. In-plane shear investigation of biaxial carbon non-crimp fabrics with experimental tests and finite element modeling. *Materials & Design*, 63(0):757–765, 2014.

[128] M. Ghazimoradi, E. A. Trejo, V. Carvelli, C. Butcher, and J. Montesano. Deformation characteristics and formability of a tricot-stitched carbon fiber unidirectional non-crimp fabric. *Composites Part A: Applied Science and Manufacturing*, 82:106366, 2021.

[129] K. D. H. N. Kahavita, E. D. McCarthy, M. Zhang, C. M. Ó. Brádaigh, and P. Harrison. Characterising the shear resistance of a unidirectional non-crimp glass fabric using modified picture frame and uniaxial bias extension test methods. *International Journal of Material Forming*, 16(5):107423, 2023.

[130] J. Wang, J. Page, and R. Paton. Experimental investigation of the draping properties of reinforcement fabrics. *Composites Science and Technology*, 58(2):229–237, 1998.

[131] S. Bel, P. Boisse, and F. Dumont. Analyses of the Deformation Mechanisms of Non-Crimp Fabric Composite Reinforcements during Preforming. *Applied Composite Materials*, 19(3):513–528, 2012.

[132] S. Bel, N. Hamila, P. Boisse, and F. Dumont. Finite element model for NCF composite reinforcement preforming: Importance of inter-ply sliding. *Composites Part A: Applied Science and Manufacturing*, 43(12):2269–2277, 2012.

[133] V. N. Khiêm, H. Krieger, M. Itskov, T. Gries, and S. E. Stapleton. An averaging based hyperelastic modeling and experimental analysis of non-crimp fabrics. *International Journal of Solids and Structures*, 2016.

[134] P. Harrison, M. F. Alvarez, and D. Anderson. Towards comprehensive characterisation and modelling of the forming and wrinkling mechanics of engineering fabrics. *International Journal of Solids and Structures*, 154:2–18, 2017.

[135] S. Deghboudj, W. Boukhedena, and H. Satha. Experimental and finite element analysis of in-plane shear properties of a carbon non-crimp fabrics at macroscopic scale. *Journal of Composite Materials*, 52(2):235–244, 2018.

[136] E. Guzman-Maldonado, S. Bel, D. Bloom, P. Fideu, and P. Boisse. Experimental and numerical analyses of the mechanical behavior during draping of non-orthogonal bi-axial non-crimp fabric composite reinforcements. *Materials & Design*, 218(3):110682, 2022.

[137] F. J. Schirmaier, D. Dörr, F. Henning, and L. Kärger. A macroscopic approach to simulate the forming behaviour of stitched unidirectional non-crimp fabrics (UD-NCF). *Composites Part A: Applied Science and Manufacturing*, 102:322–335, 2017.

[138] E. A. Trejo, M. Ghazimoradi, C. Butcher, and J. Montesano. Assessing strain fields in unbalanced unidirectional non-crimp fabrics. *Composites Part A: Applied Science and Manufacturing*, 130:105758, 2020.

[139] C. Krogh, J. A. Kepler, and J. Jakobsen. Pure and simple: investigating the in-plane shear kinematics of a quasi-unidirectional glass fiber non-crimp fabric using the bias-extension test. *International Journal of Material Forming*, 14:1483–1495, 2021.

[140] B. Schäfer, S. Haas, P. Boisse, and L. Kärger. Investigation of the Membrane Behavior of UD-NCF in Macroscopic Forming Simulations. *Key Engineering Materials*, 926:1413–1422, 2022.

[141] W.-R. Yu, P. Harrison, and A. Long. Finite element forming simulation for non-crimp fabrics using a non-orthogonal constitutive equation. *Composites Part A: Applied Science and Manufacturing*, 36(8):1079–1093, 2005.

[142] J. Pourtier, B. Duchamp, M. Kowalski, X. Legrand, P. Wang, and D. Soulat. Bias extension test on a bi-axial non-crimp fabric powdered with a non-reactive binder system. *AIP Conference Proceedings*, 1960(1):020023, 2018.

[143] C. Krogh, K. D. White, A. Sabato, and J. A. Sherwood. Picture-frame testing of woven prepreg fabric: An investigation of sample geometry and shear angle acquisition. *International Journal of Material Forming*, 13(3):341–353, 2020.

[144] S. V. Lomov, editor. *Non-crimp fabric composites: Manufacturing, properties and applications*. Woodhead Publishing Series in Composites Science and Engineering. Woodhead Publishing, Cambridge, UK, 2011.

[145] M. Ferretti, A. Madeo, F. dell'Isola, and P. Boisse. Modeling the onset of shear boundary layers in fibrous composite reinforcements by second-gradient theory. *Zeitschrift für angewandte Mathematik und Physik*, 65(3):587–612, 2014.

[146] C. Pasco, M. Khan, and K. Kendall. A novel discrete method of shear angle measurement for in-plane shear properties of thermoset prepreg using a point-tracking algorithm. *Journal of Composite Materials*, 53(14):2001–2013, 2019.

[147] J. Montesano, M. Ghazimoradi, and V. Carvelli. Characterizing and modelling the coupled in-plane shear-biaxial tension deformation response of unidirectional non-crimp fabrics. *International Journal of Material Forming*, 16(4):106857, 2023.

[148] C. Krogh, P. Broberg, J. Kepler, and J. Jakobsen. Comprehending the bending: A comparison of different test setups for measuring the out-of-plane flexural rigidity of a ud fabric. *Key Engineering Materials*, 926:1257–1267, 2022.

[149] L. M. Dangora, C. J. Mitchell, and J. A. Sherwood. Predictive model for the detection of out-of-plane defects formed during textile-composite manufacture. *Composites Part A: Applied Science and Manufacturing*, 78:102–112, 2015.

[150] U. Sachs and R. Akkerman. Viscoelastic bending model for continuous fiber-reinforced thermoplastic composites in melt. *Composites Part A: Applied Science and Manufacturing*, 100:333–341, 2017.

[151] B. Chen, P. Boisse, J. Colmars, and N. Naouar. A Hypoelastic Approach for Simulating the Independent Bending Behavior of Textile Composite within the Stress Resultant Shell. *Key Engineering Materials*, 926:1223–1233, 2022.

[152] F. T. Peirce. 26-the "handle" of cloth as a measurable quantity. *Journal of the Textile Institute Transactions*, 21(9):T377–T416, 1930.

[153] E. d. Bilbao, D. Soulat, G. Hivet, and A. Gasser. Experimental Study of Bending Behaviour of Reinforcements. *Experimental Mechanics*, 50(3):333–351, 2010.

[154] B. Liang, N. Hamila, M. Peillon, and P. Boisse. Analysis of thermoplastic prepreg bending stiffness during manufacturing and of its influence on wrinkling simulations. *Composites Part A: Applied Science and Manufacturing*, 67:111–122, 2014.

[155] B. Liang, P. Chaudet, and P. Boisse. Curvature determination in the bending test of continuous fibre reinforcements. *Strain*, 53(1):e12213, 2017.

[156] P. H. Broberg, E. Lindgaard, C. Krogh, S. M. Jensen, G. G. Trabal, A.-M. Thai, and B. Bak. One-click bending stiffness: Robust and reliable automatic calculation of moment–curvature relation in a cantilever bending test. *Composites Part B: Engineering*, 39(9):110763, 2023.

[157] H. Alshahrani and M. Hojjati. A new test method for the characterization of the bending behavior of textile prepregs. *Composites Part A: Applied Science and Manufacturing*, 97:128–140, 2017.

[158] S. Kawabata. *The Standardization and analysis of hand evaluation*. Hand Evaluation and Standardization Committee Textile Machinery Society of Japan, Osaka, 2. edition, 1980.

[159] T. J. Lahey. *Modelling Hysteresis in the Bending of Fabrics*. Dissertation, University of Waterloo, Waterloo, Ontario, Canada, 2002.

[160] A. Charmetant, J. G. Orliac, E. Vidal-Sallé, and P. Boisse. Hyperelastic model for large deformation analyses of 3D interlock composite preforms. *Composites Science and Technology*, 72(12):1352–1360, 2012.

[161] A. Madeo, M. Ferretti, F. dell'Isola, and P. Boisse. Thick fibrous composite reinforcements behave as special second-gradient materials: three-point bending of 3D interlocks. *Zeitschrift für angewandte Mathematik und Physik*, 66(4):2041–2060, 2015.

[162] S. Mathieu, N. Hamila, F. Bouillon, and P. Boisse. Enhanced modeling of 3D composite preform deformations taking into account local fiber bending stiffness. *Composites Science and Technology*, 117:322–333, 2015.

[163] T. Senner, S. Kreissl, M. Merklein, M. Meinhardt, and A. Lipp. Bending of unidirectional non-crimp-fabrics: experimental characterization, constitutive modeling and application in finite element simulation. *Production Engineering*, 9:1–10, 2015.

[164] T. Grieser, D. Becker, and P. Mitschang. Investigation of the bending behaviour of multi-ply dry carbon fibre non-crimped fabrics. *The Journal of The Textile Institute*, 109(4):455–465, 2018.

[165] F. Yu, S. Chen, J. V. Viisainen, M. Sutcliffe, L. T. Harper, and N. A. Warrior. A macroscale finite element approach for simulating the bending behaviour of biaxial fabrics. *Composite Science and Technology*, 191, 2020.

[166] F. Yu, S. Chen, L. T. Harper, and N. A. Warrior. Simulating the effect of fabric bending stiffness on the wrinkling behaviour of biaxial fabrics during preforming. *Composites Part A: Applied Science and Manufacturing*, 143(2071):106308, 2021.

[167] B. Schäfer, R. Zheng, P. Boisse, and L. Kärger. Investigation of the compaction behavior of uni- and bidirectional non-crimp fabrics. *Materials Research Proceedings*, 28:331–338, 2023.

[168] X. L. Liu, P. J. Falzon, R. Sweeting, and R. Paton. Effective Compressibility and Permeability of Multi-Layer Non-Crimp Fiberglass Reinforcements. *Journal of Reinforced Plastics and Composites*, 23(8):861–879, 2004.

[169] B. Chen, E. J. Lang, and T.-W. Chou. Experimental and theoretical studies of fabric compaction behavior in resin transfer molding. *Materials Science and Engineering*, A317:188–196, 2001.

[170] F. Robitaille and R. Gauvin. Compaction of textile reinforcements for composites manufacturing. I: Review of experimental results. *Polymer Composites*, 19(2):198–216, 1998.

[171] J. Yang, J. Xiao, J. Zeng, D. Jiang, and C. Peng. Compaction Behavior and Part Thickness Variation in Vacuum Infusion Molding Process. *Applied Composite Materials*, 19(3-4):443–458, 2012.

[172] L. Li, Y. Zhao, J. Yang, J. Zhang, and Y. Duan. An experimental investigation of compaction behavior of carbon non-crimp fabrics for liquid composite molding. *Journal of Materials Science*, 50(7):2960–2972, 2015.

[173] T. Grieser and P. Mitschang. Investigation of the compaction behavior of carbon fiber NCF for continuous preforming processes. *Polymer Composites*, 38(11):2609–2625, 2017.

[174] A. Yong, A. Aktas, D. May, A. Endruweit, S. V. Lomov, S. Advani, P. Hubert, S. G. Abaimov, D. Abliz, I. Akhatov, M. A. Ali, S. Allaoui, T. Allen, D. C. Berg, S. Bickerton, B. Caglar, P. Causse, A. Chiminelli, S. Comas-Cardona, . . . , and J. H. Wang. Experimental characterisation of textile compaction response: A benchmark exercise. *Composites Part A: Applied Science and Manufacturing*, 142(4):106243, 2020.

[175] G. D. Lawrence, S. Chen, N. A. Warrior, and L. T. Harper. The influence of inter-ply friction during double-diaphragm forming of biaxial NCFs. *Composites Part A: Applied Science and Manufacturing*, 167:107426, 2023.

[176] A. Hammami and B. R. Gebart. Analysis of the vacuum infusion molding process. *Polymer Compsites*, 21(1):28–40, 2000.

[177] S. Korkiakoski, M. Haavisto, M. Rostami Barouei, and O. Saarela. Experimental compaction characterization of unidirectional stitched non-crimp fabrics in the vacuum infusion process. *Polymer Composites*, 37(9):2692–2704, 2016.

[178] D. Droste, L. Krishnappa, S. Bornemann, J.-H. Ohlendorf, M. G. Vargas Gleason, A. S. Herrmann, and W. Lang. Investigation of the compaction behaviour of a quasi-unidirectional non-crimp fabric during the vacuum infusion process. *Journal of Composite Materials*, 56(16):2509–2524, 2022.

[179] S. V. Lomov, I. Verpoest, T. Peeters, D. Roose, and M. Zako. Nesting in textile laminates: geometrical modelling of the laminate. *Composites Science and Technology*, 63(7):993–1007, 2003.

[180] B. Schäfer, D. Dörr, R. Zheng, N. Naouar, and L. Kärger. A hyperelastic approach for modeling the membrane behavior in finite element forming simulation of unidirectional non-crimp fabrics (UD-NCF). *[submitted for review]*, 2023.

[181] P. Sousa, S. V. Lomov, and J. Ivens. Methodology of dry and wet compressibility measurement. *Composites Part A: Applied Science and Manufacturing*, 128(1):105672, 2020.

[182] B. Schäfer, N. Naouar, and L. Kärger. Investigation of the friction behavior of uni- and bidirectional non-crimp fabrics. *Materials Research Proceedings*, 41:540–548, 2024.

[183] H. M. Yoo, J. W. Lee, J. S. Kim, and M. K. Um. Influence of Non-Reactive Epoxy Binder on the Permeability and Friction Coefficient of Twill-Woven Carbon Fabric in the Liquid Composite Molding Process. *Applied Sciences*, 10(20):7039, 2020.

[184] S. Coutandin, A. Wurba, A. Luft, F. Schmidt, M. Dackweiler, and J. Fleischer. Mechanical characterisation of the shear, bending and friction behaviour of bindered woven fabrics during the forming process. *Materialwissenschaft und Werkstofftechnik*, 50(12):1573–1587, 2019.

[185] U. Sachs, R. Akkerman, K. Fetfatsidis, E. Vidal-Sallé, J. Schumacher, G. Ziegmann, S. Allaoui, G. Hivet, B. Maron, K. Vanclooster, and S. V. Lomov. Characterization of the dynamic friction of woven fabrics: Experimental methods and benchmark results. *Composites Part A: Applied Science and Manufacturing*, 67:289–298, 2014.

[186] C. Poppe, D. Dörr, F. Kraus, and L. Kärger. Experimental and numerical investigation of the contact behavior during fe forming simulation of continuously reinforced composites in wet compression molding. *AIP Conference Proceedings*, 2113:020002, 2019.

[187] J. Hüttl, F. Albrecht, C. Poppe, F. Lorenz, B. Thoma, L. Kärger, P. Middendorf, and F. Henning. Investigations on friction behaviour and forming simulation of plain woven fabrics for wet compression moulding. In *Proceedings of Sampe Europe 2017*, Stuttgart, Germany, 2017.

[188] S. Liu, J. Sinke, and C. Dransfeld. An inter-ply friction model for thermoset based fibre metal laminate in a hot-pressing process. *Composites Part B: Engineering*, 227(1–3):109400, 2021.

[189] D. Budelmann, C. Schmidt, and D. Meiners. Prepreg tack: A review of mechanisms, measurement, and manufacturing implication. *Polymer Composites*, 41(9):3440–3458, 2020.

[190] K. A. Fetfatsidis, L. M. Gamache, J. L. Gorczyca, J. A. Sherwood, D. Jauffrès, and J. Chen. Design of an apparatus for measuring tool/fabric and fabric/fabric friction of woven-fabric composites during the thermostamping process. *International Journal of Material Forming*, 6(1):1–11, 2013.

[191] K. A. Fetfatsidis, D. Jauffrès, J. A. Sherwood, and J. Chen. Characterization of the tool/fabric and fabric/fabric friction for woven-fabric composites during the thermostamping process. *International Journal of Material Forming*, 6(2):209–221, 2013.

[192] R.H.W. ten Thije, R. Akkerman, M. Ubbink, and L. van der Meer. A lubrication approach to friction in thermoplastic composites forming processes. *Composites Part A: Applied Science and Manufacturing*, 42(8):950–960, 2011.

[193] J. L. Gorczyca-Cole, J. A. Sherwood, and J. Chen. A friction model for thermostamping commingled glass–polypropylene woven fabrics. *Composites Part A: Applied Science and Manufacturing*, 38(2):393–406, 2007.

[194] J. L. Gorczyca, J. A. Sherwood, L. Liu, and J. Chen. Modeling of Friction and Shear in Thermostamping of Composites - Part I. *Journal of Composite Materials*, 38(21):1911–1929, 2004.

[195] A. Kapshammer, D. Laresser, M. C. Miron, F. Baudach, and Z. Major. Characterization and Modeling of Ply/Tool and Ply/Ply Slippage Phenomena of Unidirectional Polycarbonate CF Tapes. *Polymers*, 15(17), 2023.

[196] Z. Li, D. Zhao, B. Sun, W. Liu, and G. Yue. Experimental characterization and modeling of the inter-ply sliding behavior of unidirectional prepreg in the preforming process. *Materials Research Express*, 10:035602, 2023.

[197] D. Dörr, M. Faisst, T. Joppich, C. Poppe, F. Henning, and L. Kärger. Modelling approach for anisotropic inter-ply slippage in finite element forming simulation of thermoplastic UD-tapes. *AIP Conference Proceedings*, 1960(1):020005, 2018.

[198] S. P. Haanappel, R. t. Thije, U. Sachs, B. Rietman, and R. Akkerman. Formability analyses of uni-directional and textile reinforced thermoplastics. *Composites Part A: Applied Science and Manufacturing*, 56:80–92, 2014.

[199] R. Pierik, T. Rouwmaat, W. Grouve, S. Wijskamp, and R. Akkerman. Experimental setup and method for the characterization of ply-ply adhesion for fiber-reinforced thermoplastics in melt. *Materials Research Proceedings*, 28:267–276, 2023.

[200] American Society for Testing and Materials. *Test Method for Static and Kinetic Coefficients of Friction of Plastic Film and Sheeting: ASTM D1894-14*. ASTM International, West Conshohocken, PA, USA, 2014.

[201] N. Fulleringer and J.-F. Bloch. Forced stick-slip oscillations allow the measurement of the friction force: Application to paper materials. *Tribology International*, 91(22):94–98, 2015.

[202] B. Cornelissen, U. Sachs, B. Rietman, and R. Akkerman. Dry friction characterisation of carbon fibre tow and satin weave fabric for composite applications. *Composites Part A: Applied Science and Manufacturing*, 56:127–135, 2014.

[203] W. Najjar, C. Pupin, X. Legrand, S. Boude, D. Soulat, and P. Dal Santo. Analysis of frictional behaviour of carbon dry woven reinforcement. *Journal of Reinforced Plastics and Composites*, 33(11):1037–1047, 2014.

[204] E. I. Avgoulas, D. M. Mulvihill, A. Endruweit, M. P. Sutcliffe, N. A. Warrior, D. S. d. Focatiis, and A. C. Long. Frictional behaviour of non-crimp fabrics (NCFs) in contact with a forming tool. *Tribology International*, 121:71–77, 2018.

[205] Y. Liu, Z. Xiang, Z. Wu, and X. Hu. Experimental investigation of friction behaviors of glass-fiber woven fabric. *Textile Research Journal*, 93(1-2):18–32, 2023.

[206] L. Montero, S. Allaoui, and G. Hivet. Characterisation of the mesoscopic and macroscopic friction behaviours of glass plain weave reinforcement. *Composites Part A: Applied Science and Manufacturing*, 95(2):257–266, 2017.

[207] E. Vidal-Sallé and F. Massi. Friction Measurement on Dry Fabric for Forming Simulation of Composite Reinforcement. *Key Engineering Materials*, 504-506:319–324, 2012.

[208] B. Schäfer, R. Zheng, J. Colmars, A. Platzer, N. Naouar, P. Boisse, and L. Kärger. Experimental analysis of the forming behavior of uni- and bidirectional non-crimp fabrics for different geometries. *[submitted for review]*, 2023.

[209] P. Boisse, Y. Aimène, A. Dogui, S. Dridi, S. Gatouillat, N. Hamila, M. Aurangzeb Khan, T. Mabrouki, F. Morestin, and E. Vidal-Sallé. Hypoelastic, hyperelastic, discrete and semi-discrete approaches for textile composite reinforcement forming. *International Journal of Material Forming*, 3(2):1229–1240, 2009.

[210] J. Xie, Z. Guo, M. Shao, W. Zhu, W. Jiao, Z. Yang, and L. Chen. Mechanics of textiles used as composite preforms: A review. *Composite Structures*, 304:116401, 2023.

[211] J. Huang, P. Boisse, N. Hamila, I. Gnaba, D. Soulat, and P. Wang. Experimental and numerical analysis of textile composite draping on a square box. Influence of the weave pattern. *Composite Structures*, 267:113844, 2021.

[212] B. Chen, P. Boisse, J. Colmars, N. Naouar, R. Bai, and P. Chaudet. Analysis of the Forming of Interlock Textile Composites Using a Hypoelastic Approach. *Applied Composite Materials*, 72:195, 2021.

[213] M. A. Khan, T. Mabrouki, E. Vidal-Sallé, and P. Boisse. Numerical and experimental analyses of woven composite reinforcement forming using a hypoelastic behaviour. Application to the double dome benchmark. *Journal of Materials Processing Technology*, 210(2):378–388, 2010.

[214] P. Boisse, B. Zouari, and J.-L. Daniel. Importance of in-plane shear rigidity in finite element analyses of woven fabric composite preforming. *Composites Part A: Applied Science and Manufacturing*, 37(12):2201–2212, 2006.

[215] X. Peng and F. Ding. Validation of a non-orthogonal constitutive model for woven composite fabrics via hemispherical stamping simulation. *Composites Part A: Applied Science and Manufacturing*, 42(4):400–407, 2011.

[216] B. Chen, J. Colmars, N. Naouar, and P. Boisse. A hypoelastic stress resultant shell approach for simulations of textile composite reinforcement forming. *Composites Part A: Applied Science and Manufacturing*, 149(4):106558, 2021.

[217] R. Bai, J. Colmars, B. Chen, N. Naouar, and P. Boisse. The fibrous shell approach for the simulation of composite draping with a relevant orientation of the normals. *Composite Structures*, 285(8):115202, 2022.

[218] S. E. Arnold, M. Sutcliffe, and W. Oram. Experimental measurement of wrinkle formation during draping of non-crimp fabric. *Composites Part A: Applied Science and Manufacturing*, 82:159–169, 2016.

[219] S. Allaoui, P. Boisse, S. Chatel, N. Hamila, G. Hivet, D. Soulat, and E. Vidal-Salle. Experimental and numerical analyses of textile reinforcement forming of a tetrahedral shape. *Composites Part A: Applied Science and Manufacturing*, 42(6):612–622, 2011.

[220] V. Carvelli, J. Pazimino, and S. V. Lomov. Formability of a non-crimp 3D orthogonal weave E-glass composite reinforcement. *Composites Part A: Applied Science and Manufacturing*, 61:76–83, 2014.

[221] J. Danckert. Experimental investigation of a square-cup deep-drawing process. *Journal of Materials Processing Technology*, 50(1):375–384, 1995.

[222] X. Wang, J. Li, L. Deng, and J. Li. Metal flow control during hot forming of square cups with local-thickened plates and varied friction conditions. *Journal of Materials Processing Technology*, 253:195–203, 2018.

[223] P. Wang, X. Legrand, P. Boisse, N. Hamila, and D. Soulat. Experimental and numerical analyses of manufacturing process of a composite square box part: Comparison between textile reinforcement forming and surface 3D weaving. *Composites Part B: Engineering*, 78(9):26–34, 2015.

[224] J. Sargent, J. Chen, J. Sherwood, J. Cao, P. Boisse, A. Willem, K. Vanclooster, S. V. Lomov, M. Khan, T. Mabrouki, K. Fetfatsidis, and D. Jauffrès. Benchmark Study of Finite Element Models for Simulating the Thermostamping of Woven-Fabric Reinforced Composites. *International Journal of Material Forming*, 3(S1):683–686, 2010.

[225] J. Pazmino, V. Carvelli, S. V. Lomov, B. van Mieghem, and P. Lava. 3D digital image correlation measurements during shaping of a non-crimp 3D orthogonal woven E-glass reinforcement. *International Journal of Material Forming*, 7(4):439–446, 2014.

[226] C. Kissinger, P. Mitschang, and M. Neitzel. Advanced Materials for RTM-Processing –Characterization and Application of Non Crimp Fabrics (NCF). In P.J. Winkler, editor, *Materials for Transportation Technology*, volume 1, pages 176–182. Wiley–VCH Verlag GmbH, Weinheim, Germany, 2000.

[227] J. Sirtautas, A. K. Pickett, and P. Lépicier. A mesoscopic model for coupled drape-infusion simulation of biaxial Non-Crimp Fabric. *Composites Part B: Engineering*, 47:48–57, 2013.

[228] I. Gnaba, D. Soulat, X. Legrand, and P. Wang. Investigation of the formability behaviour during stamping of tufted and un-tufted carbon preforms: towards localized reinforcement technologies. *International Journal of Material Forming*, 14(6):1337–1354, 2021.

[229] X. Sun, J. P.-H. Belnoue, A. Thompson, B. E. Said, and S. R. Hallett. Dry Textile Forming Simulations: A Benchmarking Exercise. *Frontiers in Materials*, 9:155, 2022.

[230] E. Kunze, B. Schwarz, T. Weber, M. Müller, R. Böhm, and M. Gude. Forming Analysis of Internal Plies of Multi-Layer Unidirectional Textile Preforms using Projectional Radiography. *Procedia Manufacturing*, 47:17–23, 2020.

[231] H. Krieger, T. Gries, and S. E. Stapleton. Shear and drape behavior of non-crimp fabrics based on stitching geometry. *International Journal of Material Forming*, 11(5):593–605, 2018.

[232] A. Mallach, F. Härtel, F. Heieck, J.-P. Fuhr, P. Middendorf, and M. Gude. Experimental comparison of a macroscopic draping simulation for dry non-crimp fabric preforming on a complex geometry by means of optical measurement. *Journal of Composite Materials*, 51(16):2363–2375, 2017.

[233] T.-C. Lim and S. Ramakrishna. Modelling of composite sheet forming: a review. *Composites Part A: Applied Science and Manufacturing*, 33(4):515–537, 2002.

[234] S. G. Hancock and K. D. Potter. The use of kinematic drape modelling to inform the hand lay-up of complex composite components using woven reinforcements. *Composites Part A: Applied Science and Manufacturing*, 37(3):413–422, 2006.

[235] A. Cherouat, H. Borouchaki, and J.-L. Billoët. Geometrical and mechanical draping of composite fabric. *Revue Européenne des Éléments*, 14(6-7):693–707, 2012.

[236] H. Köke, L. Weiß, C. Hühne, and M. Sinapius. A graph-based method for calculating draping strategies for the application of fiber-reinforced materials on arbitrary surfaces. *Composite Structures*, 162:123–132, 2017.

[237] B. Fengler, L. Kärger, F. Henning, and A. Hrymak. Multi-Objective Patch Optimization with Integrated Kinematic Draping Simulation for Continuous–Discontinuous Fiber-Reinforced Composite Structures. *Journal of Composites Science*, 2(2):22, 2018.

[238] E. Syerko, S. Comas-Cardona, and C. Binetruy. Models of mechanical properties/behavior of dry fibrous materials at various scales in bending and tension: A review. *Composites Part A: Applied Science and Manufacturing*, 43(8):1365–1388, 2012.

[239] P. Boisse, R. Bai, J. Colmars, N. Hamila, B. Liang, and A. Madeo. The Need to Use Generalized Continuum Mechanics to Model 3D Textile Composite Forming. *Applied Composite Materials*, 47(11), 2018.

[240] T. Belytschko, W. K. Liu, B. Moran, and K. I. Elkhodary. *Nonlinear finite elements for continua and structures*. John Wiley & Sons, Ltd, Chichester, UK, 2. edition, 2014.

[241] P. Badel, S. Gauthier, E. Vidal-Sallé, and P. Boisse. Rate constitutive equations for computational analyses of textile composite reinforcement mechanical behaviour during forming. *Composites Part A: Applied Science and Manufacturing*, 40(8):997–1007, 2009.

[242] T. J. R. Hughes and Winget J. Finite rotation effects in numerical integration of rate constitutive equations arising in large-deformation analysis. *Numerical Methods in Engineering*, 15(12):1862–1867, 1980.

[243] A. Willems. *Forming simulations of textile reinforced composite shell structures*. Dissertation, KU Leuven, Leuven, Belgien, 2008.

[244] Y. Aimène, E. Vidal-Sallé, B. Hagège, F. Sidoroff, and P. Boisse. A Hyperelastic Approach for Composite Reinforcement Large Deformation Analysis. *Journal of Composite Materials*, 44(1):5–26, 2010.

[245] G. A. Holzapfel. *Nonlinear Solid Mechanics: A Continuum Approch for Engineering*. John Wiley & Sons Ltd, West Sussex, England, 2000.

[246] Y. Yao, X. Peng, and Y. Gong. Influence of tension–shear coupling on draping of plain weave fabrics. *Journal of Materials Science*, 54(8):6310–6322, 2019.

[247] F. Schäfer, H. O. Werner, F. Henning, and L. Kärger. A hyperelastic material model considering biaxial coupling of tension–compression and shear for the forming simulation of woven fabrics. *Composites Part A: Applied Science and Manufacturing*, 165(4):107323, 2023.

[248] G. A. Maugin. Generalized Continuum Mechanics: What Do We Mean by That? In G. A. Maugin and A. V. Metrikine, editors, *Mechanics of Generalized Continua: One Hundred Years After the Cosserats*, pages 3–13. Springer New York, New York, NY, 2010.

[249] B. Ben Boubaker, B. Haussy, and J.F. Ganghoffer. Discrete models of woven structures. Macroscopic approach. *Composites Part B: Engineering*, 38(4):498–505, 2007.

[250] S. B. Sharma and M. Sutcliffe. A simplified finite element model for draping of woven material. *Composites Part A: Applied Science and Manufacturing*, 35(6):637–643, 2004.

[251] P. P. Valentini, M. Falcone, E. Marotta, E. Pennestrì, and P. Salvini. Theoretical and experimental characterization of a FEM element assembly for the simulation of very compliant knitted mesh. *International Journal for Numerical Methods in Engineering*, 107(5):419–429, 2016.

[252] D. Colin, S. Bel, T. Hans, M. Hartmann, and K. Drechsler. Virtual Description of Non-Crimp Fabrics at the Scale of Filaments Including Orientation Variability in the Fibrous Layers. *Applied Composite Materials*, 27(4):337–355, 2020.

[253] A. A. Skordos, C. Monroy Aceves, and M. Sutcliffe. A simplified rate dependent model of forming and wrinkling of pre-impregnated woven composites. *Composites Part A: Applied Science and Manufacturing*, 38(5):1318–1330, 2007.

[254] B. B. Boubaker, B. Haussy, and J.-F. Ganghoffer. Discrete models of fabric accounting for yarn interactions. *Revue Européenne des Éléments*, 14(6-7):653–675, 2005.

[255] K. Y. Sze and X. H. Liu. A new skeletal model for fabric drapes. *International Journal of Mechanics and Materials in Design*, 2(3-4):225–243, 2005.

[256] A. Cherouata and J. L. Billoet. Mechanical and numerical modelling of composite manufacturing processes deep-drawing and laying-up of thin pre-impregnated woven fabrics. *Journal of Materials Processing Technology*, 118:460–471, 2001.

[257] J. L. Gorczyca, J. A. Sherwood, and J. Chen. A friction model for use with a commingled fiberglass-polypropylene plain-weave fabric and the metal tool during thermostamping. *Revue Européenne des Éléments Finis*, 14(6-7):729–751, 2005.

[258] S. Chen, A. Endruweit, L. T. Harper, and N. A. Warrior. Inter-ply stitching optimisation of highly drapeable multi-ply preforms. *Composites Part A: Applied Science and Manufacturing*, 71(4):144–156, 2015.

[259] M. V. d'Agostino, I. Giorgio, L. Greco, A. Madeo, and P. Boisse. Continuum and discrete models for structures including (quasi-) inextensible elasticae with a view to the design and modeling of composite reinforcements. *International Journal of Solids and Structures*, 59:1–17, 2015.

[260] A. Madeo, G. Barbagallo, M. V. D'Agostino, and P. Boisse. Continuum and discrete models for unbalanced woven fabrics. *International Journal of Solids and Structures*, 94-95:263–284, 2016.

[261] P. Harrison. Modelling the forming mechanics of engineering fabrics using a mutually constrained pantographic beam and membrane mesh. *Composites Part A: Applied Science and Manufacturing*, 81:145–157, 2016.

[262] Z. Yousaf, P. Potluri, and P. J. Withers. Influence of Tow Architecture on Compaction and Nesting in Textile Preforms. *Applied Composite Materials*, 24(2):337–350, 2017.

[263] P. Boisse, A. Gasser, B. Hagege, and J.-L. Billoet. Analysis of the mechanical behavior of woven fibrous material using virtual tests at the unit cell level. *Journal of Materials Science*, 40(22):5955–5962, 2005.

[264] P. Badel, E. Vidal-Sallé, and P. Boisse. Computational determination of in-plane shear mechanical behaviour of textile composite reinforcements. *Computational Materials Science*, 40(4):439–448, 2007.

[265] H. Lin, A. C. Long, M. Sherburn, and M. J. Clifford. Modelling of mechanical behaviour for woven fabrics under combined loading. *International Journal of Material Forming*, 1(1):899–902, 2008.

[266] Y. Wang, W. Zhang, H. Ren, Z. Huang, F. Geng, Y. Li, and Z. Zhu. An Analytical Model for the Tension-Shear Coupling of Woven Fabrics with Different Weave Patterns under Large Shear Deformation. *Applied Sciences*, 10(4):1551, 2020.

[267] S. Lomov, D. Ivanov, I. Verpoest, M. Zako, T. Kurashiki, H. Nakai, and S. Hirosawa. Meso-FE modelling of textile composites: Road map, data flow and algorithms. *Composites Science and Technology*, 67(9):1870–1891, 2007.

[268] R. Zheng, B. Schäfer, A. Platzer, J. Colmars, N. Naouar, and P. Boisse. A unit-cell mesoscale modelling of biaxial non-crimp-fabric based on a hyperelastic approach. *Materials Research Proceedings*, 28:285–292, 2023.

[269] D. Wang, N. Naouar, E. Vidal-Salle, and P. Boisse. Longitudinal compression and Poisson ratio of fiber yarns in meso-scale finite element modeling of composite reinforcements. *Composites Part B: Engineering*, 141:9–19, 2018.

[270] Q. T. Nguyen, E. Vidal-Sallé, P. Boisse, C. H. Park, A. Saouab, J. Bréard, and G. Hivet. Mesoscopic scale analyses of textile composite reinforcement compaction. *Composites Part B: Engineering*, 44(1):231–241, 2013.

[271] R. Tavana, S. S. Najar, M. T. Abadi, and M. Sedighi. Meso/macro-scale finite element model for forming process of woven fabric reinforcements. *Journal of Composite Materials*, 47(17):2075–2085, 2013.

[272] A. J. Thompson, B. El Said, J. P.-H. Belnoue, and S. R. Hallett. Modelling process induced deformations in 0/90 non-crimp fabrics at the meso-scale. *Composites Science and Technology*, 168(1–4):104–110, 2018.

[273] J. Wang, P. Wang, N. Hamila, and P. Boisse. Mesoscopic analyses of the draping of 3D woven composite reinforcements based on macroscopic simulations. *Composite Structures*, 250:112602, 2020.

[274] A. Iwata, T. Inoue, N. Naouar, P. Boisse, and S. V. Lomov. Coupled meso-macro simulation of woven fabric local deformation during draping. *Composites Part A: Applied Science and Manufacturing*, 118:267–280, 2019.

[275] A. Iwata, T. Inoue, N. Naouar, P. Boisse, and S. V. Lomov. Meso-macro simulation of the woven fabric local deformation in draping. *AIP Conference Proceedings*, 1960(1):020012, 2018.

[276] P. Boisse, H. Hamila, P. Wang, S. Gatouillat, S. Bel, and A. Charmetant. Composite reinforcement forming simulation: continous and mesoscopic approaches. In *Proceedings of the 18th International Conference on Composite Materials (ICCM18)*, 2011.

[277] P. Böhler, F. Härtel, and P. Middendorf. Identification of Forming Limits for Unidirectional Carbon Textiles in Reality and Mesoscopic Simulation. *Key Engineering Materials*, 554-557:423–432, 2013.

[278] T. Senner, S. Kreissl, M. Merklein, J. Meinhardt, and A. Lipp. A modular modeling approach for describing the in-plane forming behavior of unidirectional non-crimp-fabrics. *Production Engineering*, 8(5):635–643, 2014.

[279] A. Margossian, S. Bel, J. M. Balvers, D. Leutz, R. Freitas, and R. Hinterhoelzl. Finite element forming simulation of locally stitched non-crimp fabrics. *Composites Part A: Applied Science and Manufacturing*, 61(0):152–162, 2014.

[280] P. Boisse, N. Hamila, E. Vidal-Sallé, and F. Dumont. Simulation of wrinkling during textile composite reinforcement forming. Influence of tensile, in-plane shear and bending stiffnesses. *Composites Science and Technology*, 71(5):683–692, 2011.

[281] D. Dörr, T. Joppich, D. Kugele, F. Henning, and L. Kärger. A coupled thermomechanical approach for finite element forming simulation of continuously fiber-reinforced semi-crystalline thermoplastics. *Composites Part A: Applied Science and Manufacturing*, 125:105508, 2019.

[282] G. Barbagallo, A. Madeo, F. Morestin, and P. Boisse. Modelling the deep drawing of a 3D woven fabric with a second gradient model. *Mathematics and Mechanics of Solids*, 22(11):2165–2179, 2017.

[283] W. R. Yu, M. Zampaloni, F. Pourboghrat, K. Chung, and T. J. Kang. Analysis of flexible bending behavior of woven preform using non-orthogonal constitutive equation. *Composites Part A: Applied Science and Manufacturing*, 36(6):839–850, 2005.

[284] D. Colin. *Virtual Development of Non-Crimp Fabrics_Numerical Textile Description at the Scale of the Filaments and Forming Simulation.* Dissertation, Technical University of Munich, Munich, Germany, 2021.

[285] O. Döbrich, T. Gereke, O. Diestel, S. Krzywinski, and C. Cherif. Decoupling the bending behavior and the membrane properties of finite shell elements for a correct description of the mechanical behavior of textiles with a laminate formulation. *Journal of Industrial Textiles*, 44(1):70–84, 2014.

[286] X. Yu, B. Cartwright, D. McGuckin, L. Ye, and Y.-W. Mai. Intra-ply shear locking in finite element analyses of woven fabric forming processes. *Composites Part A: Applied Science and Manufacturing*, 37(5):790–803, 2006.

[287] N. Hamila and P. Boisse. Locking in simulation of composite reinforcement deformations. Analysis and treatment. *Composites Part A: Applied Science and Manufacturing*, 53:109–117, 2013.

[288] R. t. Thije and R. Akkerman. Solutions to intra-ply shear locking in finite element analyses of fibre reinforced materials. *Composites Part A: Applied Science and Manufacturing*, 39(7):1167–1176, 2008.

[289] P. Boisse, M. Borr, K. Buet, and A. Cherouat. Finite element simulations of textile composite forming including the biaxial fabric behaviour. *Composites Part B: Engineering*, 28(4):453–464, 1997.

[290] N. Hamila and P. Boisse. Simulations of textile composite reinforcement draping using a new semi-discrete three node finite element. *Composites Part B: Engineering*, 39(6):999–1010, 2008.

[291] N. Hamila, P. Boisse, F. Sabourin, and M. Brunet. A semi-discrete shell finite element for textile composite reinforcement forming simulation. *International Journal for Numerical Methods in Engineering*, 79(12):1443–1466, 2009.

[292] T. Abdul Ghafour, J. Colmars, and P. Boisse. The importance of taking into account behavior irreversibilities when simulating the forming of textile composite reinforcements. *Composites Part A: Applied Science and Manufacturing*, 127:105641, 2019.

[293] R. Bai, J. Colmars, N. Naouar, and P. Boisse. A specific 3D shell approach for textile composite reinforcements under large deformation. *Composites Part A: Applied Science and Manufacturing*, 139:106135, 2020.

[294] P. Wang, N. Hamila, and P. Boisse. Thermoforming simulation of multilayer composites with continuous fibres and thermoplastic matrix. *Composites Part B: Engineering*, 52:127–136, 2013.

[295] X. Peng, Z. Guo, T. Du, and W.-R. Yu. A simple anisotropic hyperelastic constitutive model for textile fabrics with application to forming simulation. *Composites Part B: Engineering*, 52:275–281, 2013.

[296] L. Kärger, F. Schäfer, and H. O. Werner. Modeling multiaxial stress states in forming simulation of woven fabrics. *Materials Research Proceedings*, 28:357–366, 2023.

[297] L. Kärger, S. Galkin, E. Kunze, M. Gude, and B. Schäfer. Prediction of forming effects in UD-NCF by macroscopic forming simulation – Capabilities and limitations. In *Proceedings of the 24th International Conference on Material Forming*, 2021.

[298] M. Ghazimoradi and J. Montesano. Macroscopic Forming Simulation for a Unidirectional Non-crimp Fabric Using an Anisotropic Hyperelastic Material Model. *Applied Composite Materials*, 55(3):171, 2023.

[299] G. Barbagallo, A. Madeo, I. Azehaf, I. Giorgio, F. Morestin, and P. Boisse. Bias extension test on an unbalanced woven composite reinforcement: Experiments and modeling via a second-gradient continuum approach. *Journal of Composite Materials*, 51(2):153–170, 2017.

[300] G. Barbagallo, M. V. D'Agostino, A. Aivaliotis, A. Daouadji, A. Makradi, G. Giunta, P. Boisse, S. Belouettar, and A. Madeo. Model reduction for the forming process of fibrous composites structures via second gradient enriched continuum models. *Mechanics of Advanced Materials and Structures*, 28(10):1061–1072, 2021.

[301] Q. Steer, J. Colmars, N. Naouar, and P. Boisse. Modeling and analysis of in-plane bending in fibrous reinforcements with rotation-free shell finite elements. *International Journal of Solids and Structures*, 222-223:111014, 2021.

[302] S. Mathieu, N. Hamila, F. Dupé, C. Descamps, and P. Boisse. Stability of 3D Textile Composite Reinforcement Simulations: Solutions to Spurious Transverse Modes. *Applied Composite Materials*, 23(4):739–760, 2016.

[303] T. X. Duong, M. Itskov, and R. A. Sauer. A general isogeometric finite element formulation for rotation–free shells with in–plane bending of embedded fibers. *International Journal for Numerical Methods in Engineering*, 123(14):3115–3147, 2022.

[304] P. Potluri and T. V. Sagar. Compaction modelling of textile preforms for composite structures. *Composite Structures*, 86(1-3):177–185, 2008.

[305] D. Colin, S. Bel, T. Hans, and M. Hartmann. Virtual description of a biaxial 0°/90° non-crimp fabric with normally distributed filament directions. *AIP Conference Proceedings*, 2113(1):020009, 2019.

[306] D. Bublitz. *A material model for the compaction process simulation of carbon fiber preforms*. Dissertation, Technical University of Munich, Munich, Germany, 2023.

[307] F. Koschnick. *Geometrische Locking-Effekte bei Finiten Elementen und ein allgemeines Konzept zu ihrer Vermeidung*. Dissertation (in german), Technical University of Munich, Munich, Germany, 2004.

[308] M. Bischoff. *Theorie und Numerik einer dreidimensionalen Schalenformulierung*. Dissertation (in German), University of Stuttgart, Stuttgart, Germany, 1999.

[309] M. Wagner. *Lineare und nichtlineare FEM: Eine Einführung mit Anwendungen in der Umformsimulation mit LS-DYNA*. Springer Vieweg, Wiesbaden, Germany, 2. edition, 2019.

[310] O. C. Zienkiewicz, D. Fox, and R. L. Taylor. *The finite element method for solid and structural mechanics*. Butterworth-Heinemann, Oxford, United Kingdom, 7. edition, 2014.

[311] K.-J. Bathe and E. N. Dvorkin. A formulation of general shell elements-the use of mixed interpolation of tensorial components. *International Journal for Numerical Methods in Engineering*, 22:697–722, 1986.

[312] J. C. Simo and M. S. Rifai. A class of mixed assumed strain methods and the method of incompatible modes. *International Journal for Numerical Methods in Engineering*, 29(8):1595–1638, 1990.

[313] K. Rah, W. van Paepegem, A. M. Habraken, R. A. d. Sousa, and R. A. F. Valente. Evaluation of different advanced finite element concepts for detailed stress analysis of laminated composite structures. *International Journal of Material Forming*, 2(S1):943–947, 2009.

[314] M. Schwarze and S. Reese. A reduced integration solid-shell finite element based on the EAS and the ANS concept-Geometrically linear problems. *International Journal for Numerical Methods in Engineering*, 80(10):1322–1355, 2009.

[315] M. Mostafa. An improved solid-shell element based on ANS and EAS concepts. *International Journal for Numerical Methods in Engineering*, 108(11):1362–1380, 2016.

[316] M. Mostafa. *A Geometric Nonlinear Solid-Shell Element Based on ANS, ANDES and EAS Concepts*. Dissertation, University of Colorado, Boulder, CO, USA, 2011.

[317] R. Hauptmann and K. Schweizerhof. A systematic development of 'solid–shell' element formulations for linear and non–linear analyses employing only displacement degrees of freedom. *International Journal for Numerical Methods in Engineering*, 42(1):49–69, 1998.

[318] M. Harnau, K. Schweizerhof, and R. Hauptmann. On solid-shell elements with linear and quadratic shape functions for small and large deformations. In *Proceedings of the European Congress on Computational Methods in Applied Sciences and Engineering (ECCOMAS 2000)*, 2000.

[319] R. Hauptmann, K. Schweizerhof, and S. Doll. Extension of the 'solid-shell' concept for application to large elastic and large elastoplastic deformations. *International Journal for Numerical Methods in Engineering*, 49(9):1121–1141, 2000.

[320] R. Hauptmann, S. Doll, M. Harnau, and K. Schweizerhof. 'Solid-shell' elements with linear and quadratic shape functions at large deformations with nearly incompressible materials. *Computers & Structures*, 79(18):1671–1685, 2001.

[321] S. Mattern. *Hocheffiziente Formulierung und Implementierung finiter Elemente für transiente Analysen mit expliziter Zeitintegration.* Dissertation (in German), Karlsruhe Institute of Technology, Karlsruhe, Germany, 2012.

[322] S. Mattern, C. Schmied, and K. Schweizerhof. Highly efficient solid and solid-shell finite elements with mixed strain–displacement assumptions specifically set up for explicit dynamic simulations using symbolic programming. *Computers & Structures*, 154:210–225, 2015.

[323] K. Jože. Multi-language and Multi-environment Generation of Nonlinear Finite Element Codes. *Engineering with Computers*, 18(4):312–327, 2002.

[324] L. Vu-Quoc and X. G. Tan. Optimal solid shells for non-linear analyses of multilayer composites. I. Statics. *Computer Methods In Applied Mechanics And Engineering*, 192(9-10):975–1016, 2003.

[325] L. Vu-Quoc and X. G. Tan. Optimal solid shells for non-linear analyses of multilayer composites. II. Dynamics. *Computer Methods In Applied Mechanics And Engineering*, 192(9-10):1017–1059, 2003.

[326] L. Vu-Quoc and X. Tan. Efficient Hybrid-EAS solid element for accurate stress prediction in thick laminated beams, plates, and shells. *Computer Methods In Applied Mechanics And Engineering*, 253:337–355, 2013.

[327] S. Reese, P. Wriggers, and B. D. Reddy. A new locking-free brick element technique for large deformation problems in elasticity. *Computers & Structures*, 75(3):291–304, 2000.

[328] R. J. Alves de Sousa, R. P. Cardoso, R. A. Fontes Valente, J.-W. Yoon, J. J. Grácio, and R. M. Natal Jorge. A new one-point quadrature enhanced assumed strain (EAS) solid-shell element with multiple integration points along thickness: Part I-geometrically linear applications. *International Journal for Numerical Methods in Engineering*, 62(7):952–977, 2005.

[329] R. J. Alves de Sousa, R. P. R. Cardoso, R. A. Fontes Valente, J.-W. Yoon, J. J. Grácio, and R. M. Natal Jorge. A new one-point quadrature enhanced assumed strain (EAS) solid-shell element with multiple integration points along thickness—part II: nonlinear applications. *International Journal for Numerical Methods in Engineering*, 67(2):160–188, 2006.

[330] R. Alves De Sousa, J. Yoon, R. Cardoso, R. Fontes Valente, and J. Gracio. On the use of a reduced enhanced solid-shell (RESS) element for sheet forming simulations. *International Journal of Plasticity*, 23(3):490–515, 2007.

[331] R. P. R. Cardoso, J. W. Yoon, M. Mahardika, S. Choudhry, R. J. Alves de Sousa, and R. A. Fontes Valente. Enhanced assumed strain (EAS) and assumed natural strain (ANS) methods for one–point quadrature solid–shell elements. *International Journal for Numerical Methods in Engineering*, 75(2):156–187, 2008.

[332] M. Schwarze and S. Reese. A reduced integration solid-shell finite element based on the EAS and the ANS concept-Large deformation problems. *International Journal for Numerical Methods in Engineering*, 85(3):289–329, 2011.

[333] M. Pagani, S. Reese, and U. Perego. Computationally efficient explicit nonlinear analyses using reduced integration-based solid-shell finite elements. *Computer Methods In Applied Mechanics And Engineering*, 268:141–159, 2014.

[334] J.-W. Simon, B. Stier, and S. Reese. A solid-shell finite element for fibre reinforced composites. *Proceedings in Applied Mathematics and Mechanics (PAMM)*, 12(1):329–330, 2012.

[335] O. Barfusz, R. Smeenk, and S. Reese. Solid-shell formulations based on reduced integration - investigations of anisotropic material behaviour at large deformations. *Proceedings in Applied Mathematics and Mechanics (PAMM)*, 18(1):e201800078, 2018.

[336] M. Schwarze, I. N. Vladimirov, and S. Reese. Sheet metal forming and springback simulation by means of a new reduced integration solid-shell finite element technology. *Computer Methods In Applied Mechanics And Engineering*, 200(5-8):454–476, 2011.

[337] K. Robertsson, E. Borgqvist, M. Wallin, M. Ristinmaa, J. Tryding, A. Giampieri, and U. Perego. Efficient and accurate simulation of the packaging forming process. *Packaging Technology and Science*, 31(8):557–566, 2018.

[338] R. A. F. Valente, R. J. A. d. Sousa, R. M. N. Jorge, R. P. R. Cardoso, F. Simões, J. W. Yoon, and J. Grácio. An overview of sheet metal forming simulations with enhanced assumed strain elements. *AIP Conference Proceedings*, 908(1):741–746, 2007.

[339] M. Parente, R. A. Fontes Valente, R. M. Natal Jorge, R. Cardoso, and R. J. Alves de Sousa. Sheet metal forming simulation using EAS solid-shell finite elements. *Finite Elements in Analysis and Design*, 42(13):1137–1149, 2006.

[340] A. B. Bettaieb, J. Velosa de Sena, R. J. Alves de Sousa, R. Valente, A. M. Habraken, and L. Duchêne. On the comparison of two solid-shell formulations based on in-plane reduced and full integration schemes in linear and non-linear applications. *Finite Elements in Analysis and Design*, 107:44–59, 2015.

[341] Q. Q. Chen, A. Saouab, P. Boisse, C. H. Park, and J. Bréard. Woven thermoplastic composite forming simulation with solid-shell element method. *International Journal for Simulation and Multidisciplinary Design Optimization*, 3(2):337–341, 2009.

[342] Q. Chen, P. Boisse, C. H. Park, A. Saouab, and J. Bréard. Intra/inter-ply shear behaviors of continuous fiber reinforced thermoplastic composites in thermoforming processes. *Composite Structures*, 93(7):1692–1703, 2011.

[343] C. Poppe, F. Albrecht, C. Krauß, and L. Kärger. A 3D Modelling Approach for Fluid Progression during Process Simulation of Wet Compression Moulding – Motivation & Approach. *Procedia Manufacturing*, 47:85–92, 2020.

[344] C. Eberl. Digital image correlation and tracking. *MATLAB Central File Exchange* - available online: `https://www.mathworks.com/matlabcentral/fileexchange/12413-digital-image-correlation-and-tracking`, 2023. last access date: 16.01.2023.

[345] S. Galkin, E. Kunze, L. Kärger, R. Böhm, and M. Gude. Experimental and Numerical Determination of the Local Fiber Volume Content of Unidirectional Non-Crimp Fabrics with Forming Effects. *Journal of Composites Science*, 3(1):19, 2019.

[346] F. Härtel and P. Harrison. Evaluation of normalisation methods for uniaxial bias extension tests on engineering fabrics. *Composites Part A: Applied Science and Manufacturing*, 67:61–69, 2014.

[347] German Industrial Standard. *Testing of plastics films and textile fabrics (excluding nonwovens), coated or not coated fabrics - Determination of stiffness in bending - Method according to Cantilever: DIN 53362 / ICS 59.080.40; 83.140.10*. Beuth Verlag GmbH, Berlin, Germany, 2003.

[348] F. Behnisch, V. Lichtner, F. Henning, and P. Rosenberg. Development of a Reactive Polyurethane Foam System for the Direct Sandwich Composite Molding (D-SCM) Process. *Journal of Composites Science*, 5(4):104, 2021.

[349] P. Boisse, J. Huang, and E. Guzman-Maldonado. Analysis and Modeling of Wrinkling in Composite Forming. *Journal of Composites Science*, 5(3):81, 2021.

[350] Y. Gong, D. Yan, Y. Yao, R. Wei, H. Hu, P. Xu, and X. Peng. An Anisotropic Hyperelastic Constitutive Model with Tension–Shear Coupling for Woven Composite Reinforcements. *International Journal of Applied Mechanics*, 09(06):1750083, 2017.

[351] J. A. Nelder and R. Mead. A Simplex Method for Function Minimization. *The Computer Journal*, 7(4):308–313, 1965.

[352] B. Schäfer, D. Dörr, and L. Kärger. Reduced-Integrated 8-Node Hexahedral Solid-Shell Element for the Macroscopic Forming Simulation of Continuous Fibre-Reinforced Polymers. *Procedia Manufacturing*, 47:134–139, 2020.

[353] B. Schäfer, D. Dörr, and L. Kärger. Potential and challenges of a solid-shell element for the macroscopic forming simulation of engineering textiles. In *Proceedings of the 24th International Conference on Material Forming*, 2021.

[354] P. Betsch and E. Stein. An assumed strain approach avoiding artificial thickness straining for a non-linear 4-node shell element. *Communications in Numerical Methods in Engineering*, 11(11):899–909, 1995.

[355] J. Simo, F. Armero, and R. Taylor. Improved versions of assumed enhanced strain tri-linear elements for 3D finite deformation problems. *Computer Methods In Applied Mechanics And Engineering*, 110:359–386, 1993.

[356] T. J. R. Hughes. Generalization of selective integration procedures to anisotropic and nonlinear media. *International Journal for Numerical Methods in Engineering*, 15(9):1413–1418, 1980.

[357] M. Smith. *ABAQUS/Standard User's Manual, Version 2022*. Dassault Systèmes Simulia Corp, United States, 2021.

[358] M. A. Puso. A highly efficient enhanced assumed strain physically stabilized hexahedral element. *International Journal for Numerical Methods in Engineering*, 49(8):1029–1064, 2000.

[359] S. Reese. A large deformation solid-shell concept based on reduced integration with hourglass stabilization. *International Journal for Numerical Methods in Engineering*, 69(8):1671–1716, 2007.

[360] D. Dörr, L. Lipowsky, F. J. Schirmaier, L. Kärger, and F. Henning. An Iterative Approach for the Determination of Tailored Blanks for Waste-Free Composite Forming by Means of FE Forming Simulation. *International Journal of Automotive Composites: Special Issue: "Automotive Composites"*, 3(2–4):323–338, 2017.

List of Publications

Journal articles

- B. Schäfer, R. Zheng, N. Naouar, and L. Kärger. Membrane behavior of uni- and bidirectional non-crimp fabrics in off-axis-tension tests. *International Journal of Material Forming*, 16(6):68, 2023.
- B. Schäfer, R. Zheng, J. Colmars, A. Platzer, N. Naouar, P. Boisse, L. Kärger. Experimental analysis of the forming behavior of uni- and bidirectional non-crimp fabrics for different geometries. *[submitted for review]*
- B. Schäfer, D. Dörr, R. Zheng, N. Naouar, and L. Kärger. A hyperelastic approach for modeling the membrane behavior in finite element forming simulation of unidirectional non-crimp fabrics (UD-NCF). *[submitted for review]*

Conference contributions | With proceedings (peer-reviewed)

- B. Schäfer, D. Dörr, and L. Kärger. Reduced-Integrated 8-Node Hexahedral Solid-Shell Element for the Macroscopic Forming Simulation of Continuous Fibre-Reinforced Polymers. *Procedia Manufacturing*, 47:134–139, ESAFORM 2020, Cottbus/Germany, 2020.

- B. Schäfer, D. Dörr, and L. Kärger. Potential and challenges of a solid-shell element for the macroscopic forming simulation of engineering textiles. *PoP-uPS of ULiège Library*, DOI: 10.25518/esaform21.883, ESAFORM 2021, Liège/Belgium, 2021.
- B. Schäfer, S. Haas, P. Boisse, and L. Kärger. Investigation of the Membrane Behavior of UD-NCF in Macroscopic Forming Simulations. *Key Engineering Materials*, 926:1413–1422, ESAFORM 2022, Braga/Portugal, 2022.
- B. Schäfer, R. Zheng, P. Boisse, and L. Kärger. Investigation of the compaction behavior of uni- and bidirectional non-crimp fabrics. *Materials Research Proceedings*, 28:331–338, ESAFORM 2023, Kraków/Poland, 2023.
- B. Schäfer, R. Zheng, N. Naouar, and L. Kärger. Investigation of the friction behavior of uni- and bidirectional non-crimp fabrics. *Materials Research Proceedings*, 41:540–548, ESAFORM 2024, Toulouse/France, 2024.

Co-authored journal articles

- B. Fengler, M. Schäferling, B. Schäfer, L. Bretz, G. Lanza, B. Häfner, A. Hrymak, and L. Kärger. Manufacturing uncertainties and resulting robustness of optimized patch positions on continuous-discontinuous fiber reinforced polymer structures. *Composite Structures*, 213(2):47–57, 2019.
- R. Zheng, N. Naouar, J. Colmars, A. Platzer, B. Schäfer, F. Morestin, L. Kärger, P. Boisse. Mesoscopic finite element modeling of biaxial non-crimp fabric including representative stitch pattern. *Composite Structures*, 339:118126, 2024.

Co-authored conference contributions

With proceedings (peer-reviewed)

- L. Kärger, S. Galkin, E. Kunze, M. Gude, and B. Schäfer. Prediction of forming effects in UD-NCF by macroscopic forming simulation – Capabilities and limitations. *PoPuPS of ULiège Library*, DOI: 10.25518/esaform21.355, ESAFORM 2021, Liège/Belgium, 2021

- R. Zheng, B. Schäfer, A. Platzer, J. Colmars, N. Naouar, and P. Boisse. A unit-cell mesoscale modelling of biaxial non-crimp-fabric based on a hyperelastic approach. *Materials Research Proceedings* 28:pp. 285–292, ESAFORM 2023, Kraków/Poland, 2023.

- R. Zheng, N. Naouar, B. Schäfer, A. Platzer, J. Colmars, L. Kärger, and P. Boisse. Draping of biaxial non-crimp fabric on hemispherical shape. *Materials Research Proceedings*, 41:623–630, ESAFORM 2024, Toulouse/France, 2024.

- R. M. Portela, B. Schäfer, L. Kärger, A. Rocha de Faria, and J. Montesano. Influence of viscosity, binder activation, and loading rate on the membrane response of an infiltrated UD-NCF. *Materials Research Proceedings*, 41:540–548, ESAFORM 2024, Toulouse/France, 2024.

- J. P. Wank, B. Schäfer, J. Mitsch, and L. Kärger. Strain gradient calculation as a basis for localized roving slip prediction in macroscopic forming simulation of non-crimp fabrics. *Materials Research Proceedings*, 41:467–476, ESAFORM 2024, Toulouse/France, 2024.

- J. Mitsch, B. Schäfer, J. P. Wank, and L. Kärger. Considering the viscoelastic material behavior in a solid-shell element for thermoforming simulation. *Materials Research Proceedings*, 41:457–466, ESAFORM 2024, Toulouse/France, 2024.

With proceedings

- R. Zheng, B. Schäfer, N. Naouar, J. Colmars, A. Platzer, and P. Boisse. Analysis of the in-plane shear behavior of biaxial non-crimp-fabric at mesoscopic scale. *Proceedings of the 2023 International Conference on Composite Materials*, ICCM 2023, Belfast/Northern Ireland, 2023.

Without proceedings

- D.Dörr, C. Poppe, C. Zimmerling, C. Krauß, B. Schäfer, F. Henning, and L. Kärger. Advanced Macroscopic Modelling Approaches for FE Composite Forming Simulation Using Abaqus, *Simulia Regional User Meeting*, Hanau, Deutschland, KITopen-ID: 1000099359, 04.12.2018